GRAIN- TO NANO-SCALE RECONSTRUCTIONS OF STRUCTURE AND CHEMISTRY IN ANCIENT LUNAR AND TERRESTRIAL ZIRCON

by

Tyler B. Blum

A dissertation submitted in partial fulfillment of the requirements for the degree of

Doctor of Philosophy

(Geoscience)

at the

UNIVERSITY OF WISCONSIN-MADISON

2019

Date of final oral examination: December 19, 2018

The dissertation is approved by the following members of the Final Oral Committee:

John W. Valley, Professor, Geoscience
Bradley S. Singer, Professor, Geoscience
Philip E. Brown, Professor, Geoscience
Huifang Xu, Professor, Geoscience
Susan Babcock, Professor, Material Science and Engineering

ACKNOWLEDGEMENTS

The Geoscience department at UW-Madison has provided a rich environment in which to develop as a geologist. The department would not run the way it does without numerous department staff each of whom have helped me on numerous occasions to answer questions, process critical paperwork, and enable research and travel opportunities, both domestic and abroad. These individuals include Michelle Szabo, Shirley Baxa, Jane Fox-Anderson, Karen Turino, the now retired Mary Schumann, and the departed Judy Gosse.

The data and results within this thesis have benefited from the contributions of numerous individuals. I feel privileged to know and learn from many talented scientists and peers (both past and present) as part of the WiscSIMS group, including Kouki Kitajima, Daisuke Nakashima, Travis Tenner, Ariel Strickland, Ken Williford, Takayuki Ushikubo, Noriko Kita, Jim Kern, and Michael Spicuzza. My training and introduction to Raman spectroscopy were provided by collaborators and co-authors Lutz Nasdala and Chutimun Chanmuang Nasdala. SHRIMP-RG age data were collected in collaboration with Matthew Coble at the Stanford-USGS facility. Preparation of atom probe specimens and atom probe experiments have been completed in collaboration with several members of CAMECA, Instruments (Yimeng Chen, David Olson, and David Reinhard), and David Reinhard is responsible my orientation with atom probe tomography (APT), as well as APT software and methods. Current and former individuals at CAMECA, Ty Prosa, David Larson, and Tom Kelly, have given ongoing support in the form of analysis, scientific commentary, and travel support. More recently, I have benefitted from collaborations with Baptiste Gault, and the atom probe group at the Max-Planck-Insitut für Eisenforschung, including Zirong Peng, Kevin Schweinar, and Leigh Stephenson. On numerous occasions, I have received technical help from a host of skilled researchers, technicians, faculty and staff including

Brian Hess, John Fournelle, Phil Gopon, Bil Schneider, Ben Abernathy, Patrick Kuhl, Peter Sobol, Neal Lord, and Michael Spicuzza, Ben Abernathy, and Harold Tobin. The UW Materials Science Center Atom Probe Facility enabled significant portions of my data processing through use of computer facilities.

My development as a geologist would not be complete without numerous interactions with talented classmates, office mates and peers, including: Adam Denny, Rachelle Turnier, Ryan J. Quinn, Emma Cameron, Jake Cammack, Anthony Pollington, Ian Orland, Andi Ellis, Allen Schaen, Richard Becker, Zach Michels, Susanna Webb, Nathan Anderson, Randy Williams, Philip Gopon, Christy Gopon, Andrew Walters, Ray Ostrander, Allie Wende, and Dana Smith.

My committee members – Professors Philip Brown, Huifang Xu, Bradley Singer, and Susan Babcock - have made important contributions to my development, including my knowledge base, my skills as a scientist, and my ability to communicate science to a variety of audiences. Their presence and evaluation have afforded opportunities for growth throughout the dissertation process. I am indebted to my advisor, John W. Valley, for his reliable financial support, his patience, and his skill as a mentor. He has, in an exacting manner, fortified my ability to think critically, and shown me the value of balancing introspection with progress. He has demonstrated how the human mind can flourish when it is focused on ideas, and not the merits of the people who produce them.

I thank my family, Mary, Ed, Tory, Travis and Trevor Blum, and who have been the single largest influence on my development as an individual. Finally, I thank my wife, Chloë E. Bonamici, one of the brightest and most talented people I have had the privilege to meet. My parents and siblings are the source of my ability to think critically, and along with Chloë, are

perpetual models of diligence, balance, pragmatism, and self-reflection. It will always be a challenge to live up to their examples.

Table of Contents

CHAPTER 1

Introduction: tracking zircon structure and chemistry through time.

Tyler B. Blum[1]

[1]Department of Geoscience, University of Wisconsin – Madison, Madison, WI, 53706 USA.

Correspondence: tbblum@geology.wisc.edu

Introduction

In the study of Earth's geological evolution, the mineral zircon remains unique in the abundance of information it can provide, as well as the continuity of the zircon record, extending back to 4.4 Ga, only ~150 million years after the formation of the Earth. Zircon grains constitute the only physical materials which can be directly linked to the Hadean, the first ~500 million years of Earth's history, and a time period for which no physical *rocks* and been found. This aspect of the terrestrial zircon record also makes it one of the only physical records that can be directly compared between different planetary bodies (e.g., the Moon).

The utility of zircon in geological study originates from its abundance as an accessory phase in many rock types, its ability to accommodate a range of geologically important trace components during crystallization, and the physical and chemical resistance of crystalline zircon during weathering and erosion. The incorporation of trace amounts of U and Th form the basis for U-Pb dating of zircon using the $^{238}U \rightarrow ^{206}Pb$, $^{235}U \rightarrow ^{207}Pb$, and $^{232}Th \rightarrow ^{208}Pb$ decay chains, and while this constitutes the most common data gathered for zircon grains, zircon also is regularly analyzed for hafnium isotopes, rare earth elements, titanium concentrations, lithium (concentrations or isotopes) and oxygen isotopes. Correlating each of these data types with zircon age allows for tracing of numerous processes from provenance and the sedimentary record, to the timing and assimilation processes in magmas, to planet-scale changes in tectonics. On the Moon, zircon crystallization ages place an indirect constraint of solidification of the lunar magma ocean, and thus formation of the Moon itself, and are one of the few means to quantify the timing of lunar magmatism geographically.

Despite the many favorable properties and wide-ranging applications, the analysis and interpretation of zircon data are not without challenges. Zircon alteration and chemical exchange

has been well documented, and is often related the accumulation of radiation damage, induced by α-decay events within the $^{238}U \rightarrow ^{206}Pb$, $^{235}U \rightarrow ^{207}Pb$, and $^{232}Th \rightarrow ^{208}Pb$ decay chains. The energetic daughter nuclei produced during α-decay events generate small amorphous domains on the scale of 5-10 nm (Ewing et al., 2003); if these domains accumulate over time and persist, they begin to overlap and form a connected network through the zircon grain at the "first percolation point." Reaction and diffusion kinetics are orders of magnitude faster in radiation damaged versus pristine zircon (Cherniak et al., 1991; Cherniak and Watson, 2003) and thus, if exposed to high temperatures or fluids, these damaged zircons are predisposed to chemical exchange and alteration. Crystalline zircon can be recovered through annealing at temperatures above ~250^{o}C (Ewing et al., 2003), which in turn helps to limit diffusive exchange, and preserve primary chemistries. Alteration of zircon or even specific domains within a zircon, will overprint the primary chemical information from crystallization, and the misinterpretation of data from altered domains as "primary" introduces inaccuracies into a valuable geological record.

Atom probe tomography (APT) provides a novel means to study trace element and isotope chemistry on the nanometer scale - the length scale of radiation damage, annealing and diffusion processes. The first analyses of zircon by APT discovered trace element nanoclusters, preserved in zircon for billions of years (Valley et al., 2012; 2014a, 2015), and record information about the thermal and structural history of the zircon during cluster formation. The ability to measure trace elements and isotopes at the near-atomic scale is unique, and allows for the interrogation of nanoclusters (their number, morphology, chemistry and isotopic composition). There remain many unanswered questions regarding these nanoscale domains, including the timing, exact structures controlling their formation and how pervasive they are in nature. The following chapters present efforts to characterize zircon mineral grains over a variety

of length scales, in order to better understand both the origin and significance of these nanoscale features, as well as their utility in understanding zircon histories. Pairing APT data with other correlative analyses informs us about numerous aspects of the zircon record, both analytical and geological, including: (1) the nanoscale features averaged by micron-scale analyses, (2) the chemical potential driving forces and mechanisms involved in element redistribution, and (3) the nanoscale chemical record of a grain's time-temperature-structural state history.

Methods

This thesis employs several correlative techniques, each chosen specifically to characterize zircon structure and/or chemistry over different spatial scales. This chapter briefly summarizes the techniques utilized throughout this work, as well as the general contents of the following chapters.

Secondary Ion Mass Spectrometry (SIMS)

Secondary ion mass spectrometry (SIMS) is a well-established technique for characterization of zircon trace element and isotope chemistry on the micron scale. A sample is bombarded with a beam of Cs or O ions, effectively dislodging and sputtering the constituents of the target material. Some of these sputtered components are ionized and are accelerated away from the sample surface. This secondary beam of ions passes through a double-focusing mass spectrometer (the current generation of large radius instruments are capable of mass resolving powers ≥10,000). The spatial resolution of the technique is selected based on primary beam size, primary beam intensity, and desired precision. Through the use of well-characterized standard materials, the SIMS is an accurate and precise means of determining trace element abundance

and isotope ratios within spots that are 1 to 20 μm in diameter and ~1 μm deep. This spatial resolution is useful in the analysis of ancient zircons with complex growth histories and/or complex internal zoning. In the context of this thesis, SIMS provides micron-scale trace element and isotope data which are spatially correlated with atom probe specimens. This enables a first order constraint on open vs. closed system chemical behavior on the micron-scale through evaluation of U-Pb isotopes, and provides a "bulk" composition for measurements of trace elements and isotopes within atom probe data sets at the nanoscale.

Electron Backscatter Diffraction (EBSD)

Electron backscatter diffraction utilizes scattered electrons to determine crystal orientation on the micron-to-nanometer scale. Within a scanning electron microscope (SEM) a subset of incident electrons undergo a combination of inelastic and elastic scattering, ending with elastic scattering from Bragg planes within the crystal structure. This elastic scattering takes place in all directions, though it is preferentially in the forward direction (relative to the incident electron beam). The diffraction of electrons generates constructive interference, resulting a "surplus" and "deficit" of electrons (relative to the "background" of inelastic elections) in specific scattering cones. Ultimately, these cones intersect with the area detector forming bright and dark bands within a map of electron intensity; the geometry of these bands (e.g., width, orientation, angular relations, and symmetry) is related to the orientation, and underlying crystallography of the target material.

Within this study, mapping of individual zircon grains by EBSD provides a means to characterize zircon microstructure, such as low-angle (sub)grain boundaries resulting from crystal-plastic deformation (e.g., Moser et al., 2009), relative differences in crystallinity due to

differential accumulation of radiation damage, or planar deformation features induced by shock metamorphism (similar to Moser et al., 2011). Each of these aspects of the zircon crystallography offers information regarding its pressure and temperature history.

Laser Raman Spectroscopy

Confocal laser Raman spectroscopy is used to investigate aspects of a material's bond structure and underlying symmetry through Raman scattering of light. The phenomenon of Raman scattering arises from the fact that the polarizability (a second rank tensor describing the material response to an electric field) of a particular bond or molecular vibration changes throughout its vibrational range. As a result, a portion of scattered light will possess a frequency shift (relative to incident light) which is characteristic of the given bond/molecular vibrational mode. The intensity of Raman scattering relates to: (1) the Raman active electronic transitions for the particular material, and (2) the given experimental geometry (propagation of the incident light, polarization of incident light, detector geometry, etc.). The peak intensities and wavenumber shifts within a Raman spectrum contain information about the symmetry relations, coordination number and electronic structure of a material. The analytical volume for confocal laser Raman spectroscopy is on the order of 5 μm^3. In this thesis, Raman spectroscopy provides a semi-quantitative assessment of zircon structural state on a length scale intermittent between APT analysis and SIMS analysis.

The Raman behavior of pure, crystalline zircon has been explored by several authors (Dawson et al., 1971; Syme et al., 1977), as have the changes in Raman behavior related to trace element substitutions, radiation damage and structural recovery process (e.g., Zhang et al., 2000; Nasdala et al., 2001; Geisler et al., 2001). Within this work, the primary use of Raman

spectroscopy revolves around quantifying the structural state (specifically the preserved, or "effective" α-dose) of zircon thorough the relationship between peak width (fullwidth at half maximum, FWHM) and frequency shift of the $v_3(SiO_4)$ vibrational mode (Nasdala et al., 2001). In *unannealed* zircon, the relationship between FWHM and α-dose follows a linear relationship up to approximately the first percolation point (~2.0×10^{15} α-decays/mg):

$$\mathrm{FWHM}_{\mathrm{v3(SiO4)}} \approx 1.2 + 1.4 \cdot D_{total} \quad [1]$$

Where $\mathrm{FWHM}_{\mathrm{v3(SiO4)}}$ is the full width at half maximum of the $v_3(SiO_4)$ vibrational mode, and D_{total} is the total α-dose in units of 10^{15} α-decays/mg. This equation can be rearranged to calculate an effective α-dose, D_{eff}, based on measured $\mathrm{FWHM}_{\mathrm{v3(SiO4)}}$ of unknowns, which may or may not preserve the entirety of their total α-dose. Above the first percolation point, low signal levels and large uncertainties in measurement of peak-broadening and frequency shift limit quantitative analysis at accumulated doses using Raman spectroscopy. The total number of α-decays since crystallization can be calculated from the U and Th concentrations, and age, based on the relationship:

$$D_{total} = 8 \cdot {}^{238}N(\exp(\lambda_{238}t) - 1) + 7 \cdot {}^{235}N(\exp(\lambda_{235}t) - 1) + 6 \cdot {}^{232}N(\exp(\lambda_{232}t) - 1) \quad [2]$$

where D_{total} is α-dose per milligram, λ_{238}, λ_{235} and λ_{232} are the decay constants for ^{238}U, ^{235}U and ^{232}Th respectively, t is the age of the zircon (or zircon domain) and ${}^{238}N$, ${}^{235}N$ and ${}^{232}N$ are the number of ^{238}U, ^{235}U and ^{232}Th atoms per milligram of zircon. By comparing D_{total} and D_{eff}, it is possible to determine whether a specific zircon domain preserves the entirely of its radiation

damage, and the approximate percentage of annealing. The spatial resolution of confocal laser Raman is sufficient to determine the uniformity of damage within a single grain (e.g., Nasdala et al., 1996), as well as the approximate structural state of a specific domain sampled for APT. The complete vs. incomplete retention of radiation damage is an important parameter for interpreting the thermal history of a zircon and its host rock, as well as the presence/absence of a heterogeneous material structure on the nanoscale.

Atom Probe Tomography

Atom probe tomography combines projection microscopy with time-of-flight mass spectrometry. A needle-shaped specimen with an end tip radius on the order of 50-100 nm is held at high voltage and constituent atoms are field evaporated through application of a timed voltage pulse (for conductive materials), or laser pulse (for semiconductors and insulators). Evaporated ions are accelerated by the local electric field near the tip surface, which varies systematically across the surface of the needle-shaped specimen. A position-sensitive detector records both the position of incident ions in detector space, as well as their time of incidence. This information is then inverted to identify individual elements and isotopes based on mass-to-charge-state ratios, and reconstruct individual ion positions based on their incident position on the detector and specimen geometry (Gault et al., 2012; Larson et al., 2013). The current generation of atom probes have sub-nanometer spatial resolution, with typical mass-resolving powers around 1100, and detection limits around 10 parts per million atomic (Larson et al., 2013).

Reconstructed atom probe data sets are three-dimensional point clouds with between 10^7-10^9 reconstructed atomic positions. Count rates up to 10^7 ions/ hour and detection efficiencies of

50-80% allow for reconstructed volumes of 10^{-3}-10^{-4} μm^3. Several data-mining techniques have been developed to characterize compositional variations and short-range order within APT data, including isoconcentration surfaces, local composition analysis, *k*th nearest neighbor analysis, and Voronoi cells. These characterization methods enable the description of distinct compositional domains in their extent, spatial relations, and composition. It is important to note that the spatial and spectral (i.e., time of flight and/or mass-to-charge state ratio) analysis of APT data are intimately related, and thus spatial and spectral uncertainties are not, strictly speaking, independent. It will remain relevant in the course of this study to determine (1) the uncertainty in isotope ratios for atom probe analyses and (2) whether spectral analysis (compositional analysis) or spatial analysis (cluster definition, etc.) is the limiting factor in evaluating unique isotope/age relations within a given data set.

Chapter Outline

Chapter 2 summarizes work towards standardizing the reporting of APT data within the geosciences. The introduction and integration of APT into the geoscience community is ongoing, with the first influential papers on the topic published only five years ago (Valley et al., 2014a). Several members of the APT geoscience community recognized the benefit of establishing, early on, reporting standards for APT data in order to both encourage efficient review of results, and build a body of analytical knowledge within the community. T. Blum led the writing and revision of this document, and includes a brief discussion of the research directions, and analytical hurdles, moving forward.

Chapter 3 focuses on the spatial and spectral characterization of Pb within APT data sets, in the context of Archean metamorphism within the Beartooth Mountains, USA. Archean

quartzite lenses within the Quad Creek/Hellroaring Plateau region are one of only a few locations on Earth with 4.0 Ga zircon grains (Mueller et al., 1992). The host rocks for these detrital zircons have persisted through multiple periods of deformation, and a granulite facies metamorphic event at 3.25-3.1 Ga (e.g., Henry et al., 1984). The studies of Valley et al. (2014a, 2015) demonstrated that the nanoscale distribution of radiogenic Pb can offer novel insight into the timing and length scales of element redistribution, and Chapter 3 looks at a series of data sets from zircon BT5-13 to systematically evaluate uncertainties in the measurement of Pb isotopes in APT data sets. Each of the three APT data sets from the core of BT5-13 contains several sub-15nm Pb-rich (>0.25 atom% Pb) domains, enriched by a factor of ~10^2-10^3 over the surrounding matrix. Zircon BT5-13 contains two, 100% concordant U-Pb age determinations (3775 Ma) by SIMS, and thus has remained a closed U-Pb isotopic system on the micron scale since crystallization. Within BT5-13 clusters, high signal-to-background ratios result in $^{207}Pb/^{206}Pb$ uncertainties that are dominated by counting statistics. The general aspects of spectral analysis within this chapter are utilized in subsequent chapters (Chapters 5 and 6) to better understand the sensitivity of measured $^{207}Pb/^{206}Pb$ ratios to the spatial and spectral processing of data.

Chapter 4 applies a combination of SIMS, EBSD, and laser Raman, to understand the chemical and structural evolution of lunar zircons. The WiscSIMS lab has studied the oxygen isotope, lithium isotope, and trace element composition of a diverse set of lunar zircons (Spicuzza et al., 2011; Spicuzza et al., unpublished data; Valley et al., 2014b). These grains originate from four different Apollo missions, and include grains collected in centimeter sized clasts of their primary lithology, zircons that were isolated grains within breccias, or as loose zircons from fine lunar soils. Chapter 4 presents Raman spectroscopy, U-Pb geochronology and EBSD mapping that documents diverse microstructures, including only the third documented

case of shock microtwin lamellae from lunar samples, and the presence of significant annealing within the sample suite. These data are combined with a compilation of published U-Pb geochronology for lunar zircon, revealing both distinct age populations in different sample types (e.g., soil zircons vs. clast and breccia zircons) and distinct age populations between the Apollo landing sites. The former discovery suggests continued analysis of zircon may be a viable means to infer different lateral/vertical mixing trends. More generally, the distinct age populations present at different landing sites suggest that either the Imbrium basin-forming impact has not preferentially contaminated the Apollo landing sites, or the post-Imbrium redistribution of regolith material has introduced unique zircon age populations into the Apollo 12 and 14 regolith. Both hypotheses are critical for understanding the provenance of lunar samples and their relationship to the general thermal and magmatic evolution of the Moon.

Chapter 5 returns to the nanoscale, and builds on both the statistical considerations of Chapter 3, and previous APT work by Valley et al. (2014a). Zircon 01JH36-69 is a 4374 ± 12 Ma (2σ) zircon from the Jack Hills, Australia, and one of the oldest known terrestrial materials. APT has previously documented subspherical 5-10 nm clusters of Y, REE, and Pb, and correlated their formation with high-temperature during re-entrainment in a magma at ~3.4 Ga (Valley et al 2014a). In this thesis, we describe the presence of two unique cluster populations with unique $^{207}Pb/^{206}Pb$ ratios. These data document two periods of cluster formation: the first at 3.8 Ga, and the second at 3.4 Ga. These data demonstrate that the nanoscale clusters have preserved their isotopic signatures over billions of years, and through subsequent periods of cluster formation. The retention of Pb within clusters through subsequent thermal events has significant implications for long held assumptions about Pb behavior during Pb-loss, specifically the interpretation of discordance in microns or grain scale zircon analyses. Chapter 5 models the

isotope evolution of zircon undergoing Pb-loss, with and without a prior period of Pb clustering. These data show how discordia, formed from data at the micron scale, are influenced by nanoscale clustering, and present a framework to utilize both nanoscale and micron-scale data to reconstruct detailed thermal histories.

Chapter 6 builds upon Chapters 4 and 5, looking at zircon 17B-4, a 4392 ± 12 Ma zircon collected during Apollo 17 as part of impact ejecta from the Serenitatis basin-forming impact (~3.96 Ga). Zircon 17B-4 preserves 5-10 nm Pb-rich regions, and similar to Chapters 3 and 5, modeling of $^{207}Pb/^{206}Pb$ places cluster formation at 3.85 ± 0.15/-0.17 Ga, within uncertainty of the Serenitatis impact age, and the $^{40}Ar/^{39}Ar$ age of the host breccia for 17B-4. This discovery represents the first identification of nanoscale clustering within lunar zircons, and the first time impact induced Pb mobility has been captured at the nanoscale. The crystallization age of zircon 17B-4 is well defined by concordant SIMS analysis and the upper discordia intercept, and we apply the complex model developed as part of Chapter 5 to infer that portions of zircon 17B-4 suffered partial Pb-loss at 3.5 Ga.

Appendices 1-5 contain a wide range of Raman, EBSD, SIMS, and APT data in support of the above chapters. This also includes a review of Raman, EBSD, SIMS and APT data for three Jack Hills zircon grains (01JH-13b 5M 4-2, 01JH-13b 5M 10-2, and 01JH-54b 2.5NM2 7-1).

REFERENCES

Cherniak, D.J., Lanford, W.A., Ryerson, F.J. (1991) Lead diffusion in apatite and zircon using ion implantation and Rutherford Backscattering techniques. Geochimica et Cosmochimica Acta, 55, 1663-1673.

Cherniak, D.J., Watson, E.B. (2003) Diffusion in zircon, Reviews in Mineralogy and Geochemistry, 53, 113-143.

Dawson, P., Hargreave, M.M., Wilkinson, G.R. (1971) The vibrational spectrum of zircon ($ZrSiO_4$), Journal of Physics C: Solid State Physics, 4, 240-256.

Ewing, R.C., Meldrum, A., Wang, L., Weber, W.J., Corrales, L.R. (2003) Radiation effects in zircon, Reviews in Mineralogy and Geochemistry, 53, 387-425.

Gault, B., Moody, M.P., Cairney, J.M., Ringer, S. (2012) Atom Probe Microscopy, 396 p. Springer.

Geisler, T., Pidgeon, R.T., Bronswijk, W.V., Pleysier, R. (2001) Kinetics of thermal recovery and recrystallization of partially metamict zircon: a Raman spectroscopic study, European Journal of Mineralogy, 13, 1163-1176.

Henry, D.J, Mueller, P.A., Wooden, J.L., Warner, J.L., Lee-Berman, R. (1984) Granulite grade supracrustal assemblages of the Quad Creek area, eastern Beartooth Mountains, Montana, Montana Bureau of Mines and Geology Special Publication, 84, 147-156.

Larson, D.L., Prosa, T.J., Ulfig, R.M., Geiser, B.P., Kelly, T.F., (2013) Local Electrode Atom Probe: A User's Guide. 318 p. Springer.

Moser, D.E., Davis, W.J., Reddy, S.M., Flemming, R.L., Hart, R.J., (2009) Zircon U-Pb strain chronometry reveals deep impact-triggered flow. Earth and Planetary Science Letters, 277, 73-79.

Moser, D.E., Cupelli, C.L., Barker, I.R., Flowers, R.M., Bowman, J.R., Wooden, J., Hart, J.R. (2011) New zircon shock phenomena and their use for dating and reconstruction of large impact structures revealed by electron nanobeam (EBSD), CL, EDS) and isotopic U-Pb and (U-Th)/He analysis of the Vredefort dome, Canadian Journal of Earth Sciences, 48, 117-139.

Mueller, P.A., Wooden, J.L., Nutman, A.P. (1992) 3.96 Ga Zircons from an Archean quartzite, Beartooth Mountains, Montana, Geology, 20, 327-330.

Nasdala, L., Pidgeon, R.T., Wolf, D. (1996) Heterogeneous metamictization of zircon on a microscale, Geochimica et Cosmochimica Acta, 60, 1091-1097.

Nasdala, L., Wenzel, M., Vavra, G., Irmer, G., Wenzel, T., Kober, B. (2001) Metamictization of natural zircon: accumulation versus thermal annealing of radioactivity-induced damage, Contributions to Mineralogy and Petrology, 141, 125-144.

Spicuzza, M.J., Valley, J.V., Kitajima, K., Ushikubo, T. (2011) Oxygen isotope ratios and trace element concentrations in zircons from lunar rocks and regolith, 42nd Lunar and Planetary Science Conference, The Woodlands Texas, #2445.

Syme, R.W.G., Lockwood, D.J., Kerr, H.J. (1977) Raman spectrum of synthetic zircon ($ZrSiO_4$) and thorite (ThSiO4), Journal of Physics C: Solid State Physics, 10, 1335-1348.

Valley, J.W., Reinhard, D.A., Snoeyenbos, D., Lawrence, D., Martin, I., Kelly, T.F., Ushikubo, T., Strickland, A., Cavosie, A.J. (2012) Elemental and isotopic tomography at single-atom-scale in 4.0 and 2.4 Ga zircons. AGU Fall Meeting Abstracts, V12A-05.

Valley J.W., Cavosie, A.J., Ushikubo, T., Reinhard, D.A., Lawrence, D.F., Larson, D.J., Clifton, P.H., Kelly, T.F., Wilde, S.A., Moser, D.E., Spicuzza, M.J. (2014a) Hadean age for post-magma-ocean zircon confirmed by atom probe tomography, Nature Geoscience, 7, 219-223.

Valley, J.W., Spicuzza, M.J., Ushikubo, T. (2014b) Correlated $\delta^{18}O$ and [Ti] in lunar zircons: a terrestrial perspective for magma temperatures and water content on the Moon, Contributions to Mineralogy and Petrology, 167, 956.

Valley, J.W. Reinhard, D.A., Cavosie, A.J., Ushikubo, T., Lawrence, D.F., Larson, D.J., Kelly, T.F., Snoeyenbos, D.R., Strickland, A. (2015) Nano- and Micro-geochronology in Hadean and Archean zircons by atom-probe tomography and SIMS: New tools for old minerals, American Mineralogist, 100, 1355-1377.

Zhang, M., Salje, E.K.H., Capitani, G.C., Leroux, H., Clark, A.M., Schlüter, J., Ewing, R.C. (2000) Annealing of α-decay damage in zircon: a Raman spectroscopic study, Journal of Phys: Condensed Matter, 12, 3131-3148.

CHAPTER 2

Best Practices for Reporting Atom Probe Analysis of Geological Materials

Tyler B. Blum[1], James R. Darling[2], Thomas F. Kelly[3], David J. Larson[3], Desmond E. Moser[4], Alberto Perez-Huerta[5], Ty J. Prosa[3], Steven. M. Reddy[6,7], David A. Reinhard[3], David W. Saxey[7,8], Robert M. Ulfig[3], John W. Valley[1]

[1]Department of Geoscience, University of Wisconsin, Madison, WI, USA.
[2]School of Earth and Environmental Sciences, University of Portsmouth, Portsmouth, GBR
[3]CAMECA Inc., Madison, WI, USA.
[4]Department of Earth Sciences, University of Western Ontario, London, ON, CAN.
[5]Department of Geological Sciences, University of Alabama, Tuscaloosa, AL, USA.
[6]School of Earth and Planetary Sciences, Curtin University, Perth, WA, AUS.
[7]Geoscience Atom Probe Advanced Characterization Facility, Curtin University, Perth, WA, AUS
[8]John de Laeter Centre, Curtin University, Perth, WA, AUS.

Correspondence: tbblum@geeology.wisc.edu

This manuscript format has been adapted following publication:

Tyler B. Blum, James R. Darling, Thomas F. Kelly, David J. Larson, Desmond E. Moser, Alberto Perez-Huerta, Ty J. Prosa, Steven M. Reddy, David A. Reinhard, David W. Saxey, Robert M. Ulfig, David J. Larson, John W. Valley (2018) Best practices for reporting atom probe analysis of geological materials, in *Microstructural Geochronology: Planetary Records Down to Atom Scale*, edited by D. Moser, F. Corfu, S. Reddy, J. Darling, and K. Tait, John Wiley & Sons, Inc., Hoboken, NJ, 232, 369–373.

Abstract

The application of atom probe tomography (APT) within the Earth and planetary sciences has produced novel data sets that answer fundamental questions about the near atomic scale distribution of elements and isotopes within minerals. APT involves the incremental evaporation, detection and subsequent computer reconstruction of charged particles from a needle-shaped specimen. The range of applications is growing such that protocols for reporting are needed for APT data comparison and quality assessment among natural materials. A particular challenge of APT science relates to documenting the instrumental and analyst-dependent conditions that affect the mass spectral and spatial qualities of the data, and their interpretation. This contribution outlines recommended data reporting procedures for publication of atom probe tomography data in terms of the sample preparation, data collection and reconstruction phases as well as the characterization and interpretation of the reconstructed volume. Coordinated reporting of this basic information will promote efficient communication of protocols, and aid in the evaluation of published atom probe data as geologists continue to explore atomic compositions and distributions at nanoscale.

Introduction

Recent work has established atom probe tomography (APT) as a unique tool within the geosciences for interrogating material chemistry at the nanoscale. In APT, a needle-shaped specimen with an end-form radius on the order of 50-100 nm is held at high voltage and constituent atoms are field evaporated through application of a timed voltage pulse, for conductive materials, or laser pulse, for semiconductors and insulators. The voltage bias and small radius of curvature produce a large electric field that is localized around, and diverging from, the end surface of the needle-shaped specimen; evaporated ions are then accelerated by the local electric field, leading to divergent trajectories for ions originating from different positions on the specimen surface. A position-sensitive detector records both the hit position of incident ions, as well as their time of incidence. This information is then converted to identify individual elements and isotopes based on mass-to-charge state ratios, and to reconstruct individual ion positions based on their incident position on the detector and the specimen geometry [*Gault* et al., 2012; *Larson* et al., 2013; *Miller and Forbes*, 2014]. This combination of time-of-flight mass spectrometry and projection microscopy allows characterization of trace and isotope chemistry in

three-dimensions with sub-nanometer resolution, and presents a novel means to interrogate materials, interfaces and the processes responsible for elemental and isotopic heterogeneities.

In APT, the needle-shaped specimen is "the primary optic of the atom probe microscope" [*Larson* et al., 2013], meaning that the field evaporation process and ion flight-trajectories, are fundamentally affected by the shape, and material properties, of the specimen itself. As a result, characterization of materials by APT requires consideration of numerous variables that influence both data quality and data analysis. The specimen's geometry, crystallography, and physical properties influence specimen yield, as well as spatial and spectral resolution; these in turn influence other aspects of quantitative data analysis, including the detection and characterization of different compositional domains [*Gault* et al., 2012; *Larson* et al., 2013; *Miller and Forbes,* 2014]. The detailed description of field evaporation for ceramics and complex oxides remains an active area of research [e.g., *Tsong and Müller*, 1970; *Oberdorfer* et al., 2007; *Oberdorfer and Schmitz*, 2011, *Silaeva* et al., 2013; *Vurpillot and Oberdorfer*, 2015; also see *Miller and Forbes,* 2014 and references therein] and optimizing acquisition conditions, such as temperature, voltage pulse magnitude/laser pulse energy, etc., on a material-by-material basis remains important for both acquiring data, and ensuring data quality and reproducibility [e.g., *LaFontaine* et al., 2017]. Interest in precise and accurate reconstructions, quantitative compositional analysis [*Valley* et al., 2014; *Valley* et al., 2015; *Saxey* et al., this volume; *Reinhard* et al., this volume], and measurement of isotope ratios for both major [e.g., *Lewis* et al., 2015; *Heck* et al., 2014; *Parman* et al., 2014] and trace components [*Valley* et al., 2014; *Valley* et al., 2015; *Peterman* et al., 2016; *Blum* et al., this volume; *Reinhard* et al., this volume; *White* et al., this volume] support continued efforts to understand the complex interaction between spatial and spectral data processing, and associated analytical uncertainties.

As analytical protocols and data mining approaches are developed for geomaterials, we anticipate the need to standardize aspects of data reporting to streamline evaluation, utilization and expansion of published literature. This note seeks to provide guidelines for APT data reporting within the geosciences in order to (1) maintain effective communication of protocols and techniques within the community, and (2) provide an efficient means to evaluate published literature. The information to be reported covers sample preparation, sample context, instrument settings, acquisition conditions, reconstruction parameters, and data metrics. We anticipate that information may be included in a variety of ways, including figures, tables and supplementary materials depending on the stylistic limitation and scientific focus of any given publication.

Basic Sample Preparation Information:

Preparation of APT specimens, as well as previous sample treatment, can influence material properties and data quality. A brief discussion of basic sample preparation information should include any pre-APT analysis processing, (e.g., mounting, polishing, coating for conductivity) as well as APT specimen preparation details, (e.g., FIB lift-out, typical vs. atypical lift-out geometries, low-voltage cleanup steps, application/use of coatings) and any correlative microscopy done between APT preparation and APT analysis, such as transmission electron backscatter diffraction [e.g., *Reinhard* et al., this volume].

Sample Context:

Given a single needle-shaped APT specimen typically encompasses a volume $\leq 10^8$ nm^3, providing context for APT specimens greatly enhances the utility and interpretability of an APT data set. The importance of the type and scale of sample characterization varies from study to

study; however, the material structure (crystallography and mineral group, if applicable), age, and bulk chemistry provide valuable basic specimen information. Imaging of the sample/lift-out locations, and the homogeneity of the sample is highly encouraged.

Data Acquisition Settings and Data Summary:

Basic information concerning specimen analysis is valuable in evaluating data quality. Much of this information can be summarized within a table similar to that shown below (Table 1). "Instrument Settings" summarizes the instrument type, and basic conditions and controls applicable to data collection. "Data Summary" summarizes various aspects of the software used in generating reconstructions (which may or may not be the proprietary IVAS software) as well as select metrics of the data sets. We note that the "percentage of ranged ions" in Table 1 is intended to represent the ranging/reconstruction of the complete data set; the spectra for specific sub-regions of the data set which are the focus of the scientific inquiry can be presented elsewhere.

Spectral Processing:

Time-of-flight data, and the resulting mass/charge ratio spectra, are a critical part of APT data, given they are an input for spatial reconstruction of data and are the basis for visualization and measurement of compositional variation throughout data sets. Publications are therefore encouraged to present a complete mass spectrum, in figure form, for each needle-shaped specimen. These should include hydrogen peaks, labeling of major peak families and a record of the highest mass-to-charge state value acquired. This may be more/less involved depending on the importance of ranging and compositional analysis within the study. In certain cases, where

large numbers of data sets are included, it may be appropriate to include "representative" spectra so long as the spectra are functionally identical for the given scientific inquiry, and relevant differences in acquisition settings, charge states, background levels, contaminant levels, and specimen geometries are accounted for. Relevant sub-regions of the spectra may be highlighted if they are analyzed in the course of the publication; for example, visualization of trace element or isotope peaks can be difficult when viewing the complete spectrum and in instances where they are of particular importance, the local spectrum structure surrounding these peaks may be highlighted in companion images. Indicating the expected peak positions and relative abundances of isotopes may be beneficial in some cases; however, we note that analysis of radiogenic isotopes and/or isotopically doped materials may preclude direct knowledge of "expected" isotope ratios. Other important information includes the bulk specimen composition, including whether this was determined using basic ranging or peak decomposition analysis, and the background correction scheme used. If any other novel analysis was done to treat challenges in spectral analysis (interferences, overlaps, etc.), they may be indicated. An example of how spectral processing may influence measured trace element (isotope) compositions is given in Blum et al., (this volume).

We also suggest monitoring a set of peaks representative of two isotopes, in two different charge states: for example, the ion-count ratios, C_{28Da}/C_{29Da}, $C_{14Da}/C_{14.5Da}$, C_{14Da}/C_{28Da}, corresponding nominally to $^{28}Si^{+}/^{29}Si^{+}$, $^{28}Si^{++}/^{29}Si^{++}$ and $^{28}Si^{+}/^{28}Si^{++}$, allowing for any interferences. This provides some measure of the electric field proximal to the specimen surface. The peaks of interest may vary depending on the material.

Reconstruction:

In addition to providing the basic details for the reconstruction (see Table 1) papers should include a short statement concerning how the reconstruction was approached: i.e., what criteria were used to evaluate an "optimal" reconstruction, and what were the dependent and independent parameters during optimization. For example:

> "Standard instrument characteristics (flight path, detector efficiency, etc.) were used in reconstructing data sets (see Table 1). Reconstruction was approached iteratively, with spatial constraints coming from the tip geometry within the pre-/post acquisition images. Final reconstructions utilized spectral ranges refined from preliminary data analysis, and optimized reconstruction parameters to best replicate the inferred evaporated dimensions from pre-/post acquisition imaging, while holding constant those parameters measured as part of pre- and post- acquisition imaging (sphere-cone radius ratio, shank angle, final end-tip radius, etc.)."

We encourage presentation of atom map images, both for the entire data set, including one or multiple ions of interest, as well as images of the regions or features of interest. In the case that correlative microscopy and/or high precision reconstructions are a principal component of the study, inclusion of pre-/post-analysis images is desirable.

Spatial Processing:

In cases where domains within APT data sets are isolated/defined, we encourage authors to communicate the analysis method utilized (e.g., isoconcentration surfaces, *k*th nearest neighbor

analysis), and the relevant input parameters (e.g., isoconcentration threshold/value, voxel size and delocalization, or nearest neighbor order parameter, N_{min}, d_{max}, E and L). Erroneous results can be generated when input parameters are not selected/calibrated appropriately. Where compositional profiles are of interest, the use of background-corrected data is preferable. The local background levels themselves should also be indicated for mass peaks of interest in cases where the noise contribution may be significant.

Uncertainties:

We encourage the inclusion of appropriate uncertainties, including a description or citation indicating how they were calculated. Often times, many uncertainties within the data may be inconsequential to the scientific question of interest, or may be difficult to calculate based on the complex relations between spatial and spectral data types; however, we encourage inclusion and discussion of those uncertainties relevant to the main scientific results and discussion.

Other Information:

Broad interest in compositional and isotopic analysis requires consideration of several variables including molecular interferences. Of particular interest are those interferences associated with contamination from the specimen or vacuum environment (e.g., hydrides), and thus may be both variable between different experiments and difficult to constrain through peak deconvolution. The nature and importance of interferences depend on the specifics of a given material and scientific inquiry, and at present, there is no framework for a holistic treatment of contaminant interferences. We suggest documenting background corrected counts within each of the 1, 2, and 3 Da peaks, as well as the 16, 17, 18 and 19 Da peaks. These data may generate a database to better understand H, O, H_2O, etc. signals within APT data sets, and to develop means to monitor

and minimize associated interferences. As a better understanding evolves, these reporting suggestions may similarly adapt to provide better reporting practices.

REFERENCES

Blum, T.B., Reinhard, D.A., Chen, Y., Prosa, T.J., Larson, D.J., Valley, J.W. (2018) Uncertainty and sensitivity analysis for spatial and spectral processing of Pb-Pb geochronology by atom probe tomography, *in* Microstructural Geochronology: Planetary Records Down to Atom Scale, edited by D. Moser, F. Corfu, S. Reddy, J. Darling, and K. Tait, John Wiley & Sons, Inc., Hoboken, NJ, 232, 327–349.

Gault, B., Moody, M.P., Cairney, J.M., Ringer, S. (2012) Atom Probe Microscopy, 396 p. Springer.

Heck, P.R., Stadermann, F.J., Isheim, D., Auciello, O., Daulton, T.L., Davis, A.M., Elam, J.W., Floss, C., Hiller, J., Larson, D.J., Lewis, J.B., Mane, A., Pellin, M.J., Savina M.R., Seidman, D.N., Stephan, T. (2014) Atom-probe analyses of nanodiamonds from Allende, Meteoritics and Planetary Science, 1-15.

La Fontaine, A., Piazolo, S., Trimby, P., Yang, L., Cairney, J., (2017) Laser-Assisted Atom Probe of Deformed Minerals: A Zircon Case Study, Microscopy and Microanalysis, 1-10, doi: 10.1017/S1431927616012745.

Larson, D.L., Prosa, T.J., Ulfig, R.M., Geiser, B.P., Kelly, T.F. (2013) Local Electrode Atom Probe Tomography: A User's Guide. 318 p. Springer.

Lewis, J.B., Isheim, D., Floss, C., Seidman, D.N. (2015) $^{12}C/^{13}C$-ratio determination in nanodiamonds by atom-probe tomography, Ultramicroscopy, 159, 248-254.

Miller, M.K., and Forbes, R.G. (2014) Atom Probe Tomography: The local Electrode Atom Probe. 437 p. Springer.

Oberdorfer, C., Stender, P., Reinke, C., Schmitz, G., (2007) Laser-Assisted Atom Probe Tomography of Oxide Materials, Microscopy and Microanalysis, 13, 342-346.

Oberdorfer, C., Schmitz, G., (2011) On the Field Evaporation Behavior of Dielectric Materials in Three-Dimensional Atom Probe: A Numeric Simulation, Microscopy and Microanalysis, 17, 15-25.

Parman, S.W., Diercks, D.R., Gorman, B.P., Cooper, R.F. (2015) Atom probe tomography of isoferroplatinum, American Mineralogist, 100, 852-860.

Peterman, E.M., Reddy, S.M., Saxey, D.W., Snoeyenbos, D.R., Rickard, W.D.A., Fougerouse, E.M., Kylander-Clark A.R.C., (2016) Nanogeochronology of discordant zircon measured

by atom probe microscopy of Pb-enriched dislocation loops, Science Advances, 2, e1601318.

Reinhard, D.A., Moser, D.E., Martin, I., Rice, K.P., Chen, Y., Olson, D., Lawrence, D., Prosa, T.J., and Larson, D.J. (2018) Atom Probe Tomography of Baddeleyite Standard Phalaborwa and Zircon Standard BR266. *in* Microstructural Geochronology: Planetary Records Down to Atom Scale, edited by D. Moser, F. Corfu, S. Reddy, J. Darling, and K. Tait, John Wiley & Sons, Inc., Hoboken, NJ, 232, 315–326.

Saxey, D. A., S. M. Reddy, D. Fougerouse, W. D. A. Rickard (2018), The Optimization of Zircon Analyses by Laser-Assisted Atom Probe Microscopy: Insights from the 91500 Zircon Standard, *in* Microstructural Geochronology: Planetary Records Down to Atom Scale, edited by D. Moser, F. Corfu, S. Reddy, J. Darling, and K. Tait, John Wiley & Sons, Inc., Hoboken, NJ, 232, 293–313.

Silaeva, E.P., Karahka, M., Kreuzer, H.J., (2013) Atom Probe Tomography and field evaporation of insulators and semiconductors: Theoretical issues, Current Opinion in Solid State and Materials Science, 17, 211-216.Tsong, T.T., Müller, E.W., (1970) Field adsorption of inert-gas atoms on field ion emitter surfaces, Physical Review Letters, 25, 911.

Valley, J.W., Cavosie, A.J., Ushikubo, T., Reinhard, D.A., Lawrence, D.F., Larson, D.J., Clifton, P.H., Kelly, T.F., Wilde, S.A., Moser, D.E., Spicuzza, M.J. (2014) Hadean age for post-magma-ocean zircon confirmed by atom probe tomography, Nature Geoscience, 7, 219-223.

Valley, J.W., Reinhard, D.A., Cavosie, A.J., Ushikubo, T., Lawrence, D.F., Larson, D.J., Kelly, T.F., Snoeyenbos, D.R., Strickland, A. (2015) Nano- and Micro-geochronology in Hadean and Archean zircons by atom-probe tomography and SIMS: New tools for old minerals, American Mineralogist, 100, 1355-1377.

Vurpillot, F., Oberdorfer, C., (2015) Modeling Atom Probe Tomography: A review, Ultramicroscopy, 159, 202-216.White, L.F., Darling, J.R., Moser, D., Reinhard, D.A., Dunlop, J., Larson, D.J., Lawrence, D. & Martin. I. Chemical nanostructures and chronostructures defined in shock metamorphosed baddeleyite by atom probe tomography. This volume

Table 1. Atom Probe Tomography data acquisition settings and data summary.

Specimen/Data Set	**M5_491**	**M1_568**	**M3_609**
Instrument Model	**LEAP 5000 XR**	**LEAP 5000 XR**	**LEAP 5000 XR**
Instrument Settings			
Laser Wavelength (nm)	355	355	355
*Laser Pulse Energy (pJ)	200	200	200
*Voltage Pulse Fraction	15%	15%	15%
Pulse Frequency (kHz)	125	125	125
Evaporation Control	Detection Rate	Detection Rate	Detection Rate
Target Detection Rate (ions/pulse)	0.01	0.01	0.01
Nominal Flight Path (mm)	382	382	382
Set Point Temperature (K)	50	50	50
Sample Temperature (K)	55	55	55
Chamber Pressure (Torr)	1.3×10^{-10}	1.4×10^{-10}	5.4×10^{-11}
Data Summary			
LAS Root Version	15.41.342j	15.41.342j	15.41.342j
CAMECAROOT Version	15.43.393e	15.43.393e	15.43.393e
Analysis Software	IVAS 3.6.10a	IVAS 3.6.10a	IVAS 3.6.10a
Total Ions:	150,792,481	163,057,160	213,529,143
Single	66.1%	69.2%	68.1%
Multiple	33.1%	30.1%	31.2%
Partial	0.8%	0.7%	0.7%
Reconstructed Ions:	140,428,802	155,697,119	194,541,231
Ranged	79.4%	75.2%	76.7%
Unranged	20.6%	24.8%	23.3%
Volt./Bowl Corr. Peak (Da)	16	16	16
Mass Calib. (peaks/interp.)	10/Lin.	11/Lin.	11/Lin.
†(M/ΔM) for $^{16}O_2^+$	1130	1200	1180
††($M/\Delta M_{10}$)	530	550	540
time independent background (ppm/ns)	20.5	19.7	18.7
Reconstruction			
Final specimen state	intact	intact	fractured
Pre-/Post-analysis Imaging	TEM/SEM	tEBSD/SEM	TEM/n.a.
Radius Evolution Model	"shank"	"shank"	"shank"
Field Factor (k)	3.3	3.3	3.3
Image Compression Factor	1.65	1.65	1.65
Assumed E-Field (V/nm)	28	28	28
Detector Efficiency	52%	52%	52%
Avg. Atomic Volume (nm^3)	0.0108	0.0108	0.0108
$V_{initial}$; V_{final} (V)	4546; 9608	4305; 10383	4848; 11719

*Entries are mutually exclusive
†ΔM is full width at half maximum.
††ΔM_{10} is full width at tenth maximum.

CHAPTER 3

Uncertainty and sensitivity analysis for spatial and spectral processing of Pb isotopes in zircon by atom probe tomography

Tyler B. Blum[1], David A. Reinhard[2], Yimeng Chen[2], Ty J. Prosa[2], David J. Larson[2], and John W. Valley[1]

[1]Department of Geoscience, University of Wisconsin, Madison, WI, 53706 USA. [2]CAMECA Inc., Madison WI, 53711 USA.

Correspondence: tbblum@geology.wisc.edu

This manuscript format has been adapted following publication:

Tyler B. Blum, David A. Reinhard, Yimeng Chen, Ty J. Prosa, David J. Larson, John W. Valley (2018) Uncertainty and sensitivity analysis for spatial and spectral processing of Pb-Pb geochronology by atom probe tomography, in *Microstructural Geochronology: Planetary Records Down to Atom Scale*, edited by D. Moser, F. Corfu, S. Reddy, J. Darling, and K. Tait, John Wiley & Sons, Inc., Hoboken, NJ, 232, 327–349.

Abstract

Measuring $^{207}Pb/^{206}Pb$ ratios by atom probe tomography (APT) has provided new insight into the nanoscale behavior of trace components in zircon, and their relationship to time, temperature and structure. Here, we analyze three APT data sets for a 3.77 Ga zircon from the Beartooth Mountains, USA, and apply systematic ranging approaches to understand the spatial and spectral uncertainties inherent in $^{207}Pb/^{206}Pb$ analysis by APT. This zircon possesses two, 100% concordant U-Pb analyses by secondary ion mass spectrometry (SIMS), indicative of closed U-Pb systematics on the micron scale since crystallization. APT data sets contain sub-spherical Pb-rich (>0.25% atomic) domains with diameter <15 nm. Broadly consistent Pb-rich regions are defined in applying six different permutations of the two most common cluster identification algorithms. Measured $^{207}Pb/^{206}Pb$ ratios within Pb-rich domains vary between 0.794±0.15 (±2σ) and 0.715±0.052 depending on the ranging approach, cluster definition protocol and number of clusters interrogated. For the bulk APT data sets, $^{207}Pb/^{206}Pb$ = 0.353±0.18; this is indistinguishable from the bulk $^{207}Pb/^{206}Pb$ ratio by SIMS (0.367±0.0037), and statistically distinct from the $^{207}Pb/^{206}Pb$ ratio within clusters. Bulk and clustered $^{207}Pb/^{206}Pb$ ratios are consistent with Pb clustering at ~2.8 Ga, during protracted metamorphism and magmatism in the Beartooth Mountains.

1 INTRODUCTION

Zircon is heavily utilized in understanding earth systems and their evolution through time. The chemical and physical resistance of zircon, and its slow diffusion for most major and trace components [e.g., *Cherniak and Watson*, 2003], allows zircon to contribute to numerous studies of the silicate Earth, from detailed calibration of stratigraphic relations and the geological time scale [e.g., *Bowring and Schmitz*, 2003], to tracing of magmatic processes [e.g., *Schoene* et al., 2012], to secular trends in Earth's evolution [e.g., *Valley* et al., 2005], to provenance and the sedimentary record [e.g., *Fedo* et al., 2003]. Zircon chemistry remains one of the few means to directly study the earliest portions of Earth's history [e.g., *Cavosie* et al., 2006] and the Moon [e.g., *Nemchin* et al., 2009; *Valley* et al., 2014b]. The ability to identify the chemical manifestations of structural modification are a means to better understand controls on open system chemical behavior, as well as the timing and length scales of element mobility.

The study of zircon chemistry is intimately related to nanoscale phenomenon; a zircon's

trace element and isotope chemistry, as well as its physical and chemical properties, are related to the atomistic processes of crystal growth, crystal deformation, radiation damage, structural recovery and diffusion. *Crystalline* zircon possesses slow diffusion and offers a robust record of primary chemistry; however, open system behavior of zircon components is well documented, and is most often linked to the accumulation of structural damage due to self-irradiation. Trace amounts of U and Th are incorporated into the zircon during crystallization and alpha decay events within the $^{238}U \rightarrow {}^{206}Pb$, $^{235}U \rightarrow {}^{207}Pb$, and $^{232}Th \rightarrow {}^{208}Pb$ decay chains disrupt the zircon crystal structure on the nanoscale. The energetic daughter nuclei generate 5-10 nm damage domains comprised of an amorphous core which grades radially to defect rich, strained then unstrained zircon [*Ewing* et al., 2003]. If damage domains are not annealed, they become more numerous and eventually overlap to form a connected network at the "first percolation point." The accumulation of damage from this self-irradiation causes a macroscopic increase in volume, micro-fracturing, as well as a reduction in clarity, birefringence, and durability. At the atomic scale, reaction and diffusion kinetics are orders of magnitude faster for damaged zircon relative to pristine zircon [*Cherniak* et al., 1991]. As a result, zircon which reaches the first percolation point is far more likely to exhibit open system chemical behavior and may possess disturbed or unreliable age and chemical systematics. Structural reconstitution acts to re-form the crystal structure where it has been damaged by alpha recoil events; however, the number, energetics, and damage state dependencies of annealing mechanisms are poorly understood [e.g. *Ewing* et al., 2003]. As a result, the importance of annealing at low temperature (<300°C), the relative rates of trace element diffusion and structural reconstitution, and their influence on trace element and isotope distributions remain poorly resolved. Ultimately, zircon durability and the mobility of major and trace components are functions of a zircon's nanoscale structure, and a thorough

understanding of a zircons structural evolution contributes to the robust interpretation of associated geochemical information.

Atom probe tomography (APT) possesses a unique combination of spatial resolution and chemical sensitivity that is well-suited to explore the geochemical and isotopic evolution of zircon at the nanoscale. APT combines projection type microscopy with time-of-flight mass spectrometry to generate three-dimensional compositional maps with near-atomic scale resolution [*Larson* et al., 2013]. A needle-shaped specimen with an end tip radius on the order of 50-100 nm is held at high voltage while constituent atoms are field evaporated though application of a timed voltage pulse (for conductive materials), or laser pulse (for semiconductors and insulators). Evaporated ions are accelerated by the local electric field near the tip surface, which varies systematically across the specimen. A position sensitive detector records both the position of incident ions in detector space, as well as their time of incidence. Chemical information can be extracted from an ion's time-of-flight (which is related to the ion's mass-to-charge state ratio) while the spatial coordinates of individual ions are reconstructed based on their incident position on the detector, and specimen geometry [*Gault* et al., 2012; *Larson* et al., 2013]. The current generation of atom probe instrumentation possesses sub-nanometer spatial resolution, with typical mass resolving powers up to 1100 for inverted FWHM (m/□m), and detection limits down to 10 parts per million atomic (ppma) [*Larson* et al., 2013]. These capabilities allow the three-dimensional characterization of zircon trace element and isotope chemistry on the scale of crystal deformation, radiation damage and annealing processes. Atom probe of ancient zircons have revealed heterogeneous distributions of several trace components, including Y, Yb, Dy, Lu and radiogenic Pb, on the scale of 10's of nanometers. The morphology and chemistry of these domains is varied, and multiple structural/mechanistic

controls on trace element re-distribution have been proposed, including diffusion to alpha-recoil damage domains [*Valley* et al., 2014, 2015], and partitioning/trapping by defect structures within deformed and/or reconstituted zircon [*Reddy* et al., 2016; *Peterman* et al., 2016; *Piazolo* et al.,2016]. The number of time, temperature, and structural histories that lead to cluster formation remains poorly constrained; however, studies that have reported Pb isotope ratios within clusters, and conclude that (1) the clustered Pb is of radiogenic origin and thus the clusters are not primary features associated with initial zircon crystallization, and (2) Pb isotope ratios both inside and outside of enriched domains can in certain cases be linked (either directly or indirectly) to the timing of nanoscale element mobility and cluster formation. In cases where cluster formation is related to a discrete, short-lived episode, the ability to measure $^{207}Pb/^{206}Pb$ isotope ratios at the nanoscale can provide quantitative information regarding the timing of element redistribution. With certain assumptions, this can be used as a novel geochronometer to understand the cryptic deformation or thermal history of submicron zircon domains.

Applying this broadly to resolve episodes of element migration on the nanoscale requires both (1) characterizing the uncertainties inherent in the measurement of Pb isotopes by APT, and (2) understanding the approximations and simplifications inherent in modeling cluster ages. This contribution utilizes correlative electron backscatter diffraction (EBSD), secondary ion mass spectrometry (SIMS) and APT in a 3.77 Ga zircon from the Beartooth Mountains, Montana, to (1) provide an assessment of uncertainties in spectral analysis of Pb isotopes in APT data (especially for clusters/regions enriched in Pb and with higher signal-to-noise) and (2) evaluate how cluster identification can influence measured isotope ratios. These results provide a basis for assessing *analytical* limits of interpretation originating from measurement of $^{207}Pb/^{206}Pb$ ratios within APT data.

1.1 Spatial and spectral uncertainties in Pb/Pb ratios by APT

An atom probe data set consists of a point cloud of ion positions and identities; construction (and subsequent analysis) of these data involve two distinct, but interacting, data types. One is an ion's time-of-flight, which is transformed into a mass-to-charge state ratio and forms the basis for affixing a user-defined ion identity. The second are the ion's XY-position (in detector space) and the evaporation sequence which are used to reconstruct an ion's xyz-position in specimen space. Uncertainties associated with one or both of these data types are not necessarily straightforward to calculate, or to propagate. There remain no community-wide "standard" analysis procedures due to in large part to (1) unique spectral and spatial complexities associated with different materials and/or material structures, and (2) the need to maintain flexibility in prioritizing spatial vs. spectral aspects of APT data sets (i.e., given the unique combination of data types in APT, different scientific questions of interest can be more appropriately answered using different permutations on data reduction). This work does not treat the general complexities of spatial and spectral analysis by APT, but focuses on those aspects of data analysis which contribute to uncertainty in measurement of Pb isotopes in zircon. This provides a general framework to assess the statistical significance of different Pb isotope ratios measured in different sub-volumes of a given data set.

Ranging (i.e., identification of peaks and placement of peak integration bounds) of APT mass spectra is a critical component of both compositional analysis and the generation of accurate atom probe reconstructions. As described elsewhere, accurate and precise ranging of peaks within the mass spectrum aims to include the entire signal, while not degrading precision by including extraneous background [e.g., *Gedcke*, 2001; *Larson* et al., 2013]. While

qualitatively simple, ranging approaches vary in their ability to reproduce specimen composition [e.g., *Hudson* et al., 2011], and development of ranging protocols that yield stoichiometric compositions for any given material (particularly complex oxides) remains an active area of research [e.g., *Oberdorfer* et al., 2007; *Vella* et al., 2011; *Kirchhofer* et al., 2013]. These considerations are particularly relevant to assessing the accuracy and precision of *absolute* concentrations for major and trace components (including Pb) within zircon by APT. Importantly, both characterizing the spatial distribution of trace components, and measuring isotope ratios, are based on the *relative* concentrations, and thus can be considered independently of the more general uncertainties in compositional analysis by APT.

Lead isotope ratios are calculated through identification and ranging of ^{207}Pb and ^{206}Pb isotopes within the APT mass spectrum. Lead is a trace component in bulk zircon, and thus low total counts and significant noise mean the systematic application of "standard" ranging practices (e.g., defining range bounds at full width at one-tenth maximum, full width at one-hundredth maximum, etc.) can be both difficult to apply rigorously and sensitive to variables such as spectral bin width. No study has systematically interrogated the dependence of ^{207}Pb/^{206}Pb ratios (measured by APT) on spectral binning, placement of range bounds, and counting statistics, and we provide a framework for Pb isotope analysis through assessment of reproducibility and scatter in ^{207}Pb/^{206}Pb ratios for a series of ranging approaches and spectral binning.

In addition to the uncertainties in Pb isotope ratios originating from spectral analysis, spatial aspects of data can also influence observed Pb isotope ratios. Measuring Pb signals within distinct domains of an APT data set requires defining domain boundaries; even in ideal data with no background or spatial uncertainty, different boundary definitions/thresholds will isolate distinct spatial subsets of the data. The morphology (size, shape, etc.) and composition of

domains can be sensitive to these aspects of data reduction, particularly in cases where they are defined based on dilute components or components having significant gradients in composition [e.g., *Valley* et al., 2014]. In APT, this situation is further complicated by both spatial uncertainty inherent in reconstructing ion positions, and the fact that while background levels can be quantified *spectrally*, it is not currently possible to uniquely identify background counts *spatially*. All these factors manifest as uncertainty in the uniqueness and characteristics of "compositionally distinct domains" (their size, shape, number, average composition, etc.), and have implications for the measurement and interpretation of Pb isotope ratios at the nanoscale. The general treatment of uncertainty in *compositional* analysis due to *spatial* aspects of data analysis is complex, and is beyond the scope of this contribution. We treat this aspect of analysis empirically, by isolating domains based on several permutations of two common cluster analysis algorithms to look for first-order differences that may influence geological interpretation of the data.

1.2 Cluster Age Modeling

Extracting temporal information from spatially heterogeneous Pb isotope ratios requires modeling of the zircon U-Pb system through time; $^{207}Pb/^{206}Pb$ ratios alone are non-unique and require assumptions and/or boundary conditions in order to interpret their geological significance. We follow the general model of *Valley* et al. [2015], and calculate the timing of element mobility assuming clustering of radiogenic Pb produced between the time of zircon crystallization (t_{xln}, in years before present) and a discrete clustering episode in the zircon's history (t_2). This simple model is applicable to well-behaved systems with U-Pb systematics that can be related between the micron and nanoscale. Assuming no open system behavior at the

scale of observation, and vanishingly small initial Pb, the radiogenic $^{207}Pb/^{206}Pb$ ratio for the bulk specimen at any time t_2 is given by:

$$\left(\frac{^{207}Pb}{^{206}Pb}\right)^{*} = \left(\frac{^{235}U}{^{238}U}\right)_{xln}\left(\frac{1-\exp(-\lambda_{235}(t_{xln}-t_2))}{1-\exp(-\lambda_{238}(t_{xln}-t_2))}\right) \quad (1)$$

where (t_{xln}-t_2) represents the time elapsed since crystallization, λ_{235} and λ_{238} are the ^{235}U and ^{238}U decay constants respectively, and the (*) denotes radiogenic Pb. If all radiogenic Pb present at time t_2 migrates into a cluster volume fraction f_c, the concentration of ($^{207}Pb^{*}$+$^{206}Pb^{*}$) within the clusters becomes:

$$Pb^{*\prime}_{t2} = f_c^{-1}\left[^{235}U(1-\exp(-\lambda_{235}(t_{xln}-t_2))) + {}^{238}U(1-\exp(-\lambda_{238}(t_{xln}-t_2)))\right] \quad (2)$$

$$\left(\frac{^{207}Pb}{^{206}Pb}\right)^{*\prime}_{t2} = \left(\frac{^{207}Pb}{^{206}Pb}\right)^{*} = \left(\frac{^{235}U}{^{238}U}\right)_{xln}\left(\frac{1-\exp(-\lambda_{235}(t_{xln}-t_2))}{1-\exp(-\lambda_{238}(t_{xln}-t_2))}\right) \quad (3)$$

Where ($'$) indicates Pb within clusters. If one assumes a homogeneous ingrowth of radiogenic Pb between t_2 and the present, and no element migration occurred between t_2 and the present, the present day isotope ratio in clusters becomes a simple mixture of clustered Pb* at t_2 and Pb* accrued since:

$$Pb^{*\prime}_{T} = Pb^{*\prime}_{t2} + \left[^{235}U(1-\exp(-\lambda_{235}(t_2))) + {}^{238}U(1-\exp(-\lambda_{238}(t_2)))\right] \quad (4)$$

$$X'_{t2} = \frac{Pb'_{t2}}{Pb'_{T}} \quad (5)$$

$$\left(\frac{^{207}Pb}{^{206}Pb}\right)^{*\prime}_{P} = X'_{t2}\left(\frac{^{207}Pb}{^{206}Pb}\right)^{*\prime}_{t2} + (1-X'_{t2})\left(\frac{^{235}U}{^{238}U}\right)_{t2}\left(\frac{1-\exp(-\lambda_{235}(t_2))}{1-\exp(-\lambda_{238}(t_2))}\right) \quad (6)$$

The observed ratio within clusters is thus (at its simplest) a function of the crystallization age, the volume fraction of clusters, and the timing of cluster formation. If the initial concentration of Pb is negligible, and the ingrowth of Pb* between t_2 and present is sufficiently dilute relative to Pb'_{t2} (i.e., $X'_{t2} \rightarrow 1$), then eqn. (3) may be used to calculate the timing of cluster formation. Several additional simplifications and/or boundary conditions within this age model, include: (1)

the parent isotope distribution (and whether they are expected to influence one or more daughter nuclide distributions), (2) the degree of partitioning of Pb between clustered domains and surrounding zircon, (3) the initial Pb isotope composition (concentration and initial ratio) of the specimen and the "bulk" Pb evolution since crystallization, and (4) the relationship between the rate of Pb migration and duration of the migration event. Despite several simplifications in the age model derived above (eqns. 1-6), the need to incorporate increasingly complex elements into this age model is based, in part, on the achievable analytical accuracy and precision for $^{207}Pb/^{206}Pb$ ratios from APT data, and the spatial heterogeneity present in the data sets.

2 SAMPLES AND METHODS

Zircon BT5-13 is a 3.77 Ga detrital zircon from the Beartooth Mountains, Montana, originating from an Archean quartzite lens within the Quad Creek/Hellroaring Plateau region (Fig. 1). *Mueller* et al. [1992] documented concordant zircon domains up to 4.0 Ga within these quartzite lenses, and proposed a depositional age for the quartzite host of ~3.3 Ga. These rocks have persisted through several periods of deformation and metamorphism, including granulite facies metamorphism at ~3.25-3.1 Ga, subsequent retrograde amphibolite facies metamorphism [e.g., *Henry* et al., 1984], and local intrusion of the Long Lake igneous complex [*Mueller* et al., 1988]. Zircon BT5-13 was selected for APT study based on (1) homogeneous U and Th concentrations, and (2) two, 100% concordant SIMS U-Pb age analyses within the core with $^{207}Pb/^{206}Pb$ ages of 3778 ± 16 Ma and 3772 ± 10 Ma (±2σ).

EBSD point mapping of BT5-13 shows crystallographic/structural trends generally consistent with the compositional trends observable in backscattered electron (BSE) and cathodoluminescence (CL) imaging (see Fig. 1 for EBSD summary, and Table 1 for EBSD analysis information). The zircon core possesses oscillatory and sector zoning typical of igneous

zircon, surrounded by discontinuous concentric fractures separating the zircon core from an oscillatory zoned, bright in BSE (dark in CL) rim domain. Within the rim, fine scale fractures are visible, along with intermittent patches where BSE and CL contrast locally crosscuts oscillatory bands. Some of these rim features contain numerous micron-scale inclusions; combined with the patchy BSE and CL contrast, and the poor band contrast in EBSD, this is taken as evidence that the rim domain is partially to fully metamict and preserves a complex history of damage accumulation plus/minus recrystallization. (We note that band contrast is a measure of the contrast difference between the bands and background within the electron backscatter diffraction pattern; as such, it is a complex function of sample characteristics including sample polish/preparation, crystal structure, crystallinity, etc. and thus no quantitative measure of the present structural state ("effective" alpha dose) for BT5-13 is attempted based on this information.) Within the core, small (<2°) relative misorientations are associated with fractures, though the exact timing of fracturing is unknown. Important to this study is the lack of any discernable misorientation or crystallographic complexity within the domain sampled by atom probe lift-out (Fig 1a). Closed system U-Pb systematics, dominantly igneous textures in SEM imaging, and uniform crystallography by EBSD, are taken as strong evidence for closed system chemical behavior on the micron scale throughout the zircon core region. This is in spite of the fact that the calculated dose from radioactive decay of U and Th is 7.1×10^{15} α-decays/mg over the 3.77 Ga history of the zircon, well above that required to exceed the first percolation point in the absence of annealing (~1-2 $\times 10^{15}$ α-decays/mg [e.g., *Ewing* et al., 2003]). We do not know, in detail, the structural state of zircon BT5-13 as a function of time (i.e., annealing rate as a function of time, preservation of distinct damage structures, etc.); however, the U-Pb systematics from SIMS suggest that high temperature events within BT5-13's history (including, but perhaps

not limited to, granulite facies metamorphism) did not coincide with a significantly damaged crystal structure in the zircon core. If this were the case, we would expect micron scale Pb mobility, and more complex U-Pb systematics.

Three needle-shaped specimens were prepared from a single FIB (focused ion beam) lift-out taken from the core of the zircon, with the long axis of the specimens normal to the imaged surface in Fig. 1a; the lift-out was deliberately taken along visible banding to limit compositional and structural variability between adjacent atom probe specimens. Needle-shaped specimens were run on a LEAP 5000 XR (local electrode atom probe, with reflectron) at the CAMECA Atom Probe Technology Center in Madison, Wisconsin in laser pulsing mode. Run conditions and data reconstruction are summarized in Table 2. Two of the three specimens survived through the end of analysis. Reconstructions, ranging and cluster analysis have been performed using CAMECA's Integrated Visualization and Analysis Software (IVAS 3.6.10), with mass spectra showing consistent behavior from specimen-to-specimen (Fig. 2). The reconstruction of data sets was approached individually and iteratively, utilizing spectral ranges refined during preliminary reconstruction and data analysis. Reconstruction optimization held constant those parameters measured as part of pre- and post-acquisition imaging (sphere-cone radius ratio, shank angle, final end-tip radius, etc.) and aimed to reproduce the inferred dimensions of evaporated material, as estimated from pre-/post-analysis imaging. The bulk composition is consistent with that of zircon, with Hf, Y, Yb, and Pb constituting the detectable minor and trace elements. Pb isotopes appear as doubly charged ions within the mass spectrum (Fig. 2); no singly charged ions are detectable at 204, 206, 207 and 208 Da. There is no detectible $^{204}Pb^{2+}$ at 102 Da, and $^{208}Pb^{2+}$ occurs along with an isobaric interference from $^{28}Si_2{}^{16}O_3{}^{+}$ at 104 Da. No attempt at decomposing this interference is made here.

Each of the three APT data sets contain several sub-15 nm domains, enriched by a factor of ~10^2-10^3 over the surrounding matrix (Fig. 3). While these domains are similar in size and shape to other clusters in zircon [e.g., *Valley* et al., 2015; *Peterman* et al., 2016], they are distinct in that only some clusters possess a colocalization of Y, P and other REE. Although Pb-rich domains are not numerous, Pb is sufficiently concentrated in clusters that that they may be reliably isolated based directly on the spatial distribution of Pb.

2.1 Cluster Analysis

For any given APT data set, the absolute number of clusters, their dimensions and the total number of constituent atoms in each is, strictly speaking, dependent upon the cluster identification protocol and protocol inputs [e.g., *Gault* et al., 2012]. In order to evaluate the dependence of observed isotope ratios on the cluster definition (i.e., whether there is statistically significant spatial variability in Pb-isotope ratios), Pb-rich domains are isolated using six permutations of the two most common cluster identification methods: κth order Nearest Neighbor cluster analysis (κNN), and isoconcentration surfaces [e.g., *Gault* et al., 2012; *Larson* et al., 2013]. Cluster analysis is completed using IVAS 3.6.10 (see Table 2). Each cluster analysis permutation is applied to individual data sets, and the Pb-rich regions in the different data sets are concatenated to produce a composite mass spectra for the complete set of equivalently-defined BT5-13 clusters. In defining isoconcentration surfaces, several different delocalization and voxelation permutations were explored. Because Pb is a dilute component (particularly in the matrix) isoconcentration surface position and morphology becomes particularly sensitive to small fluctuations in Pb ion positioning when voxel sizes are too small, and when the delocalization is highly localized [e.g., *Larson* et al., 2013]. For all datasets, a

voxel size of [1.0, 1.0, 1.0] nm and a delocalization of [6.0, 6.0, 3.0] nm in the [x, y, z] dimensions describes the general cluster extent and shape, and effectively smooth the high-density layering associated with complex field evaporation behavior (see Fig. 3, and discussion below). For κNN cluster analysis, algorithm inputs were calibrated for each individual data set following the general methodology guided by κNN distributions (Fig. 4), cluster size distributions, and cluster count distributions [e.g., *Larson* et al., 2013]. The nearest neighbor distances between Pb atoms are determined for order parameters, κ, between one and ten (Fig. 4). At each κ, two peaks are observed; one at smaller Pb-Pb distances associated with Pb in clusters, and a peak at larger distances associated with Pb-Pb distances between more dilute Pb in the matrix. A third peak can be seen at very small Pb-Pb distances in two data sets, which occurs when a large proportion of clustered Pb atoms are reconstructed within high density layers. Given the broad separation of peaks associated with clustered and matrix Pb for κ>2, κNN cluster analyses were completed for orders κ=2, 3, 4, 5 (Fig. 4). For each κNN analysis, the maximum separation parameter, d_{max}, was taken to be the approximate minimum between the matrix and clustered Pb peaks in the nearest neighbor distribution. Following the rationale of *Chen* et al., [2014] we take the envelope parameter, $L=d_{max}$, and the erosion parameter, E, equal to d_{max} minus the maximum for the clustered Pb distribution. The consistent calibration of algorithm inputs, rather than unilateral application of a single set of inputs, helps to minimize any systematic differences between data sets introduced during data reconstruction. We note that the details of the reconstruction introduce uncertainties in the *absolute* position of ions and can introduce systematic error in the absolute size and shape of clusters. As a result, κNN algorithm inputs, and the position of a given isoconcentration surface, may vary slightly based on the exact reconstruction. This said, small changes in the reconstruction will result in small changes to the

relative position of closely spaced (nearest neighbor) ions. This, combined with a consistent calibration of the κNN algorithm inputs for each individual data set is expected to mitigate the dependence of observed isotope ratios to small variations in reconstruction parameters.

2.2 Ranging and Uncertainties

Determination of Pb isotope ratios and uncertainties requires the calculation of Pb isotope signals and the propagation of uncertainties, both those resulting from counting statistics and those resulting from data reduction. The $^{206}Pb^{2+}$ and $^{207}Pb^{2+}$ signals (^{206}S and ^{207}S, respectively) are calculated from the background correction of the total integrated peak counts (^{206}T and ^{207}T) in the 103 and 103.5 Da peaks, respectively:

$$^{207}S = {}^{207}T - {}^{207}B \qquad {}^{206}S = {}^{206}T - {}^{206}B \qquad (7)$$

Accurate isotope ratios ($^{207}Pb/^{206}Pb = {}^{207}S/^{206}S = {}^{207}Pb^{2+}/^{206}Pb^{2+}$) requires that the same fraction of each signal is integrated, and this is influenced by (1) the placement of integration bounds, and (2) characterization and correction of counts for peak overlaps/interferences. In order to evaluate the reproducibility of measured signal levels and their sensitivity to various parameters, this work utilizes a series of ranging protocols to identify peak integration bounds for the 103.0 and 103.5 Da peaks. In general, Pb isotope signals levels and signal-to-noise ratios vary significantly based on the data set and analytical volume. We explore two different ranging schemes that incorporate different assumptions of spectral complexity. In situations of well-separated peaks where peak overlaps are either absent or obscured, a simple ranging scheme can often be applied that identifies range bounds relative to the local background. In cases where peak tails are present or peak overlaps do not allow for a simple statistical approach, modeling of peak shapes can allow for both placement of range bounds and correction of counts within neighboring peaks

for a more accurate estimation of signals.

In cases where peak overlaps are ignored, we identify peak integration bounds by identifying *the continuous domain (for each peak) for which all individual bins exceed some statistical threshold*; this threshold is function of the local background, and the desired confidence level. In this work, the average background level per bin, B_1, and the standard deviation, $\sigma_{B,1}$, are calculated from the featureless portion of the spectrum between ~102.25 Da and ~102.75 Da. Because the background is well-described by Poisson statistics [*Larson* et al., 2013], $\sigma_{B,1} \approx \sqrt{B_1}$. While several different statistical thresholds can be used in to define ranges, we explore use of the critical level, L_C, and detection level, L_D, as discussed by [*Currie*, 1968]. The critical level can be considered the level at which counts exceed the background at some confidence level, and the detection level can the considered the level at which a signal is "detected" (i.e., exceeds the critical level) with a specified confidence level.

In establishing whether a single bin is included within the integrated signal, we start at the nominal peak position (103.0 and 103.5 Da, respectively) and move to the high or low side, considering counts in the *i*th bin relative to the threshold value, C_1 (Fig. 5). Determining L_C and L_D require consideration of the uncertainty in S_i as $S_i \rightarrow 0$, which is given by:

$$^{207}S_1 = {}^{207}T_1 - B_1 \qquad {}^{207}\sigma_{S0} = \sqrt{{}^{207}T_1 + B_1} = \sqrt{({}^{207}S_1 + B_1) + B_1} = \sqrt{2B_1} = \sqrt{2}\,\sigma_{B,1} \qquad (8)$$

$$^{206}S_1 = {}^{206}T_1 - B_1 \qquad {}^{206}\sigma_{S0} = \sqrt{{}^{206}T_1 + B_1} = \sqrt{({}^{206}S_1 + B_1) + B_1} = \sqrt{2B_1} = \sqrt{2}\,\sigma_{B,1} \qquad (9)$$

When C_1 is set equal to L_C (i.e., bins where $C_i > C_1 = L_C$ are statistically above the background level for a given confidence level), C_1 becomes [*Currie* et al., 1968; *Larson* et al., 2013]:

$$^{207}C_1 = L_C = B_1 + k\,{}^{207}\sigma_{S0} = B_1 + k\sqrt{2}\,\sigma_{B,1} \qquad (10)$$

$$^{206}C_1 = L_C = B_1 + k\,{}^{206}\sigma_{S0} = B_1 + k\sqrt{2}\,\sigma_{B,1} \qquad (11)$$

Where *k* represents the quantile for a given (single tailed) confidence level. We use a confidence level of 95%, corresponding to *k*=1.645; this represents the level at which there is only a 5% chance of C_i exceeding $B_1 + k\sigma_{S0}$ when no signal is present. On the low-m/n side of each peak, the range bound is identified as the outermost bin (relative to peak center) for which counts in the *i*th bin, C_i, exceed C_1, while $C_{(i-1)}$ does not (Fig. 5b). On the high side, range bounds are set at the outermost bin (relative to the peak center) for which $C_i > C_1$ exceed the cutoff, while $C_{(i+1)}$ does not. When C_1 is set equal to L_D, (i.e., the point at which *signal* in the *i*th bin exceeds L_C at some confidence limit) is given by:

$$^{207}C_1 = L_D = B_1 + k^2 + 2k^{207}\sigma_{S0} = B_1 + k^2 + 2k\sqrt{2}\,\sigma_{B,1} \qquad (12)$$

$$^{207}C_1 = L_D = B_1 + k^2 + 2k^{207}\sigma_{S0} = B_1 + k^2 + 2k\sqrt{2}\,\sigma_{B,1} \qquad (13)$$

where we again set *k*=1.649, corresponding to a single tailed confidence level of 95%. Analogous to above, this represents where there is only a 5% chance of C_i exceeding L_D when the true signal is less than (L_C - B_1).

In the approach above, we have assumed that the 103.0 and 103.5 Da peaks share a common background level, and there is no statistically significant tail on the 103.0 Da peak which contributes to the 103.5 Da peak (discussed in more detail below). In this simple case, the background counts integrated in each peak (^{206}B and ^{207}B) and their uncertainties ($^{206}\sigma_B$ and $^{207}\sigma_B$) can be calculated from B_1 and $\sigma_{B,1}$:

$$^{207}B = B_1 n_{bin,207} \qquad ^{207}\sigma_B = \sqrt{^{207}B} = \sqrt{B_1 n_{bin,207}} = \sigma_{B,1}\sqrt{n_{bin,207}} \qquad (14)$$

$$^{206}B = B_1 n_{bin,206} \qquad ^{206}\sigma_B = \sqrt{^{206}B} = \sqrt{B_1 n_{bin,206}} = \sigma_{B,1}\sqrt{n_{bin,206}} \qquad (15)$$

For any given spectrum, this procedure is a simple way to statistically identify range bounds, assuming well-separated peaks with minimal signal in peak tails. We repeat this procedure at

spectral binnings between 0.001 to 0.045 Da, in increments of 0.001 Da, in order to ascertain the variability in measured signal and calculated ratios associated with spectral binning. This range of bin widths form a continuum between overly fine bin widths (highly resolved bins with significant noise), through well-defined peak shapes, to overly coarse bin widths having oversimplified peak shapes. Each of these spectra are representations of the same underling data, but with different effective smoothing and count levels (per bin). The calculation of isotope ratios can be done at any spectral binning, though for reasons discussed below, there are practical considerations in the range of bin widths that will generate accurate and precise ratios, and how sensitive a ranging approach is to bin width.

This general procedure is a pragmatic approach that balances several aspects of the ranging process, and can be consistently and reproducibly applied to both the 103.0 and 103.5 Da peaks. This said, Pb isotope signals remain a function of integration bounds, and there exists some uncertainty in the placement of bounds within real data, particularly in cases where integrated signal level approach the limits of detection, and thus a large number of bins within a given peak occur at or near L_C (or L_D). If peak overlaps are considered negligible, accurate determination of isotope ratios requires that equivalent proportions of each peak be integrated. For a single peak, wider integration bounds will integrate more of the peak and will (1) include a better estimate of the true signal (while incorporating additional uncertainty from background correction) and (2) be less sensitive to spectral characteristics (bin width, etc.). Uncertainty in ranging of peaks can be estimated by integrating a proportionally wider region of the two peaks, and comparing this ratio to that calculated initially. If, for example, the 103.5 peak was significantly "under-ranged," then there will be a larger shift in ^{207}S, and increase in the $^{207}Pb/^{206}Pb$ ratio. If the range bounds defined based on L_C (or L_D) integrate regions $^{206}\eta_1$ and

$^{207}\eta_1$, we integrate an additional 25% of each peak on both the high and low side, and estimate $\sigma_{ranging}$ (Fig. 5d):

$$\sigma_{7/6,\text{ranging}} = \frac{\left(^{207}\text{Pb}/^{206}\text{Pb}\right)_{\eta 2}}{\left(^{207}\text{Pb}/^{206}\text{Pb}\right)_{\eta 1}} - 1 \quad (16)$$

This uncertainty can be propagated along with uncertainties from counting statistics and background correction to represent a more complete uncertainty in the measured ^{207}Pb/^{206}Pb ratio.

We note that for the BT5-13, there exists a subset of the spectral binnings for which the identified range bounds result in the total number of bins *between* the $^{206}\eta_1$ and $^{207}\eta_1$ ranges is less than ($^{206}\eta_1$ + $^{207}\eta_1$)/4 (Fig. 5). While this is a natural product of how counts are distributed within bins, there would be overlap in the regions integrated by $^{206}\eta_2$ and $^{207}\eta_2$, and thus the counts within such a region would result in "double counting" of some spectral bins. In such situations, the counts between $^{206}\eta_1$ and $^{207}\eta_1$ are divided equally between ^{206}Pb and ^{207}Pb in order to avoid this complexity. From an analytical standpoint, more of the counts between the two peaks have been attributed (according to the ranging procedure above) as either $^{207}Pb^{2+}$ or $^{206}Pb^{2+}$ in placement of $^{206}\eta_1$ and $^{207}\eta_1$, and the effective uncertainty in integrated signal as a function of the middle two integration bounds decreases.

In calculating the total uncertainty in the ^{207}Pb/^{206}Pb ratio, $\sigma_{7/6}$, we propagate errors originating from counting statistics, background correction and ranging:

$$^{207}\sigma_S = \sqrt{^{207}\sigma_{CS}{}^2 + {}^{207}\sigma_B{}^2} = \sqrt{^{207}T + B_1 n_{bin,207}} \quad (17)$$

$$^{206}\sigma_S = \sqrt{^{206}\sigma_{CS}{}^2 + {}^{206}\sigma_B{}^2} = \sqrt{^{206}T + B_1 n_{bin,206}} \quad (18)$$

$$\sigma_{7/6} = \sqrt{^{207}\sigma_S{}^2 \left(\frac{\partial \text{R}_{76}}{\partial ^{207}S}\right)^2 + {}^{206}\sigma_S{}^2 \left(\frac{\partial \text{R}_{76}}{\partial ^{206}S}\right)^2 + \sigma_{7/6,ranging}{}^2} \quad (19)$$

Where $^{207}\sigma_S$ and $^{206}\sigma_S$ are uncertainties in ^{207}S and ^{206}S from background correction and counting statistics, and $\sigma_{7/6,ranging}$ is the uncertainty from eqn. (16) above.

For the BT5-13 cluster data sets, there do exist small, but observable, tails to on the high-m/n side of the 103.0 and 103.5 Da peaks. The signal levels within these tails are sufficiently small to permit the ranging and background correction scheme above to largely ignore this complexity; however, qualitatively speaking there is a loss of accuracy when this is unaccounted for, both in determining the most accurate ^{206}S and ^{207}S, but also in correcting ^{207}S for $^{206}Pb^{2+}$ ions within the 103.0 Da peak tail. We look to treat this aspect of ranging for two reasons: (1) to evaluate the difference in $^{207}Pb/^{206}Pb$ ratio when accounting for and correcting counts based on peak tails, and (2) the general occurrence of higher backgrounds, larger peak tails and peak overlaps can necessitate accounting for these spectral features in order to derive accurate and precise $^{207}Pb/^{206}Pb$ ratios. We explore alternative means to define the range bounds and correct signal levels associated with the 103.0 and 103.5 Da peak for situations where peak tails are more pronounced.

Here, the modeling of peak tails to calculate signal levels and correct peak overlaps is approached very generally; there exists no analytical peak form for fitting of peaks (or peak tails) given peak shapes vary as a function of numerous variables including specimen properties (e.g., material properties, specimen geometry, etc.), instrument configuration (e.g., straight flight path vs. reflection geometry), run conditions (specimen base temperature, laser spot size, laser pulse energy, pulse frequency, etc.) and spectral calibration [e.g., *Kellogg and Tsong*, 1980; *Bunton* et al., 2007]. The time dependence of field evaporation varies between samples, given each specimen possesses small differences in geometry, which in turn influences the thermal response of the specimen during laser pulsing. Strictly speaking, these differences in thermal behavior will

manifest as small differences in peak shapes between various mass spectra. While several studies have fit peak tails based on numerical modeling of peak thermal evolution which incorporates geometric and material properties of the specimen [e.g., *Vurpillot* et al., 2004; *Bunton* et al., 2007; *Bachkav* et al., 2011] these methods are not as suitable for evaluation of *concatenated* spectra, sourced from multiple specimen (such as those analyzed here). In light of this, we fit background corrected peak tails on the high-m/n side of the 103.0 and 103.5 Da peaks, starting at approximately the full width at tenth maximum, using a functional form:

$$C = a_1 \exp(a_2 x^p) \qquad (20)$$

Where a_1, a_2, and p are fit constants, and x is the mass-to-charge state ratio. The general purpose of our modeling is estimation, correction and calculation of Pb isotope signals, and we stress that the general procedure presented here is not dependent upon this peak shape model, and can be implemented and/or adapted using a variety of fitting functions or with more robust modeling of peak forms (e.g., thermal modeling of peak tails).

Calculating signal levels and isotope ratios using fits to the peak tails follow a similar approach to the procedure presented above, but with several adaptations (Fig. 6). Peak fitting and placement of range bounds is approached using an iterative background stripping scheme; the background corrected fit to the 103.0 Da peak tail is used to correct the 103.5 Da peak for ^{206}Pb, and the tail of the 103.5 Da peak is then fit. The fits to the corrected spectra are used to establish integration bounds within the peak tails by establishing when the fit drops below the critical limit, L_C. The low-side integration bounds of each peak are placed analogous to above: by finding for the continuous range where $C_i > C_1 = L_C$; however, because we now treat the 103.5 Da peak as sitting on the tail of the 103.0 Da peak, the "background" relevant for establishing significant $^{207}Pb^{2+}$ counts requires consideration of 103.0 Da peak tail (in this case, the fit of the

103.0 peak tail). Thus, $^{207}C_{1,i} = L_C$ is a function of position within the peak tail, and becomes:

$$^{207}C_{1,i} = \left(B_1 + {}^{206}S_{i,fit}\right) + k\,{}^{207}\sigma_{S0} = \left(B_1 + {}^{206}S_{i,fit}\right) + k\sqrt{2}\sqrt{\left({\sigma_{B,1}}^2 + {}^{206}S_{i,fit}\right)} \quad (21)$$

where $^{206}S_{i,fit}$ is the modeled $^{206}Pb^{2+}$ signal in the *i*th bin.

The $^{207}Pb^{2+}$ and $^{206}Pb^{2+}$ signals are calculated by summing the spectra between the designated integration bounds, and correcting for both background counts and modeled peak overlaps. This procedure is repeated at bin widths of data between 0.001 Da and 0.045 Da, in increments of 0.001 Da. Fitting of peak tails is used principally for placement of range bounds, and correction of the 103.5 Da peak (Fig. 6); $^{206}Pb^{2+}$ signal levels are estimated from the peak fit *only* in the small number of cases where the fitting of the peak tail results in peak integration bounds which overlap. We do not attempt to estimate the uncertainty in signal levels associated with placement of range bounds for the 103.0 or 103.5 Da peaks based on fitting. Because counts within the ^{207}Pb and ^{206}Pb tails are small, these errors will be minimal and do not influence the conclusions below; however, this may be an important source of uncertainty in cases where larger peak overlaps occur.

Accounting for the estimated $^{206}Pb^{2+}$ contribution to the 103.5 Da peak, the total uncertainty in the $^{207}Pb/^{206}Pb$ ratio then becomes:

$$^{207}\sigma_S = \sqrt{{}^{207}\sigma_{CS}{}^2 + {}^{207}\sigma_B{}^2} = \sqrt{{}^{207}T + \left(B_1 n_{bin,207} + \sum_i^n {}^{206}S_{i,fit}\right)} \quad (22)$$

$$^{206}\sigma_S = \sqrt{{}^{206}\sigma_{CS}{}^2 + {}^{206}\sigma_B{}^2} = \sqrt{{}^{206}T + B_1 n_{bin,206}} \quad (23)$$

$$\sigma_{7/6} = \sqrt{{}^{207}\sigma_S{}^2 \left(\frac{\partial \mathrm{R}_{76}}{\partial {}^{207}S}\right)^2 + {}^{206}\sigma_S{}^2 \left(\frac{\partial \mathrm{R}_{76}}{\partial {}^{206}S}\right)^2} \quad (24)$$

One spectral complication that is not treated here is the potential of a $^{206}Pb^1H^{2+}$ contribution to the 103.5 Da peak. This interference cannot be resolved within this data and the magnitude and

nature of hydride interferences remains an active area of research. We follow the rationale of *Valley* et al., [2015] and consider this contribution negligible for the analytical precision determined here.

3 RESUTS AND DISCUSSION

3.1 Cluster Analysis

The consistent application of clustering algorithms isolates broadly similar regions within the three BT5-13 data sets, though different approaches generate small differences in the total number of clusters, their size, and the total number of Pb atoms (Fig. 7-9, Table 3). The similarity between the different approaches is somewhat expected given the 10^2 to 10^3 relative enrichment of Pb within most clusters, and the relatively sharp boundary between clusters and matrix. Several smaller, more dilute clusters are identified within the M1_491 and M1_568 data sets; these small clusters are largely excluded when using the higher concentration 0.5% atom Pb threshold for the isoconcentration surfaces. As will be discussed later, both the small total number of clusters, and the small total number of Pb atoms within smaller more dilute clusters, make it difficult to identify a definitive difference in phase relations, genesis, or timing of formation relative to larger clusters. The consistent application of the κNN cluster algorithm led to identification of all clusters >0.25 atom% Pb, though parsing data for individual clusters still allows one to discern a general difference in low- vs. high-Pb clusters.

Several of the large clusters possess a high density of reconstructed ions (all ions, not only Pb) in layers on the upper surface of the Pb-rich domains (Fig. 3); similar features have been observed before [e.g., *Peterman* et al., 2016] and are associated with increased evaporation of constituent atoms upon exposure of the Pb-rich domains at the surface of the specimen. It is

evident that Pb-rich domains possess a distinct evaporation field relative to the surrounding zircon. Whether these domains constitute a distinct nanoscale phase within the BT5-13 zircon remains unclear based on the present data. The Pb-rich domains have an approximate "zircon composition" based on the Zr, Si, and O, however they contain up to 3% atomic Pb. The comparison of bulk APT compositions and those of clusters, suggest that Pb is accommodated by a decrease in Zr. As noted above, the quantitative compositional analysis, particularly of complex oxides, remains an active area of research, and while the evaporation behavior and composition are distinct from those of the surrounding zircon, the structure, accommodation, and detailed composition of these nanoscale domains requires further study. These details have important implications for the genesis and origin of clusters; however, given high density layers are associated with clusters and are identified as such by the approaches above, these details are largely independent of the *analytical* limitations on Pb isotopic measurement discussed here.

3.2 Ranging and $^{207}Pb/^{206}Pb$ ratios

Within the concatenated BT5-13 cluster data sets, signal-to-background ratios are relatively high (between 20-85), and $^{207}Pb^{2+}$ and $^{206}Pb^{2+}$ signal levels are within 30% of one another. For any given cluster definition, all three ranging approaches generate relatively consistent trends for signal levels and isotope ratios as a function of bin width (representative data for the 0.5% atomic Pb clusters is shown in Fig. 10). At very fine bin widths, ranged signals are systematically low, particularly for range definitions based on L_C and L_D. As bin width increases, signal levels increase and stabilize at an approximately constant level, with the signal level, and scatter in the signal level, being dependent on the ranging approach. Ranging based on fitting of peak tails is less sensitive to bin width, as it effectively smooths data as the signal

within the peak tails approaches the background. The measured $^{207}Pb/^{206}Pb$ ratios possess similar trends to those of the signal levels: ratios are low and scattered at fine bin widths where there is increased scatter in ranged $^{206}Pb^{2+}$ and $^{207}Pb^{2+}$ signal levels, and the ratios stabilize as binning becomes coarser. Importantly, only data at fine bin widths are statistically distinct from the majority of isotope ratios.

Each ranging approach above possesses advantages and disadvantages which are not independent of the signal levels and background levels inherent in the data. Basing ranges on L_D is simpler to apply to data sets, however, this approach generates thinner ranges and includes fewer counts from peak edges where counts approach the background level. The thinner ranges result in isotope ratios which possess more scatter as a function of bin width; the 2σ scatter in isotope ratios as a function of bin width between 0.010 and 0.045 Da bin widths (filled circles in Fig. 10) is 0.008 or just under 2%. This can be compared to ranges based on L_C and fitting of peak tails which each possess 2σ scatter of 0.008 (1.1%) over the same range in bin widths. These differences make intuitive sense, as thinner ranges are more sensitive to the distribution of counts within bins at any given bin width. While all three ranging approaches are likely to generate accurate isotope ratios, ranges based on L_C and fitting of peak tails are considered more reproducible and precise. Because peak overlaps are largely negligible, these two approaches produce virtually identical measured $^{207}Pb/^{206}Pb$ ratios for the signal levels and isotope ratios within the BT5-13 cluster data sets. Both of these procedures are capable of identifying consistent signal and isotope ratios in cases where peak overlaps are minimal, and while the work here demonstrates how fitting and ranging may work in practice for overlapping peaks, the accuracy of this decomposition (as it pertains to $^{207}Pb/^{206}Pb$ ratios) requires further testing.

The results above demonstrate that for bin widths that are not overly fine, the ranging

approaches above generate consistent ratios which are statistically equivalent over a broad range of bin widths. For each cluster definition, representative ratios at or near the mean of ratios between 0.010 Da and 0.045 Da bin widths is summarized in Table 3. All of the ranging approaches (L_C, L_D, Fit) for all the cluster definitions (2CA, 3CA, 4CA, 5CA, 0.25 % atomic Pb, 0.5% atomic Pb) result in statistically identical $^{207}Pb/^{206}Pb$ isotope ratios, varying between 0.794±0.15 (±2σ; 470 atoms) and 0.715±0.052 (3343 atoms). While the consistency of ratios give the appearance of a "systematic offset" between the *κ*NN cluster analysis and isoconcentration surface cluster definitions, this difference cannot be considered statistically significant. The most direct comparison of the Pb isotope structure of clusters, is between the 0.5 atom% Pb isosurface and 0.25 atom% Pb isosurface definitions, with these results indicating identical Pb isotope ratios within uncertainty.

For the BT5-13 clustered data sets, counting statistics are the largest contributor to uncertainty in the $^{207}Pb/^{206}Pb$ ratios. Maximizing detection efficiency based on technological advances and/or instrument geometry may serve as a means to collect a larger number of ions for the same volume, and improve the precision of Pb isotope ratios. For the LEAP 5000 series of instruments manufactured by CAMECA Inc., nominal detection efficiencies are 50% and 80% for the reflection and straight flight path geometries, respectively. The data presented here were collected on a LEAP 5000 XR (reflection geometry) and an increase in Pb counts by 60% has potential to improve aspects of precision in APT Pb isotope determinations. However, the consistency in isotope ratio determination here benefits from well-defined and well-separated peaks; the increase in detection efficiency is balanced by broader peaks and other aspects of spectral analysis, such as fitting and constraining peak overlaps, may become increasingly important (and perhaps limiting) aspects of $^{207}Pb/^{206}Pb$ analysis by APT.

Signal-to-noise ratios within the bulk data sets are far lower than those of the clusters, with ^{207}Pb approaching the statistical detection limit; these factors drastically alter the applicability of the ranging approaches outlined above. For the concatenated bulk data sets (i.e., bulk data for all three specimens), ranging based on L_C results in $^{207}Pb/^{206}Pb = 0.191 \pm 0.080$ (2σ). This value is statistically distinct from that measured by SIMS (for spot BT5-13-2: $^{207}Pb/^{206}Pb = 0.3675 \pm 0.0037$; $(^{207}Pb/^{206}Pb)^* = 0.3666 \pm 0.0044$, 2σ) and we do not assign significance to this ratio derived from APT for several reasons: (1) low signal-to-noise results in $^{207}Pb/^{206}Pb$ ratios which are much more sensitive to bin width and ranging, (2) the lower relative signal-to-noise for the 103.5 Da peak leads to a systematic "under-ranging" when applied based on L_C (thus the calculated ratio is considered inaccurate), and (3) the uncertainty in background correction (particularly for ^{207}Pb) becomes the largest contributor to overall uncertainty. The relevance of this last point is particularly clear when considering that, while they are within uncertainty, ^{207}Pb counts within clusters exceed the total ^{207}Pb counts determined within the bulk data set (Table 3). Poorly resolved peak shapes (due to much higher background) makes peak fitting untenable, and fitting was not attempted on the bulk data sets.

Due to the above factors, we have also ranged the 103.0 and 103.5 Da peaks "by hand", holding constant the integration bounds and correcting each peak using the background level *directly adjacent* (as opposed to using a single background range between ~102.25 and ~102.75 Da). This results in an isotope ratio of $^{207}Pb/^{206}Pb=0.353 \pm 0.18$ (2σ), excluding any estimation of errors due to ranging (Table 3; Fig. 11). These data are relatively imprecise, and as such it is difficult to ascribe them geological significance; however, these data are both (1) a striking match to SIMS based $^{207}Pb/^{206}Pb$ measurements, and (2) significantly lower than isotope ratios within clusters. This may be (cautiously) treated as supporting evidence in favor of closed

system U-Pb systematics on the micron scale (within the zircon core). For BT5-13, the strongest evidence for this is the uniform chemical and isotopic composition within the zircon core measured by SIMS.

The data sets above highlight both the strengths and limitations of statistical or fit based ranging (as they are applied here). Most notably the statistical and fit based approaches become increasingly unreliable for isotope ratio determinations as signals approach the limits of detection, particularly if this occurs for one isotope but not another. It remains true that there is no singular method for ranging, and the relevant uncertainties and limits of interpretation must be considered on a data set-by-data set (and spectrum-by-spectrum) basis. The approaches outlined above in section 2.2 are well-suited for reproducible measurement of Pb isotope ratios, and the appropriate uncertainties, for data at moderate to high signal-to-noise levels. In general, peak fitting is considered the most likely to result in accurate and precise signals, as this approach effectively smooths data as it approaches the background, and allows for estimation of overlapping signals in adjacent 103.0 and 103.5 Da peaks; however, in such a situation, range bounds become dependent upon data fitting, and thus the functional form/method used in fitting peak tails. An in-depth investigation of this type of analysis is beyond the scope of this paper. In general, the analysis above supports the general considerations for ranging presented elsewhere [e.g., *Larson* et al., 2013]. For "well-separated peaks" (taken here to mean those peaks where C_i drops below L_c between peaks) with moderate signal-to-noise ratios, reasonable ranges that include a large percentage of the $^{207}Pb^{2+}$ and $^{206}Pb^{2+}$ signals should generate reproducible $^{207}Pb/^{206}Pb$ ratios within error; errors due to background correction and counting statistics should provide a good estimate of the total uncertainty in $^{207}Pb/^{206}Pb$. In cases where peak overlaps are present, peaks are not well-separated, or geological interpretations are at the limits of these

uncertainties, consideration of other factors limiting accuracy and precision may be required.

3.3 Model Ages for Cluster Formation:

Above, we have been largely concerned solely with spatial and spectral aspects of measuring $^{207}Pb/^{206}Pb$ isotope ratios; here we look to make first order interpretations about their geological significance. Given the systematic trends in bulk and clustered Pb ratios in the BT5-13 data sets, clustered Pb is taken to represent ancient reorganization of radiogenic Pb; as discussed above, the timing of Pb mobility and cluster formation can be modeled based on cluster $^{207}Pb/^{206}Pb$ ratios. We make several simplifications in calculating "model cluster ages." Firstly, we assume the initial Pb component is vanishingly small and thus all Pb within the APT data is radiogenic in origin; this is supported by no detectable ^{204}Pb at 102 Da within the APT data, and the low level of common Pb within SIMS analyses. We also assume there was complete partitioning of Pb into cluster domains at t_2 (within analytical uncertainty), and $X'_{Pb,t2} \rightarrow 1$ (i.e., $^{207}Pb/^{206}Pb$ ratios within clustered domains represent the isotope ratios of cluster Pb at t_2: eqn. (5,6)). The partitioning behavior of Pb at t_2 is difficult to quantify directly, given the differences in matrix Pb concentrations for large vs. infinite partitioning are expected to be subtle in the present data; however, the large relative concentration of Pb between matrix and clusters supports this assumption and differences in theoretical and calculates ages based on incomplete partitioning of Pb is expected to be small for the cluster volume fraction in the BT5-13 zircon [*Blum* et al., *in prep*.]. The two 100% concordant SIMS U-Pb analyses for the BT5-13 core, and an imprecise but statistical match between $^{207}Pb/^{206}Pb$ ratios derived from bulk APT data sets and SIMS, are consistent with a 3.775 Ga crystallization age and subsequent closed system U-Pb behavior on the micron scale. Using these assumptions, we can solve numerically for t_2 and a

model cluster age for each of the cluster definitions (Fig. 12, and Table 3); these ages vary between 2.76 to 2.80 Ga. These model cluster ages are consistent with clustering of radiogenic Pb during high temperature event(s) within the Beartooth Mountains. The estimated ages for granulite facies metamorphism (~3.25-3.1 Ga) and retrograde amphibolite facies metamorphism are within uncertainty of the calculated ages; however, the 2.76-2.8 Ga age range coincides particularly well with the intrusion of the Long Lake igneous complex at ~2.74-2.79 Ga [*Mueller* et al., 1988]. Independent of the exact event leading to cluster formation, these cluster model ages are yet another example of where Pb mobility and clustering (1) is temporally associated to high temperature periods in a zircon's history, and (2) the nanoscale domains are stabilized and preserved through geologic time. Understanding uncertainties surrounding measurement of isotope ratios within nanoscale domains allows for more robust evaluation of the timing and genesis of these nanoscale domains within zircon.

4 CONCLUSIONS

The ranging approaches presented here is a systematic means to assess the uncertainties associated with measurement of $^{207}Pb/^{206}Pb$ ratios in nanoscale zircon domains by APT. For the BT5-13 cluster data sets, statistical and fit based approaches to placement of range bounds can provide accurate and precise Pb isotope ratios, where the precision in $^{207}Pb/^{206}Pb$ ratio is limited primarily by counting statistics. At lower signal-to-noise, such as in bulk zircon data sets, these procedures are less successful and the high background results in lower signal peaks (i.e., $^{207}Pb^{2+}$ at 103.5 Da) being systematically under-ranged. In such situations, accuracy is improved by "manual" ranging, though caution is advised in assigning geological significance to these results without considering the source and magnitude of variability due to ranging and bin width. The

ability to place errors on the $^{207}Pb/^{206}Pb$ ratios measured in APT provides an objective means to evaluate the significance of different ratios within different domains. The signal levels, and spatial distribution of Pb within zircon BT5-13 APT data sets result in very consistent $^{207}Pb/^{206}Pb$ ratios for the consistent application of several cluster identification algorithms. The ratios and uncertainties for $^{207}Pb/^{206}Pb$ from SIMS, and bulk vs. clustered domains by APT support that clustered domains represent ancient reorganization of radiogenic Pb, and thus modeling of ratios may be used to estimate the timing of cluster formation. Model cluster ages of 2.8 Ga correlate with both granulite facies and amphibolite facies metamorphism within the Beartooth Mountains, as well as the intrusion of the Long Lake igneous complex. These results relate cluster formation to high-T periods within the history of BT5-13. The spatial, spectral and age data presented here highlight the potential for understanding the timing and driving forces for element reorganization as a function of time and temperature through the correlative application of APT, EBSD, and SIMS.

ACKNOWLEDGEMENTS

We thank the Beijing CAGS SHRIMP Lab, and particularly D. Liu and A. Cavosie for their help in SIMS data collection and analysis. This research was funded by the US National Science Foundation (EAR-1144454, EAR-1524336), and the US Department of Energy, Office of Science, Office of Basic Energy Sciences, Chemical Sciences, Geosciences and Biosciences Division under award number DE-FG02-93ER14389. WiscSIMS is partly supported by the U.S. National Science Foundation (EAR-1355590). The authors acknowledge the use of facilities supported by the University of Wisconsin, College of Engineering and the Materials Research and Engineering Center (NSF DMR-121288) and Nanoscale Science and Engineering Center

(NSF DMR-0832760).

REFERENCES

Bachhav, M.N., Danoix, R., Vurpillot, F., Hannoyer, B., Ogale, S.B., Danoix, F. (2011) Evidence of lateral heat transfer during laser assisted atom probe tomography analysis of large band gap materials, Applied Physics Letters, 99, 084101.

Tyler B. Blum, James R. Darling, Thomas F. Kelly, David J. Larson, Desmond E. Moser, Alberto Perez-Huerta, Ty J. Prosa, Steven M. Reddy, David A. Reinhard, David W. Saxey, Robert M. Ulfig, David J. Larson, John W. Valley (2018) Best practices for reporting atom probe analysis of geological materials, in *Microstructural Geochronology: Planetary Records Down to Atom Scale*, edited by D. Moser, F. Corfu, S. Reddy, J. Darling, and K. Tait, John Wiley & Sons, Inc., Hoboken, NJ, 232, 369–373.

Bowring, S.A., Schmitz, M.D. (2003) High-precision U-Pb zircon geochronology and the stratigraphic record, Rev. in Min. and Geochem., 53, 305-326.

Bunton, J.H., Olson, J.D., Lenz, D.R., Kelly, T.F. (2007) Advances in Pulsed-Laser Atom Probe: Instrument and Specimen Design for Optimum Performance, Microscopy and Microanalysis, 13, 418-427.

Cavosie, A.J., Valley, J.W., Wilde, S.A., E.I.M.F. (2006) Correlated microanalysis of zircon: Trace element, $\delta^{18}O$, and U-Th-Pb isotopic constrains on the igneous origin of complex >3900 Ma detrital grains, Geochimica et Cosmochimica Acta, 70, 5601-5616.

Chen, Y., Chou, P.H., Marquis, E.A. (2014) Quantitative atom probe tomography characterization of microstructures in a proton irradiated 304 stainless steel, Journal of Nuclear Materials, 451, 130-136.

Cherniak, D.J., Lanford, W.A., Ryerson, F.J. (1991) Lead diffusion in apatite and zircon using ion implantation and Rutherford Backscattering techniques, Geochimica et Cosmochimica Acta, 55, 1663-1673.

Cherniak, D.J., Watson, E.B. (2003) Diffusion in zircon, Rev. in Min. and Geochem., 53, 113-143.

Currie, L.A. (1968) Limits for Qualitative Detection and Quantitative Determination: Application to Radiochemistry, Analytical Chemistry, 40(3), 586-59.

Ewing, R.C., Meldrum, A., Wang, L., Weber, W.J., Corrales, L.R. (2003) Radiation effects in zircon, Rev. in Min. and Geochem., 53, 387-425.

Fedo, C.M., Sircombe, K.N., Rainbird, R.H. (2003) Detrital zircon analysis in the sedimentary record, Rev.in Min. and Geochem., 53, 277-303.

Gault, B., Moody, M.P., Cairney, J.M., Ringer, S. (2012) Atom Probe Microscopy, 396 p.

Springer.

Gedcke, D.A. (2001) How counting statistics control detection limits and peak precision. ORTEC Application Note AN59.

Henry, D.J, Mueller, P.A., Wooden, J.L., Warner, J.L., Lee-Berman, R. (1984) Granulite grade supracrustal assemblages of the Quad Creek area, eastern Beartooth Mountains, Montana, Montana Bureau of Mines and Geology Special Publication, 84, 147-156.

Hudson, D., Smith, G.D.W., Gault, B. (2011) Optimization of mass ranging for atom probe microanalysis and application to the corrosion process in Zr alloys, Ultramicroscopy, 111, 480-486.

Kirchhofer, R., Teague M.C., Gorman, B.P. (2013) Thermal effects on mass and spatial resolution during laser pulse atom probe tomography of cerium oxide, Journal of Nuclear Materials, 436, 23-28.

Kellogg, G.L., Tsong, T.T. (1980) Pulsed-laser atom-probe field-ion microscopy, Journal of Applied Physics, 51, 1184-1192.

Larson, D.L., Prosa, T.J., Ulfig, R.M., Geiser, B.P., Kelly, T.F., (2013) Local Electrode Atom Probe: A User's Guide. 318 p. Springer.

Mueller, P.A., Shuster, R.D., Graves, M.A., Wooden, J.L., Bowes, D.R. (1988) Age and Complexation of a Later Archean Magmatic Complex, Beartooth Mountains, Montana-Wyoming, Montana Bureau of Mines and Geology Special Publication, 96, 7-22

Mueller, P.A., Wooden, J.L., Nutman, A.P. (1992) 3.96 Ga Zircons from an Archean quartzite, Beartooth Mountains, Montana, Geology, 20, 327-330.

Nasdala, L., Wenzel, M., Vavra, G., Irmer, G., Wenzel, T., Kober, B. (2001) Metamictization of natural zircon: accumulation versus thermal annealing of radioactivity-induced damage, Contributions to Mineralogy and Petrology, 141, 125-144.

Nemchin, A., Timms, N., Pidgeon, R., Geisler, T., Reddy, S., Meyer, C. (2009) Timing of crystallization of the lunar magma ocean constrained by the oldest zircon, *Nature Geoscience*, 2, 133-136.

Oberdorfer, C., Stender, P., Rinke, C., Schmitz, G. (2007) Laser-Assisted Atom Probe Tomography of Oxide Materials, Microscopy and Microanalysis, 13, 342-346.

Oltman, E., Ulfig R.M., Larson, D.J. (2009) Background Removal Methods Applied to Atom Probe Data, Microscopy and Microanalysis, 15(S2), 256-257.

Peterman, E.M., Reddy, S.M., Saxey, D.W., Snoeyenbos, D.R., Rickard, W.D.A., Fougerouse, E.M., Kylander-Clark A.R.C., (2016) Nanogeochronology of discordant zircon measured by atom probe microscopy of Pb-enriched dislocation loops, Science Advances, 2, e1601318.

Piazolo, S., La Fontaine, A., Trimby, P., Harley, S., Yang, L., Armstrong, R., Cairney, J.M. (2016) Deformation-induced trace element redistribution in zircon revealed using atom probe tomography, Nature Communications, 7, 10490.

Reddy, S.M., van Riessen, A., Saxey, D.W., Johnson, T.E., Rickard, W.D.A., Fougerouse, D., Fischer, S., Prosa, T.J., Rice, K.P., Reinhard, D.A., Chen, Y., Olson, D. (2016) Mechanisms of deformation-induced trace element migration in zircon resolved by atom probe and correlative microscopy, Geochimica et Cosmochimica Acta, 195, 158-170.

Reinhard, D.A., Moser, D.E., Barker, I.R., Olson, D., Martin, I., Rice, K.P., Chen, Y., Lawrence, D., Prosa, T.J., Larson, D.J., (2015) Atom Probe Tomography of Zircon and Baddeleyite Geochronology Standards, Microscopy and Microanalysis, 21(3), 0426.

Schoene, B., Schaltegger, U., Brack, P., Latkoczy, C., Stracke, A., Günther, D. (2012) Rates of magma differentiation and emplacement in a ballooning pluton recorded by U-Pb TIMS-TEA, Adamello batholith, Italy, Earth and Planetary Science Letters, 355-356, 162-173.

Valley, J.W. (2003) Oxygen isotopes in zircon, Reviews in Mineralogy and Geochemistry, 53, 343-385.

Valley, J.W., Lackey, J.S., Cavosie, A.J., Clechenko, C.C., Spicuzza, M.J., Basei, A.S., Bindeman, I.N., Ferreira, V.P., Sial, A.N., King, E.M., and others, (2005) 4.4 billion years of crustal maturation: oxygen isotope ratios of magmatic zircon, Contributions to Mineralogy and Petrology, 150, 561-580.

Valley J.W., Cavosie, A.J., Ushikubo, T., Reinhard, D.A., Lawrence, D.F., Larson, D.J., Clifton, P.H., Kelly, T.F., Wilde, S.A., Moser, D.E., Spicuzza, M.J. (2014a) Hadean age for post-magma-ocean zircon confirmed by atom probe tomography, Nature Geoscience, 7, 219-223.

Valley, J.W., Spicuzza, M.J., Ushikubo, T. (2014b) Correlated $\delta^{18}O$ and [Ti] in lunar zircons: a terrestrial perspective for magma temperatures and water content on the Moon, Contributions to Mineralogy and Petrology, 167, 956.

Valley, J.W. Reinhard, D.A., Cavosie, A.J., Ushikubo, T., Lawrence, D.F., Larson, D.J., Kelly, T.F., Snoeyenbos, D.R., Strickland, A. (2015) Nano- and Micro-geochronology in Hadean and Archean zircons by atom-probe tomography and SIMS: New tools for old minerals, American Mineralogist, 100, 1355-1377.

Vella, A., Mazumder, G., Da Costa, G., Deconihout, B., (2011) Field evaporation mechanism of bulk oxides under ultra-fast laser illumination, Journal of Applied Physics, 110:044321.

Vurpillot, F., Larson, D.J., Cerezo, A. (2004) Improvement of multilayer analyses with a three-dimensional atom probe, Surface and Interface Analysis, 36, 552-558.

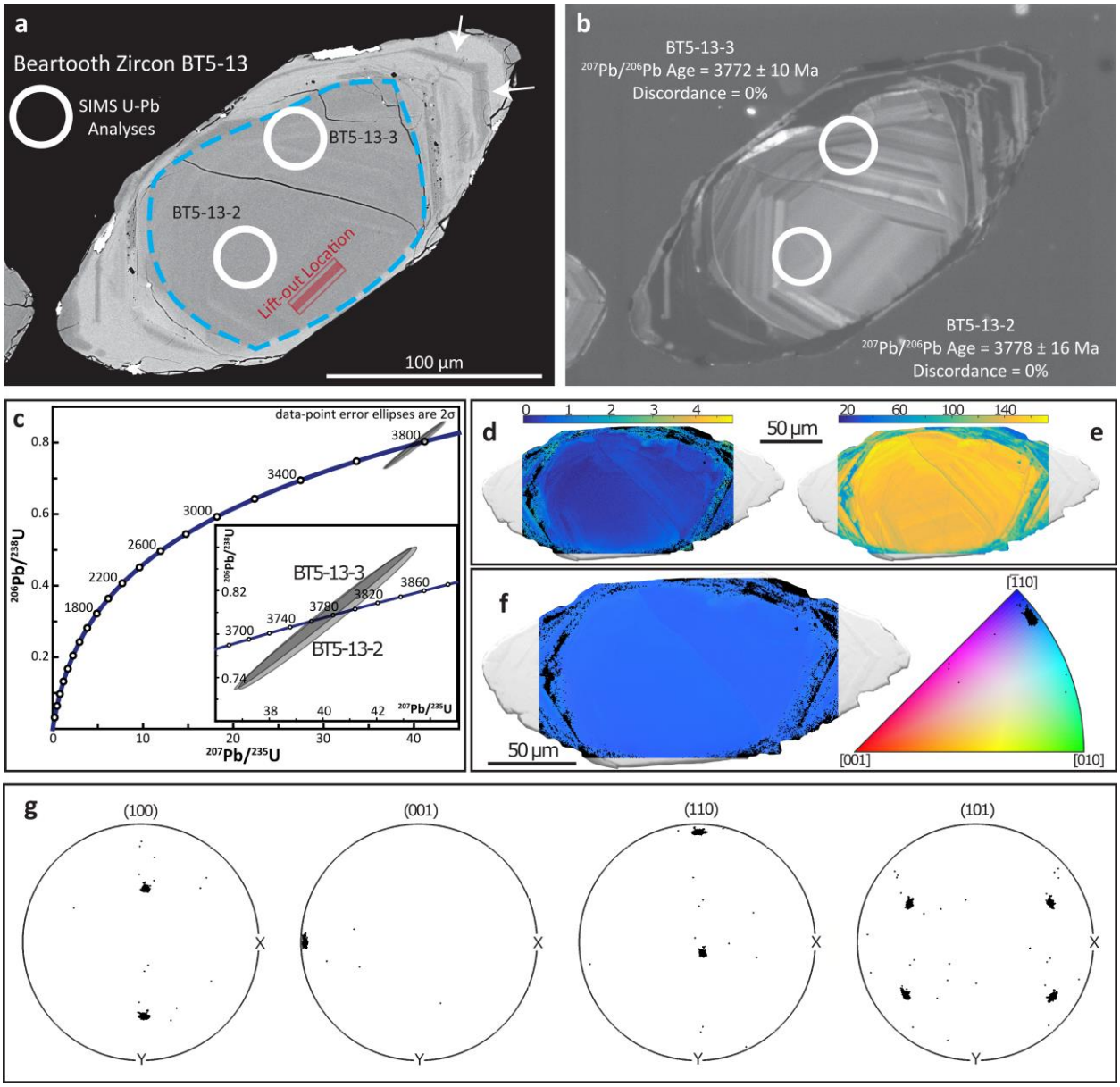

Figure 1. (**a**) Backscatter electron (BSE) image of zircon BT5-13. Lift-out location indicated with red outline indicating cuts, and solid region indicating the wedge used to generate APT specimens. Small fractures shown with white arrows. (**b**) Cathodoluminescence (CL) image of BT5-13 showing location of SIMS U-Pb age analyses. (**c**) Concordia showing the two U-Pb age analyses for BT5-13. (**d**) Relative misorientation map (units of degrees). Reference orientation is the mean orientation of the grain. (**e**) Band contrast map. (**f**) inverse pole figure orientation map. (**g**) Pole figures for BT5-13. Note: grain maps (d-f) and pole figures are the same orientation.

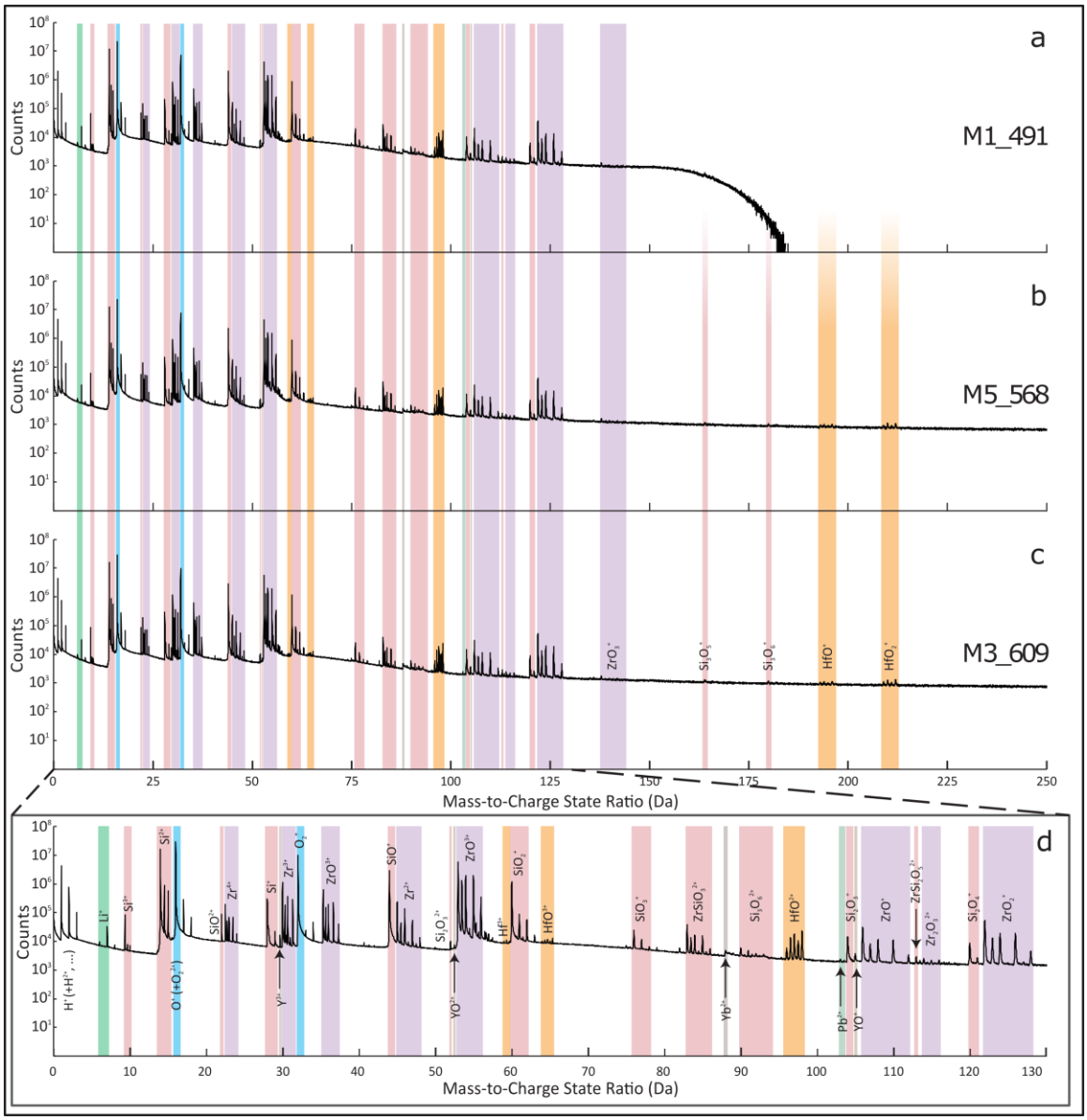

Figure 2. Atom probe mass spectra for BT5-13 data sets; showing major and selected trace element peaks/peak families. Note: colored regions are schematic identifiers, and do not equate to range bounds used in analysis. Bin width is set to 0.020 Da for all spectra. (**a**) Mass spectrum for specimen M1_491. Note spectrum cutoff at 200 Da. (**b**) Mass spectrum for specimen M5_568. Spectrum cutoff at 400 Da. (**c**) Mass spectrum for specimen M3_609. Spectrum cutoff at 400 Da. (**d**) Expanded section of M3_609 mass spectrum between 0 and 130 Da showing major peak families.

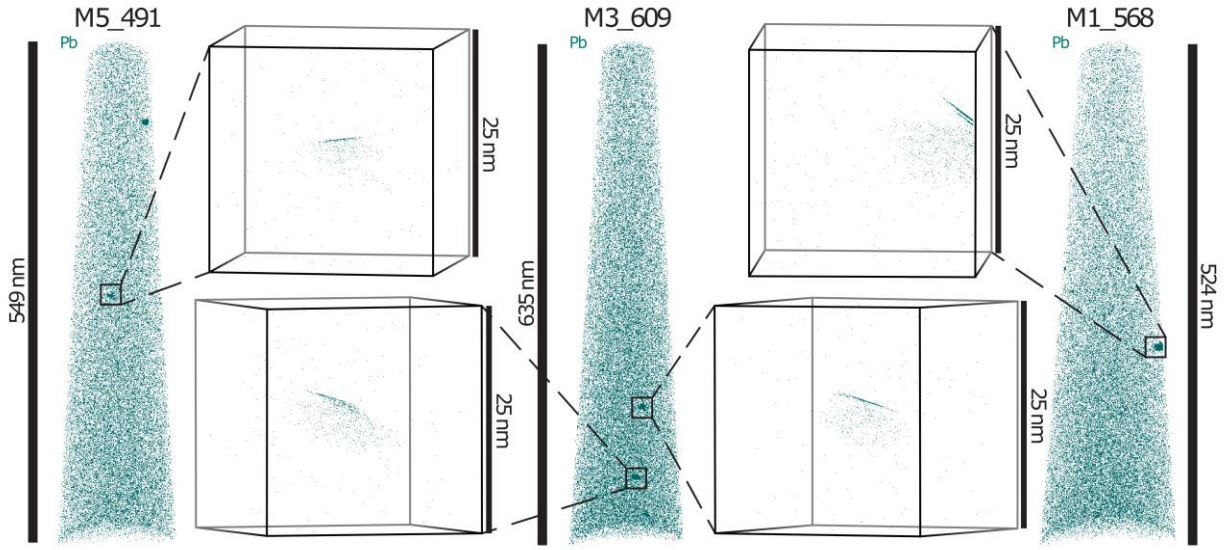

Figure 3. Pb atom maps for M5_491, M3_609, and M5_568. Expanded views are 25x25x25 nm cubes highlighting cluster morphology and are oriented to show high density layering at the upper surface of clusters. Only Pb ions are shown, however all ions, not only Pb, are co-localized within high density layers.

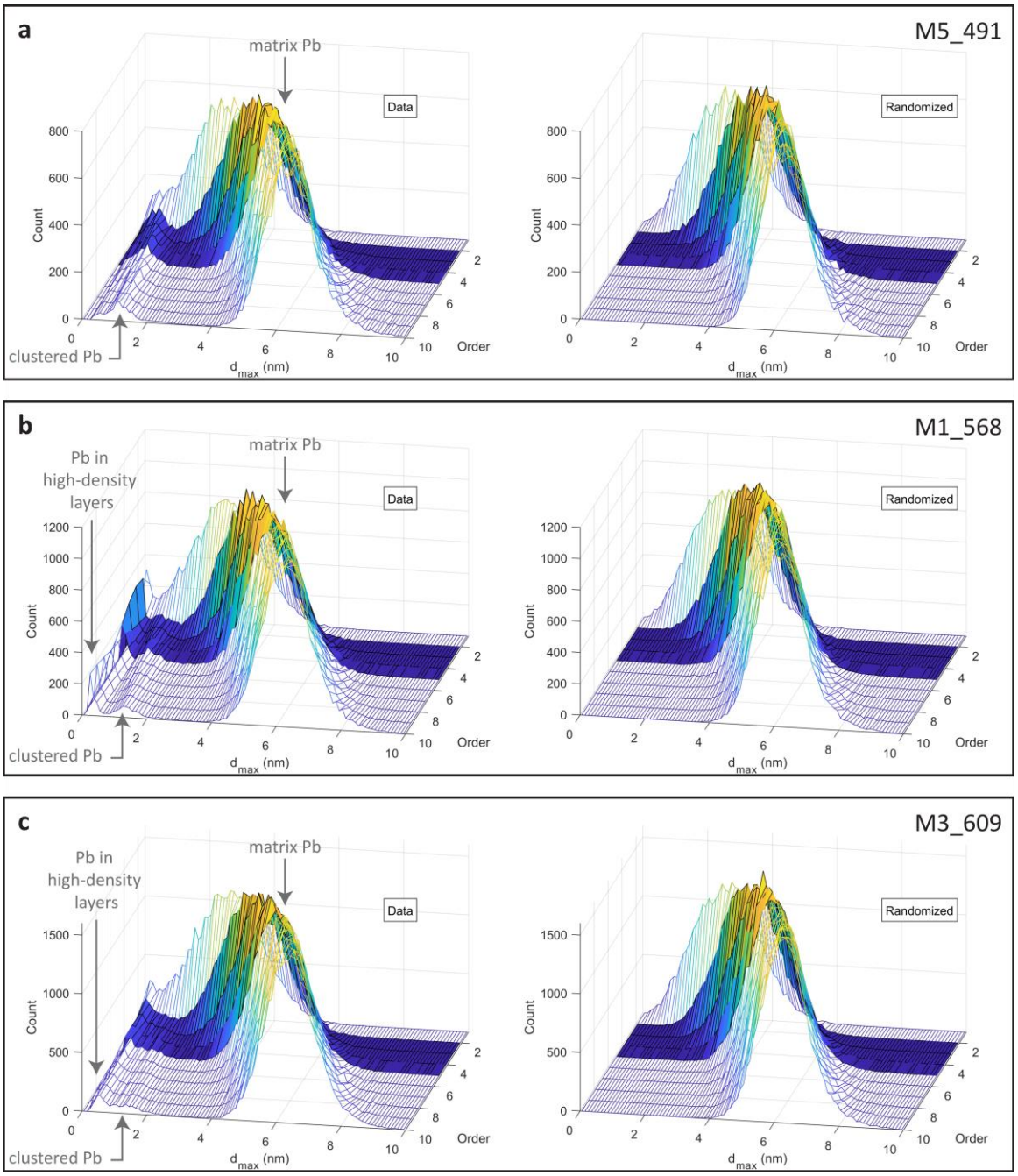

Figure 4. κth nearest neighbor distributions for order, κ, 1 through 10, completed on 250 nm segments of the (**a**) M5_491, (**b**) M5_568, and (**c**) M3_609 data sets. The distributions from the BT5-13 data sets are shown (left), along with the expected distribution if Pb were randomly distributed (right). Distributions represent the number of occurrences of a given Pb-Pb spacing between the κth nearest Pb atom. The rightmost peak at any given κ is associated with the distribution of distances for widely spaced matrix Pb. At shorter *d*, there exists a peak for clustered Pb (which possesses shorter inter-Pb distances relative to the matrix) and a peak at small *d* which is an artifact of the high density layering within the reconstruction (see Fig. 3). For κNN analysis, the maximum separation parameter input is taken as the minimum between the matrix and clustered distributions. Randomized distributions represent ion positions and bulk compositions identical to the input data, but with the random assignment of ion identity (see *Larson et al*., [2013]).

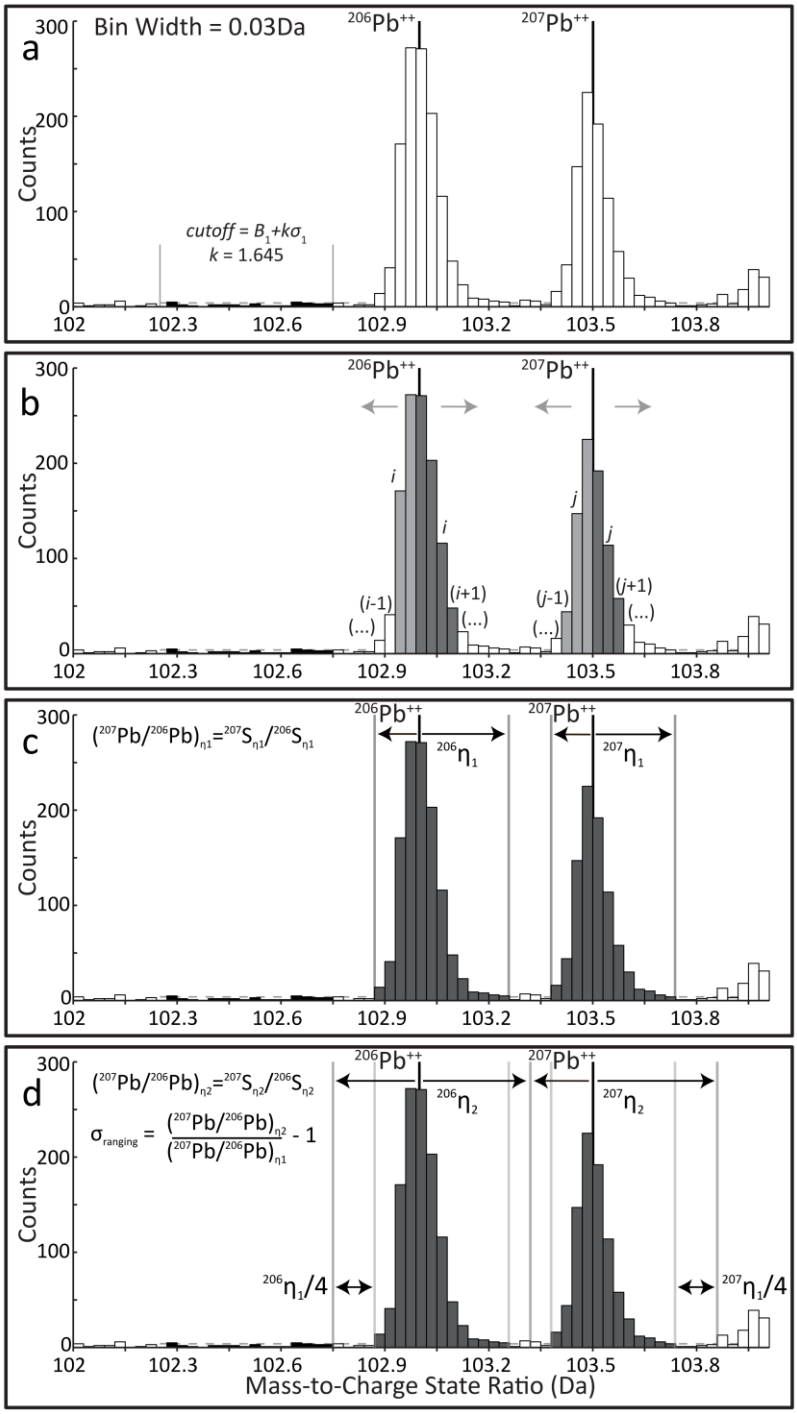

Figure 5. Schematic representation of the ranging methodology based on comparing counts within a single bin, C_i, to a statistical cutoff, taken here as either the critical limit for counts within a single bin (L_C) or as the detection limit for counts within a single bin (L_D) (both L_C and L_D are calculated based on a confidence level of 95%: see text for details). (a) Approximate locations of backgrounds B_1, and the associated C_1=L_C cutoff level used in defining range bounds. Detailed position of bins shifts slightly based on binning of data. (b) Systematic comparison of counts in the *i*th bin *C*i, and adjacent bins to establish range bounds. (c) Final range bounds, with range widths equal to $^{206}\eta_1$ and $^{207}\eta_1$. (d) Estimation of uncertainty in $^{207}Pb/^{206}Pb$ due to ranging, where ~25% of the $^{206}\eta_1$ and $^{207}\eta_1$ are added to each side of the initial ranges. In the case shown, the region between $^{206}\eta_1$ and $^{207}\eta_1$ is less than $(^{206}\eta_1+^{207}\eta_1)/4$ and thus counts between $^{206}\eta_1$ and $^{207}\eta_1$ are divided equally in calculation of $(^{207}Pb/^{206}Pb)_{\eta 2}$.

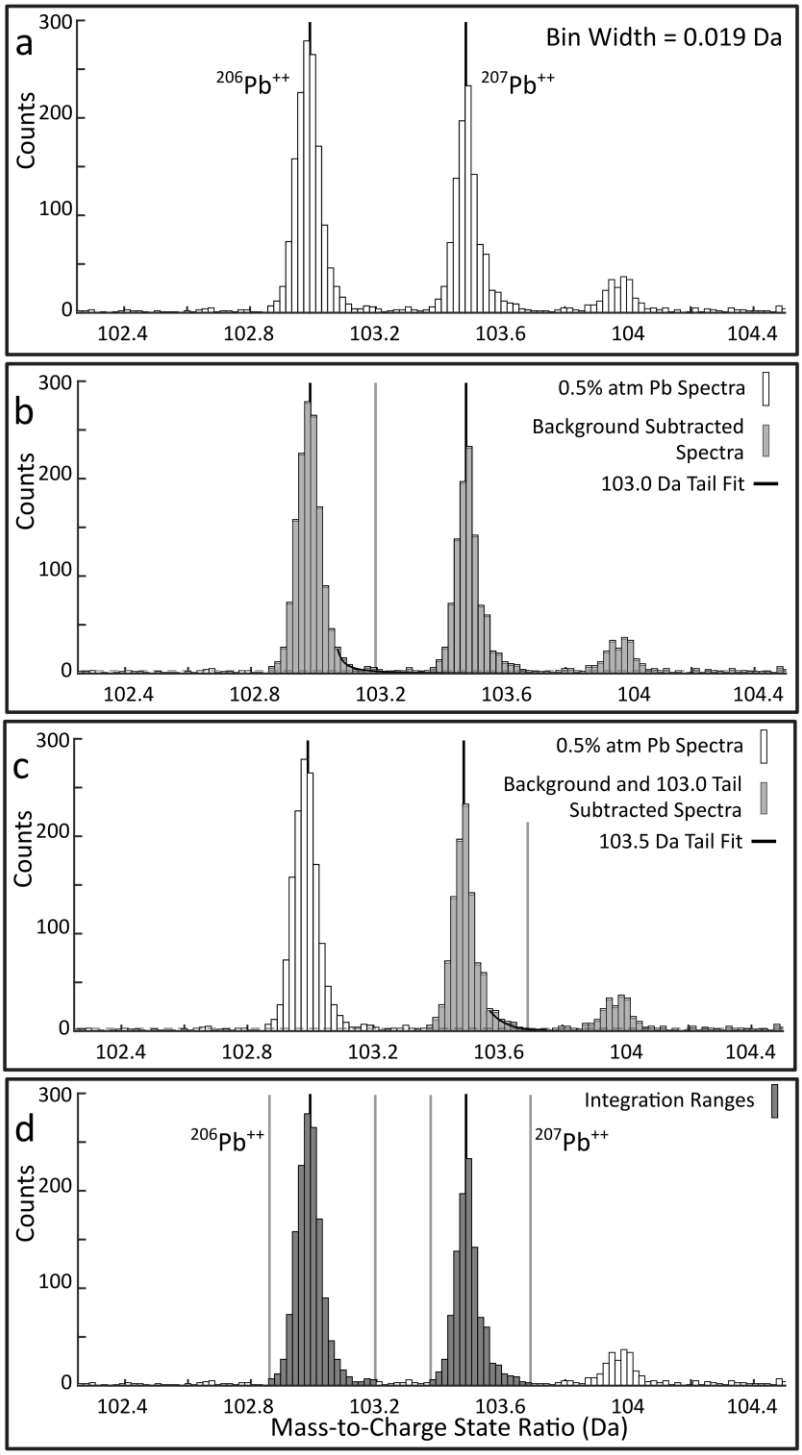

Figure 6. Schematic representation of ranging based on fitting of peak tails. Starting spectrum shown in (a). Peak fitting and determination of range bounds is approached using an iterative background stripping scheme; the background corrected fit to the 103.0 Da peak tail (b) is used to correct the 103.5 Da peak for ^{206}Pb, and the tail of the 103.5 Da peak is then fit (c). The fits to the corrected spectra are used to establish integration bounds within the peak tails by establishing when the fit drops below the critical limit, L_C. The low-side integration bounds of each peak are placed analogous to above, accounting for the additional "background" counts present under the 103.5 Da peak. (See text for details).

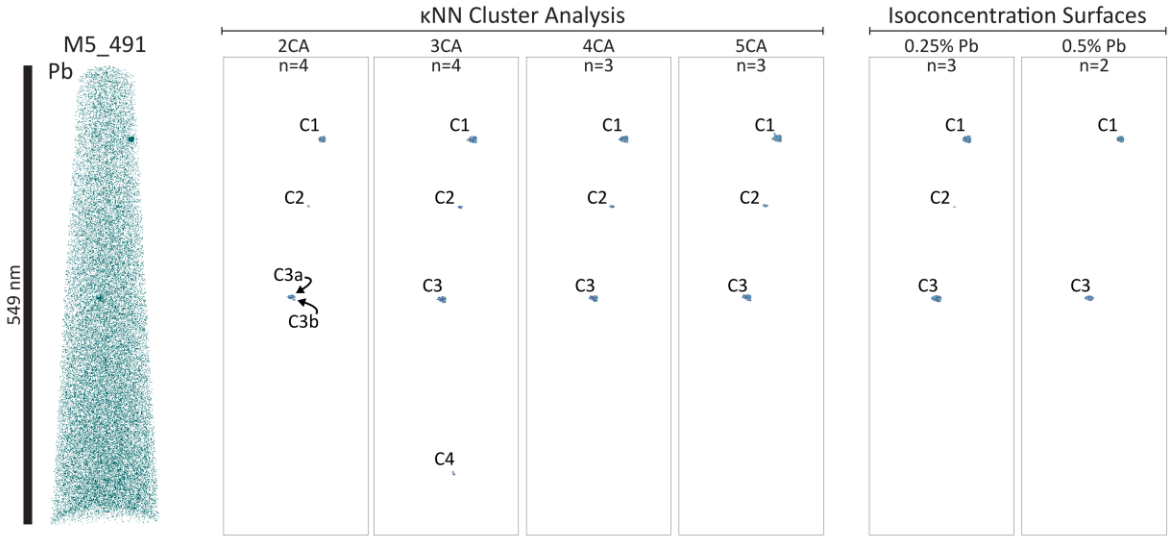

Figure 7. Results for cluster analyses showing atoms of Pb in specimen M5_491 (left) and clusters identified within the *κ*th order Nearest Neighbor cluster analysis (i.e., *κ*CA) and the 0.25% and 0.5% atomic Pb isoconcentration surfaces. All ions shown in the identified clusters. *n* refers to the number of distinct clusters.

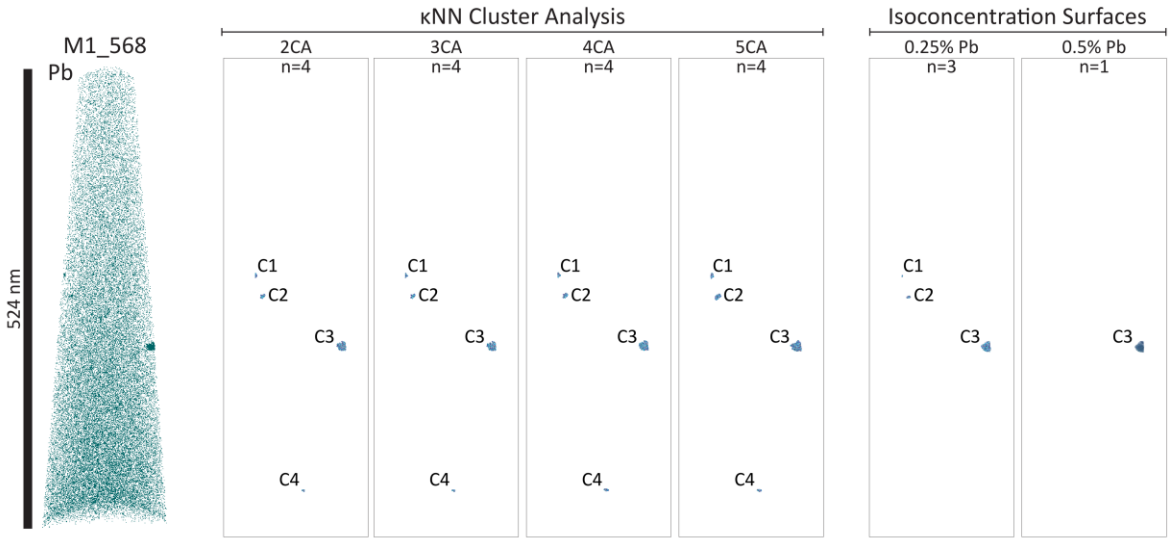

Figure 8. Results for cluster analyses showing atoms of Pb in specimen M1_568 (left) and clusters identified within the *κ*th order Nearest Neighbor cluster analysis (i.e., *κ*CA) and the 0.25% and 0.5% atomic Pb isoconcentration surfaces. All ions shown in the identified clusters. *n* refers to the number of distinct clusters.

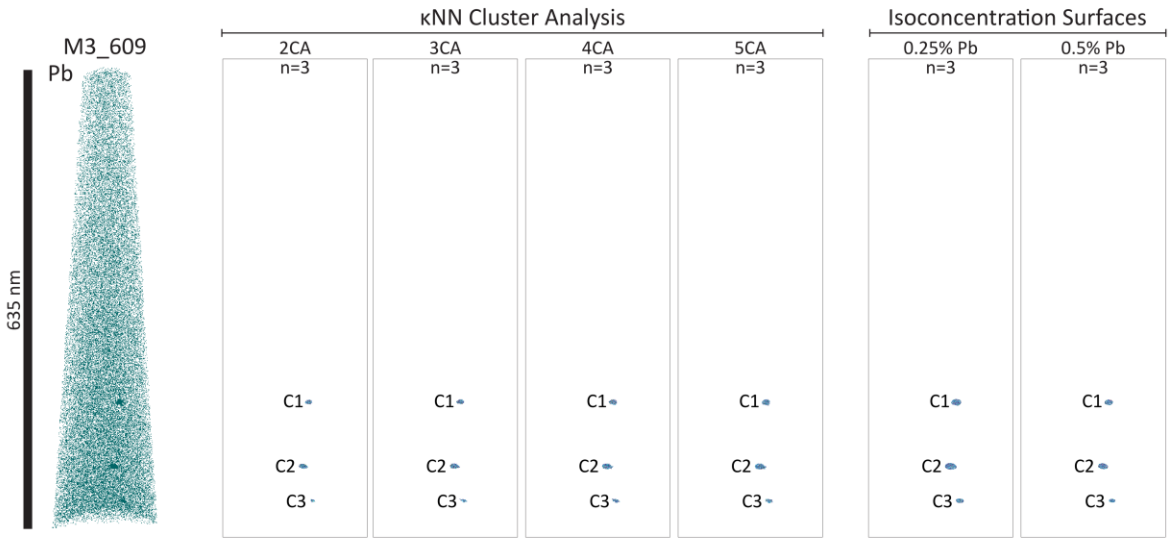

Figure 9. Results for cluster analyses showing atoms of Pb in specimen M3_609 (left) and clusters identified within the κth order Nearest Neighbor cluster analysis (i.e., κCA) and the 0.25% and 0.5% atomic Pb isoconcentration surfaces. All ions shown in the identified clusters. *n* refers to the number of distinct clusters.

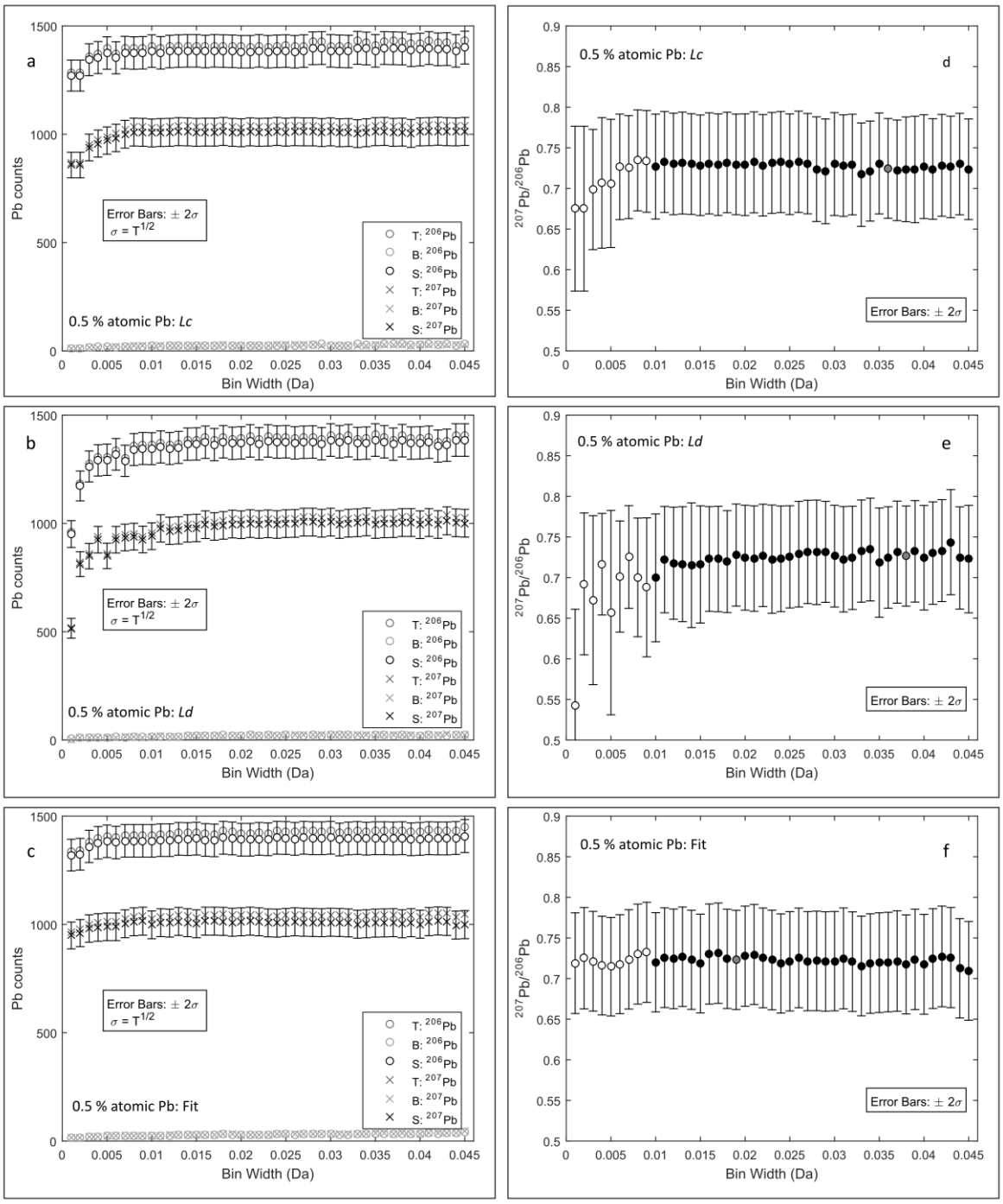

Figure 10. Summary of ranging and uncertainty analysis for the concatenated 0.5% atomic Pb clusters, (Fig. 7-9). (**a-c**) Total counts, background and signal levels for ^{206}Pb and ^{207}Pb using the ranging procedure outlined in Figs. 5 and 6; (a) ranging based on L_C, (b) ranging based on L_D and (c) ranging based on fitting of peak tails. (**d-f**) calculated $^{207}Pb/^{206}Pb$ ratios as a function of bin width, for ranging procedures outlined in Figs. 5 and 6. Error bars are ±2σ uncertainties. (d) ranging based on L_C, (e) ranging based on L_D and (f) ranging based on fitting of peak tails. Filled black data points represent a range of bin widths between 0.010 and 0.045 Da over which signal levels and calculated ratios are relatively stable (see text). Red data point represents data summarized in Table 3, and quoted in text.

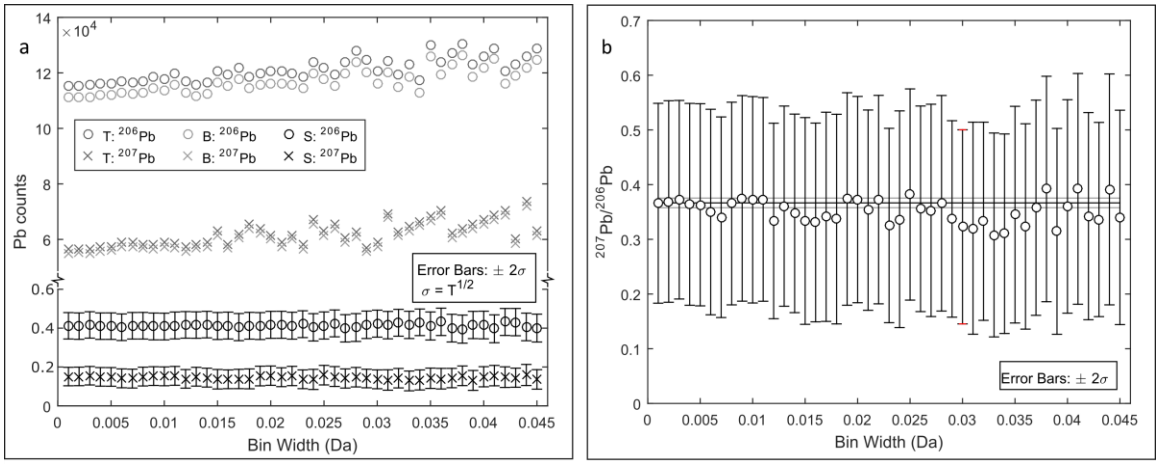

Figure 11 .Summary of ranging and uncertainty analysis for concatenated bulk APT data sets, using constant integration bounds at ~102.8-103.2 Da for the 103.0 peak, and ~103.4-103.6 Da for the 103.5 Da peak. Backgrounds for each peak are calculated over the regions ~102.4-102.8 Da for the 103.0 Da range, and ~103.2-103.4 Da for the 103.5 Da range. If the single range between ~102.4-102.8 Da is used to correct the 103.5 Da range, calculated ^{207}Pb signals are below zero. (**a**) Total counts, background and signal levels for ^{206}Pb and ^{207}Pb plotted versus bin width. Errors are ±2σ, and only include errors from background correction and counting statistics (not ranging). (**b**) calculated ^{207}Pb/^{206}Pb ratios as a function of bin width. Horizontal lines show the (^{207}Pb/^{206}Pb)* = 0.3666 ± 0.0044 ratio measured by SIMS (black line) along with ±2σ (red lines). Red data point represents data summarized in Table 3 and quoted in text.

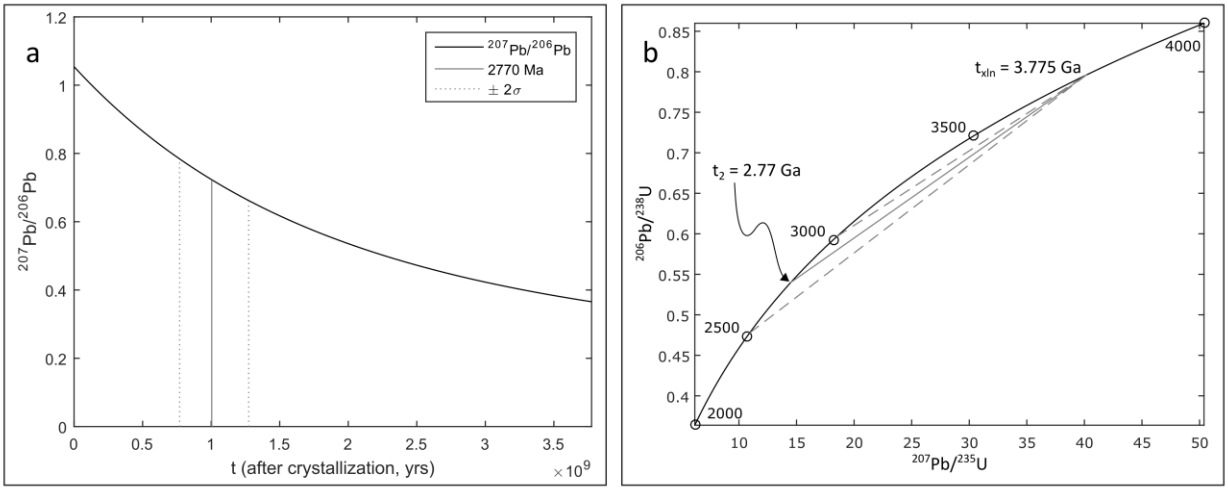

Figure 12. $^{207}Pb/^{206}Pb$ isotope evolution for BT5-13 based on present day U concentrations and a crystallization age of 3.775 Ga. (a) $^{207}Pb/^{207}Pb$ as a function of time after crystallization. The solid red vertical line represents the modeled cluster age for $^{207}Pb/^{206}Pb = 0.723 \pm 0.061$ measured within the concatenated 0.5% atomic Pb clusters. Dashed vertical red lines show upper and lower bounds based on uncertainty in the $^{207}Pb/^{206}Pb$ ratio.

Table 1. Summary of electron backscatter diffraction (EBSD) acquisition and analysis.

SEM Model	**Hitachi S3400-N**
Instrument Settings	
EBSD Software	HKL Channel 5
Conductive Coat	None
Acc. Voltage	20.0kV
Working Distance	23.5mm
Spot Size	-
Tilt	70°
Software and Acquisition Settings	
EBSP collection time per frame (ms)	45
EBSP noise reduction (frames)	400
Binning	2x2
Gain	(high)
Hough Resolution	70
Band Detection (min/max)	6/7
Mean band contrast (zircon)	139.7
X steps	348
Y steps	209
Step Distance (μm)	0.5
Average mean angular deviation	0.4434
Noise Reduction – "wildspike"	No
n neighbor zero solution extrapolation	-
Kuwahara Filter	-
Data Analysis Software	MATLAB: MTEX Toolbox (version 4.3.1)

Table 2. Atom Probe Tomography data acquisition settings and run summary (for summary of terms, see *Blum* et al., [this volume]).

Specimen/Data Set	**M5_491**	**M1_568**	**M3_609**
Instrument Model	**LEAP 5000 XR**	**LEAP 5000 XR**	**LEAP 5000 XR**
Instrument Settings			
Laser Wavelength (nm)	355	355	355
Laser Pulse Energy (pJ)	200	200	200
Pulse Frequency (kHz)	125	125	125
Evaporation Control	Detection Rate	Detection Rate	Detection Rate
Target Detection Rate (ions/pulse)	0.01	0.01	0.01
Nominal Flight Path (mm)	382	382	382
Set Point Temperature (K)	50	50	50
Sample Temperature (K)	55	55	55
Chamber Pressure (Torr)	1.3×10^{-10}	1.4×10^{-10}	5.4×10^{-11}
Data Summary			
LAS Root Version	15.41.342j	15.41.342j	15.41.342j
CAMECAROOT Version	15.43.393e	15.43.393e	15.43.393e
Analysis Software	IVAS 3.6.10a	IVAS 3.6.10a	IVAS 3.6.10a
Total Ions:	150,792,481	163,057,160	213,529,143
Single	66.1%	69.2%	68.1%
Multiple	33.1%	30.1%	31.2%
Partial	0.8%	0.7%	0.7%
Reconstructed Ions:	140,428,802	155,697,119	194,541,231
Ranged	79.4%	75.2%	76.7%
Unranged	20.6%	24.8%	23.3%
Volt./Bowl Corr. Peak (Da)	16	16	16
Mass Calib. (peaks/interp.)	10/Lin.	11/Lin.	11/Lin.
†(M/ΔM) for $^{16}O_2^+$	1130	1200	1180
††($M/\Delta M_{10}$)	530	550	540
time independent background (ppm/ns)	20.5	19.7	18.7
Reconstruction			
Final specimen state	intact	intact	fractured
Pre-/Post-analysis Imaging	SEM/SEM	SEM/SEM	SEM/n.a.
Radius Evolution Model	"shank"	"shank"	"shank"
Field Factor (k)	3.3	3.3	3.3
Image Compression Factor	1.65	1.65	1.65
Assumed Electric Field	28 V/nm	28 V/nm	28 V/nm
Detector Efficiency	52%	52%	52%
Average Atomic Volume	$0.0108 nm^3$	$0.0108 nm^3$	$0.0108 nm^3$
$V_{initial}$; V_{final}	4546 V; 9608 V	4305 V; 10383 V	4848 V; 11719 V

†ΔM is full width at half maximum.
††ΔM_{10} is full width at tenth maximum.

Table 3. Summary of SIMS U-Pb and APT Pb isotope data. Uncertainties are 1σ unless otherwise stated.

SIMS	U†	Th†	$^{204}Pb/^{206}Pb$	$^{208}Pb/^{206}Pb$	$^{207}Pb^*/^{206}Pb^*$	$^{208}Pb^*/^{232}Th$	$^{206}Pb^*/^{238}U$	$^{207}Pb^*/^{235}U$	Err. Corr.	$^{207}Pb^*/^{206}Pb^*$ Age	Conc.
BT5-13-2	320	97	0.000097	0.082±0.006	0.3666±0.0022	0.1996±0.0072	0.7945±0.027	40.16±1.365	0.987	3778±8	100%
BT5-13-3	325	102	0.000016	0.085±0.006	0.3652±0.0011	0.2074±0.0073	0.794±0.027	39.98±1.359	0.996	3772±5	100%

† Concentrations in µg/g
* Radiogenic

APT		Pb Counts (ions)									Pb Ratios			
Cluster Definition	*n*	^{207}T	^{207}B	^{207}S	^{206}T	^{206}B	^{206}S	$^{207}\sigma_S$	$^{206}\sigma_S$	$\sigma_{7/6,ranging}$	$^{207}Pb/^{206}Pb$	±2σ	**Cluster Model Age (Ga)**	
Bulk														
APT (L_C)	-	30947	29886	1061	71938	67243	4695	0.070	0.040	0.019	0.226	0.188	-	-
APT ("manual")	-	58882	57408	1474	120461	116289	4172	341.0	486.6	-	0.353	0.183	-	-
SIMS (BT5-13-2)	-	-	-	-	-	-	-	-	-	-	0.367	0.0037	-	-
SIMS (BT5-13-3)	-	-	-	-	-	-	-	-	-	-	0.365	0.0022	-	-
κNN (clusters)														
2CA (L_C)	11	1343	18.24	1325	1862	20.06	1842	36.9	43.4	0.0019	0.719	0.053	2.754	+0.21/-0.23
2CA (L_D)	11	1334	15.50	1319	1843	15.5	1828	36.7	43.1	0.0003	0.722	0.052	2.767	+0.20/-0.23
2CA (Fit)	11	1345	24.28	1321	1871	23.33	1848	36.6	43.1	-	0.715	0.052	2.738	+0.21/-0.23
3CA (L_C)	11	1393	22.20	1371	1935	25.90	1909	37.6	44.3	0.0029	0.718	0.052	2.750	+0.20/-0.23
3CA (L_D)	11	1379	17.50	1362	1904	16.62	1887	37.4	43.8	0.0022	0.722	0.052	2.767	+0.20/-0.23
3CA (Fit)	11	1396	27.39	1369	1938	26.67	1911	37.3	43.9	-	0.716	0.051	2.742	+0.20/-0.23
4CA (L_C)	10	1408	25.80	1382	1950	28.67	1921	37.9	44.5	0.0023	0.719	0.052	2.754	+0.20/-0.23
4CA (L_D)	10	1395	21.84	1373	1920	20.16	1900	37.6	44.0	0.0018	0.723	0.052	2.771	+0.20/-0.23
4CA (Fit)	10	1410	32.20	1378	1955	31.11	1924	37.1	44.1	-	0.716	0.051	2.742	+0.20/-0.23
5CA (L_C)	10	1429	30.60	1398	1979	35.70	1943	38.2	44.9	0.0015	0.720	0.052	2.759	+0.20/-0.23
5CA (L_D)	10	1410	26.00	1384	1956	28.89	1927	37.9	44.6	0.0031	0.718	0.052	2.750	+0.20/-0.23
5CA (Fit)	10	1433	39.44	1394	1987	38.11	1949	37.5	44.4	-	0.715	0.051	2.738	+0.20/-0.23
Isosurface (clusters)														
0.25% atm Pb (L_C)	9	1084	39.20	1045	1471	44.8	1426	33.5	38.9	0.0001	0.733	0.061	2.811	+0.23/-0.26
0.25% atm Pb (L_D)	9	1076	36.00	1040	1448	36.00	1412	33.3	38.5	0.0005	0.737	0.062	2.827	+0.23/-0.27
0.25% atm Pb (Fit)	9	1091	51.55	1039	1477	50.4	1427	32.9	38.5	-	0.728	0.061	2.791	+0.23/-0.27
0.5% atm Pb (L_C)	6	1041	28.20	1013	1429	31.33	1398	32.7	38.2	0.0004	0.725	0.061	2.771	+0.23/-0.27
0.5% atm Pb (L_D)	6	1028	24.00	1004	1406	24.00	1382	32.4	37.8	0.0023	0.727	0.061	3.016	+0.25/-0.29
0.5% atm Pb (Fit)	6	1041	30.68	1010	1427	30.00	1397	32.0	37.7	-	0.723	0.061	2.771	+0.23/-0.27
Single Cluster (L_C)	1	215	8.00	207	271	8.00	263	14.9	16.7	0.0017	0.787	0.152	3.016	+0.47/-0.65
Single Cluster (L_D)	1	184	3.50	181	256	5.06	251	13.7	16.2	0.0190	0.721	0.149	2.763	+0.53/-0.75
Single Cluster (Fit)	1	215	7.40	208	269	7.30	262	14.4	16.4	-	0.794	0.152	3.041	+0.47/-0.64

CHAPTER 4

Resolving the thermal, structural and chemical histories of lunar zircon through correlative SIMS, EBSD, and Raman spectroscopy

Tyler B. Blum[1]*, Michael J. Spicuzza[1], Lutz Nasdala[2], Chutimun Chanmuang N.[2], Matthew A. Coble[3], Aaron J. Cavosie[4], John W. Valley[1]

[1]Department of Geoscience, University of Wisconsin – Madison, Madison, WI, 53706 USA.
[2]Institut für Mineralogie und Krystallographie, Universitat Wien, Wien, A-1090 Austria.
[3]Stanford University, Stanford, CA, USA
[4]School of Earth and Planetary Science, Curtin University, Perth, WA, Australia

Correspondence: tbblum@geology.wisc.edu

ABSTRACT

The trace element and isotope chemistry of lunar zircon grains place constraints on the solidification and thermal evolution of the Moon. At the Moon's surface, zircons exist in a cool, dry environment, which kinetically inhibits both structural recovery and the migration of chemical tracers; this state is interrupted periodically by impacts and "gardening" of the lunar regolith. There are few published studies focused on the combined structural evolution of lunar zircons including deformation, radiation damage accumulation and thermal annealing. Each of these processes influences the nanoscale structure of zircon, which ultimately controls the retention and/or disruption of primary zircon chemistry in the lunar environment.

This study presents secondary ion mass spectrometry (SIMS), electron backscatter diffraction (EBSD), and Raman spectroscopy for a suite of lunar zircon grains from four Apollo landing sites that possess a variety of lithologic contexts. Zircon grains exhibit a range of internal structures including non-planar fractures, shock microtwin lamellae, and radiation damage-induced loss of crystallinity. For all the zircons analyzed here, the retained radiation damage, calculated as the ratio of effective dose (i.e. present-day damage state based on Raman measurements) and total dose, varies from 0.22 to 0.77. These are the lowest fractional doses reported for lunar zircon and require that some process(es) driving annealing are relatively young. Our observations imply that (1) annealing can occur in a large percentage of lunar zircon grains, and (2) damage states can reflect periods of incomplete annealing, complicating any broad application of Raman-based "radiation-damage ages" to study the thermal histories of lunar zircon. We combine these data with a compilation of lunar zircon U-Pb age data to evaluate the uniqueness of individual landing sites. The observed differences between landing sites may reflect either (1) differences in secondary processes (preferential resetting of zircon grains at Apollo 12 and 14), or (2) differences in the source material samples at the different landing sites. The later can subdivided further to argue that either (1) age spectra represent distinct sources and have not suffered pervasive contamination from the Imbrium impact, or (2) age spectra record distinct inputs *after* the Imbrium impact. Each of these hypotheses are useful for understanding lunar history, and these hypotheses can be further tested by continued characterization of lunar zircon grains from a variety of sample types.

1 INTRODUCTION

Analysis of zircon offers many advantages to lunar science; it is a common accessory phase in lunar rocks and regolith, a relatively robust geochronometer, and preserves microstructural records of shock deformation. Zircon saturation in lunar magmas requires enrichment of melts in zirconium, and in the context of lunar evolution, zircon crystallization is linked to formation of the KREEP reservoir following differentiation of the lunar magma ocean (Nemchin et al., 2009a). As a result, the ages, trace elements and isotope ratios in magmatic lunar zircon grains track both the formation of lunar crust (e.g., Nemchin et al., 2009a), as well

as the longevity, and spatial extent of crustal lunar magmatism (e.g., Meyer et al., 1996; Nemchin et al., 2008).

The measurement and interpretation of lunar zircon ages can be challenging, as aspects of a grain's growth and thermal/structural history are both complex and cryptic. Zircon grains sampled from the lunar surface come from a discontinuous set of interlayered volcanics and impact ejecta (both proximal and distal). This surface veneer exists as a combination of meteoritic (implanted and/or sourced from the greater solar system), authigenic (melted/fused formed in place) and *ex situ* material (blocks and clasts of material, redistributed/reworked during impacts and "farming" of the lunar surface). Zircon grains are a passive participant in this continual formation, breakdown and redistribution of surface material, meaning virtually all lunar zircon grains are left with varying degrees of primary and secondary petrologic context. Despite often lacking primary lithologic context, the *ex situ* or "detrital" nature of zircon, and the abundance of microstructural and geochemical information they provide, makes them a useful tool for tracking lunar processes.

This publication characterizes a small but diverse set of lunar zircons, both lithologically and geographically, to further explore the broad utility of zircon to understand lunar evolution. This includes both the evolution of zircon microstructure and damage state in the lunar environment and how zircon age distributions may distinguish surface deposits and processes. We characterize the combined U-Th-Pb and grain-scale structural evolution of lunar zircon through a combination of secondary ion mass spectrometry (SIMS), electron backscatter diffraction (EBSD), and Raman spectroscopy. These results bear directly on (1) the microstructural evolution of zircon in the lunar environment, (2) the potential controls on trace element and/or isotope mobility through time, (3) variability in age, microstructure and damage

state from zircon-to-zircon, sample-to-sample and site-to-site. These data are combined with published *in situ* U-Pb age data for Apollo 12, 14, 15, and 17, (498 total grains) enabling a statistical review of how age information may be recorded both geographically and lithologically.

1.1 Zircon Microstructure, Radiation Damage, and Annealing

Crystalline zircon possesses slow diffusion and can preserve primary crystal chemistries over billions of years (e.g., Valley et al., 2005); however, open system behavior of zircon domains is well documented. Element mobility is a function of several factors including zircon microstructure, radiation-damage state, and temperature. Zircons exhibit several different microstructural responses to stress, including development of subgrains, planar fractures (PFs), non-planar fractures (NPFs), planar deformation bands (PDFs), microtwin lamellae, reidite lamellae, and granular morphology (e.g., Cavosie et al., 2015). These processes can influence zircon composition by either (1) wholesale re-crystallization, (2) generation of defect-rich regions where non-formula elements can preferentially segregate (Reddy et al., 2016), or (3) development of fast pathways for exchange. Only two microstructures in zircon represent unambiguous evidence of shock metamorphism, these being the presence of microtwin lamellae on {112} possessing a 65º rotation about <110>, and the presence of the high-pressure polymorph, reidite (Cavosie et al., 2015). The positive identification of all of the above microstructures has been aided by new techniques (e.g., electron backscatter diffraction). Although the prevalence of diagnostic shock microstructures in lunar zircon remains ambiguous (Timms et al., 2012), progress in understanding zircon deformation behavior (e.g., Timms et al.,

2017) suggests continued microstructural characterization of lunar zircon is a promising means to characterize the early lunar bombardment history.

While zircon microstructure exerts an important control on chemical behavior, open system behavior in terrestrial zircon is commonly associated with the accumulation of radiation damage. Trace amounts of U and Th, incorporated into a zircon during crystallization, undergo α-decay within the $^{238}U \rightarrow {}^{206}Pb$, $^{235}U \rightarrow {}^{207}Pb$, and $^{232}Th \rightarrow {}^{208}Pb$ decay chains; "α-recoil" events result in ejection of an α-particle, and recoil of the more massive daughter nucleus. The α-particle travels several microns, and causes a small number (100-200) atomic displacements near the end of its trajectory. The energetic daughter nucleus is responsible most of the damage to the crystal lattice, traveling 20-35 nm and generating ~1000 atomic displacement as part of a 5-10 nm damage domain; this domain grades from an amorphous core, to defect-rich, to strained then unstrained zircon (Trachenko et al., 2003). If damage domains are not annealed, they become more numerous as radiation damage accrues through time and eventually overlap to form a connected network at the "first percolation point," approximately $1\text{-}2\times10^{15}$ α-decay events/mg (Ewing et al., 2003). At the atomic scale, reaction and diffusion kinetics are orders of magnitude faster for damaged zircon relative to pristine zircon (e.g., Cherniak et al., 1991; Cherniak et al., 2003) and zircon domains which reach the first percolation point are more susceptible to grain scale element mobility and alteration. Pb migration can result in disturbed/discordant isotope systematics or even complete resetting of U-Pb ages. Structural reconstitution and annealing acts to reverse the damage induced by α-recoil and α-particles; however, the number, energetics, and damage state dependences of annealing mechanisms remain incompletely defined (e.g., Nasdala et al., 2001, 2004, 2005; Geisler et al., 2002; Ewing et al., 2003). Radiation-damage state is also an important control on the structural response of zircon to shock deformation (Moser et al.,

2011; Reddy et al., 2016; Timms et al., 2018). Few studies have made quantitative observations of damage states for lunar zircons. In this work, we utilize the present-day structural state of zircon to provide (1) a semi-quantitative constraint on the relative amount of retained damage, (2) relative constraints on the timing of annealing, and (3) an assessment of how radiation damage may influence trace element migration.

Knowledge of zircon age, and U and Th concentrations enables calculation of the total α-dose, D_{total}, which can be derived from rearrangement of the $^{238}U \rightarrow {}^{206}Pb$, $^{235}U \rightarrow {}^{207}Pb$ and $^{232}Th \rightarrow {}^{208}Pb$ decay equations:

$$D_{total} = 8 \cdot {}^{238}N(\exp(\lambda_{238}t) - 1) + 7 \cdot {}^{235}N(\exp(\lambda_{235}t) - 1) + 6 \cdot {}^{232}N(\exp(\lambda_{232}t) - 1) \quad [1]$$

where D_{total} is the number of α-decays/mg, λ_{238}, λ_{235} and λ_{232} are the decay constants for ^{238}U, ^{235}U and ^{232}Th respectively, t is the age of the zircon (or zircon domain) and ^{238}N, ^{235}N and ^{232}N are the number of ^{238}U, ^{235}U and ^{232}Th atoms per milligram zircon at present. This represents the total number of α-decays/mg experienced by a given zircon domain since crystallization. The total α-dose (eqn. 1) can be compared to the "effective dose", D_{eff}, which is the preserved dose after annealing, estimated from one or more characterization methods. In this work, we utilize Raman spectroscopy, specifically, the broadening of the $\nu_3(SiO_4)$ band ($FWHM_{\nu3(SiO4)}$) to characterize present-day zircon damage states. In *unannealed* zircon, the relationship between $FWHM_{\nu3(SiO4)}$ and α-dose follows a linear relationship up to approximately the first percolation point (Nasdala et al., 2001):

$$FWHM_{\mathrm{v3(SiO4)}} \approx 1.2 + 1.4 \cdot D_{total} \quad [2]$$

Where D_{total} is in units of 10^{15} α-decays/mg. This equation can be rearranged to calculate an effective α-dose, D_{eff}, based on measured $FWHM_{v3(SiO4)}$ of unknowns, which may or may not preserve the entirety of their total α-dose. By comparing the total α-dose (from eqn. 1) and the effective α-dose (i.e. the present-day damage state calculated from eqn. 2 for the measured Raman bandwidth) it is possible to determine whether a specific zircon domain preserves the entirety of its radiation damage and the approximate percentage of annealing (fractional annealing).

2 SAMPLES

This study contains data for thirteen zircon grains from five different individual samples and four different Apollo landing sites (see Appendix 1), spanning a lateral distance of over 1700 km. We review sample details in the context of the zircon grains separated from them. Ti, Li, and REE concentrations, and oxygen isotopes have previously been measured for the zircons in this study (Spicuzza et al., 2011; Valley et al., 2014).

2.1 Apollo 12: Sample 12023

Sample 12023,1 is a regolith sample collected during Apollo 12 from the bottom of a trench (~20 cm deep) on the east rim of Sharp Crater, a "fresh" crater approximately 14 m in diameter and 3 m deep (Shoemaker et al., 1970). Barra et al., (2006) found evidence in $^{40}Ar/^{39}Ar$ release patterns of 12023 regolith fragments for formation ages >2000 Ma and reheating at ~700-800 Ma. Both Barra et al. (2006) and Korotev et al. (2011) interpreted the ~700-800 Ma ages in

Apollo 12 regolith fragments as reheating during the Copernicus impact event. The current study presents data for five zircons (Fig. 4a-4e) separated from the <1 mm size fractions by hand-picking under UV lamp illumination. There is no previous geochronologic data for zircons from sample 12023.

2.2 Apollo 14: Sample 14240

Sample 14240 is a submature regolith sample collected from Station G during Apollo 14 EVA-2 (Swann et al., 1977). The sample was taken the bottom of a trench (~30 cm deep); however, slumping of material from the sides of the trench may have contributed surface/near-surface material to the deeper sample (Swann et al., 1977). Four zircons (Fig. 4f-4h, and Fig. 4l) were separated from splits 14240,1 and 14240,80, by hand-picking under UV lamp illumination. There is no previous geochronologic data for zircons from sample 14240.

2.3 Apollo 15: Samples 15405 and 15455

Sample 15405 is a clast-bearing impact-melt rock collected during Apollo 15 from a prominent isolated boulder on the northern slope of Hadley Delta (Swann et al., 1972). Two zircons (zircons 15Q-3 and 15Q-4; Fig. 4i and 4j) originate from a single quartz monzodiorite (QMD) clast. The QMD clast contains symplectic plagioclase – alkali feldspar – quartz, as well as high-Ca pyroxene, low-Ca pyroxene, olivine, zircon, and ilmenite. QMD zircons in 15405 possess a range of U-Pb behavior (Meyer et al. 1996; Grange et al., 2013a; Crow et al., 2017); published $^{207}Pb/^{206}Pb$ ages extend between 4429 ± 110 Ma and 2053 ± 30 Ma and include significant discordance. Zircon grains studied by Grange et al., (2013a) show systematic variations in $^{207}Pb/^{206}Pb$ ages, and U and Th concentrations, with low U and Th grains having

relatively concordant ages clustering around 4330 Ma, while high U and Th grains have younger $^{207}Pb/^{206}Pb$ ages. Grange et al. (2013a) note that the observed trends are consistent with Pb mobility controlled by radiation damage. Additional U-Pb analyses for 15405 zircon grains have been published by Crow et al. (2017).

Discordia regressed for U-Pb data from zircon (Meyer et al., 1996; Grange et al., 2013a) and phosphates (Grange et al., 2013a) suggest sample 15405 was reheated, presumably by impacts, at approximately 1940 ± 10 and 1407 ± 57 Ma (Grange et al., 2013a). This younger date is broadly consistent with previous estimates of breccia formation at ~1.3 Ga, based on U-Pb discordia (Meyer et al., 1996) and a $^{40}Ar/^{39}Ar$ plateau age (Bernatowicz et al., 1978).

Sample 15455 is an impact melt breccia, containing several large plutonic clasts, including anorthosite and norite (e.g., Ryder and Bower, 1977). Clasts within 15455 have some of the oldest Rb/Sr and Sm/Nd ages for lunar rocks (Shih et al., 1993). Dating of the breccia matrix, which dominates the sample, yields poorly defined plateaus in the range of ~3.8-3.9 Ga (Alexander and Kahl, 1974; Shih et al., 1993). This study analyses a single isolated grain from the 15455 breccia matrix (Fig. 4k). Dating of 15455 zircon grains by Crow et al. (2017) yielded $^{207}Pb/^{206}Pb$ ages between 4101 ± 28 and 4347 ± 8 Ma (2SD).

2.4 Apollo 17: Samples 73235

Sample 73235 is a clast-rich aphanitic breccia collected on the rim of a 10 m crater incident upon “light mantle” material, on the south side of the Taurus-Littrow Valley. This mantle has been interpreted as landslide deposits sourced from the adjacent South Massif (Wolfe et al., 1981; Hurwitz and Kring, 2016). The sample is comprised of a dark, aphanitic matrix component, and a younger, lighter more “porous” breccia component (Dence et al., 1976; Wolfe

et al., 1981). Dating of the dark matrix material by Turner and Cadogan (1975) yielded $^{40}Ar/^{39}Ar$ plateau ages of 3927 ± 16 Ma. These $^{40}Ar/^{39}Ar$ ages have been recalculated using a preferred total ^{40}K decay constant of $\lambda = 5.463 \times 10^{-10}$ yr^{-1} (Min et al., 2000), and fluence monitor ages referenced to a Fish Canyon Tuff sanidine age of 28.201 Ma (Schmitz, 2012; MMhb-1 = 527.0 ± 0.3 Ma, Renne et al., 1998; Hb3gr = 1081.5 ± 2.4 Ma, Jourdan et al., 2006).

Several zircons from 73235 have been studied, with a variety of morphologies and age relationships (Meyer et al., 1996; Pidgeon et al., 2007; Nemchin et al., 2008; 2009b; Grange et al., 2011; Bellucci et al., 2017). This study reviews data for a single zircon from lunar breccia sample 73235 (17B-4; Fig. 4m). Additional data for this zircon is found in this thesis, Chapter 6.

3 METHODS

Individual zircons were cast in epoxy either as individual grains or as part of small rock chips; these mounts were polished to expose zircon interiors and analyzed by SIMS for oxygen isotope ratios and trace elements (Spicuzza et al., 2011, unpublished data; Valley et al., 2014). Prior to U-Th-Pb analysis, a subset of zircon grains were remounted by trimming existing mounts and recasting individual epoxy blocks along with U-Pb standards.

SEM imaging was completed to characterize the internal zircon textures; this included secondary electron, backscattered electron, and cathodoluminescence imaging modes using a Hitachi S3400-N SEM at UW-Madison in the Ray and Mary Wilcox SEM Lab. Electron backscatter diffraction (EBSD) mapping is presented for three of the thirteen zircon grains (EBSD mapping for zircon 17B-4 can be found in Chapter 6). Run conditions for each map are summarized in the Appendix 2. EBSD data collection and initial data analysis was completed in

HKL Channel 5 software with additional analysis and visualization done using the MTEX toolbox (v.4.5.0) in MATLAB.

Uranium and lead isotopes, as well as U, Th, and Hf trace element concentrations were quantified using a Sensitive High Resolution Ion Microprobe with Reverse Geometry (SHRIMP-RG) at the Stanford-USGS SHRIMP-RG Lab. Each analysis consisted of pre-sputter rastering of the beam followed by analysis in a 18-23-µm spot. Six peak hopping cycles, from low to high mass, included analysis of $^{90}Zr_2{}^{16}O^+$ (a normalizing species), $^{180}Hf^{16}O^+$, $^{204}Pb^+$, a $^{204}Pb^+$ background, $^{206}Pb^+$, $^{207}Pb^+$, $^{208}Pb^+$, $^{238}U^+$, $^{232}Th^{16}O^+$, $^{238}U^{16}O^+$ and $^{238}U^{16}O_2{}^+$. A total of four epoxy mounts were analyzed; zircon standards were incorporated as pre-cast/polished blocks within two of the epoxy mounts, allowing standardization of two adjacent mounts within the SHRIMP-RG analysis chamber. Zircon standard reference material 91500 (Wiedenbeck et al., 2004) is used as both for U and Th concentration reference, as well as an age standard. Common Pb is monitored through measurement of ^{204}Pb; common Pb in all analyses is extremely low, and corrections to both $^{207}Pb^*$ and $^{206}Pb^*$ are based on Stacey and Kramers (1975). Reduction of raw data was completed in SQUID with further data analysis and visualization completed using Isoplot v4.15.

The local structural state of zircon domains is monitored through Raman spectroscopy, and measurement of the full width at half maximum of the $v_3(SiO_4)$ vibrational mode ($FWHM_{v3(SiO4)}$). Spot analyses were completed on either a LabRAM HR or LabRAM HR Evo at the Institut für Mineralogie und Kristallographie at the University of Vienna, Austria. Raman spots are correlated with individual SIMS U-Pb analysis pits. All analyses used a 632.8 nm He-Ne laser, with a 1800 groove/mm grating, and make a spike correction through completion of two analysis cycles. Counting times varied between 5 sec. (x2) and 60 sec. (x2). Measured

$FWHM_{v3(SiO4)}$ were corrected for the apparatus function following Váczi (2014), assuming a convolution of Gaussian (instrumental) and Lorentzian (physical) band shapes. Background correction and peak fitting for spot analyses was completed in PeakFit v4.12. The signal level and peak forms allow for robust background subtraction and fitting schemes in all but one of the lunar zircon grains (17B-4), for which Raman signals were sufficiently low that the measured peak position and bandwidth are highly sensitive to background subtraction and assumed peak structure (see discussion in Nasdala et al., 2002). For all other spot analyses, uncertainties are assigned at 10% for individual analyses.

Compositional variations are expected to contribute one of the most significant uncertainties in correlating between SIMS U-Pb data, and Raman spot analyses; SIMS analyses average U and Th concentrations over ~300 μm^3, while Raman analyses integrate signals from $\geq$5 μm^3. Between 2-5 spot analyses were positioned around each SIMS analysis pit to characterize the natural variability in structural state associated with a given SIMS analysis.

4 RESULTS

4.1 EBSD

Zircons in this study show a variety of internal textures and can be separated into three subgroups based on internal CL zonation (see Figure 1, Valley et al., 2014; this thesis, Appendix 4); those with clear primary growth zoning (15Q-3, 15Q-4), those with subtle/featureless internal texture (14R-4, 15B-B-1) and those with varying degrees of ambiguous, or complex internal texture (12R-1, 12R-2, 12R-3, 12R-7, 12R-8, 14R-2). These trends mirror underlying microstructural and crystallographic trends including non-planar fractures, development of low-

angle grain boundaries, shock microtwin lamellae, and advanced stages of radiation damage accumulation.

4.1.1 QMD clast zircons (15Q-3 and 15Q-4)

The two QMD zircons (15Q-3 and 15Q-4) have numerous non-planar fractures dividing each zircon into several subgrains (Figs. 1 and 2); fractures are filled by a combination of silicate glass and inclusions. Coherent, primary growth zoning is visible in CL imaging, and can be traced across fractures between the larger (>25 μm) individual fragments. Large fragments do not show significant *internal* deformation but have up to 10º of total rotation accommodated across individual non-planar fractures. A small number of <5 μm grain fragments in the more pervasively fractured 15Q-4 have experienced more significant rotations (Fig. 1c).

4.1.2 Breccia zircon grains (17B-4 and 15B-1-1)

Zircon 17B-4 is a large breccia zircon with CL banding perpendicular to its long dimension. The grain possesses extremely low CL intensity, which is broadly consistent with loss of crystallinity due to the accumulation of radiation damage. This observation is further supported by combination with low band contrast in EBSD mapping, and Raman spectra (this thesis, Chapter 6). A more detailed discussion of zircon 17B-4 can be found in Chapter 6 of this thesis.

4.1.3 Regolith zircons

Zircon 12R-2 is an anhedral zircon fragment with regions of chaotic/feathery internal CL zonation, and a series of curvi-planar inclusion trails running between fractured zircon faces (Valley et al., 2014). EBSD mapping shows minimal (less than 2º) total misorientation across the grain.

Zircon 12R-7 is an anhedral zircon having chaotic and "feathery" internal CL textures; superimposed on this are several lamellar features, and two trails of inclusions running subparallel to the long dimension of the zircon (Fig. 3a). The lamellae are discontinuous along their length, exhibiting both bright and dark contrast in CL, and are difficult to resolve where they cross dark-Cl feathery bands. In EBSD, lamellae are associated with a systematic decrease in band contrast and possess a 65º misorientation about [110], consistent with shock microtwin lamellae (Moser et al., 2011). Zircon 12R-7 also contains small subgrains near the edge of the zircon with <4º of misorientation localized along a series of low angle grain boundaries (Fig. 3b). These subgrain boundaries may be interpreted as annealed fractures, but possess no evidence (visual, crystallographic or spectroscopic) for inclusions or other phases.

4.2 SIMS U-Pb and α-Dose:

Individual SIMS analyses yield $^{207}Pb/^{206}Pb$ ages varying between 3957 ± 24 and 4392 ± 12 Ma, with a total range in discordance between +6% to -4% (Table 1, Fig. 5). External errors range from 0.7 to 3.5% (average = 1.4%; 1σ) for $^{206}Pb^*/^{238}U$ and 0.2 to 3.2% (average 0.9%) for $^{207}Pb^*/^{206}Pb^*$. Three zircon grains (14R-3, 14R-4, 15B-1-1) were sufficiently small that only a single analysis was made; data for all three of these zircons overlap concordia and $^{207}Pb^*/^{206}Pb^*$ ages are taken as the best estimate of crystallization ages. The remaining ten out of thirteen grains were analyzed at least twice. Four grains (12R-1, 12R-3, 12R-8, 14R-1) have uniformly concordant analyses, in addition to $^{207}Pb/^{206}Pb$ ages which are statistically indistinguishable at the 2σ level. These grains are interpreted as reliably preserving crystallization ages. We note that these grains include: (1) grains sourced from regolith samples and (2) grains with both regular,

oscillatory zoning and ages extending down to 4055 ± 10 Ma (12R-1, Fig. 5; also see Appendix 4).

A total of three grains (12R-2, 15Q-3, 15Q-4) have consistent $^{207}Pb/^{206}Pb$ ages (at the 2σ level), but one or more analyses that are statistically discordant (up to +6%). In such cases, we take the $^{207}Pb/^{206}Pb$ age for the most concordant analysis as the best estimate of the grain's crystallization age. Zircon 17B-4 contains the oldest $^{207}Pb/^{206}Pb$ age (4392 ± 12 Ma), and the crystallization age is 4416 ± 50 Ma (see thesis, Chapter 6). Out of all thirteen grains, zircon 12R-7 is the only grain that contains multiple, statistically distinct analyses of age that individually overlap concordia, and, as discussed above, it is the only grain to possess microstructures unique to shock deformation.

The total range in U and Th spans an order of magnitude from 10 to 200 µg/g U, and 4 to 115 µg/g Th, and Th/U wt. ratios vary from 0.31 to 0.68. Total α-doses ($D_{\alpha total}$) calculated from age, U and Th data range from 0.29×10^{15} α-decays/mg (analysis 14R.1-1.2) to 6.1×10^{15} α-decays/mg (analysis 17B.4-1.2); this correlates with total α-doses ranging from a factor of five below the first percolation point (~2×10^{15} α-decays/mg), to a factor of five above it. Excluding the high U and Th zircon 17B-4, the total range in U, Th and dose is more restricted (<82 µg/g U, and <30 µg/g Th), with a range in D_{total} ranging from $0.29x10^{15}$ to $2.4x10^{15}$ α-decays/mg. Within this subset of the data, 23 out of 33 individual analyses have D_{total} which fall below $1.5x10^{15}$ α-decays/mg.

4.3 Raman Spectroscopy

The lunar zircon grains in this study possess a broad range in Raman behavior as measured by individual spot analyses. Only one zircon, 17B-4, has sufficiently degraded

crystallinity as to inhibit quantification of the $\nu_3(SiO_4)$ Raman signal. Excluding this zircon, the total range in $\nu_3(SiO_4)$ bandwidth ($FWHM_{\nu3(SiO4)}$) is between 3.8 and 13.0 cm^{-1}, while $\nu_3(SiO_4)$ band position ranges from 1001.0 to 1007.0 cm^{-1} (Fig. 6a and b; Appendix 3). Variability in $FWHM_{\nu3(SiO4)}$ on the scale of an individual SIMS U-Pb analysis ranges from 0.0 to 4.5 cm^{-1}; significant variability ($[(FHWM_{max} - FWHM_{min})/FWHM_{avg.}] \times 100 > 10\%$) occurs in eight of the 28 SIMS analyses (29%). This is indicative of micron-scale heterogeneity in U and Th content, that has been averaged during SIMS analysis. The average $FWHM_{\nu3(SiO4)}$ and band position for individual SIMS analyses range from 4.1 to 12.9 cm^{-1}, and 1001.0 to 1006.7 cm^{-1} respectively.

A comparison of D_{total} and D_{eff} offers a semi-quantitative estimate of retained damage (fractional dose, $F_{retained} = (D_{total}-D_{eff})/D_{total} \times 100$) and varies between 0.21 and 0.83. These fractional doses include some of the lowest measured in lunar zircon. On a spot-by-spot basis, there is no correlation between discordance, total α-dose, or effective dose. With the exception of zircon 17B-4, which possesses the highest total α-doses and $FWHM_{\nu3(SiO4)}$, zircon grains have $\nu_3(SiO_4)$ band width and peak position consistent with previously documented "radiation damage accumulation trend" (Fig. 6b) (e.g., Geisler et al., 2002; Nasdala et al., 2002). Zircon 17B-4 preserves peak positions elevated from the radiation damage accumulation trend; this is consistent with annealing along the trends discussed by Geisler et al., (2001) (Fig. 6b).

5 DISCUSSION

5.1 Zircon Microstructures

The zircon structures (both microstructures and damage states) observed in this study are indicative of three distinct processes: (1) deformation (broadly defined) including fragmentation, crystal-plastic deformation, and shock deformation, (2) the accumulation of radiation damage, and (3) the annealing of radiation damage. With the notable exception of zircon 12R-7, zircons

are largely devoid of significant microstructural complexity; none of the mapped zircon grains (other than 12R-7) contain more than 2° of cumulative offset across *individual grain fragments*, and any crystal plastic deformation within grains/ grain fragments is within analytical limits.

The presence of shock microtwin lamellae in zircon 12R-7 is only the third published account of diagnostic shock features in lunar zircon. Shock microstructures have now been documented from Apollo 12 (this study), Apollo 14 (Crow et al., 2014), and Apollo 17 (Timms et al., 2012). Given the abundant geomorphic preservation of impacts on the Moon, shock microstructures have appeared infrequently in the lunar zircon literature; it is unclear if this is symptomatic of their rarity or lack of characterization (Timms et al., 2012). Zircon microtwin lamellae are indicative of shock pressures in excess of 19 GPa (Timms et al., 2012). The nature of twin lamellae, which crosscut "feathery" CL patterning (interpreted as a secondary texture) in addition to the U-Pb systematics suggest 12R-7 has undergone more than one deformational episode. The timing of shock deformation is somewhat cryptic, as it is unclear whether Pb migration was commensurate with development of shock microstructures. U-Pb analyses are discordant, with a lower discordia intercept of 2742 ± 540 Ma (2SD). This is suggestive of Pb migration at some time around ~3.0 Ga. However, if Pb efficiently segregated to and remained at crystallographic boundaries, this would generate a multi-domain structure that would make 2742 ± 540 Ma a *minimum* age for Pb-loss (see this thesis, Chapter 5).

5.2 Zircon Annealing in the Lunar Environment

Despite persisting in a relatively cool and water-free state, the zircon grains within this study have partly annealed over geological timescales (Fig. 6a). This observation is independent of sample type, sample location, or lithology. Combined with the data of Pidgeon et al. (2016),

These data suggest annealing episodes have influenced a large portion of the lunar zircon population now residing at the surface. Importantly, the Apollo 14 zircon grains in this study preserve significantly lower fractional α-doses relative to those of Pidgeon et al. (2016) (Fig. 6a); this reinforces the hypothesis that the magnitude of annealing is variable for different landing sites, and between individual zircon grains/samples.

An extension of calculating the fractional annealing of individual analyses is to correlate the effective α-doses with "radiation damage ages" (*sensu* Pidgeon, 2014). Individual Raman spots show limited scatter outside of analytical uncertainty (Fig. 7), which is likely the result of imperfect correlation between U and Th concentrations on the scale of SIMS analyses and Raman analyses (see discussion above). The radiation damage ages calculated from the *average* FWHM data for individual SIMS analyses, vary by up to 500-900 Myr *within individual zircon grains.* We interpret this as the presence of incomplete or heterogeneous annealing within individual grains. Implicit in the calculation of radiation damage ages are the assumptions (1) that the present-day damage states represent complete damage retention since the most recent reheating event, and (2) that reheating was sufficient to completely anneal any existing structural damage (e.g., Nasdala et al., 2001; Pidgeon 2014). As a result, the calculated radiation damage ages in this study do not provide robust *quantitative* information regarding zircon thermal histories; however, these data still offer valuable *qualitative* constraints on the timing of reheating and suitable driving forces. While the presence of more complex annealing dynamics limit the quantitative nature of radiation damage ages, ages can still be interpreted as the *maximum* time elapsed since the *most recent* annealing. The presence of abundant radiation damage ages <3.0 Ga requires a widespread annealing mechanism (affecting at least Apollo sites 12, 14, and 15) that acted within the last 3 billion years.

Based on the inferred thermal inputs at the lunar surface, and the effectiveness of crustal reworking, it has been considered unlikely that many lunar zircons will show significant annealing. Annealing of zircon grains is largely the result of prolonged heating of zircon grains at temperature in excess of ~250-300^{o}C (Ewing et al., 2003). On Earth, these temperatures are largely associated with magmatism and metamorphism that can persist to the present day, while similar processes on the Moon are restricted to the first several hundreds of millions of years. The initial phase of lunar plutonism is largely restricted to within the first ~500 million years of lunar history (Meyer et al., 1996; Nemchin et al., 2008; Crow et al., 2018; see discussion below). Mare volcanics cover approximately 17% of the lunar surface with the youngest radiometric ages at ~3.0 Ga; younger (1-2 Ga) mare volcanism is thought to be volumetrically limited (Head, 1976; Hiesinger et al., 2000). While lunar surface temperatures can *fluctuate* by ~300^{o}C between the lunar daytime (average equatorial maximum temperature of 119^{o}C) and nighttime (average equatorial minimum of -179^{o}C) (Williams et al., 2017), these diurnal fluctuations are below the thermal threshold to induce significant annealing, even when integrated over geological timescales.

Given the current knowledge of thermal influences within the lunar crust (see above), it is most probable that annealing of zircon reflects the thermal influence of impactors. This accounts for both (1) the presence of significant annealing across different lithologies and sample sites, and (2) the presence of different degrees of radiation damage within individual sites. It's also likely that many zircon grains were annealed early in their history during residence in the lunar crust and early impactor bombardment; however, resolving older annealing events is difficult due to younger annealing.

The importance of radiation damage as a control on element mobility in lunar zircons can be considered qualitatively, based on the accumulation of damage and the abundance/timing of thermal episodes in lunar history. Grain-scale element migration can occur in zircon damaged beyond the first percolation point; however, this requires accumulation of greater than ~2×10^{15} α-decays/mg, *followed* by high temperatures *after* the accumulation of significant radiation damage. Grange et al. (2013b) suggested that radiation damage exerts a relatively minor influence on *early* trace element and isotope systematics because (1) U and Th concentrations are relatively low (<100 μg/g) in most lunar zircons, and (2) the distribution of impact bombardment (inferred to be an important thermal driver for annealing) is concentrated in the first 500-750 million years of lunar history. As a result, most lunar zircons will not have accumulated sufficient damage to predispose them to grain-scale element migration. This hypothesis is supported by this study, particularly the conclusions that impacts, which are focused early in lunar history, are an important thermal input to anneal the structure. A small number of zircon grains in the published literature do show large degrees of discordance (e.g., Meyer et al., 1996; Grange et al., 2013b), and these data reinforce the interpretation that, while radiation damage is an important factor in controlling element mobility in lunar zircon, it may play a secondary role due to the broad trends in lunar magmatism and impact history.

5.3 The Lunar Zircon Record

Zircons within this study preserve a range of microstructures, damage states and U-Pb ages, all consistent with the observed or anticipated behavior of zircon from the lunar environment. In order to evaluate the similarities and distinctions present between different sample types and landing sites, and aspects of the Moon's magmatic and impact history, we have

compiled >1000 SIMS U-Pb analyses on 498 zircons (including this study) returned during the Apollo missions. This compilation includes analyses of zircon grains from Apollo 12 (Meyer et al., 1996; Zang et al., 2012; Liu et al., 2012; Thiessen et al., 2018; this study), Apollo 14 (Meyer et al., 1996; Nemchin et al., 2006, 2008, 2009b; Grange et al., 2013b; Hopkins and Mojzsis, 2015; Crow et al., 2017; this study), Apollo 15 (Meyer et al., 1996; Grange et al., 2013a; Crow et al., 2017; this study), and Apollo 17 (Meyer et al., 1996; Nemchin et al., 2008, 2009a; Grange et al., 2009, 2011; 2013b; Crow et al., 2017; this study). We have excluded zircon grains that can be demonstrably linked to crystallization of impact melts (e.g., Type 2 and Type 3 zircons of Grange et al., 2009; Crow et al., 2017; Zhang et al., 2018). While impact melt zircons offer important petrographic and geochemical information, they are often small with acicular/skeletal morphologies, and (1) do not appear to be petrographically representative of the vast majority of zircons in lunar literature, and (2) are less likely to be preserved either as part of second or third generation breccias, or in the lunar regolith. We have systematically assigned a single best estimate for the crystallization age of individual zircon grains, so as to avoid distorting age distributions due to repeated analyses on well characterized grains. Where possible, we have excluded zircon grains with highly discordant (>20% discordant) U-Pb systematics from consideration, though this is difficult to apply unilaterally without taking into consideration differences in reporting standards and analytical precision.

Age distributions for the compiled data (Fig. 8) show several first-order trends previously discussed in the literature. These include: (1) a small number of ages older than 4390 Ma, which are by themselves, significant in constraining solidification of the lunar surface and formation of the KREEP reservoir (Nemchin et al., 2009a; this thesis, Chapter 6), (2) an abundance of ages between 4300-4350 Ma at all landing sites, and (3) distinct differences in the number of <4150

Ma zircons (see also, Nemchin et al., 2008; Crow et al., 2017). Both Apollo 12 and 14 have significantly more <4150 Ma zircon grains, while Apollo 15 and 17 contain significantly fewer. Different rationales have been invoked to explain this including: (1) different degrees of U-Pb age resetting (Crow et al., 2017), (2) the systematic localization of lunar magmatism around the Procellarum KREEP Terrane (Nemchin et al., 2008), and (3) impact-induced magmatism (Crow et al., 2017). It is difficult to distinguish these trends from aggregate data; however, multiple concordant analyses preserved in young (4.0 Ga) regolith grains with igneous zoning patterns at Apollo 12 (zircon 12R-1, above; Valley et al., 2014; Appendix 4) argue in favor of preservation of magmatic ages in lunar zircon, even in regolith grains, and that magmatism (irrespective of the ultimate source) may have persisted until 4.0 Ga.

To pursue a more quantitative comparison of age distributions (both between sample types, and landing sites), this work utilizes the two-tailed Kolmogorov-Smirnov test (K-S test) to evaluate the uniqueness of empirical distributions. This test offers two important advantages: (1) as a non-parametric method, it does not require comparison with analytical or assumed distribution types, and (2) *p*-values are relatively accurate for tests meeting the criteria $(n_1 \times n_2)/(n_1+n_2) \geq 4$, where n_1 and n_2 are the sample sizes for the two empirical distributions being compared. This condition is met in all but a very limited number of cases when comparing the full range of sample types and landing sites (Table 2). The K-S test is suited for identifying *distinct* distributions but passing the K-S test does not imply the underlying distributions are the same.

Prior to evaluating the similarity and differences between Apollo *sites*, this work first compares age distributions from different sample *types* (i.e. clast, breccia and regolith grains). Qualitatively, the transition from clast-hosted zircon, to breccia-hosted zircon, to isolated

regolith grains represents an increase in the time and breakdown of the zircon host material at the lunar surface. Zircons from these difference sample types should preserve identical age information if (1) they represent the sequential breakdown and redistribution of a common parent material, *and* (2) zircon geochemistry has been unaffected by the breakdown process. Significant vertical and lateral mixing of material will introduce and mix distinct zircon-age populations in second or third generation breccias, and the lunar regolith, and should be detectable based on the observable age distributions.

Apollo 14 represents the landing site with the largest number of analyses and largest sampling of the individual sample types. Apollo 14 clast and Apollo 14 regolith zircon populations can be distinguished at the 95% confidence level ($p=0.000375$); all others cannot. This result suggests regolith material contains distinct information relative to other material. This may represent either (1) a sampling of distinct lithologies, or (2) prolonged exposure to impacts and the associated metamorphism. It is possible, and perhaps likely, that the differences/similarities between different sample types may change between different sample sites, suggesting there are geographic differences in the mixing and/or breakdown of lunar material.

Age distributions Apollo 12 and Apollo 14 are the only aggregate age distributions that **cannot** be distinguished at the 95% confidence level. This is indicative of most landing sites having distinct age distributions. The differences (or the lack thereof) between aggregate age spectra parallel the statistical differences (or lack thereof) when comparing identical *subpopulations* for different landing sites. For example, aggregate spectra for Apollo 12 and 14 are not distinct at the 95% confidence level, and this same statement applies when comparing Apollo 12 clast zircons with Apollo 14 clast zircons, or Apollo 12 breccia zircons to Apollo 14

breccia zircons. Similarly, aggregate spectra for all other Apollo landing sites are statistically distinct, and with limited exceptions, identical subpopulations are distinct as well. Given that there is a general consistency in distinguishing age distributions when comparing similar sample types across landing sites, the following discussion focuses on aggregate age distributions to discuss the differences between different landing sites.

Differences (or lack thereof) in zircon age spectra from Apollo 12, 14, 15 and 17 have significant implications for interpretation of site-specific geology, particularly with regards to the distribution and abundance of ejecta deposits from basin-forming impacts. One hypothesis is that the aggregate zircon age distributions is process related – i.e. differences are related to systematic differences in the magnitude/abundance of partial age resetting. In compiling data, we have attempted to minimize biases associated with age discordance by (1) screening data for large degrees of discordance, (2) removing unambiguous examples of impact melt zircon, and (3) assigning single crystallization ages to individual zircon grains (e.g., reconstructing zircon ages from discordia, and correcting for observable Pb-loss). Despite this, the antiquity of both the individual grains and the potential for ancient (>3.9 Ga) Pb-loss episodes makes detection and unambiguous assessment of grain-scale element mobility difficult; and the presence/absence of this behavior is treated in the context of lunar geology, below.

An important question within lunar geology remains the relative importance of the Imbrium impact (3.7-3.8 Ga; see Stöffler et al., 2006 for discussion of Imbrium impact age) in contaminating different Apollo sites (e.g., Bottke and Norman, 2017). In the instance of significant Imbrium contamination across the lunar nearside, differences in age spectra (most notably the presence of 3.9-4.15 Ga zircon ages at Apollo 12 and 14) would reflect *post-Imbrium* mixing of 3.9-4.15 material into the Apollo 12 and 14 landing sites. This is compatible with

evidence for mixing of distal material at Apollo 12 (e.g., Barra et al., 2006; Korotev et al., 2011) though ultimate source of 3.9-4.15 Ga material remains cryptic. An alternative interpretation is that the *absence* of 3.9 - 4.15 Ga zircon grains at Apollo 15 and Apollo 17 makes a compelling case *against* the hypothesis that the Imbrium event has effectively overprinted or contaminated the lunar nearside (and the Apollo landing sites). While ~3.9 Ga impact melt zircon have been identified at Apollo 17 (e.g., Zhang et al., 2018), these grains are morphologically and petrographically distinct from the remainder of the zircons analyzed at Apollo 12, 14 , 15 and 17 (see above); the difference in 3.9-4.15 Ga zircons between Apollos 12 and 14, and Apollos 15 and 17 is based on a larger group of coarser, pre-3.9 grains. The hypothesis that Imbrium *has* uniquely contaminated virtually all the Apollo landing sites implies that, to a first degree, the pre-3.9 Ga zircon population at different sites should be similar, as all of these grains are pre-Imbrium and accessible for redistribution during the Imbrium impact. The significant fraction of 3.9-4.15 Ga zircon grains preserved at Apollo 12 and 14, should therefore be present at Apollo 17. The fact that it is absent would suggest that material at several sites is *not* uniquely linked to Imbrium, and at Apollo 17. Linking individual samples to specific events is complex, however the qualitatively limited contamination of Apollo 17 (by Imbrium) would link the ~3.9 Ga thermal footprint at Apollo 17 more closely with the Serenitatis basin forming impact (3970 ± 27 Ma) (e.g., Wolfe et al., 1981; Hurwitz and Kring, 2016; Stöffler et al., 2006; this study, Chapter 6). This association would place the Imbrium and Serenitatis basin forming impacts within a very brief time window in lunar history (e.g., Thiessen et al., 2018) and remains significant in determining magnitude and significance of the late heavy bombardment.

Independent of the cause of any differences between the different landing sites, age distributions hint at the indirect importance of Imbrium, as the final large basin forming impact

proximal to the Apollo landing sites. The combined age spectra for lunar zircon support the presence of silicic magmatism (and zircon crystallization) until at least ~3.9 Ga; however, *the younger limit on this remains poorly defined*. Zircon data with "ages younger than 3.9 Ga generally fall into two categories – either the analyses themselves are highly discordant, and represent Pb-loss at more recent times (e.g., Meyer et al., 1996; Grange et al., 2013a), or they are analyses of impact melt zircons (e.g., Grange et al., 2013a). Imbrium represents the last basin-forming impact to redistribute large portions of crustal material proximal to the Apollo landing sites, and silicic magmatism which *post-dates* ~3.8 Ga may be significantly underrepresented in lunar surface deposits as subsequent impacts have declined in mass, frequency, and are increasingly incident upon both (1) younger basaltic volcanics and (2) a maturing mega-regolith of interlayer ejecta deposits. As a result, the lack of coarser "magmatic" zircons with ages younger than ~3.9 Ga may represent either a cessation of silicic magmatism on the Moon, or it may point to an implicit bias in our understanding of zircon crystallization due to limited post-3.9 Ga excavation of younger magmas preserved within the lunar crust.

CONCLUSIONS

The combination of SIMS, EBSD and Raman data presented here document individual zircon grains which have a range in crystallization ages, and a variety of thermal/structural histories; This includes the presence of shock lamellae within one Apollo 12 regolith zircon. Annealing within lunar zircon is more widespread than previously recognized. The magnitude and "young" ages for annealing are consistent with a combination of residence within the lunar crust and impact heating as the main driving forces for annealing of zircons. Compilations of U-Pb ages show that zircon grains from different sample types (clast, breccia, and regolith) contain

distinct information that may be related to either different processes, or unique aspects of provenance, and the vertical and lateral mixing of the regolith. Additional analysis of zircon grains from each of the different sample types will provide a unique means to evaluate the influence of the Imbrium Basin-forming impact, vertical and lateral material transport, and the longevity of silicic lunar magmatism.

ACKNOWLEDGEMENTS

We thank Brian Hess, for aid and attention in preparing valuable zircon samples. This research was funded by the U.S. National Science Foundation (EAR-1144454, EAR-1524336), and the U.S. Department of Energy, Office of Basic Energy Sciences, Geosciences Division under award number DE-FG02-93ER14389. WiscSIMS is supported by NSF (EAR-1658823) and the University of Wisconsin- Madison. The authors acknowledge the use of facilities supported by the University of Wisconsin, College of Engineering and the Materials Research and Engineering Center (NSF DMR-121288) and Nanoscale Science and Engineering Center (NSF DMR-0832760).

REFERENCES

Alexander, E.C., Kahl, S.B. (1974) ^{40}Ar-^{39}Ar studies of lunar breccias. Proceedings of the 5th Lunar Science Conference, 2, 1353-1373.

Barboni, M., Boehnke, P., Keller, B., Kohl, I., Schoene, B., Young, E., McKeegan, K., (2017) Early formation of the Moon 4.511 billion years ago. Science Advances, 3, e1602365.

Barra, F., Swindle, T.D., Korotev, R.L., Jolliff, B.L., Zeigler R.A., Olson, E. (2006) ^{40}Ar/^{39}Ar dating of Apollo 12 regolith: Implications for the age of Copernicus and the source of non-mare materials. Geochimica et Cosmochimica Acta, 70, 6016-6031.

Belluci, J.J., Whitehouse, M.J., Nemchin, A.A., Snape, J.F., Pidgeon, R.T., Grange, M., Reddy, S.M., Timms, N. (2017) A scanning ion imaging investigation into the micron-scale U-Pb systematics in a complex lunar zircon. Chemical Geology, 438, 112-122.

Bernatowicz T.J., Hohenberg, C.M., Hudson, B., Kennedy, B.M., Podosek, F., (1978) Argon ages for lunar breccias 14064 and 15405. Proc. 9th Lunar Planet. Sci. Conf., 905-919.

Bottke, W.F., Norman, M.D. (2017) The Late Heavy Bombardment. Annual review in Earth and Planetary Sciences, 45, 619-647.

Cavosie, A.J., Erickson, T.M., Timms, N.E., Reddy, S.M., Talavera, C., Montalvo, S.D., Pincus, M.R., Gibbon, R.J., Moser, D. (2015) A terrestrial perspective on using *ex situ* shocked zircons to date lunar impacts. Geology, 43, 999-1002.

Cherniak, D.J., Lanford, W.A., Ryerson, F.J. (1991) Lead diffusion in apatite and zircon using ion implantation and Rutherford Backscattering techniques. Geochimica et Cosmochimica Acta, 55, 1663-1673.

Cherniak, D.J., Watson, E.B. (2003) Diffusion in zircon, Reviews in Mineralogy and Geochemistry, 53, 113-143.

Crow, C.A., Moser, D.E., McKeegan, K.D., Barker, I. (2014) Impact shock microstructures in Apollo 14 zircons. 77th Annual Meteoritical Society Meeting, Sept 7-12 LPI Cont. 1800.

Crow, C.A., McKeegan, K.D., Moser, D.E. (2017) Coordinated U-Pb geochronology, trace element, Ti-in-zircon thermometry and microstructural analysis of Apollo zircons. Geochimica et Cosmochimica Acta, 202, 264-284.

Dence, M.R., Grieve, R.A.F., Plant, A.G. (1976) Apollo 17 grey breccias and crustal composition in the Serenitatis Basin region. Proc. 7th Lunar Sci Conf., 1821-1832.

Ewing, R.C., Meldrum, A., Wang, L., Weber, W.J., Corrales, L.R. (2003) Radiation effects in zircon, Reviews in Mineralogy and Geochemistry, 53, 387-425.

Geisler, T., Pidgeon, R.T., Bronswijk, W.V., Pleysier, R. (2001) Kinetics of thermal recovery and recrystallization of partially metamict zircon: a Raman spectroscopic study, European Journal of Mineralogy, 13, 1163-1176.

Grange, M.L., Nemchin, A.A., Pidgeon, R.T., Timms, N., Muhling, J.R., Kennedy, A.K. (2009) Thermal history recorded by the Apollo 17 impact melt breccia 73217. Geochimica et Cosmochimica Acta, 73, 3097-3107.

Grange, M.L., Nemchin, A.A., Timms, N., Pidgeon, R.T., Meyer, C. (2011) Complex magmatic and impact history prior to 4.1 Ga recorded in zircon from Apollo 17 South Massif aphanitic breccia 73235. Geochimica et Cosmochimica Acta, 75, 2213-2232.

Grange, M.L., Nemchin, A.A., Pidgeon, R.T. (2013a) The effect of 1.9 and 1.4 Ga impact events on 4.3 Ga zircon and phosphate from Apollo 15 melt breccia. Journal of Geophysical Research: Planets, 118, 2180-2197.

Grange, M.L., Pidgeon, R.T., Nemchin, A.A., Timms, N.E., Meyer, C. (2013b) Interpreting U-Pb data from primary and secondary features in lunar zircon. Geochimica et Cosmochimica Acta, 101, 112-132.

Head, J.W. (1976) Lunar volcanism in time and space. Reviews of Geophysics and Space Physics, 14, 265-300.

Hiesinger, H.J., Jaumann, R., Neukum, G., Head, J.W. (2000) Ages of mare basalts on the lunar nearside. Journal of Geophysical Research, 105, 29259-29275.

Hopkins, M.D. and Mojzsis, S.J. (2015) A protracted timeline for lunar bombardment from mineral chemistry, Ti thermometry and U-Pb geochronology of Apollo 14 melt breccia zircons. Contributions to Mineralogy and Petrology, 169, 30.

Huang, Y.-H., Minton, D.A., Hirabayashi, M., Elliot, J.R., Richardson, J.E., Fassett, C.L., Zellner, N.E.B. (2017) Heterogeneous impact transport on the Moon. Journal of Geophysical Research: Planets, 122, doi:10.1002/2016JE005160.

Hurwitz, D., and Kring, D.A. (2016) Identifying the geologic context of Apollo 17 impact melt breccias. Earth and Planetary Science Letters, 436, 64-70.

Jourdan, F., Verati, C., Feraud, G. (2006) Intercalibration of the Hb3gr $^{40}Ar/^{39}Ar$ dating standard. Chemical Geology (231) 177-189.

Korotev, R., Jolliff, B.L., Zeigler, R.A., Seddio, S.M., Haskin, L.A. (2011) Apollo 12 revisited. Geochimica et Cosmochimica Acta, 75, 1540-1573.

Liu, D., Jolliff, B.L., Zeigler, R.A., Korotev, R.L., Wan, Y., Xie, H., Zhang, Y., Dong, C., Wang, W. (2012) Comparative zircon U-Pb geochronology of impact melt breccias from Apollo 12 and lunar meteorite SaU 169, and implications for the age of the Imbrium impact. Earth and Planetary Science Letters, 319-320, 277-286.

Meyer, C., Williams, I.S., Compston, W. (1996) Uranium-lead ages for lunar zircons: Evidence for a prolonged period of granophyre formation from 4.32 to 3.88 Ga, Meteoritics and Planetary Science, 31, 370-387.

Min, K., Mundil, R., Renne, P., Ludwig, K. (2000) A test for systematic errors in $^{40}Ar/^{39}Ar$ geochronology through comparison with U/Pb analysis of 1.1-Ga rhyolite. Geochimica et Cosmochimica Acta, (64) 73-98.

Moser, D.E., Davis, W.J., Reddy, S.M., Flemming, R.L., Hart, R.J., (2009) Zircon U-Pb strain chronometry reveals deep impact-triggered flow. Earth and Planetary Science Letters, 277, 73-79.

Moser, D.E., Cupelli, C.L., Barker, I.R., Flowers, R.M., Bowman, J.R., Wooden, J., Hart, J.R. (2011) New zircon shock phenomena and their use for dating and reconstruction of large impact structures revealed by electron nanobeam (EBSD, CL, EDS) and isotopic U-Pb and (U-Th)/He analysis of the Vredefort dome. Canadian Journal of Earth Sciences, 48, 117-139.

Nasdala, L., Pidgeon, R.T., Wolf, D. (1996) Heterogeneous metamictization of zircon on a microscale, Geochimica et Cosmochimica Acta, 60, 1091-1097.

Nasdala, L., Wenzel, M., Vavra, G., Irmer, G., Wenzel, T., Kober, B. (2001) Metamictization of natural zircon: accumulation versus thermal annealing of radioactivity-induced damage, Contributions to Mineralogy and Petrology, 141, 125-144.

Nasdala, L., Irmer, G., Jonckheere, R. (2002) Radiation damage ages: Practical concept or impractical vision? – Reply to two comments on "Metamictization of natural zircon: accumulation versus thermal annealing of radioactivity-induced damage", and further discussion, Contributions to Mineralogy and Petrology, 143, 758-765.

Nemchin, A.A., Whitehouse, M.J., Pidgeon, R.T., Meyer, C. (2006) Oxygen isotopic signature of 4.4-3.9 Ga zircons as a monitor of differentiation processes on the Moon. Geochimica et Cosmochimica Acta, 70, 1864-1872.

Nemchin, A.A., Pidgeon, R.T., Whitehouse, M.J., Vaughn, J.P., Meyer, C. (2008) SIMS U-Pb study of zircon from Apollo 14 and 17 breccias: Implications for the evolution off lunar KREEP. Geochimica et Cosmochimica Acta, 72, 668-689.

Nemchin, A., Timms, N., Pidgeon, R., Geisler, T., Reddy, S., Meyer, C. (2009a) Timing of crystallization of the lunar magma ocean constrained by the oldest zircon, Nature Geoscience, 2, 133-136.

Nemchin, A.A., Pidgeon, R.T., Healy, D., Grange, M.L., Whitehouse, M.J., Vaughn, J. (2009b) The comparative behavior of apatite-zircon U-Pb systems for the thermal history of the Fra Mauro Formation. Meteoritics and Planetary Science, 44, 1717-1734.

Pidgeon, R.T., Merle, R.E., Grange, M.L., Nemchin, A.A., Whitehouse, M.J. (2016) Annealing of radiation damage in zircons from Apollo 14 impact breccia 14311: Implications for the thermal history of the breccia, Meteoritics and Planetary Science, 51, 155-166.

Reddy, S.M., Riessen, A., Saxey, D.W., Johnson, T.E., Rickard, W.D.A., Fougerouse, D., Fisher, S., Prosa, T.J., Rice, K.P., Reinhard, D.A., Chen, Y., Olson, D. (2016) Mechanisms of deformation-induced trace element migration in zircon resolved by atom probe tomography and correlative microscopy. Geochimica et Cosmochimica Acta, 195, 158-170.

Ryder, G., Bower, J.F. (1977) Petrology of Apollo 15 black-and-white rocks 15445 and 15455: fragments of the Imbrium impact melt sheet? Proceedings of the 8th Lunar Science Conference, 1895-1923.

Schmitz, M., (2012) Radiogenic Isotope Geochemistry, *in* Geologic Time Scale 2012, edited by Felix M. Gradstein, James G. Ogg, Mark Schmitz, Gabi Ogg, Elsevier, 115-126.

Shih, C.-Y., Nyquist, L.E., Dacsh, E.J., Bogard, D.D., Bansal, B.M., Wiesman, H. (1993) Ages of pristine noritic clasts from lunar breccias 15445 and 15455. Geochimica et Cosmochimica Acta, 57, 915-931.

Shoemaker, E.M., Batson, R.M., Bean, A.L., Conrad Jr., C., Dahlem, D.H., Goddard, E.N., Hait, M.H., Larson, K.B., Schaber, G.G., Schleicher, D.L., Sutton, R.L., Swann, G.A., Waters, A.C. (1970) Preliminary Geologic Investigation of the Apollo 12 Landing Site: Part A. *in* Apollo 12 Preliminary Science Report, NASA SP-235.

Spicuzza, M.J., Valley, J.W., Kitajima, K., Ushikubo, T. (2011) Oxygen isotope ratios and trace element concentrations in zircons from lunar rocks and regolith, 42nd Lunar and Planetary Science Conference, The Woodlands Texas, #2445.

Stacey, J.S., and Kramers, J.D. (1975) Approximation of terrestrial lead isotope evolution by a two-stage model. Earth and Planetary Science Letters, 26, 207-221.

Swann, G.A., Bailey, N.G., Batson, R.M, Freeman, V.L., Hait, M.H., Head, J.W., Holt, H.E., Howard, K.A., Irwin, J.B., Larson, K.B., et al. (1972) Preliminary geologic investigation of the Apollo 15 landing site, *in* Apollo 15 Preliminary Science Report, NASA SP-298.

Swann, G.A., Bailey, N.G., Batson, R.M., Eggleton, R.E., Hait, M.H., Holt, H.E., Larson, K.B., Reed, V.S., Schaber, G.G., Sutton, R.L., Trask, N.J., Ulrich, G.E., Wilshire, H.G. (1977) Geology of the Apollo 14 landing site in the Fra Mauro Highlands. US Geological Survey Professional Paper 880.

Thiessen, F., Nemchin, A.A., Snape, J.F., Bellucci, J.J., Whitehouse, M.J. (2018) Apollo breccia 12013: Impact-induced partial Pb loss in zircon and its implications for lunar geochronology. Geochimica et Cosmochimica Acta, 230, 94-111.

Timms, N.E., Reddy, S.M., Healy, D., Nemchin, A.A., Grange, M.L., Pidgeon, R.T., Hart, R. (2012) Resolution of impact-related microstructures in lunar zircon: A shock-deformation mechanism map. Meteoritics and Planetary Science, 47, 120-141.

Timms, N.E., Erickson, T.M., Pearce, M.A., Cavosie, A.J., Schmieder, M., Tohver, E., Reddy, S.M., Zanetti, M.R., Nemchin, A.A., Wittmann, A (2017) A pressure-temperature phase diagram for zircon at extreme conditions. Earth-Science Reviews, 165, 185-202.

Timms, N.E., Healy, D., Erickson, T.M., Montalvo, P.E., Prado, D.C., Cintron, N.O., Gibbon, R.J. (2018), Role of elastic anisotropy in the development of deformation microstructures in

zircon. *in* Microstructural Geochronology: Planetary Records Down to Atom Scale, edited by Moser, D.E., Corfu, F., Reddy, S.M., Darling, J.R., Tait, K., John Wiley & Sons, Inc., Hoboken, NJ, 232, 183–202.

Trachenko, K., Dove, M.T., Salje, E.K.H. (2003) Large swelling and percolation in irradiated zircon, Journal of Physics: Condensed Matter, 15, L1-L7.

Turner, G., and Cadogan, P.H. (1975) The history of lunar bombardment inferred from $^{40}Ar/^{39}Ar$ dating of highland rocks. Proc. 6th Lunar Sci. Conference, 1509-1538.

Váczi, T. (2014) A new, simple approximation for the deconvolution of instrumental broadening in spectroscopic band profiles. Applied Spectroscopy, 68, 11.

Valley, J.W., Lackey, J.S., Cavosie, A.J., Clechenko, C.C., Spicuzza, M.J., Basei, A.S., Bindeman, I.N., Ferreira, V.P., Sial, A.N., King, E.M., and others, (2005) 4.4 billion years of crustal maturation: oxygen isotope ratios of magmatic zircon, Contributions to Mineralogy and Petrology, 150, 561-580.

Valley, J.W., Spicuzza, M.J., Ushikubo, T. (2014) Correlated $\delta^{18}O$ and [Ti] in lunar zircons: a terrestrial perspective for magma temperatures and water content on the Moon, Contributions to Mineralogy and Petrology, 167:956.

Wiedenbeck, M., Hanchar, J.H., Peck, W.H., Sylvester, P., Valley, J., Whitehouse, M., Kronz, A., Morishita, Y., Nasdala, L., Fiebig, J., et al. (2004) Further characterization of the 91500 zircon crystal. Geostandards and Geoanalytical Research, 28, 9-39.

Williams, J.-P., Paige, D.A., Greenhagen, B.T., Sefton-Nash, E. (2017) The global surface temperatures of the moon as measured by the Diviner lunar Radiometer Experiment. Icarus, 283, 300-325.

Wolfe, E.W., Bailey, N.G., Lucchitta, B.K., Muehlberger, W.R., Scott, D.H., Sutton, R.L., Wilshire, H.G. (1981) The Geologic Investigation of the Taurus-Littrow Valley: Apollo 17 Landing Site. U.S. Geological Survey Professional Paper 1080.

Wopenka, B., Jolliff, B.L., Zinner, E., Kremser, D.T. (1996) Trace element zoning and incipient metamictization in a lunar zircon: Application of three microprobe techniques. American Mineralogist, 81, 902-912.

Zhang, A.-C., Taylor, L.A., Wang, R.-W., Li, Q.-L., Li, X.-H., Patchen, A.D., Liu, Y. (2012) Thermal history of Apollo 12 granite and KREEP-rich rock: Clues from Pb/Pb ages of zircon in lunar breccia 12013. Geochimica et Cosmochimica Acta, 95, 1-14.

Zhang, B., Lin, Y., Moser, D.E., Shieh, S.R., Bouvier, A. (2018) Imbrium zircon age for Apollo 73155 Serenitatis impact melt breccia: implications for the lunar bombardment history. LPI Contrib. No. 2107.

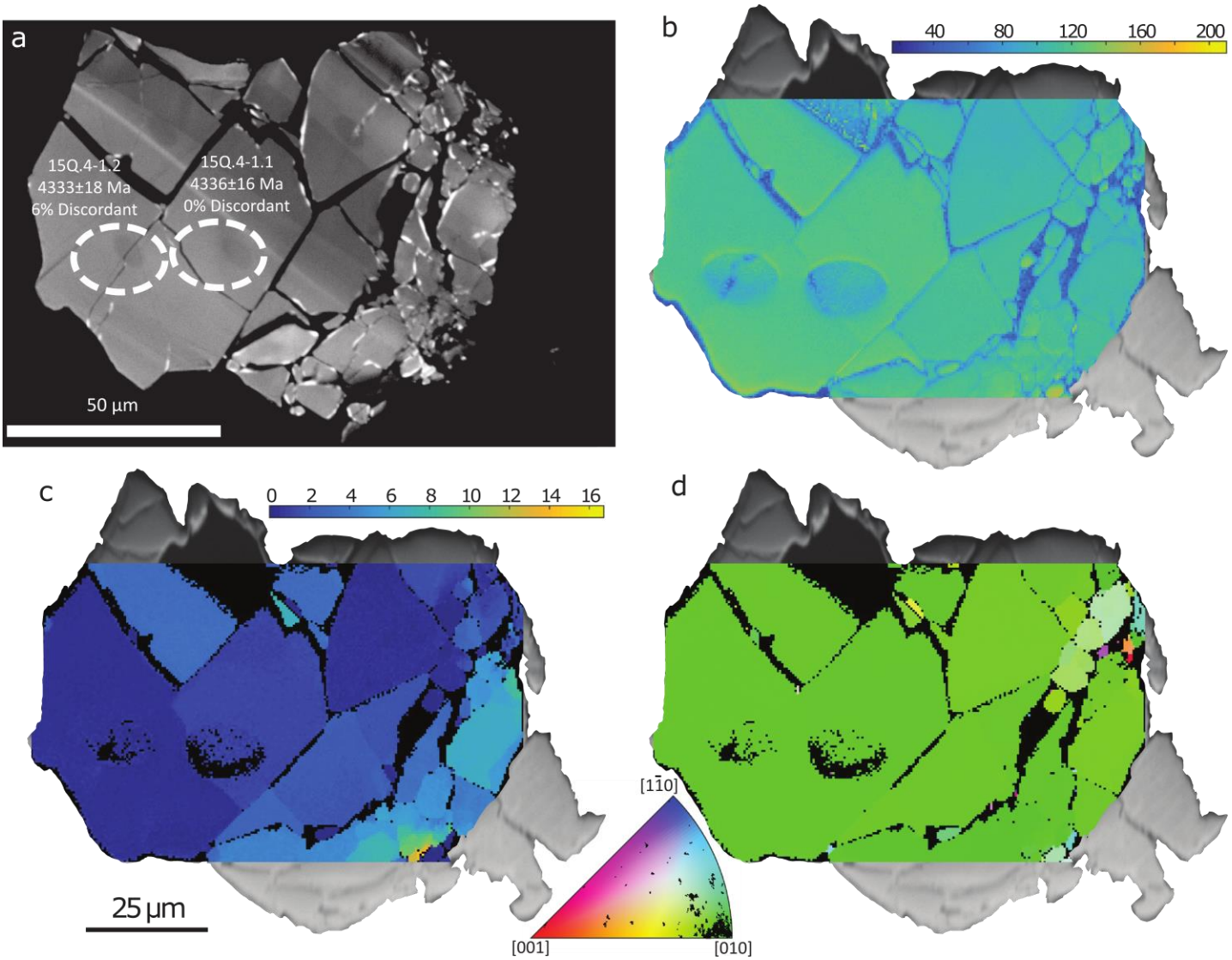

Figure 1: Summary of U-Pb analyses and imaging for zircon grain 15Q-4, separated from a quartz monzodiorite clast within lunar sample 15405. (a) Cathodoluminescence showing location of SIMS U-Pb analyses. (b) EBSD band contrast map (relative units). (c) EBSD misorientation map, in units of degrees. (d) Zircon orientation colored according to the inverse pole figure. (b-d) are shown overlain on 15Q-4 forescatter image.

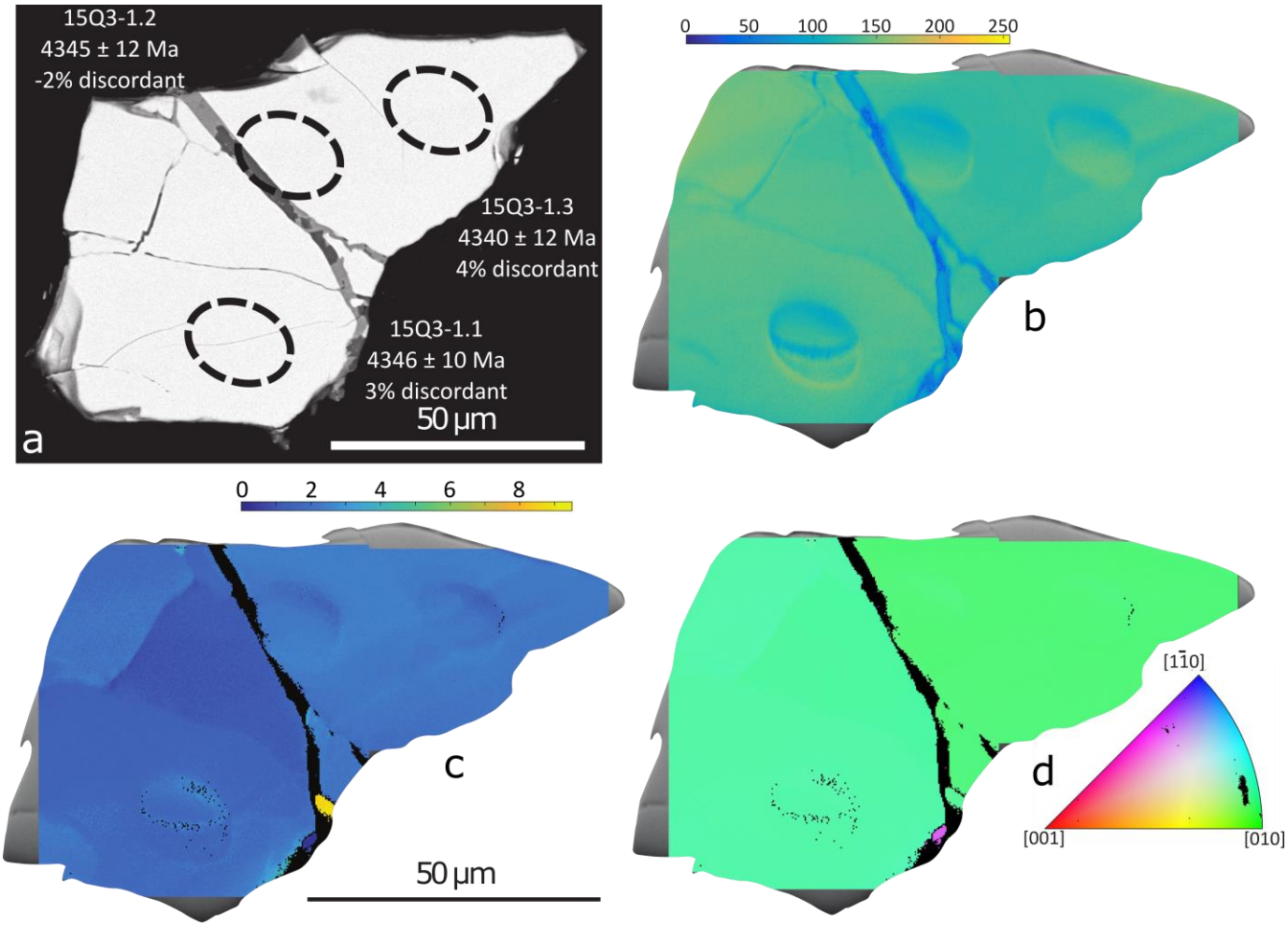

Figure 2: Summary of U-Pb analyses and imaging for lunar zircon grain 15Q-3, separated from a quartz monzodiorite clast within sample 15405. (a) Backscattered electron image, showing location of SIMS U-Pb analyses. (b) EBSD band contrast map (relative units). (c) EBSD misorientation map, in units of degrees. (d) Zircon orientation colored according to the inverse pole figure. (b-d) are shown overlain on 15Q-4 forescatter image.

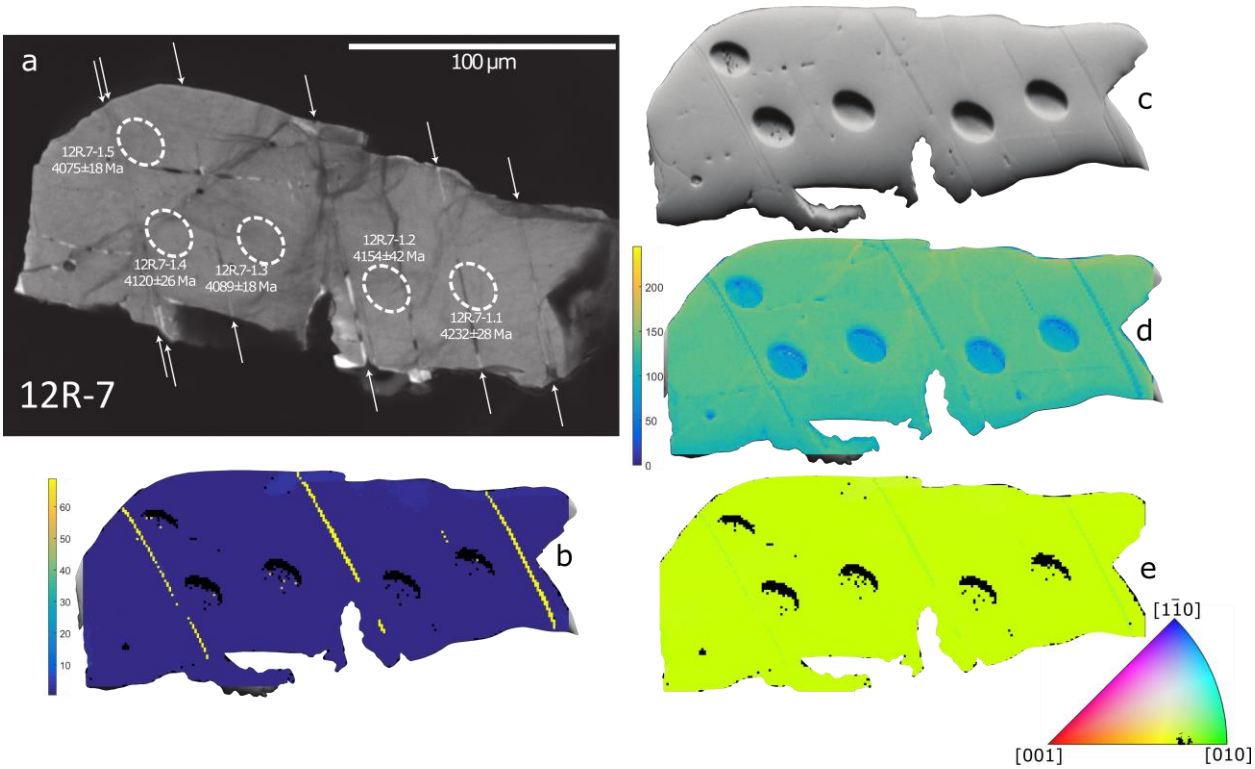

Figure 3: Summary of U-Pb analyses, imaging, and EBSD mapping for lunar zircon grain 12R-7 picked from the fine fraction of lunar regolith sample 12023. (a) CL image of zircon 12R-7; dashed outlines show outlines of SIMS U-Pb analysis pits. Arrows point to shock microtwin lamellae visible in forescatter imaging (c) as well as EBSD mapping (b-e). (b) EBSD Misorientation map showing 65^{o} misorientation characteristic of shock microtwin lamellae (color scale in units of degrees). (c) Forescatter image showing contrast between host zircon and shock microtwin lamellae. (d) EBSD band contrast image (relative units). (e) Crystallographic orientation, colored by inverse pole.

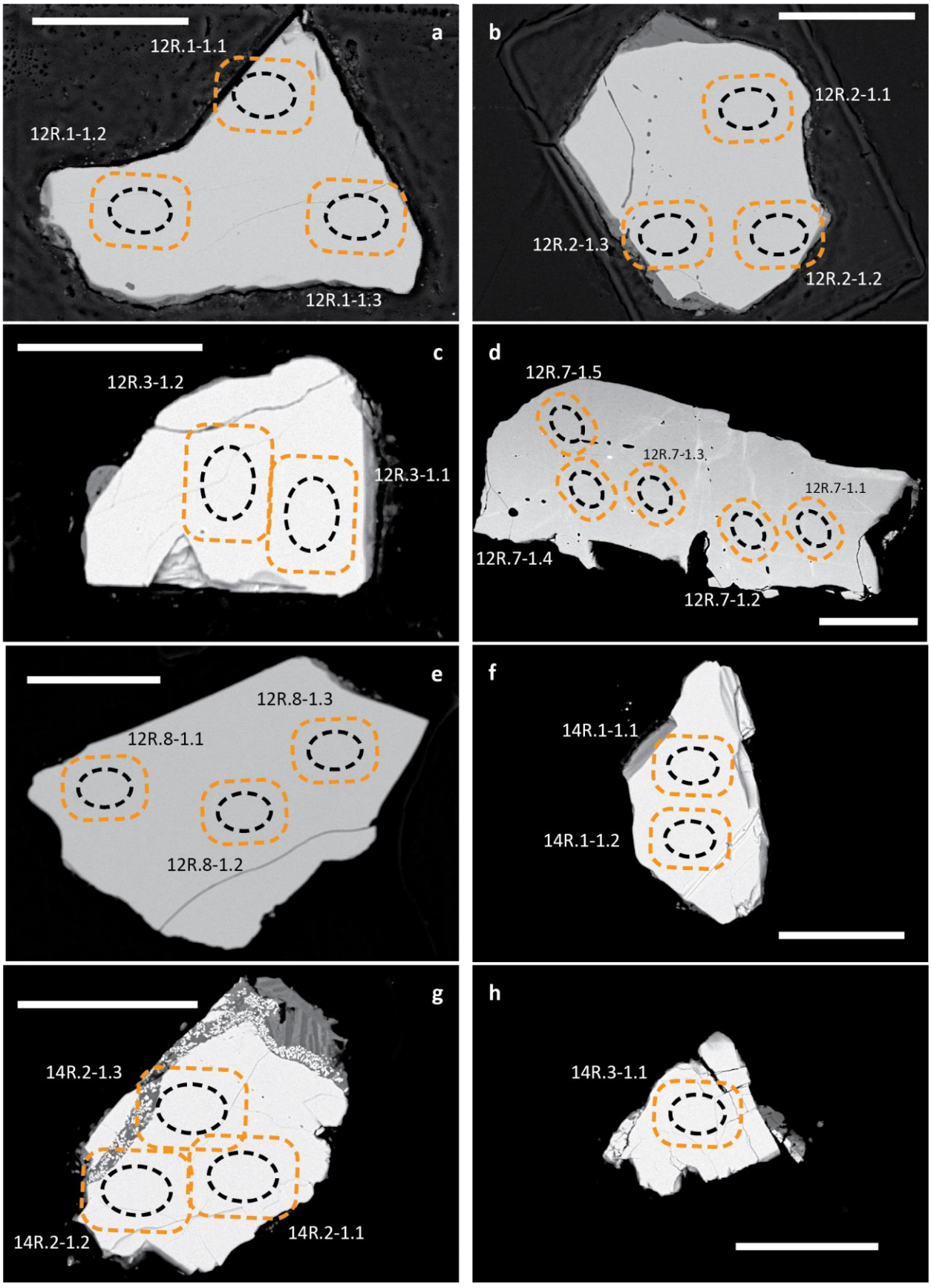
a
12R.1-1.1
12R.1-1.2
12R.1-1.3
b
12R.2-1.1
12R.2-1.3
12R.2-1.2
c
12R.3-1.2
12R.3-1.1
d
12R.7-1.5
12R.7-1.3
12R.7-1.1
12R.7-1.4
12R.7-1.2
e
12R.8-1.3
12R.8-1.1
12R.8-1.2
f
14R.1-1.1
14R.1-1.2
g
14R.2-1.3
14R.2-1.2
14R.2-1.1
h
14R.3-1.1

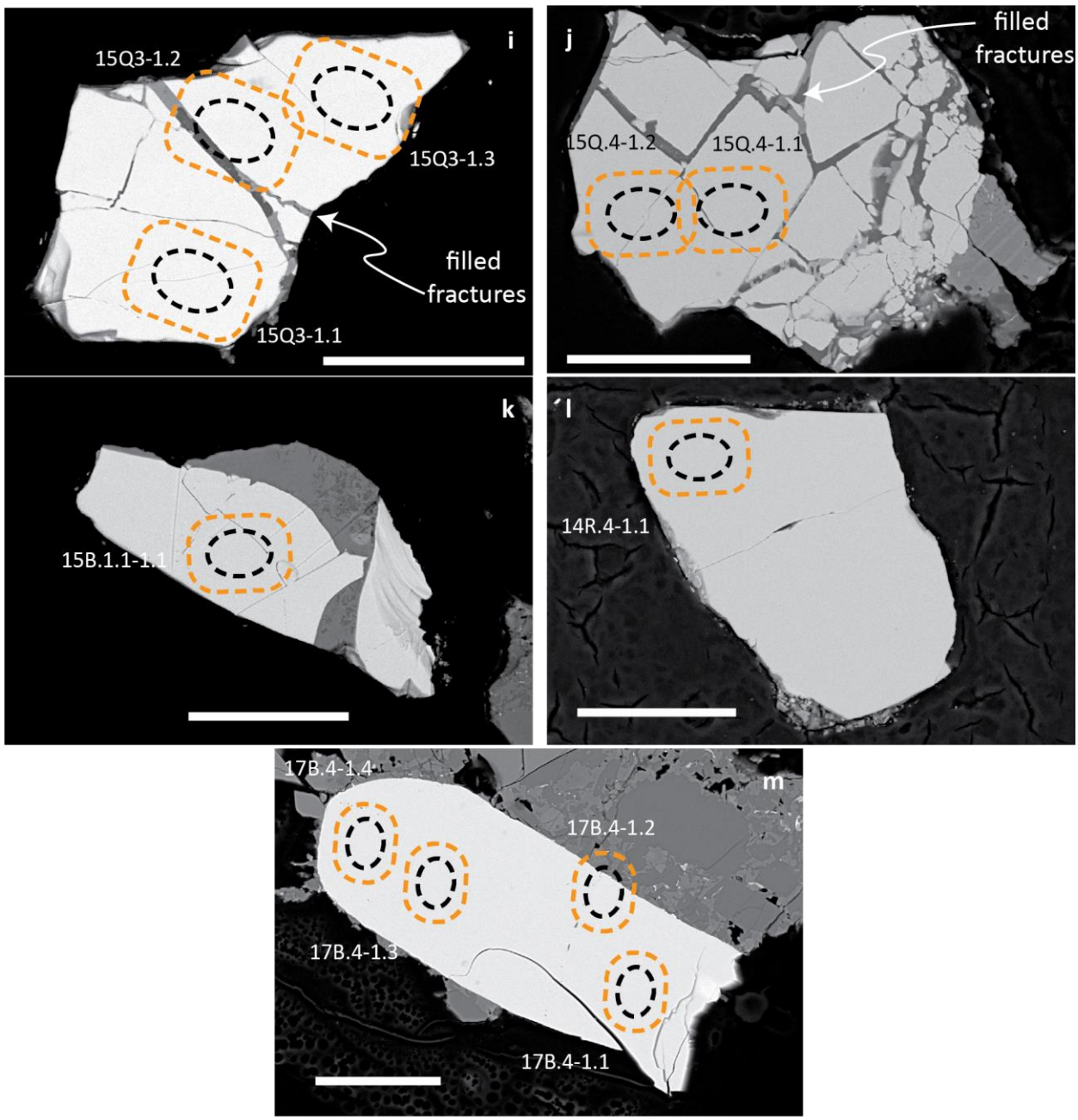

Figure 4: (a-m) Backscattered electron images for zircon grains studied in this work. Scale bar is 50 μm in each image. Dashed lines show location of SIMS U-Pb analyses (Table 1, Fig. 5); black dashed lines show pits, with orange outlines showing pre-analysis raster.

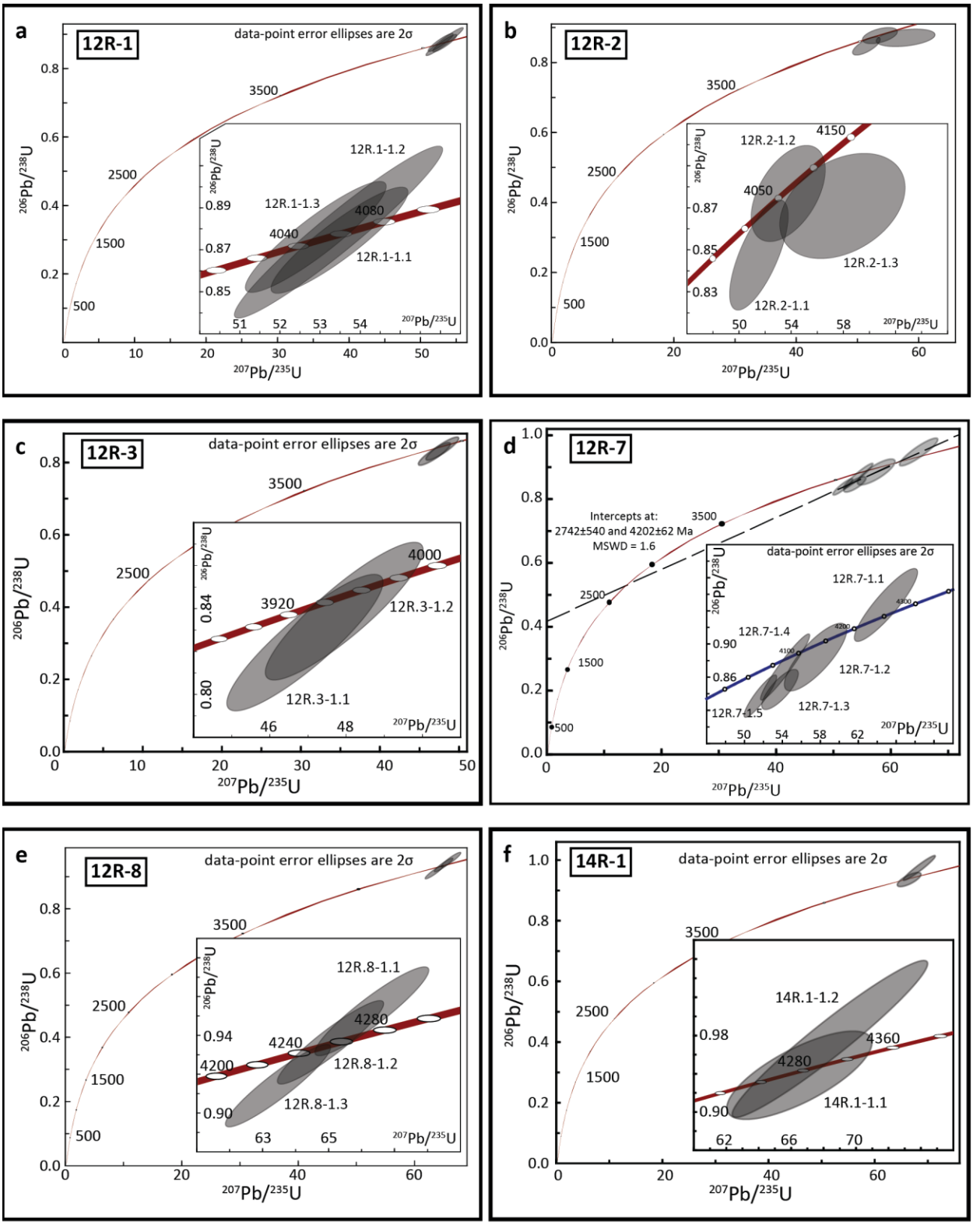
a
12R-1
data-point error ellipses are 2σ
12R.1-1.2
12R.1-1.3
12R.1-1.1
4080
4040
3500
2500
1500
500
b
12R-2
12R.2-1.2
12R.2-1.3
12R.2-1.1
4150
4050
c
12R-3
12R.3-1.2
12R.3-1.1
4000
3920
d
12R-7
Intercepts at:
2742±540 and 4202±62 Ma
MSWD = 1.6
12R.7-1.1
12R.7-1.4
12R.7-1.2
12R.7-1.3
12R.7-1.5
e
12R-8
12R.8-1.1
12R.8-1.2
12R.8-1.3
4280
4240
4200
f
14R-1
14R.1-1.2
14R.1-1.1
4360
4280
206Pb/238U
207Pb/235U

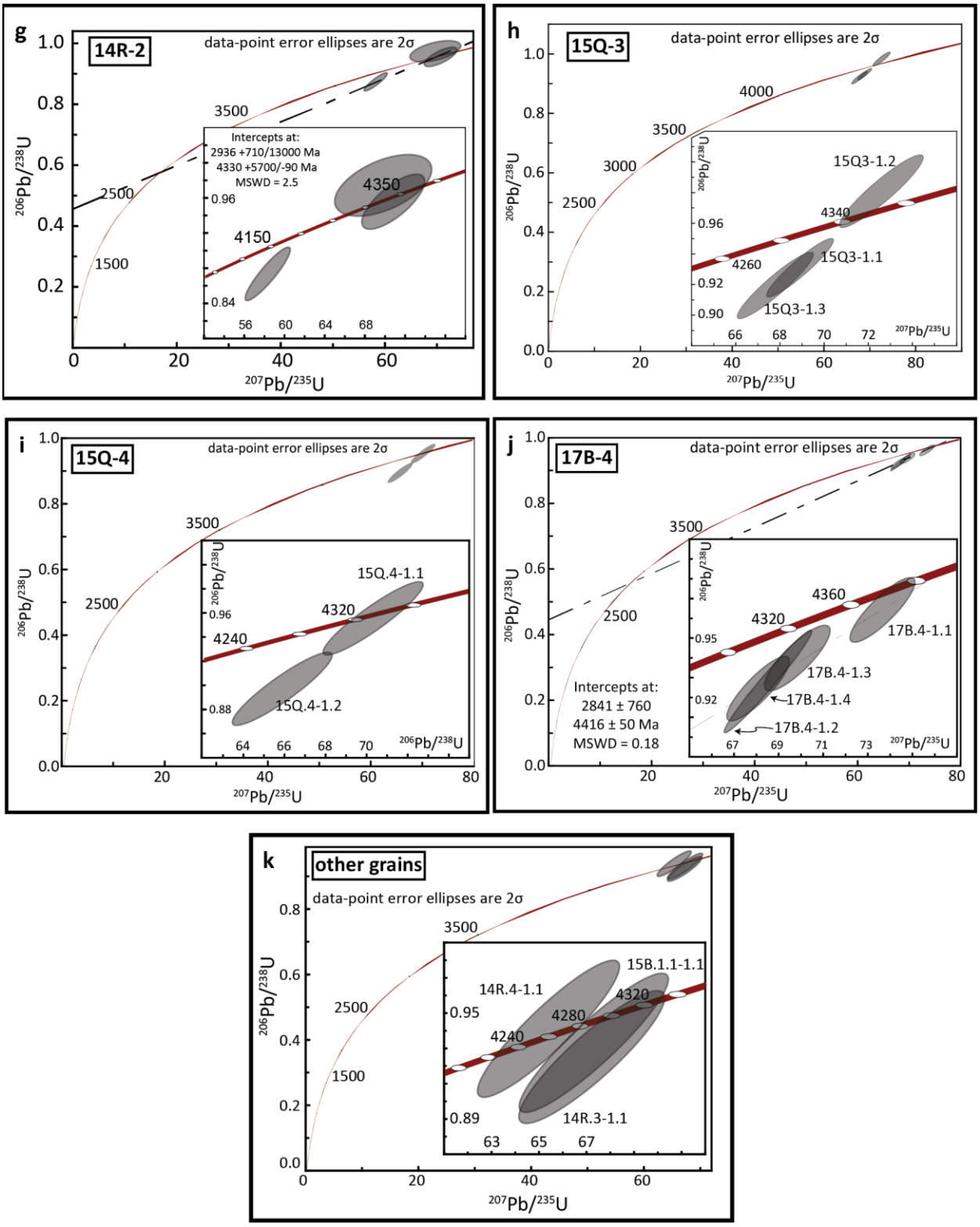

Figure 5: (a-k) Summary of SIMS U-Pb data for luanr zircon grains in this work. Analyses correlate with data in Table 1, and spot locations in Fig. 4.

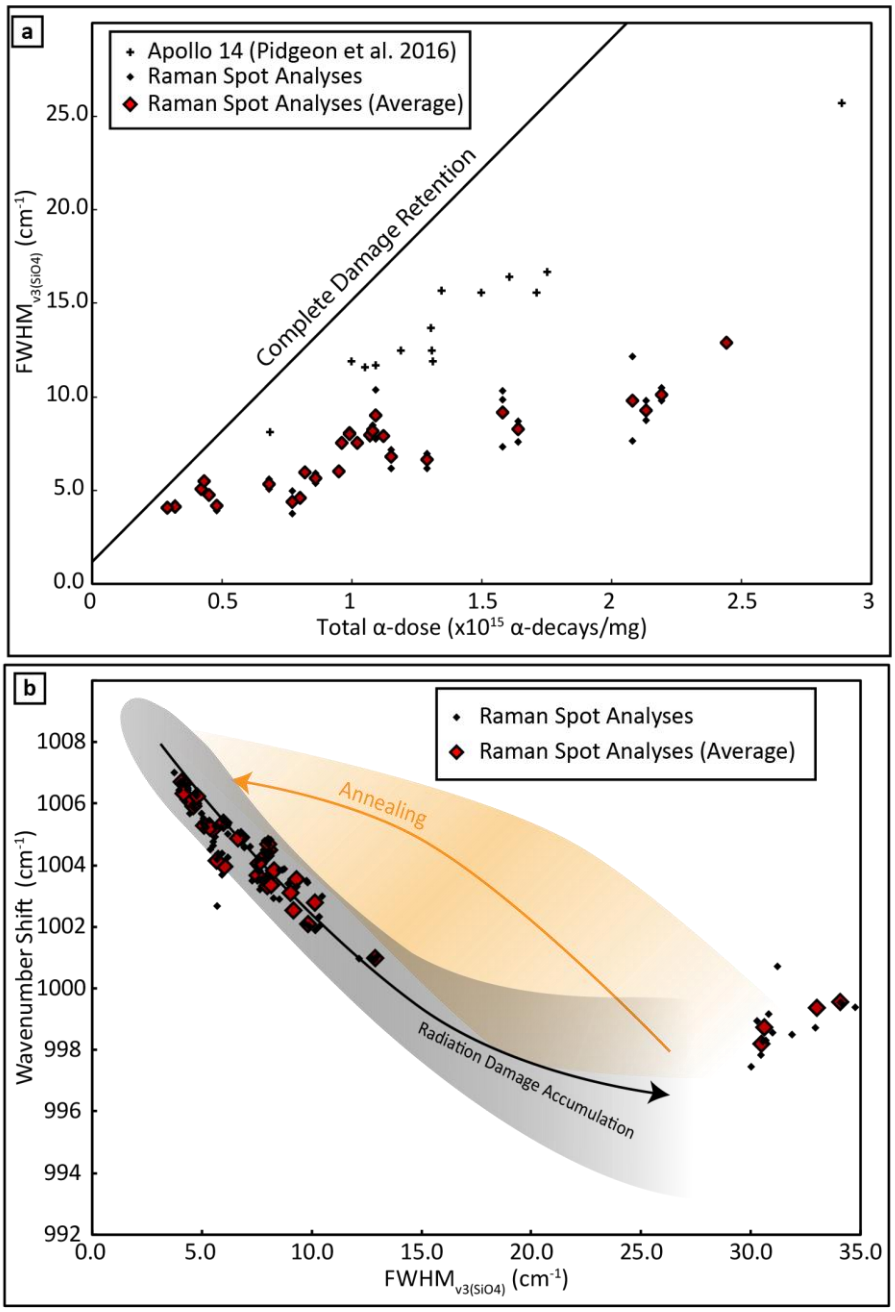

Figure 6: Summary of Raman measurements of the $\nu_3(SiO_4)$ vibrational mode in lunar zircon. (a) $FWHM_{v3(SiO4)}$ versus total calculated α-dose for lunar zircon grains. Individual Raman analyses are shown as black diamonds, while red diamonds are averages for Raman analyses correlated to an individual SIMS analysis pit. Crosses are data for Apollo 14 zircons form Pidgeon et al. (2016). Solid black line is the complete damage retention trend of Nasdala et al. (2001). (b) Band position versus band broadening for lunar zircon grains in this study. Also shown are the empirical trends for "Radiation Damage Accumulation" and "Annealing." (Geisler et al., 2001).

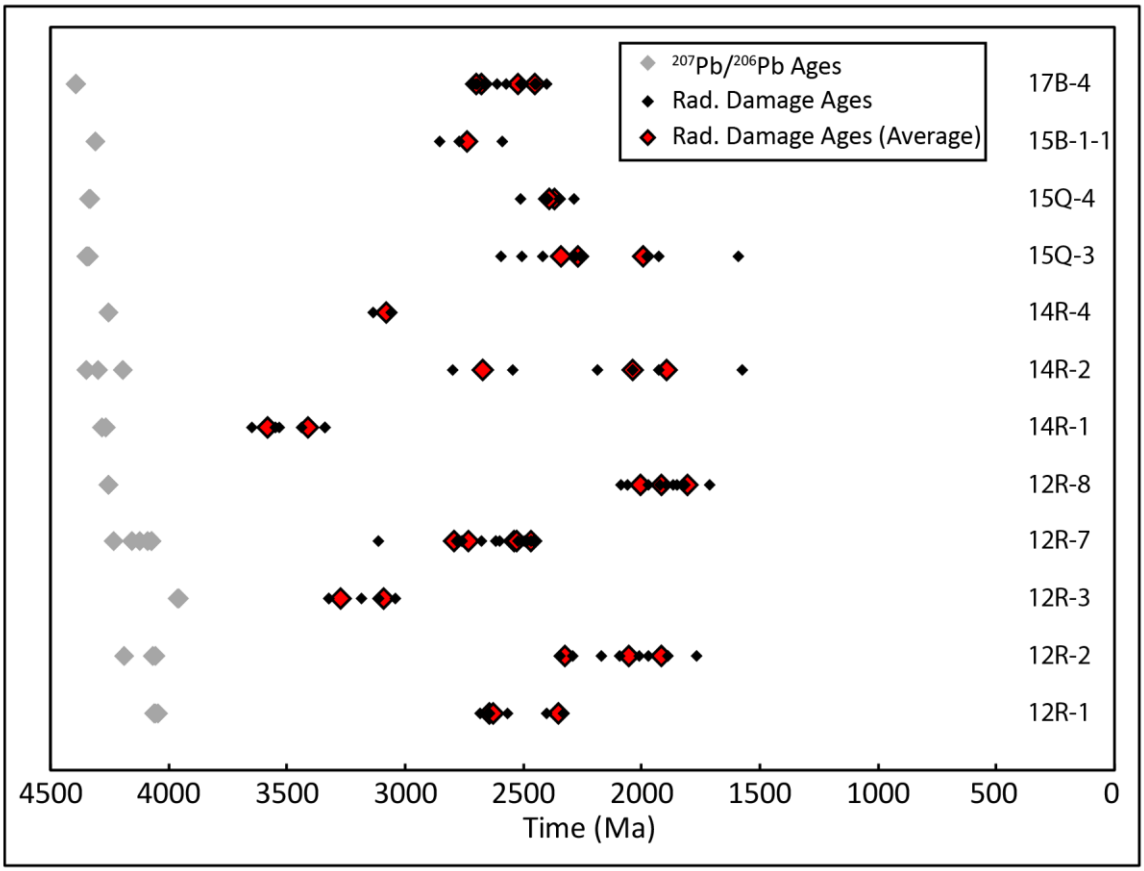

Figure 7: Radiation damage ages based on Raman spot analyses (Fig. 6) assuming no annealing. Damage ages calculated from individual Raman analyses are shown as black diamonds, while radiation damage ages calculated from average Raman bandwidths around individual SIMS analysis pits are shown as red diamonds. $^{207}Pb/^{206}Pb$ ages are shown as grey diamonds.

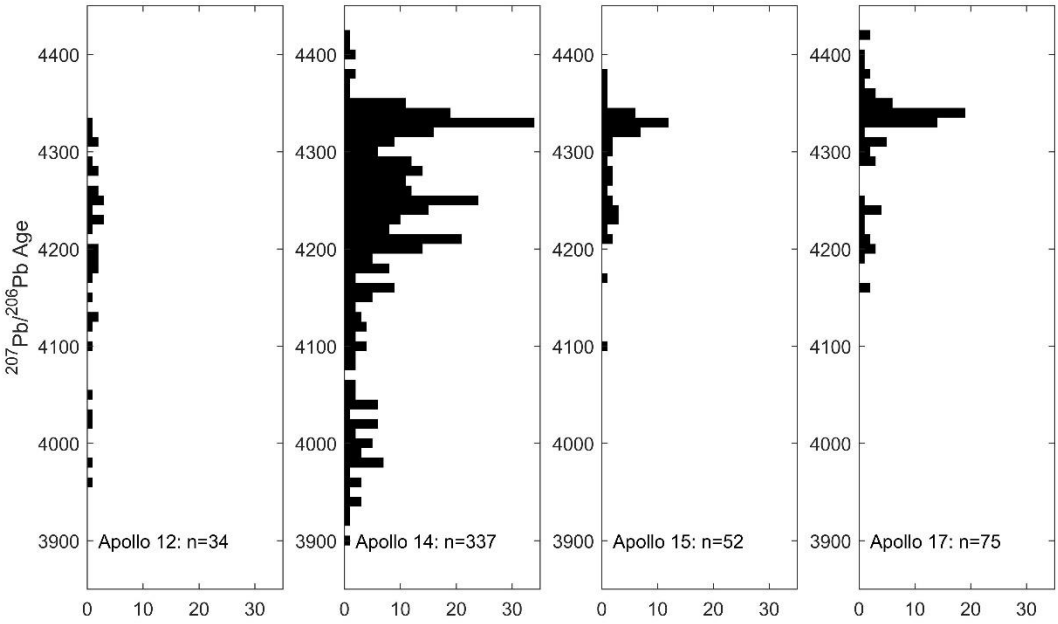

Figure 8: Histograms showing age distributions of zircon grains from four Apollo landing sites. See references in text. Individual zircon grains have been assigned a best estimate for crystallization age based on available data, and data quality metrics – see text for further details. With the exception of Apollo 12 and Apollo 14, all four of the distributions are distinct at the 95% confidence level based on the two-tailed Kolomogov-Smirnov test.

Table 1: Summary of SHRIMP-RG U-Pb age analyses for lunar zircon.

Zircon - Spot	Th (µg/g)	U (µg/g)	Th/U	$^{204}Pb/^{206}Pb$	1σ	$^{207}Pb^*/^{206}Pb^*$	1σ	$^{207}Pb^*/^{235}U$	1σ	$^{206}Pb^*/^{238}U$	1σ	ρ	$^{206}Pb^*/^{238}U$ Age (Ma)	1σ (Ma)	$^{207}Pb^*/^{206}Pb^*$ Age (Ma)	1σ (Ma)	Disc.
17B.4-1.1	109	187	0.58	-3.4E-6	100	0.554	0.42	73.7	0.8	0.964	0.7	0.86	4351	22	4392	6	+1
17B.4-1.2	115	200	0.57	1.6E-5	50	0.536	0.25	68.5	1.2	0.928	1.2	0.98	4230	36	4342	4	+3
17B.4-1.3	81	158	0.51	-1.2E-5	58	0.539	0.47	69.8	0.9	0.939	0.7	0.84	4270	23	4351	7	+3
17B.4-1.4	105	156	0.68	2.0E-5	45	0.534	0.43	68.1	0.8	0.924	0.7	0.86	4218	23	4338	6	+4
15Q.4-1.1	11	32	0.34	6.2E-5	58	0.534	0.56	70.3	1.4	0.956	1.3	0.92	4323	41	4336	8	+0
15Q.4-1.2	11	29	0.36	2.5E-5	100	0.533	0.62	65.9	1.5	0.897	1.4	0.91	4127	42	4333	9	+6
12R.2-1.1	11	32	0.35	4.2E-5	71	0.441	1.26	51.5	1.8	0.847	1.3	0.71	3956	38	4054	19	+3
12R.2-1.2	14	45	0.32	7.0E-5	45	0.445	1.89	53.7	2.2	0.877	1.1	0.49	4058	32	4067	28	+0
12R.2-1.3	17	47	0.37	1.7E-5	100	0.482	3.20	57.9	3.4	0.871	1.2	0.35	4037	35	4188	47	+5
15B.1.1-1.1	8	16	0.51	-1.2E-4	58	0.523	0.78	67.3	1.9	0.933	1.7	0.91	4248	54	4307	11	+2
14R.4-1.1	6	16	0.37	3.9E-5	100	0.504	0.78	65.4	1.9	0.941	1.7	0.91	4275	53	4252	12	-1
12R.1-1.1	25	37	0.67	1.8E-5	100	0.444	0.55	53.5	1.3	0.874	1.2	0.91	4050	36	4063	8	+0
12R.1-1.2	25	37	0.67	-5.5E-5	58	0.441	0.56	53.5	2.0	0.878	1.9	0.96	4063	58	4056	8	-0
12R.1-1.3	29	42	0.68	5.5E-5	58	0.438	0.57	52.9	1.4	0.876	1.2	0.91	4055	37	4044	8	-0
12R.8-1.1	20	58	0.35	3.2E-5	58	0.505	0.41	66.3	1.1	0.952	1.0	0.92	4312	31	4255	6	-2
12R.8-1.2	29	75	0.39	6.4E-5	38	0.504	0.38	65.0	1.0	0.936	0.9	0.93	4259	29	4252	6	-0
12R.8-1.3	30	77	0.38	3.8E-5	50	0.504	0.38	63.5	1.0	0.914	1.0	0.93	4184	29	4252	6	+2
14R.1-1.1	5	11	0.41	1.5E-4	58	0.508	1.01	68	3.6	0.976	3.5	0.96	4390	111	4264	15	-4
14R.1-1.2	4	10	0.38	1.5E-4	58	0.514	1.86	66	2.8	0.937	2.0	0.74	4264	63	4282	27	+1
14R.3-1.1	15	37	0.40	4.5E-5	58	0.527	0.83	67	1.9	0.925	1.7	0.90	4221	52	4318	12	+3
15Q.3-1.1	28	82	0.34	4.0E-5	41	0.537	0.32	69	0.9	0.931	0.8	0.93	4241	26	4346	5	+3
15Q.3-1.2	20	53	0.38	6.3E-5	41	0.537	0.40	73	1.1	0.981	1.0	0.93	4406	32	4345	6	-2
15Q.3-1.3	26	70	0.38	9.4E-6	100	0.535	0.38	68	1.0	0.919	1.0	0.93	4202	30	4340	6	+4
12R.7-1.1	20	33	0.60	-3.5E-5	71	0.497	0.94	65	2.1	0.948	1.9	0.90	4297	59	4232	14	-2
12R.7-1.2	24	39	0.61	1.6E-5	100	0.471	1.40	58	2.4	0.885	1.9	0.80	4085	57	4154	21	+2
12R.7-1.3	26	40	0.64	-1.6E-5	100	0.451	0.59	54	2.0	0.873	1.9	0.95	4044	56	4089	9	+1
12R.7-1.4	24	39	0.63	1.7E-5	100	0.461	0.91	54	1.5	0.846	1.2	0.79	3950	34	4120	13	+6
12R.7-1.5	23	38	0.61	6.0E-5	58	0.447	0.59	52	1.4	0.838	1.2	0.90	3923	37	4075	9	+5
14R.2-1.1	15	26	0.59	1.6E-4	38	0.538	1.23	71	1.8	0.955	1.3	0.74	4322	42	4347	18	+1
14R.2-1.3	11	23	0.49	-2.4E-5	100	0.520	2.42	70	2.8	0.974	1.5	0.52	4383	47	4298	36	-3
14R.2-1.2	9	28	0.31	5.3E-5	71	0.484	0.66	58	1.6	0.872	1.4	0.91	4044	43	4193	10	+5
12R.3-1.1	9	17	0.53	2.9E-4	35	0.413	0.83	47	1.8	0.824	1.6	0.89	3874	46	3957	12	+3
12R.3-1.2	9	17	0.55	1.4E-4	50	0.415	0.81	48	1.8	0.839	1.6	0.89	3926	46	3963	12	+1

*indicates ^{204}Pb corrected radiogenic Pb.
errors are 1σ (%) unless otherwise specified.

Table 2: Summary of K-S test results comparing lunar zircon age distributions (side and top); *p*-values denote the probability of observing a K-S test statistic at least as extreme assuming the two distributions share a parent distribution (see text for details).

	Apollo 12	*clast*	*breccia*	*regolith*	**Apollo 14**	*clast*	*breccia*	*regolith*	**Apollo 15**	*clast*	*breccia*	*soil*	**Apollo 17**	*clast*	*breccia*
Apollo 12	-				**0.0639**				**1.2E-05**				**7.7E-10**		
clast		-	0.1297	*0.0803**		0.1005				0.4576				0.8265	
breccia			-	0.4042			0.0953				0.00022				7.6E-09
regolith				-				0.0699				0.0013			
Apollo 14					-				**3.70E-05**				**0.001**		
clast						-	0.0528	0.00038		0.0011				0.2594	
breccia							-	0.1877			0.0022				3.1E-07
regolith								-				0.00022			
Apollo 15									-				**0.0018**		
clast										-	0.0497	*0.0193**		0.1877	
breccia											-	*0.0065**			0.0036
soil												-			
Apollo 17													-		
clast														-	0.00026
breccia															-

* Denotes comparisons in which $(n_1 \times n_2)/(n_1+n_2)<4$. Under these circumstances, *p*-values are significantly less reliable.

CHAPTER 5

A nanoscale record of thermal cycling through time in a 4.4 Ga Jack Hills zircon, and implications for the scale dependence of Pb-loss isotope systematics.

Tyler B. Blum[1]*, David A. Reinhard[2], Yimeng Chen[2], Aaron J. Cavosie[3], John W. Valley[1]

[1]Department of Geoscience, University of Wisconsin – Madison, Madison, WI, USA.
[2]CAMECA Inc. Madison, WI, USA
[3]School of Earth and Planetary Science, Curtin University, Perth, WA, AUS

Correspondence: tbblum@geology.wisc.edu

ABSTRACT

Zircon grains often possess complex histories, and can occur *ex situ*, thus missing compositional, textural, and mineralogical associations with their primary lithology and its subsequent geological evolution. This paper reviews the trace element and U-Pb behavior of zircon 01JH36-69, a 4374 ± 12 Ma detrital zircon grain from the Jack Hills, Australia. Previous characterization of this zircon has documented: (1) concordant U-Pb systematics on the micron scale within the zircon core, and (2) the presence of nanoscale clusters enriched in Y, REE, and Pb, which formed in association with a high temperature episode at ~3.4 Ga, recorded as a magmatic overgrowth. This work further explores the isotopic information available in two large atom probe data sets for zircon 01JH36-69. Clusters within the individual data sets can be subdivided based on distinct volumetric and compositional information (e.g., cluster volume, and Y content), showing two distinct cluster populations having distinct $^{207}Pb/^{206}Pb$ ratios. The $^{207}Pb/^{206}Pb$ ratios and uncertainties within these cluster subpopulations correlate with two different thermal episodes: (1) a previously unrecognized thermal episode at 3.77 (+0.23/-0.26) Ga, and (2) entrainment of the zircon within a younger magma at ~3.4 Ga. While the younger episode is preserved as a magmatic overgrowth and dated by SIMS, there is virtually no μm-scale record of the earlier event. The presence of two distinct cluster generations, reinforces the proposal that nanoscale clusters can immobilize radiogenic Pb through subsequent thermal episodes. This motivates exploring the implications for how immobilization of specific Pb isotope components at the nanoscale can influence micro-to-grain scale U-Pb systematics for grains with complex thermal histories.

INTRODUCTION

Analyses of zircon grains are an increasingly important resource for understanding the early Earth and secular evolution in Earth system processes. The ability to collect spatially correlated age, trace element, and isotopic data from subdomains in individual zircon grains provides a powerful tool for tracking geochemical information through time, as well as the initiation and duration of numerous geological processes. This ability, combined with the chemical and physical durability of crystalline zircon, and slow diffusion of almost all major and trace components, makes it the only mineral to form a record extending into the Hadean, where the rock record is absent.

Driven by improvements in instrumentation and analytical capabilities, a major theme in U-Pb zircon geochronology has been the decrease in sample size and improvement in analytical precisions and accuracy; samples themselves have transitioned from multi-grain separates, to

individual zircon grains, to fragments and *in situ* analysis. Coupled with imaging and corelative analyses, site specific analysis of zircon age, trace element and isotope chemistry has led to more meaningful and accurate geological interpretations, with the ability to identify and avoid alteration, and better correlate data to specific growth domains. While *crystalline* zircon is highly retentive of its primary chemistry, the formation of deformation microstructures and the accumulation of radiation damage can enable grain-scale element mobility and alteration. Trace amounts of U and Th incorporated during crystallization form the basis for $^{238}U \rightarrow ^{206}Pb$, $^{235}U \rightarrow ^{207}Pb$, and $^{232}Th \rightarrow ^{208}Pb$ radiometric dating, but also result in eight, seven and six α-decay events in the respective decay chains, which form energetic daughter nuclei with sufficient energy to damage the zircon lattice. The recoil of daughter nuclei generates 5-10 nm damage domains comprised of an amorphous core which grades radially to defect-rich, strained, then unstrained zircon (Ewing et al., 2003; for alternative damage accumulation model, see Ketcham et al., 2013). If damage domains are not annealed, they become more numerous and eventually overlap to form a connected network at the "first percolation point." At the atomic scale, reaction and diffusion kinetics are orders of magnitude faster for damaged zircon relative to pristine zircon (Cherniak et al., 1991; Cherniak and Watson 2003). As a result, zircon which reaches the first percolation point is far more likely to exhibit open system chemical behavior, and have disturbed internal textures and unreliable compositional information. Despite decades of research on zircon and the disruption of U-Pb systematics, there remains a significant lack of understanding regarding fundamental aspects of U-Pb isotope systematics at the nanoscale, such as the relative rates of diffusion and annealing (and their temperature dependencies), and how trace components, particularly U, Pb and the intermediate decay species, interact with defect structures related to both radiation damage and annealing.

Atom probe tomography (APT) possesses a unique combination of spatial resolution and chemical sensitivity that is well-suited to interrogate the geochemical and isotopic evolution of zircon at the length scale of diffusion, radiation damage and annealing. In APT, a needle-shaped specimen with an end tip radius on the order of 50-100 nm is held at high voltage, enabling controlled evaporation of constituent atoms through application of a timed voltage pulse (for conductive materials), or laser pulse. Evaporated ions are accelerated radially away from the tip's surface by the diverging electric field and are incident upon a position sensitive detector, which records both the position of incident ions in detector space and their time of incidence. This results in both a chemical identity for evaporated species (extracted from an ion's mass to charge state ratio, based on its time-of-flight) and three-dimensional position within the original specimen (based on evaporation sequence, and *xy*-position on the detector) (Gault et al., 2012; Larson et al., 2013). The current generation of atom probe instrumentation possesses sub-nanometer spatial resolution, with typical mass resolving powers ($m/\Delta m$) up to 1100, and detection limits down to 10 parts per million atomic (ppma) (Larson et al., 2013). These capabilities enable the chemical mapping of trace components and isotopes in zircon at the sub-nanometer scale.

The application of APT to ancient zircon grains has revealed nanoscale heterogeneity and clustering of several trace components, including Y, Yb, Dy, Lu and radiogenic Pb (Valley et al., 2014; 2015; Peterman et al., 2016; Piazolo et al., 2016; Reddy et al., 2016; Blum et al., 2018). The number of time, temperature, and structural conditions that lead to cluster formation remains incompletely resolved; however, each of these published studies of zircon correlates the formation of these domains with high temperature episodes. High temperatures are thought to enable migration of trace components to specific defect structures, and in some cases thermal

activation of processes such as annealing may be important in generating or actively modifying the zircon structure during this process. The combination of micron and nanoscale U-Pb data (e.g., Valley et al., 2014, 2015; Blum et al., 2018) have demonstrated that (1) clustered Pb is of radiogenic origin and thus clusters did not form during initial zircon crystallization, and (2) in the presence of additional constraints, Pb isotope ratios inside clusters are related to the timing of nanoscale element mobility and cluster formation. Ratios of $^{207}Pb/^{206}Pb$ within clusters can be combined with crystallization ages, to model cluster-formation ages (Valley et al., 2014; Blum et al., 2018).

In this work, we revisit two large APT data sets for zircon 01JH36-69, a 4374 ± 12 Ma (2SD) zircon from the Jack Hills Australia, which was previously analyzed by SIMS and APT (Valley et al., 2014, 2015), and is the oldest reliably-dated terrestrial zircon grain. We document the presence of distinct nanoscale cluster populations recorded in several metrics including the Y-content, cluster volume, and $^{207}Pb/^{206}Pb$ ratio. The isotopic differences between these cluster populations lead to the important conclusions that (1) there have been at least two thermal episodes recorded at the nanoscale, and (2) clusters can be highly retentive of their isotope ratio after formation. Critically, SIMS analyses document that the multistage clustering of Pb isotopes has not caused disturbed U-Pb isotope systematics at the micron-scale for zircon 01JH36-69. The possibility of multiple clustering episodes motivates exploration of how the quantitative retention of Pb isotopes in clusters may influence grain-scale element mobility. We incorporate clustering dynamics into general models of U-Pb systematics to predict how U-Pb isotope ratios will respond on different length scales to complex thermal histories (including clustering and subsequent Pb-loss). These data provide better understanding of scale-dependent U-Pb systematics, and the accurate interpretation of grain thermal histories.

SAMPLES AND METHODS

Zircon 01JH36-69

Zircon 01JH36-69 (also called JH4.4) is a well-characterized detrital zircon grain collected from near Eranondoo Hill in the Jack Hills within the Yilgarn craton of Western Australia (Cavosie et al., 2004; 2006; Cavosie, 2005). Detailed descriptions of the region (e.g., Wang and Wilde, 2018), samples (Cavosie 2005; Cavosie et al., 2004, 2006), and zircon (Valley et al., 2014, 2015) have been published. A total of six U-Pb analyses were performed on surface 3 of zircon 01JH36-69, including analyses of the zircon core and rim domains (Valley et al., 2014; Table 1). The three $^{207}Pb/^{206}Pb$ ages for the core domain range from 4365 ± 10 to 4382 ± 10 Ma, overlap within uncertainty, and are between 100 and 101% concordant (Fig. 1c); all analyses are within uncertainty of concordia. The combination of concordance and consistency in age for these analyses demonstrate the presence of closed system behavior on the micron scale within the core of the zircon grain (Valley et al., 2014, 2015). Three additional SIMS analyses were placed on a bright-in-CL rim domain, with $^{207}Pb/^{206}Pb$ ages between 3379 ± 26 and 3430 ± 16 Ma, and concordance between 83 and 101%. The regression of these rim analyses suggests the rim domain has undergone recent Pb-loss, and gives a weighted mean $^{207}Pb/^{206}Pb$ age for rim growth is 3396 ± 59 Ma.

Atom Probe Tomography and nanoscale characterization:

Two needle-shaped specimens for atom probe tomography (~100 nm diameter x ~1000 nm long) were taken from the zircon core adjacent to U-Pb analysis 3 (Table 1; Valley et al., 2014, 2015); these two APT data sets resulted in a total of >500 million ions. Each APT data set contains

several hundred sub-spherical trace-element-rich clusters 5-10 nm in diameter, enriched primarily in non-formula-unit elements including Y, REE, and Pb (Valley et al., 2014). In this work, we utilize the *k*th nearest neighbor approach (*k*NN) to characterize short range order in reconstructed data, and to define unique compositional domains. This approach operates on the premise, that for domains containing a higher concentration of a given component (in this case, Y), the distance between neighboring solute ions is smaller than outside of these solute-rich regions (Gault et al., 2012; Larson et al., 2013). This logic extends to higher-order neighbors (first nearest neighbor, second nearest neighbor, *k*th nearest neighbor, etc.) with natural limitations based on the size and solute content of clusters. In the 01JH36-69 data sets, the difference in short range order between the clusters and matrix domains can be well separated using 4^{th} order nearest neighbor relations, though differences in the two compositional domains are readily observed for $k>3$. The *k*NN methods utilized here identify broadly similar sub-regions of the data sets compared to isoconcentration surfaces (Valley et al., 2014), though *k*NN analyses in this study identify a larger total number of clusters (see below). Previous characterization using proxigrams and radial distributions show Y and Pb are strongly co-localized in the 01JH36-69 APT data sets (Valley et al., 2015).

In quantifying Pb signals and $^{207}Pb/^{206}Pb$ ratios, low total counts for both ^{207}Pb and ^{206}Pb on a *per-cluster* basis prevent statistically reliable calculations of $^{207}Pb/^{206}Pb$ for *individual clusters*. Given the compositional and morphological distinctions above, we calculate background and signal levels for both the aggregate cluster data (for comparison with Valley et al., 2014, 2015) and cluster sub-populations. The Pb isotopes occur in the doubly charged state, at 103.0 and 103.5 Da for $^{206}Pb^{2+}$ and $^{207}Pb^{2+}$ respectively. Background counts are based on average counts over the broad range between ~101.5-102.5 Da, and scaled to the range widths

appropriate for the 103.0 and 103.5 Da peaks. Mass spectra from Y clusters possess well-separated peaks at 103.0 and 103.5 Da with good signal to noise; thus, ^{207}Pb and ^{206}Pb signals can be effectively and uniquely identified. Under such circumstances, uncertainties resulting from spectral processing and peak overlaps are considered negligible and the primary source of analytical uncertainty will be counting statistics (Larson et al., 2013; Blum et al., 2018).

RESULTS

Defining clusters within the 01JH36-69 APT data sets using the *k*NN technique results in a total of 582 individual clusters (including partial clusters on the edge of the data sets) between the two data sets. The difference in total cluster count between this work and Valley et al. (2014) (n ~ 400) derives from differing approaches to cluster definitions (isoconcentration surfaces vs. *k*NN distributions) with the smaller cluster counts resulting from the more restrictive criteria in defining trace-element rich domains (using a >3 at. % Y isoconcentration threshold). Thus, significantly Y-enriched clusters with less than 3 at. % Y will not be identified by the 3% isoconcentration surface algorithm. Despite the ~30% difference in total cluster count, visual inspection and bulk ^{207}Pb/^{206}Pb ratios within clusters are compelling evidence that the domains capture similar clustering dynamics as described by Valley et al. (2014, 2015). Pb isotopes within the aggregate cluster population give a ^{207}Pb/^{206}Pb ratio of 1.287 ± 0.12 (2SD). While the total signal levels are higher in this study due to the larger number of clusters, this isotope ratio matches closely the previously calculated ratios (see Table 3 in Valley et al., 2015). The fact that these isotope ratios are directly comparable reinforces that, despite different cluster definitions, the regions of interest between these two studies share the critical isotopic relations of interest.

The presence of two sub-populations of Y-rich clusters was first proposed based on bimodality in cluster volumes (see Fig. 16 in Valley et al., 2015). This hypothesis is further supported here based on a plot of cluster volume vs. Y-content (Fig. 3a), where in Fig. 3a cluster populations have been separated based on a simple dividing line. This results in two cluster populations, with a subequal numbers of larger, more Y-rich clusters (C1, *n*=295), smaller, more Y-poor clusters (C2, *n*=287). Both the C1 and C2 populations are relatively uniformly distributed throughout the two specimens. The same sub-populations are observed in cluster data that exclude partial clusters that intersect the edge of the data sets (not shown). In the following sections, we include "edge clusters" within the cluster data, as assignment of clusters to the appropriate cluster population is sufficiently robust. Looking at the two cluster populations independently, the C1 and C2 populations give dramatically different $^{207}Pb/^{206}Pb$ ratios, with C1 clusters having a $^{207}Pb/^{206}Pb$ ratio of 1.367 ± 0.12 (5688 total Pb ions) and C2 clusters having $^{207}Pb/^{206}Pb$ ratio of 0.891 ± 0.20 (2SD) (912 total Pb ions; Table 2). Both of these ratios are elevated relative to the ratio measured by SIMS (0.5504 ± 0.0038). These data provide additional support to the uniqueness of the two cluster populations; the temporal significance of these data is discussed in the context of cluster age modeling, below.

DISCUSSION

The data for zircon 01JH36-69 described above demonstrate the occurrence of two distinct cluster populations having different cluster composition, and importantly, different $^{207}Pb/^{206}Pb$ ratios. The occurrence of these distinct cluster populations documents two important phenomenon: first, the structural associations controlling cluster formation and preservation are sufficiently robust that clusters can be stabilized over billions of years, and through subsequent

cluster-forming episodes. Second, clusters generate a multidomain chemical space at the nanoscale, with different Pb mobility in the cluster and matrix. Differential retention of Pb within these two domains could result in dramatically different isotope relations during subsequent grain-scale Pb-loss. The first of these points is discussed in the context of zircon 01JH36-69, while modeling of the second phenomenon is outlined and discussed below.

APT constraints on the thermal history of 01JH36-69

Modeling the nanoscale Pb isotope ratios in zircon 01JH36-69 as a function of time requires consideration of several constraints on both the grain scale and nanoscale movement of radiogenic Pb. This includes (1) closed system micron-scale U-Pb (preserved in multiple concordant SIMS analyses from the zircon core) and the well-defined crystallization age of 4374 ± 12 Ma, and (2) the preservation of two distinct cluster populations at the nanoscale, having different $^{207}Pb/^{206}Pb$ ratios. The preservation of compositions in a closed-system on the micron scale provides strong evidence that Pb isotopes within the two cluster populations reflect the temporal pattern of cluster formation, and thus, the distinct $^{207}Pb/^{206}Pb$ ratios reflect two distinct cluster formation episodes within the zircon. As $^{207}Pb/^{206}Pb$ ratios monotonically decrease through time in a zircon (Fig. 3b) higher $^{207}Pb/^{206}Pb$ ratios within the C1 cluster population (1.37 ± 0.12) establish that they formed prior to the C2 clusters (0.89 ± 0.20).

Inferring the relative ages of the C1 and C2 cluster populations, we model the nanoscale $^{207}Pb/^{206}Pb$ evolution of zircon 01JH36-69 based on two clustering episodes. This includes the following general Pb evolution (Fig. 3c):

1. Crystallization at t_1.
2. Homogeneous ingrowth of radiogenic Pb between ages t_1 and t_2.

3. Formation of C1 clusters at some age t_2. Depletion of the matrix in all radiogenic Pb. No bulk (micron scale) movement of Pb.
4. Homogeneous ingrowth of Pb between t_2 and t_3.
5. Formation of C2 clusters within the zircon matrix at some age t_3. Depletion of the matrix in all radiogenic Pb. No bulk (micron scale) movement of Pb.
6. Homogeneous ingrowth of Pb between t_3 and the present.

We extract a cluster model age for the C1 cluster population based on a simple $^{207}Pb/^{206}Pb$ ($R_{7/6}$) evolution from time t_1 = (4374 Ma), identical to previous approaches (Blum et al., 2018):

$$R_{7/6}(t_1, t) = \left(\frac{^{207}Pb}{^{206}Pb}\right)_{1,t} = \left(\frac{^{235}U}{^{238}U}\right)_1 \left(\frac{1 - \exp(-\lambda_{235}(t_1 - t))}{1 - \exp(-\lambda_{238}(t_1 - t))}\right) \quad [1]$$

This yields a C1-cluster model age of 3770 Ma (+230/-260 Ma, 2SD) (Fig. 3b). This is significantly older than the previously proposed clustering age of ~3.4 Ga and is a direct consequence of the discovery that there are two cluster generations. Any mixing with subsequently formed Pb will lower the $^{207}Pb/^{206}Pb$ ratio of C1 clusters, and thus this high ratio is a testament to both cluster formation in the early Archean, and quantitative retention of Pb over the subsequent ~3.8 billion years.

Sequestering radiogenic Pb within the C1 cluster population effectively removes the pre-3.77 Ga radiogenic Pb from the matrix, and thus subsequent evolution of the matrix and cluster formation is considered without the pre-3.77 Ga component. We can model the subsequent ingrowth of Pb outside of the C1 clusters, with the $^{207}Pb/^{206}Pb$ ratio of this region following eqn. 1, but an initial age of starting age of 3770 Ma (i.e., the formation of the C1 cluster population).

The formation of C2 clusters from this region will preserve the $^{207}Pb/^{206}Pb$ ratio since 3770 Ma, and yields a cluster age of 3360 Ma (+410/-720 Ma, 2SD), which correlates well with both (1) the rim formation age determined by SIMS, and (2) previous estimate for the cluster formation age based on aggregating APT data from all clusters (C1 and C2).

The similarity in model ages for the C2 population and for the aggregated one-population model (Valley et al., 2014) can be understood in terms of the Pb behavior leading up to 3.4 Ga. Valley et al., (2014, 2015) modeled all clusters as a single population, assuming that the radiogenic Pb accumulated between crystallization (~4.4 Ga) and cluster formation (~3.4 Ga) partitions into clusters with an average measured ratio of ~1.2. Because both Valley et al. (2014, 2015) and the model above assume complete partitioning of Pb into clusters during their formation, both the single and double clustering models have an aggregate cluster population which contains all pre-3.4 Ga Pb. In modeling two clustering episodes, this process is completed in two steps, however the $^{207}Pb/^{206}Pb$ ratio within all the clusters will still reflect the clustering of all pre-3.4 Ga Pb. This result is useful, as it emphasizes the bulk APT specimen has remained a closed U-Pb system, and (2) suggests Pb has indeed partitioned completely into clusters during each high temperature episode, an assumption in application of eqn. 1. This result also implies that, as long as Pb has completely partitioned into clusters leading up to a final clustering episode, aggregate $^{207}Pb/^{206}Pb$ ratio of clusters within a data set should represent the youngest Pb clustering episode in the zircon history, even if older and younger events cannot be statistically resolved.

Zircon geochronology and cluster modeling:

The observation that cluster isotope ratios can be preserved through distinct periods of metamorphism has significant implications for the broader understanding of Pb migration and age discordance, particularly within ancient zircon grains. Figs. 4a and 4b show the general isotope relations through time for the closed system evolution any zircon grain. The ingrowth curves terminate at present-day $^{207}Pb/^{206}Pb$ and $^{238}U/^{206}Pb$ values for concordant U-Pb analyses. The interpretation of discordance has followed from prediction of how $^{207}Pb/^{206}Pb$, $^{238}U/^{206}Pb$ (or $^{206}Pb/^{238}U$ and $^{207}Pb/^{235}U$) ratios will respond during bulk Pb-loss (i.e., Pb-loss on the micron-scale or greater, such that the zircon is no longer a closed system on the scale of typical U-Pb SIMS analysis). It is traditionally assumed that both ^{207}Pb and ^{206}Pb isotopes will be affected proportionally, while U and Th remain immobile. On a Tera-Wasserburg diagram, this results in a horizontal translation of ancestral isotope ratios away from the closed system ingrowth curve, with the translation being proportional to the fractional mass of Pb lost during the Pb-loss event (Fig. 4c). Following a clustering event, Pb ingrowth will follow a new trajectory, terminating on a cord (a discordia) with an upper intercept at the time of crystallization, and a lower intercept at the time of Pb-loss (Fig. 4d). This represents "mixing" between domains that share a common crystallization and Pb-loss history, but have varying degrees of Pb-loss.

This model is powerful for understanding zircon crystallization and thermal history however, it assumes that all Pb behaves identically throughout the zircon. The discovery that a zircon preserves multiple generations of clusters (above) contributes to a growing body of evidence that the Pb isotope ratios in these nanoscale domains are stable over geological timescales, which in turn implies these clusters (and their underlying structure) are "stable," even during subsequent metamorphism. As a result, these nanoscale domains create a multidomain structure, where Pb in different regions (having different $^{207}Pb/^{206}Pb$ ratios) may be retained

during subsequent Pb-loss. Such situations require incorporation of additional complexity into Pb-loss modeling to predict bulk (micron-scale) U-Pb isotope systematics.

Modeling Clustering and Pb-Loss:

In order to better quantify the influence of scale-dependent U-Pb behavior during Pb-loss, we compare the U-Pb evolution for two general Pb-loss scenarios (unrelated to 01JH36-69): (1) Pb-loss assuming no clustering ("scenario 1"), and (2) Pb-loss assuming some radiogenic Pb component is locked within clusters ("scenario 2"). In both cases, U is assumed to be immobile and Pb-loss refers to the migration of Pb out of micron scale domains (i.e., SIMS analysis or larger) without isotope fractionation. The first scenario follows a simple Pb-loss history including:

1. Crystallization at some age, t_1.
2. Pb-loss from the matrix at some age t_L, with *retention* of a mass fraction of f_L.
3. Homogeneous ingrowth of Pb between t_L and the present

We utilize the convention that *t* is time before present, as it is often the preferred convention in interpreting geological events. In this first scenario, the cumulative $^{207}Pb/^{206}Pb$ ratio at time $t>t_L$, will follow eqn. 1 above, while the $^{206}Pb/^{238}U$ ratios for $t>t_L$ (i.e., t between crystallization at t_1 and reheating at t_L) are given by:

$$R_{6/8}(t_1, t) = \left(\frac{^{206}Pb}{^{238}U}\right)_{1,t} = \exp\left(\lambda_{238}(t_1 - t)\right) - 1 \qquad [2]$$

Because all Pb is assumed mobile in scenario 1, Pb-loss will not affect the bulk $^{207}Pb/^{206}Pb$ ratio during Pb-loss but will influence the $^{238}U/^{206}Pb$ ratio. The result is an "instantaneous" shift horizontally to the right at $t=t_L$ (Fig. 4c). For $t<t_L$ (i.e., after Pb-loss) the $^{207}Pb/^{206}Pb$ and $^{238}U/^{206}Pb$ ratios in the bulk material can be calculated based on the mixing relations:

$$\frac{^{207}Pb}{^{206}Pb} = X_{1,L}(t)\, R_{7/6}(t_1, t_L) + \left[1 - X_{1,L}(t)\right] R_{7/6}(t_L, t) \quad [3]$$

$$\frac{^{206}Pb}{^{238}U} = f_L R_{6/8}(t_1, t_L)[\exp(\lambda_{238}(t_L - t))] + R_{6/8}(t_L, t) \quad [4]$$

Where f_L is the fraction of ^{206}Pb *remaining* after Pb-loss, and $X_{1,2}(t)$ is the normalized fraction of ^{206}Pb at any time $t<t_2$ originating from the time interval t_1 to t_2:

$$^{206}X_{1,L} = {}^{206}X(t_1, t_L) = \left(\frac{1 - \exp(-\lambda_{235}(t_1 - t_L))}{1 - \exp(-\lambda_{238}(t_1))}\right) \quad [5]$$

$$^{206}X_{1,L}(t) = \frac{f_L\, ^{206}X_{1,L}}{f_L\, ^{206}X_{1,L} + (^{206}X_{1,t} - {}^{206}X_{1,L})} \quad [6]$$

Eqns. 5 and 6 give relative normalized ^{206}Pb concentrations in order to avoid calculations with arbitrary U concentration inputs. We note that the exponential in the first term of the righthand side of eqn. 4 effectively corrects the $^{206}Pb/^{238}U$ ratio at t_L (after Pb-loss) for subsequent decay of ^{238}U (between t_L and $t<t_L$).

The evolution of the U-Pb isotope ratios can be observed in Fig. 4c and 4d. As described above, (Pb-loss $t=t_L$ with no clustering) Pb ingrowth proceeds until t_L, at which point the Pb-ingrowth curve shifts horizontally proportional to the fraction of Pb lost. This shift leaves the bulk $^{207}Pb/^{206}Pb$ ratio unchanged, but induces an "instantaneous" increase in the $^{238}U/^{206}Pb$ ratio.

Subsequent ingrowth proceeds to the present, terminating on a discordia between the concordia points corresponding to closed system U-Pb evolution t_1 and t_L; in Fig. 4c and 4d, t_1 = 4.4 Ga, and t_L = 3.0 Ga. We have assumed no common-Pb in this model, and as a result, the *y*-intercept of the discordia regression will give the $^{207}Pb/^{206}Pb$ ratio at the time of Pb-loss (Fig. 4d).

In accounting for nanoscale clustering (scenario 2), we incorporate additional complexity, including clustering at some time t_2 (without micron-scale Pb-loss), and subsequent Pb-loss at time t_L:

1. Crystallization at some age, t_1.
2. Homogeneous ingrowth of Pb between t_1 and t_2.
3. Clustering of all available radiogenic Pb into a cluster volume fraction of f_c at some age t_2. No larger micron-scale movement of Pb. No movement of U.
4. Homogeneous ingrowth of Pb between t_2 and t_L.
5. Pb loss from the zircon matrix at some age t_L, with retention of a mass fraction of f_L. (All matrix Pb is ingrown between t_2 and t_L).
6. Homogeneous ingrowth of Pb between t_L and the present.

The initial $^{207}Pb/^{206}Pb$ and $^{206}Pb/^{238}U$ evolution between t_1 and t_2 will follow an identical trend to that of scenario 1 (eqns. 1 and 2). At time t=t_2, all Pb migrates into clusters having a volume fraction f_c. At this point, the matrix becomes devoid of Pb, while the $^{207}Pb/^{206}Pb$ and $^{206}Pb/^{238}U$ ratios of clusters at time t_2 are given by eqns. 1 and 2 above (setting t=t_2). The relative ^{206}Pb enrichment within clusters is given by:

$$^{206}X_{1,2}^{c} = f_c^{-1}\ ^{206}X_{1,2} \qquad [7]$$

Where $^{206}X_{1,2}$ is given by eqn. 5 above. We assume no Pb-loss on the micron scale at t_2, and thus the *bulk* $^{207}Pb/^{206}Pb$ and $^{206}Pb/^{238}U$ ratios for $t_2>t>t_L$ will continue to follow eqns. 1 and 2. The isotopic evolution of the matrix domains in this same time interval will follow from:

$$^{206}X^{m}_{2,t} = {}^{206}X^{m}(t_2, t) = {}^{206}X_1(t) - {}^{206}X_{1,2} \quad [8]$$

$$R^{m}_{7/6}(t) = \left(\frac{^{207}Pb}{^{206}Pb}\right)^{m}_{2,t} = \left(\frac{^{235}U}{^{238}U}\right)_2 \left(\frac{1-\exp(-\lambda_{235}(t_2-t))}{1-\exp(-\lambda_{238}(t_2-t))}\right) \quad [9]$$

$$R^{m}_{6/8}(t) = \left(\frac{^{206}Pb}{^{238}U}\right)^{m}_{2,t} = \exp\left(\lambda_{238}(t_2-t)\right) - 1 \quad [10]$$

Where the "*m*" superscript denotes "matrix," and the subscript assignments in eqn. 8 denote the normalized component of ^{206}Pb accumulated between t_2 and any subsequent time, $t_2>t>t_L$. The related equations for cluster domains (identified by the superscript *c*) for times $t_2>t>t_L$ are given by:

$$^{206}X^{c}_{1,2}(t) = \frac{^{206}X^{c}_{1,2}}{^{206}X^{c}_{1,2} + {}^{206}X^{m}_{2,t}} \quad [11]$$

$$R^{c}_{7/6}(t) = \left(\frac{^{207}Pb}{^{206}Pb}\right)^{c}_{t} = {}^{206}X^{c}_{1,2}(t) \times R_{7/6}(t_1, t_2) + {}^{206}X^{m}_{2,t} \times R_{7/6}(t_2, t) \quad [12]$$

$$R^{c}_{6/8}(t) = \left(\frac{^{206}Pb}{^{238}U}\right)^{c}_{t} = f_c^{-1}\, R_{6/8}(t_1, t_2)\left[\exp\left(\lambda_{238}(t_2-t)\right)\right] + R_{6/8}(t_2, t) \quad [13]$$

Where eqn. 11 gives the normalized component of ^{206}Pb in clusters originating from between time t_1 and t_2, while accounting for subsequent ingrowth of Pb between t_2 and t.

At time t=t_L in scenario 2, Pb-loss occurs. The model treats Pb-clusters as perfectly retentive of Pb, and thus Pb-loss only affects Pb in the matrix region. For t<t_L, the relevant mixing relations for the matrix are:

$$^{206}X_T^m(t) = f_L\ ^{206}X_{2,L} + (^{206}X_{1,t} - ^{206}X_{1,L}) \quad [14]$$

$$^{206}X_{2,L}^m(t) = \frac{f_L\ ^{206}X_{2,L}^m}{^{206}X_T^m(t)} \quad [15]$$

$$R_{7/6}^m(t) = \left(\frac{^{207}Pb}{^{206}Pb}\right)_t^m = {}^{206}X_{2,L}^m(t) \times R_{7/6}(t_2, t_L) + (1 - {}^{206}X_{2,L}^m(t)) \times R_{7/6}(t_L, t) \quad [16]$$

$$R_{6/8}^m(t) = \left(\frac{^{206}Pb}{^{238}U}\right)_t^m = f_L\ R_{6/8}(t_2, t_L)\left[\exp\left(\lambda_{238}(t_L - t)\right)\right] + R_{6/8}(t_L, t) \quad [17]$$

For clusters, we assume that Pb ingrowth between t_2 and t_L is fully retained, and thus the mixing relations for clusters become:

$$^{206}X_T^c(t) = f_c^{-1}\ ^{206}X_{1,2} + {}^{206}X_{2,L} + (^{206}X_{1,t} - {}^{206}X_{1,L}) \quad [18]$$

$$^{206}X_{1,2}^c(t) = \frac{f_c^{-1}\ ^{206}X_{1,2}}{^{206}X_T^c(t)} \quad [19]$$

$$^{206}X_{2,L}^c(t) = \frac{^{206}X_{2,L}}{^{206}X_T^c(t)} \quad [20]$$

$$^{206}X_{L,t}^c = \frac{(^{206}X_{1,t} - {}^{206}X_{1,L})}{^{206}X_T^c(t)} \quad [21]$$

$$R^{c}_{7/6}(t) = \left(\frac{^{207}Pb}{^{206}Pb}\right)^{c}_{t} = {}^{206}X^{c}_{1,2}(t)\, R_{7/6}(t_1, t_2) + {}^{206}X^{c}_{2,L}(t)\, R_{7/6}(t_2, t_L) + {}^{206}X^{c}_{L,t}\, R_{7/6}(t_L, t) \quad [22]$$

$$R^{c}_{6/8}(t) = \left(\frac{^{206}Pb}{^{238}U}\right)^{c}_{t} = f_c^{-1}\, R_{6/8}(t_1, t_2)\left[\exp\left(\lambda_{238}(t_2 - t)\right)\right] + R_{6/8}(t_2, t) \quad [23]$$

Finally, the $^{207}Pb/^{206}Pb$ and $^{206}Pb/^{238}U$ relations for the bulk can be constructed from appropriate mixing of the clustered and matrix domains:

$${}^{206}X^{b}_{T}(t) = {}^{206}X_{1,2} + f_L(1 - f_c){}^{206}X_{2,L} + f_c\,{}^{206}X_{2,L} + ({}^{206}X_{1,t} - {}^{206}X_{1,L}) \quad [24]$$

$${}^{206}X^{b}_{1,2}(t) = \frac{^{206}X_{1,2}}{^{206}X^{b}_{T}(t)} \quad [25]$$

$${}^{206}X^{bm}_{2,L}(t) = \frac{f_L(1 - f_c)^{206}X_{2,L}}{^{206}X^{b}_{T}(t)} \quad [26]$$

$${}^{206}X^{bc}_{2,L}(t) = \frac{f_c\,^{206}X_{2,L}}{^{206}X^{b}_{T}(t)} \quad [27]$$

$${}^{206}X^{b}_{L,t} = \frac{({}^{206}X_{1,t} - {}^{206}X_{1,L})}{^{206}X^{c}_{T}(t)} \quad [28]$$

$$R^{b}_{7/6}(t) = {}^{206}X^{b}_{1,2}(t)\, R_{7/6}(t_1, t_2) + ({}^{206}X^{bc}_{2,L}(t) + {}^{206}X^{bm}_{2,L}(t))R_{7/6}(t_2, t_L) + {}^{206}X^{b}_{L,t}(t)\, R_{7/6}(t_L, t) \quad [29]$$

$$R^{b}_{6/8}(t) = R_{6/8}(t_1, t_2)\left[\exp\left(\lambda_{238}(t_2 - t)\right)\right] + f_c R_{6/8}(t_2, t_L)\left[\exp\left(\lambda_{238}(t_L - t)\right)\right] + f_L(1 - f_c)\, R_{6/8}(t_2, t_L)\left[\exp\left(\lambda_{238}(t_L - t)\right)\right] + R_{6/8}(t_L, t) \quad [30]$$

To illustrate the influence clustering may have on bulk U-Pb systematics, we construct a forward model for an arbitrary thermal history involving crystallization at t_1 = 4.4 Ga, clustering at t_2 = 4.0 Ga and Pb loss at t_L = 3.0 Ga, a cluster volume fraction of f_c = 0.015, and a ^{206}Pb mass retention of between f_L = 0.5 to 0.05 (this is equivalent to between 50% to 95% ^{206}Pb mass loss). We construct a comparable model for scenario 1, such that t_1 = 4.4 Ga, t_L = 3.0 Ga, and f_L varies from 0.75 to 0.01. Before 3.0 Ga, the bulk ^{207}Pb/^{206}Pb and ^{238}U/^{206}Pb ratios are identical for closed system evolution, simple Pb-loss, and clustered Pb-loss (Fig. 4c and 4d; Fig. 5a and 5b). The influence of clustering at t_2=4.0 Ga in scenario 2 is visible in Fig. 5a. The values of ^{207}Pb/^{206}Pb and ^{238}U/^{206}Pb are shown after clustering for both the clustered (^{238}U/^{206}Pb → 0) and matrix (^{238}U/^{206}Pb → ∞) regions. The difference between the two Pb-loss scenarios (and the influence of clustering) can be seen in the Pb-loss trajectory at t_L=3.0 Ga. In a Tera-Wasserburg diagram, instead of moving horizontally to the right as in scenario 1 (Fig. 4c) the Pb-loss trajectory moves the *bulk* ^{207}Pb/^{206}Pb and ^{238}U/^{206}Pb composition diagonally (black line, up to the right, Fig. 5a); this trajectory forms a regression which projects from the ^{207}Pb/^{206}Pb ratio of the *matrix* at time t_L=3.0 Ga. The presence of ^{207}Pb and ^{206}Pb trapped in clusters places a limit on the maximum displacement of the bulk ^{207}Pb/^{206}Pb and ^{238}U/^{206}Pb ratios along this Pb-loss trajectory; in the limit of f_L→0 (i.e., 100% loss of Pb from the matrix) the bulk ^{207}Pb/^{206}Pb ratio approaches that of the cluster.

Relative to scenario 1, the present-day ^{238}U/^{206}Pb ratios for scenario 2 are systematically smaller, while ^{207}Pb/^{206}Pb ratios are systematically higher for the same f_L; the retention of Pb (having a high ^{207}Pb/^{206}Pb ratio) within clusters limits the total mass of Pb lost and shifts its ratio

during the Pb-loss event. Variability in f_L results in a distinct regression (black dashes, Fig. 5b) relative to that in scenario 1 (dots in Fig. 4d, blue line in Fig. 5b). The lower intercept for the false discordia in scenario 2 (Fig. 5b) does *not* coincide with the age of Pb-loss as the conventional discordia does in scenario 1. In scenario 1, the lower intercept is (correctly) inferred to be the age of Pb-loss; however, the lower intercept for scenario 2 does not possess any age significance. The correct age for Pb loss (3.0 Ga) *can* be reconstructed in scenario 2, using the combination of crystallization age, cluster $^{207}Pb/^{206}Pb$ ratio, and the y-intercept of the pseudo-discordia regression. *The y-intercept of the pseudo-discordia will equal the $^{207}Pb/^{206}Pb$ ratio of the **matrix** at the time of Pb-loss* (Fig. 5b), which can be found using the crystallization age, and cluster isotope ratios. This enables calculation of a cluster formation age, and modeling the subsequent $^{207}Pb/^{206}Pb$ evolution of the matrix (eqn. 9). Importantly, correcting the micron- to grain-scale discordia requires knowledge of U-Pb behavior on the nanoscale, reinforcing the scale-dependent nature of clustered, domain specific Pb loss in scenario 2. It is relevant to note that the geological significance of the upper discordia intercept (i.e., crystallization age) is the same in both scenarios 1 and 2, and thus the scale dependence of U-Pb isotopes do not add additional complexity to discordia-based estimates of crystallization ages.

An additional observation from modeling is that the results of scenario 2 (clustering and domain-specific Pb loss) result in discordant data points, but these points are in closer proximity to the t_1 concordia intercept (age of crystallization) relative to the results of scenario 1. This is a consequence of how the two cluster models are constructed, in that the total mass fraction of Pb lost is systematically different. Scenario 1, without clustering, will lose a higher fraction of Pb accumulated prior to t_L, and as a result, the resulting Pb ingrowth curve terminates closer to the t_L concordia intercept. This captures an additional aspect of domain specific Pb-loss; the retention

of Pb within clusters will result in micron-scale analyses that are closer to concordia and the grain's crystallization age. This is an observation that can be useful in trying to infer or detect scale-dependent behavior; however, the *quantitative* realization of this depends on the exact time-temperature history the grain experienced, as well as the mass fraction of Pb lost.

CONCLUSIONS

The APT data sets for zircon 01JH36-69 preserve the first identification of two cluster generations having distinct $^{207}Pb/^{206}Pb$ ratios, and preserving a record of cluster formation at two distinct times in the past. These data reinforce the interpretations that nanoscale clusters preserve $^{207}Pb/^{206}Pb$ ratios over geological timescales, and can retain isotope signatures associated with their formation, even through subsequent thermal episodes. This suggests that clustering phenomena preserve unique information about the thermal conditions experienced through time, and that clustering at the nanoscale can aid retention of daughter isotopes, and preservation of concordant U-Pb behavior on the micron-scale.

In addition, these data suggest that retention of Pb within clusters through subsequent thermal episodes can invalidate the general assumptions used in interpreting isotope systematics during Pb-loss. The modeling of this more general case of open system behavior enables predictions about the temporal and structural information preserved in clusters, and suggests that scale-dependent U-Pb behavior above can contribute to the complex U-Pb systematics observed in ancient zircons. Importantly, the combination of multiscale U-Pb characterization affords unique means to correct and extract cryptic information. APT and correlative microscopies present a novel means to better understand this behavior, while extracting cryptic records from zircon grains with complex thermal and structural histories.

ACKNOWLEDGEMENTS

We thank Brian Hess, for his aid and attention in preparing valuable zircon samples. This research was funded by the US National Science Foundation (EAR-1144454, EAR-1524336), and the US Department of Energy, Office of Basic Energy Sciences, Geosciences Division under award number DE-FG02-93ER14389. WiscSIMS is supported by NSF (EAR-1355590, -1658823) and UW-Madison. The authors acknowledge the use of facilities supported by the University of Wisconsin, College of Engineering and the Materials Research and Engineering Center (NSF DMR-121288) and Nanoscale Science and Engineering Center (NSF DMR-0832760).

REFERENCES

Blum, T.B., Reinhard, D.A., Chen, Y., Prosa, T.J., Larson, D.J., Valley, J.W. (2018) Uncertainty and sensitivity analysis for spatial and spectral processing of Pb-Pb geochronology by atom probe tomography, in Microstructural Geochronology: Planetary Records Down to Atom Scale, edited by D.E. Moser, F. Corfu, S.M. Reddy, J.R. Darling, and K. Tait, John Wiley & Sons, Inc., Hoboken, NJ, 232, 327–349.

Cavosie, A.J., Wilde, S.A., Liu, D., Weiblen, P.W., Valley, J.W. (2004) Internal zoning and U-Th-Pb chemistry of Jack Hills detrital zircons: a mineral record of early Archean to Mesoproterozoic (4348-1576 Ma) magmatism. Precambrian Research, 135, 251-279.

Cavosie, A.J. (2005) Geochemistry of greater than 3900 Ma detrital zircons from Jack Hills, Western Australia. University of Wisconsin-Madison, Doctoral Thesis.

Cavosie, A.J., Valley, J.W., Wilde, S.A., E.I.M.F. (2006) Correlated microanalysis of zircon: Trace element, $\delta^{18}O$, and U-Th-Pb isotopic constrains on the igneous origin of complex >3900 Ma detrital grains, Geochimica et Cosmochimica Acta, 70, 5601-5616.

Cavosie, A.J., Valley, J.W., Wilde, S.A. (2019) The Oldest Terrestrial Mineral Record: Thirty Years of Research on the Hadean Zircon From Jack Hills, Western Australia. *In* The Oldest Rocks (Second Edition), edited by Van Kranendonk, M., Bennett, V., Hoffmann, E., Elsevier, 255-278.

Cherniak, D.J., Lanford, W.A., Ryerson, F.J. (1991) Lead diffusion in apatite and zircon using ion implantation and Rutherford Backscattering techniques, Geochimica et Cosmochimica Acta, 55, 1663-1673.

Cherniak, D.J., Watson, E.B. (2003) Diffusion in zircon, Reviews in Mineralogy and Geochemistry, 53, 113-143.

Chen, Y., Chou, P.H., Marquis, E.A. (2014) Quantitative atom probe tomography characterization of microstructures in a proton irradiated 304 stainless steel, Journal of Nuclear Materials, 451, 130-136.

Ewing, R.C., Meldrum, A., Wang, L., Weber, W.J., Corrales, L.R. (2003) Radiation effects in zircon. Reviews in Mineralogy and Geochemistry, 53, 387-425.

Gault, B., Moody, M.P., Cairney, J.M., Ringer, S. (2012) Atom Probe Microscopy, 396 p. Springer.

Gedcke, D.A. (2001) How counting statistics control detection limits and peak precision. ORTEC Application Note AN59.

Ketcham, R.A., Guenthner, W.R., Reiners, P.W. (2013) Geometric analysis of radiation damage connectivity in zircon, and its implications for helium diffusion. American Mineralogist, 98, 350-360.

La Fontaine A., Piazolo, S., Trimby, P., Yang, L., Cairney, J.M. (2017) Laser-Assisted Atom Probe Tomography of Deformed Minerals: A Zircon Case Study. Microscopy and Microanalysis, 23, 404-413.

Larson, D.L., Prosa, T.J., Ulfig, R.M., Geiser, B.P., Kelly, T.F. (2013) Local Electrode Atom Probe: A User's Guide. Springer. 318 p.

Nasdala, L., Wenzel, M., Vavra, G., Irmer, G., Wenzel, T., Kober, B. (2001) Metamictization of natural zircon: accumulation versus thermal annealing of radioactivity-induced damage, Contributions to Mineralogy and Petrology, 141, 125-144.

Peterman, E.M., Reddy, S.M., Saxey, D.W., Snoeyenbos, D.R., Rickard, W.D.A., Fougerouse, E.M., Kylander-Clark A.R.C., (2016) Nanogeochronology of discordant zircon measured by atom probe microscopy of Pb-enriched dislocation loops, Science Advances, 2, e1601318.

Piazolo, S., La Fontaine, A., Trimby, P., Harley, S., Yang, L., Armstrong, R., Cairney, J.M. (2016) Deformation-induced trace element redistribution in zircon revealed using atom probe tomography, Nature Communications, 7, 10490.

Reddy, S.M., Riessen, A., Saxey, D.W., Johnson, T.E., Rickard, W.D.A., Fougerouse, D., Fisher, S., Prosa, T.J., Rice, K.P., Reinhard, D.A., Chen, Y., Olson, D. (2016) Mechanisms of deformation-induced trace element migration in zircon resolved by atom probe tomography and correlative microscopy. Geochimica et Cosmochimica Acta, 195, 158-170.

Valley, J.W., Lackey, J.S., Cavosie, A.J., Clechenko, C.C., Spicuzza, M.J., Basei, A.S., Bindeman, I.N., Ferreira, V.P., Sial, A.N., King, E.M., Peck, W.H., Sinha, A.K., Wei, C.S. (2005) 4.4 billion years of crustal maturation: oxygen isotope ratios of magmatic zircon, Contributions to Mineralogy and Petrology, 150, 561-580.

Valley J.W., Cavosie, A.J., Ushikubo, T., Reinhard, D.A., Lawrence, D.F., Larson, D.J., Clifton, P.H., Kelly, T.F., Wilde, S.A., Moser, D.E., Spicuzza, M.J. (2014) Hadean age for post-magma-ocean zircon confirmed by atom probe tomography, Nature Geoscience, 7, 219-223.

Valley, J.W. Reinhard, D.A., Cavosie, A.J., Ushikubo, T., Lawrence, D.F., Larson, D.J., Kelly, T.F., Snoeyenbos, D.R., Strickland, A. (2015) Nano- and Micro-geochronology in Hadean and Archean zircons by atom-probe tomography and SIMS: New tools for old minerals, American Mineralogist, 100, 1355-1377.

Wang, Q., Wilde, S.A. (2018) New constraints on the Hadean to Proterozoic history of the Jack Hills belt, Western Australia. Gondwana Research, 55, 74-91.

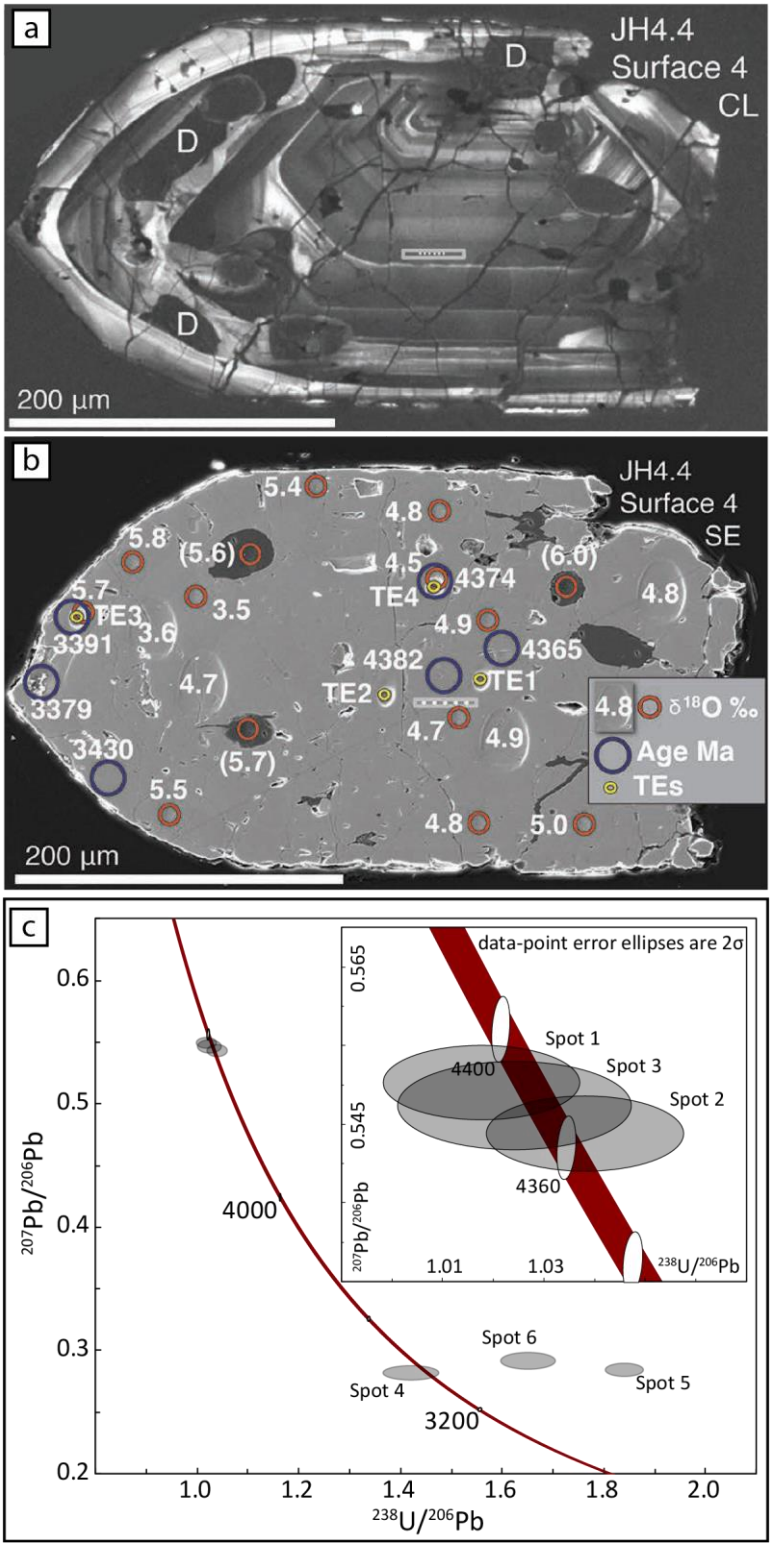

Figure 1: Imaging and geochronology for zircon 01JH36-69, after Valley et al. (2014, 2015). (a) Cathodoluminescence image, showing internal zonation. Rectangular region marks the location of the APT lift-out, while "D" denotes "damaged" domains. (b) secondary electron imaging summarizing in situ analyses for $\delta^{18}O$, trace elements, and U-Pb ages. (c). Inverse concordia diagram for U-Pb geochronology; see Table 1.

Figure 2 (on the following 2 pages): Summary of 3-D maps of Y and Pb atom probe data projected onto a plane for zircon 01JH36-69. The smallest dots are single atoms. Also shown are the clustered domains C1 and C2. Note that the two right-most panels show all ions within the C1 and C2 clusters, not only Y ions. Clusters were identified based on the 4^{th} order kNN distributions for Y (see text for details).

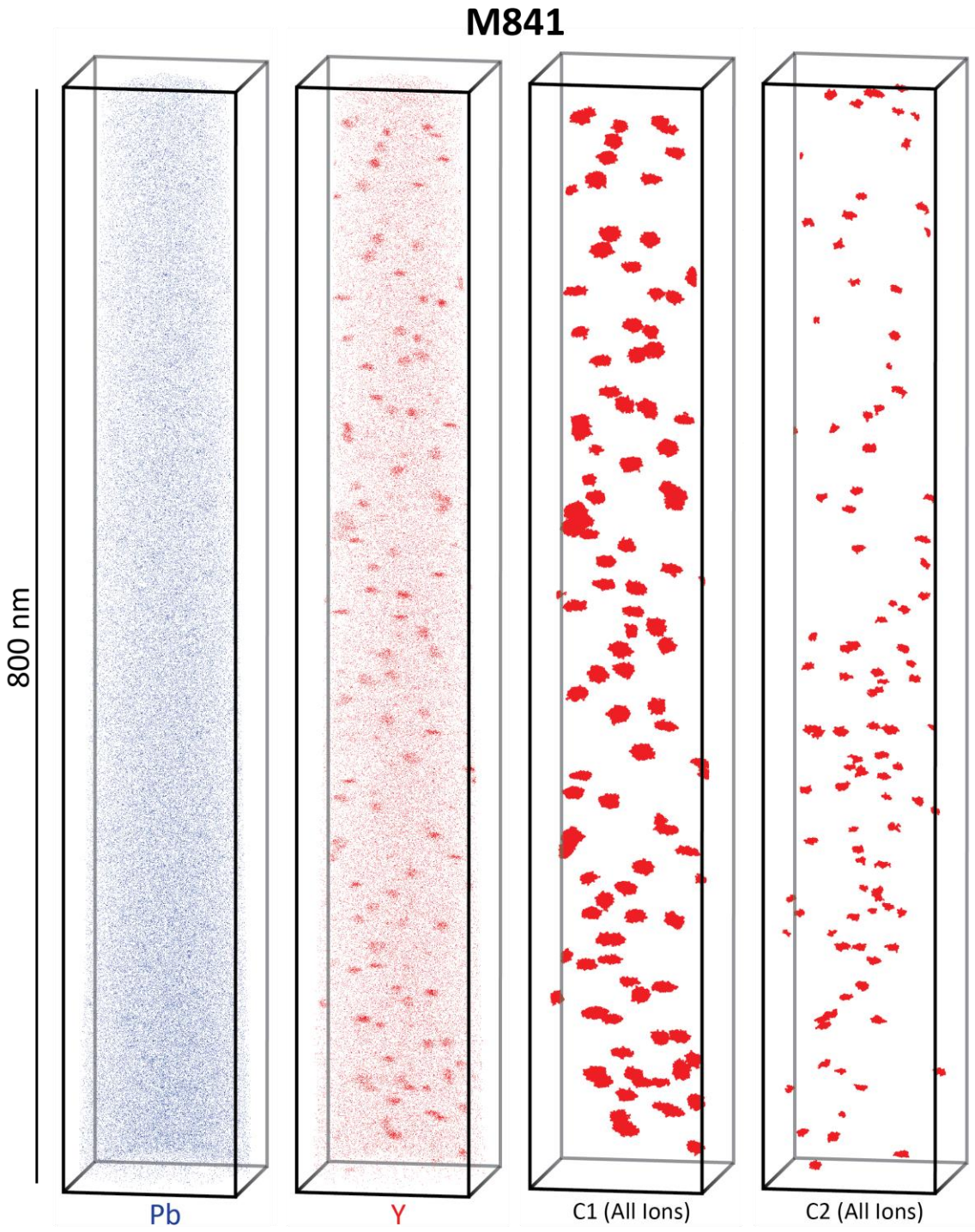
M841
800 nm
Pb
Y
C1 (All Ions)
C2 (All Ions)

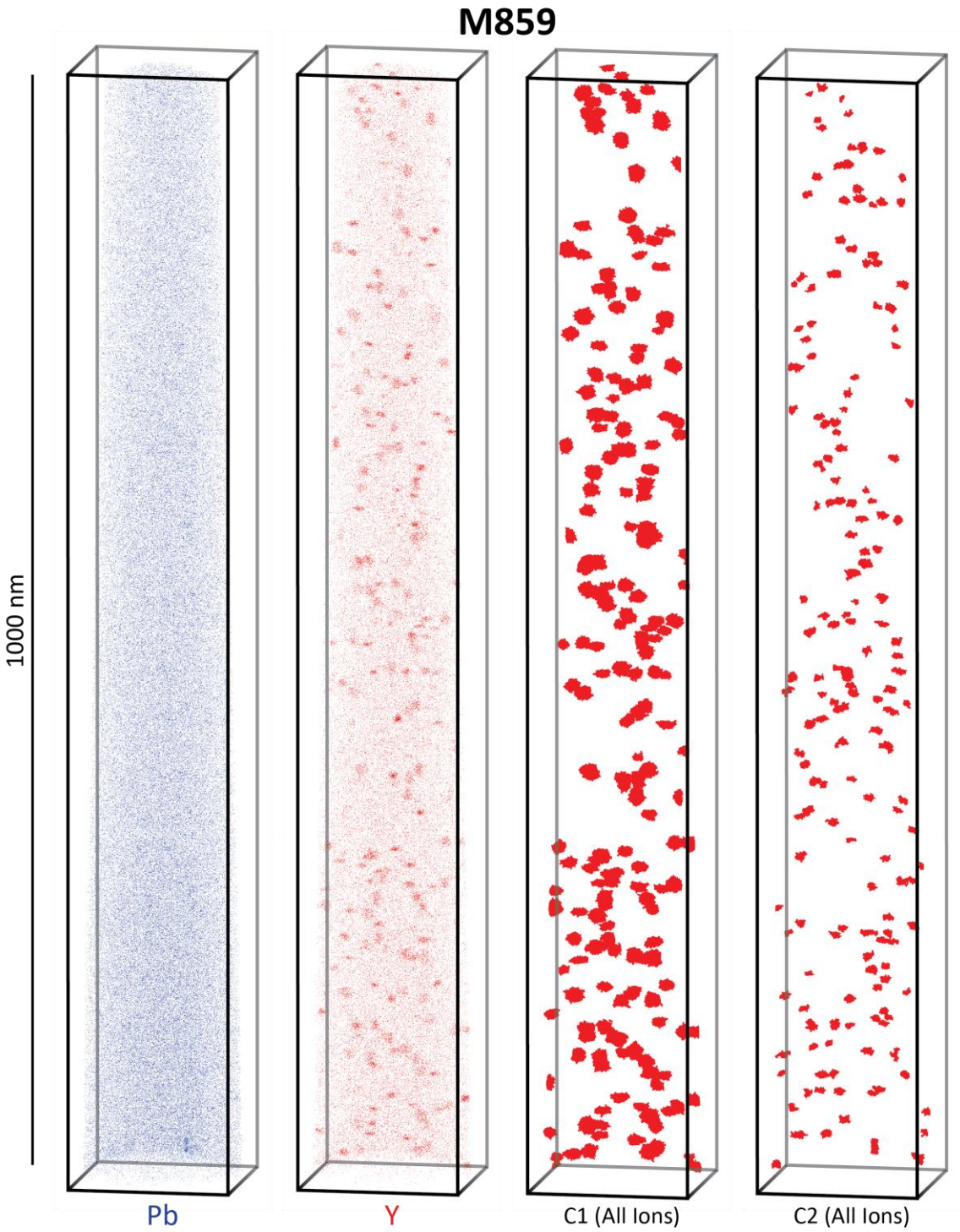
M859
1000 nm
Pb
Y
C1 (All Ions)
C2 (All Ions)

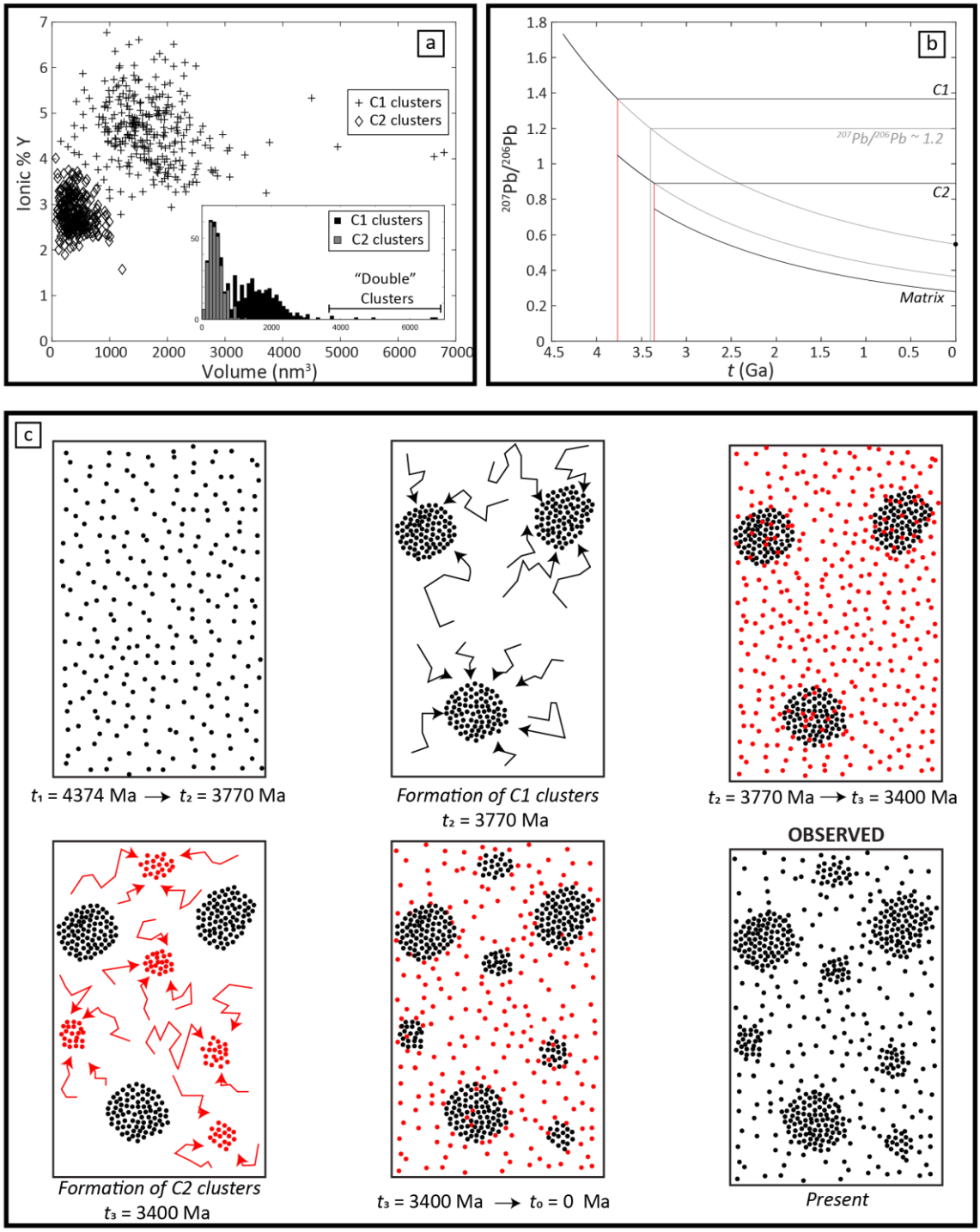

Figure 3: Summary of clustering within zircon 01JH36-69. (a) Y vs. cluster volume showing the C1 and C2 cluster populations. Inset shows histogram of cluster volumes. (b) cluster age modeling for the C1 and C2 cluster populations. The bulk cluster ratio of $^{207}Pb/^{206}Pb \approx 1.2$ (Valley et al., 2015) is included. (c) schematic representation of Pb atoms, Pb ingrowth, and Pb clustering in zircon 01JH36-69. C1 clusters form at 3770 Ma (black dots) and C2 clusters form at 3400 Ma (red dots).

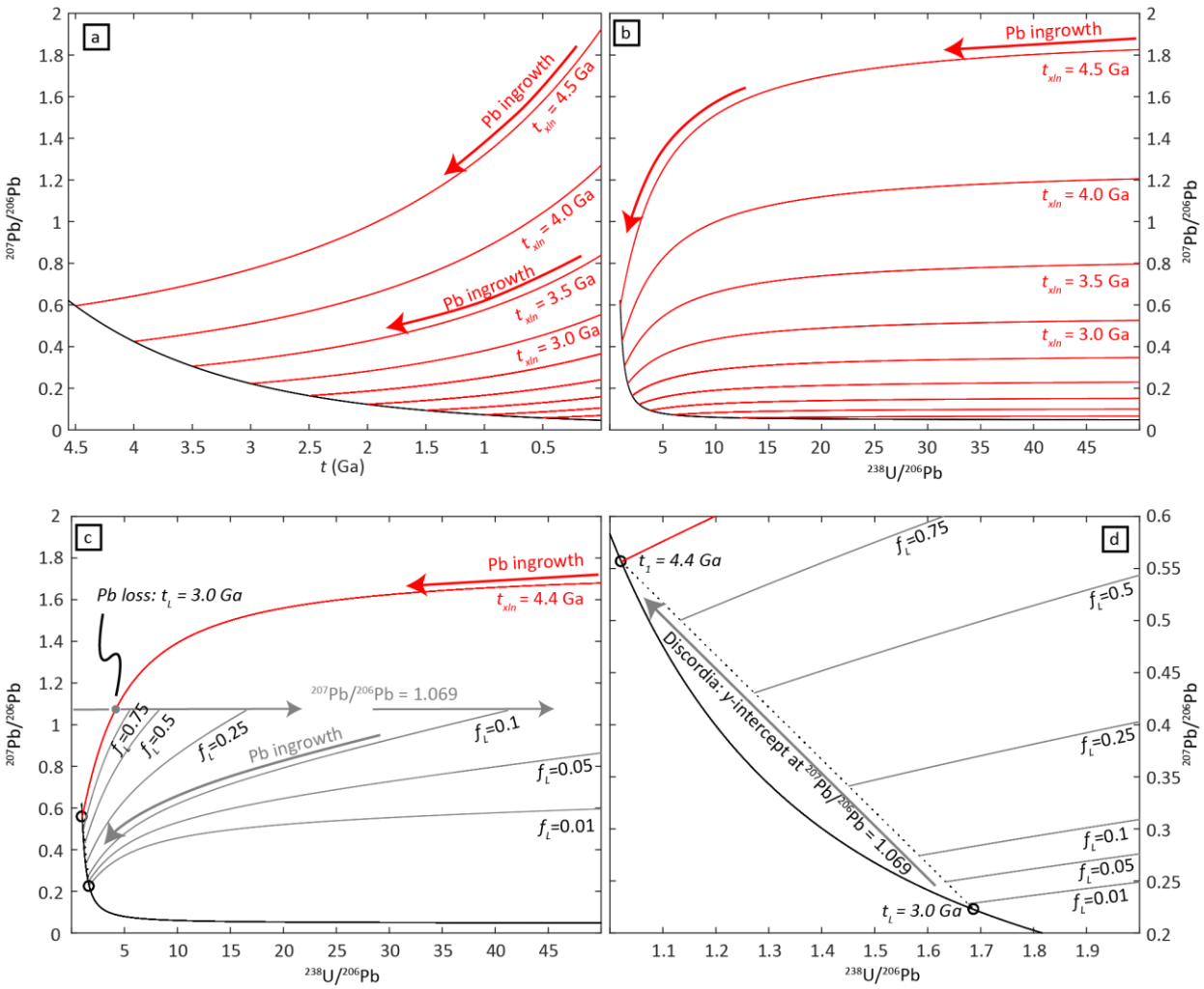

Figure 4: (a-b) $^{207}Pb/^{206}Pb$ ingrowth and $^{238}U/^{206}Pb$ evolution, showing the trajectory for bulk ingrowth of Pb beginning at different crystallization ages (t_{xln}). (c) $^{207}Pb/^{206}Pb$ and $^{238}U/^{206}Pb$ systematics for bulk Pb loss for a 4.4 Ga zircon at 3.0 Ga (no clustering, scenario 1). (d) closer view of concordia showing the crystallization age, age of Pb loss, and the discordia formed due to variable amounts of Pb-loss (no clustering, scenario 1).

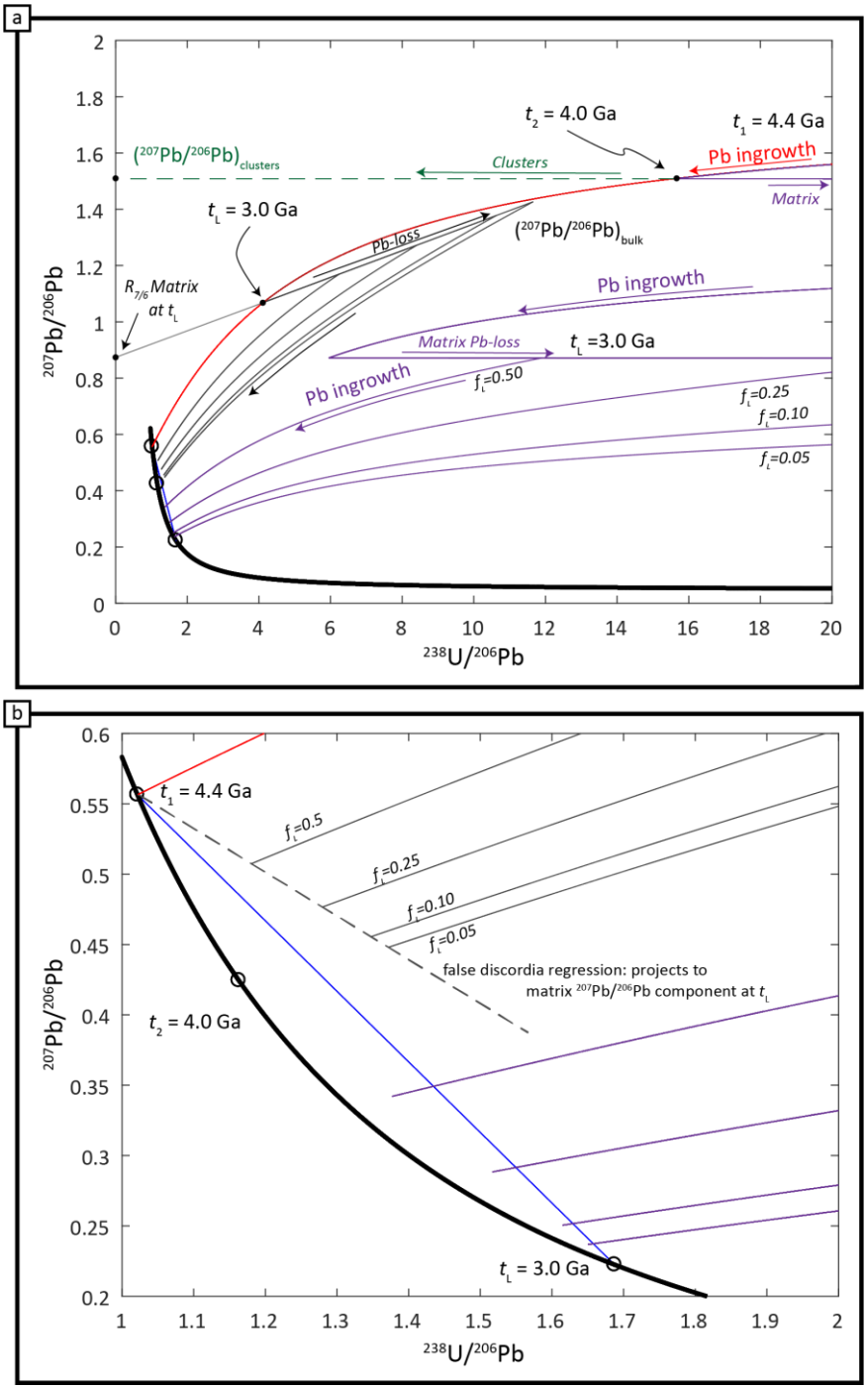

Figure 5: Modeling of the scale-dependent U-Pb evolution of a zircon during clustering, and subsequent Pb-loss. Model assumes a crystallization age of 4.4 Ga, clustering at 4.0 Ga, and Pb loss at 3.0 Ga (see text for further details). (a) Pb ingrowth, clustering, and Pb-loss curves in clustered domains (green), the bulk zircon (black), and matrix (purple) domains (see text for further details). The cluster volume fraction is set to 0.015. (b) Close-up view of concordia, showing a traditional discordia in blue, along with the formation of a false discordia, (dashed line); the projection of the false discordia corresponds to the matrix $^{207}Pb/^{206}Pb$ at 3.0 Ga (see Fig. 5a).

Table 1: Summary of U-Pb SIMS analyses for zircon 01JH36-69. Data are from Valley et al., (2014)

Spot	Domain	U (µg/g)	Th (µg/g)	Th/U	$^{204}Pb/^{206}Pb$	1σ	$^{207}Pb^*/^{206}Pb^*$	1σ	$^{207}Pb^*/^{235}U$	1σ	$^{206}Pb^*/^{238}U$	1σ	ρ	$^{207}Pb^*/^{206}Pb^*$ Age (Ma)	1σ (Ma)
1	core	140	92	0.68	0.00002	45.58	0.55039	0.35	74.57	0.86	0.9826	0.78	0.9111	4382	5
2	core	138	95	0.71	0.00007	28.94	0.54389	0.36	72.23	0.85	0.9632	0.77	0.9074	4365	5
3	core	93	66	0.74	0.00010	9.31	0.54745	0.42	73.69	1.02	0.9763	0.92	0.9086	4374	6
4	rim	61	16	0.27	0.00027	25.82	0.28282	0.83	27.46	1.80	0.7041	1.59	0.8859	3379	13
5	rim	119	189	1.64	0.00061	14.59	0.28505	0.78	21.36	1.15	0.5435	0.85	0.7372	3391	12
6	rim	58	43	0.77	0.00036	26.73	0.29235	1.00	24.42	1.66	0.6058	1.33	0.7983	3430	16

*indicates ^{204}Pb corrected radiogenic Pb.
errors are 1σ (%) unless otherwise specified.

Table 2: Summary of Pb isotope data for $^{206}Pb^{2+}$ and $^{207}Pb^{2+}$ within Y clusters in for the combined data sets M841 and M859.

Cluster Population	*n*	^{206}T	^{206}B	^{206}S	^{207}T	^{207}B	^{207}S	$^{207}Pb/^{206}Pb$	±2σ	Cluster Model Age (Ma)	±2σ
C1	295	4844	2441.0	2403.0	5726	2441.1	3285.0	1.367	0.12	3770	+230/ -260
C2	287	941	454.0	487.0	888	454.0	434.0	0.891	0.20	3360	+410/ -720
TOTAL	582	5785	2895.0	2890.0	6614	2895.1	3719.0	1.287	0.09		

n = number of clusters; T = total counts; B = background counts; S = signal = T-B

CHAPTER 6

A nanoscale record of impact induced Pb mobility in lunar zircon

Tyler B. Blum[1]*, David A. Reinhard[2], Matthew A. Coble[3], Michael J. Spicuzza[1], Yimeng Cheng[2], Aaron J. Cavosie[4], Lutz Nasdala[5], Chutimun Chanmuang N.[5], Ty J. Prosa[2], David J. Larson[2], John W. Valley[1]

[1]Department of Geoscience, University of Wisconsin, Madison, WI, 53706 USA.
[2]CAMECA Inc., Madison, WI, USA
[3]Stanford University, Stanford, CA, USA
[4]School of Earth and Planetary Science, Curtin University, Perth, WA, Australia
[5]Institut für Mineralogie und Krystallographie, Universitat Wien, Wien, Austria.

Correspondence: tbblum@geology.wisc.edu

ABSTRACT

Atom probe tomography (APT) represents a novel means to characterize elemental and isotopic composition on the scale of tens of nanometers. In terrestrial zircons, nanoscale clustering of Pb within single zircons has been linked to transient thermal episodes and, when combined with micron-scale U-Pb analysis from secondary ion mass spectrometry (SIMS), Pb isotopes in nano-clusters record the timing of Pb mobility. Applying these techniques, this study demonstrates the presence of 5- to 10-nm Pb-rich clusters in lunar zircon 17B-4, a 4392 ± 12 Ma (2SD) zircon from sample 73235 collected during Apollo 17. The timing of cluster formation at 3860 +150/-170 Ma (2SD), based on modeling of $^{207}Pb/^{206}Pb$ ratios inside Pb-rich clusters, matches the $^{40}Ar/^{39}Ar$ age for the host breccia matrix (3946 ± 96 Ma; Turner and Cadogan, 1975; revised using preferred decay constants and reference mineral ages), which has been linked to the Serenitatis basin-forming impact event. These data represent the first documented occurrence of Pb clustering on the Moon, and the first correlation of nanoscale Pb clustering to impact processes. Younger Pb-loss is modeled assuming retention of Pb within clusters; in such a model, the age of Pb-loss is recalculated to be ~3.5 Ga, ~700 Myr older than the age associated with the lower discordia intercept. Zircon 17B-4 is devoid of diagnostic shock microstructures. Relatively high U and Th concentrations suggest that radiation damage facilitated trace element mobility at the nanoscale. The in-depth characterization of zircon 17B-4 provides a high degree of confidence that the $^{207}Pb/^{206}Pb$ age of 4392 Ma reflects crystallization, making 17B-4 is one of the oldest known lunar zircons. The antiquity of zircon 17B-4, as well as other >4.39 Ga zircon grains, argues against a "young" (4.35 – 4.37 Ga) age for the Moon forming impact.

INRTRODUCTION

Lunar zircon grains constitute an important source of information concerning the evolution of the Earth-Moon system, and by association, dynamic processes within the early inner solar system. Zircon ages place a lower limit on the age of the Moon (Nemchin et al., 2009a), while zircon ages, trace elements, and isotope ratios record numerous aspects of lunar evolution including: the initiation, duration, and spatial extent of lunar magmatism (Meyer et al., 1996; Nemchin et al., 2008); the water content and temperatures of lunar magmas (Valley et al., 2014a; Crow et al., 2017); and the provenance and thermal cycling of zircon grains in the lunar crust (Pidgeon et al., 2016; this thesis, Chapter 4). In addition, recrystallization of zircon during impact (e.g., Cavosie et al., 2015) and crystallization directly from impact melts (e.g., Grange et al., 2009; Zhang et al., 2018) can constrain the timing of impacts on the Moon, while zircon

deformation structures are sufficiently well defined to enable reconstructions of crystal plastic deformation and shock metamorphism (Timms et al., 2012, 2017).

Despite being a powerful tool for understanding lunar evolution, the *ex situ* nature of many lunar zircon grains has long complicated both their geological interpretation, and evaluation of grain-scale element mobility. The Moon's surface is covered in a complex, interlayered, and imperfectly mixed veneer of volcanic and impact ejecta deposits. As a result, virtually all the samples collected or sourced from the Moon have undergone varying degrees of thermal and mechanical disturbance. Often, disturbance can be cryptic, affecting some but not other geochemical systems in individual clasts or multigenerational breccias. While zircon remains one of the most robust phases for studying the moon, debate persists concerning the both the magnitude, prevalence, and driving forces for Pb mobility in zircons from the lunar environment, as well as the important structural associations controlling element migration (Nemchin et al., 2008; Zhang et al., 2012; Grange et al., 2013; Cavosie et al., 2015; Hopkins and Mojzsis, 2015; Crow et al., 2017; Thiessen et al., 2018). This debate is exacerbated by the fact that Pb-mobility in zircon grains can be particularly difficult to detect and quantify at times prior to ~3.8 Ga; Pb-loss at these times move data along an array sub-parallel to concordia, and *in situ* U-Pb analytical methods can struggle to resolve statistical discordance. Furthermore, the period prior to 3.8 Ga is the most dynamic and formative period in lunar history, making it particularly advantageous to have geochronological constraints. The prevalence of age resetting and discordance has significant implications for how the zircon record is interpreted relative to the timing and duration of lunar magmatism, the uniqueness of lunar surface deposits from site-to-site, and the provenance of regolith deposits across the lunar surface (this thesis, Chapter 4).

Atom probe tomography (APT) is uniquely suited to study the cryptic U-Pb evolution of lunar zircon grains. In terrestrial zircon, APT has revealed trace element heterogeneity at the nanoscale, (Valley et al., 2014b, 2015; Piazolo et al., 2016; Peterman et al., 2016; Blum et al., 2018). Combined with knowledge of a zircon crystallization age, Pb isotopes within clusters permit modeling the timing of cluster formation (Valley et al., 2015; Blum et al., 2018). In zircons with well-behaved micron-scale U-Pb systematics, Pb isotope ratios within small clusters have been correlated with known thermal episodes, and result from the migration within a zircon of Pb and other incompatible elements to crystallographic defects (subgrain boundaries, radiation-damage domains, dislocation loops, etc.) (Valley et al., 2014b, 2015; Piazolo et al., 2016; Peterman et al., 2016; Blum et al., 2018). Importantly, samples known to have undergone multiple thermal episodes can retain unique $^{207}Pb/^{206}Pb$ isotope ratios within clusters through subsequent thermal episodes (this thesis, Chapter 5). APT has been applied to study shocked zircon (Reddy et al., 2016), demonstrating that low angle grain boundaries and reidite lamellae in shock-metamorphosed zircon can concentrate non-formula trace elements (Y, Al, Be, Mg). Due to a lack of quantifiable Pb in APT data sets, the Reddy et al., (2016) study was not able to determine the timing of element migration based on Pb isotopes; this timing is important for resolving whether element migration occurred *during* impact metamorphism, or whether formation of grain boundaries and element segregation occurred during distinct thermal episodes. Observation and quantification of Pb segregation associated with impacts is critical to understanding the extent to which shock microstructure and disruption of U-Pb systematics are intrinsically related (e.g., Cavosie et al., 2015). Zircon recrystallization and formation of neoblasts has been linked to impact resetting (Cavosie et al., 2015); however, evidence is missing for a causal relationship between the formation of other shock microstructures (shock

twin lamellae, planar deformation features, fractures, etc.) and U-Pb resetting (partial or complete).

This work presents detailed analysis of a single 4392 ± 12 Ma zircon grain from lunar sample 73235 using secondary ion mass spectrometry (SIMS), Raman spectroscopy, and APT. These data allow for characterization of Pb isotopes between the nano-scale and grain-scale, placing clustering dynamics in the context of the magmatic and impact history of the Apollo 17 landing site. The presence of nanoscale clusters, and the preservation of clustered $^{207}Pb/^{206}Pb$ ratios through geologic time (including through subsequent thermal episodes) highlights the potential of single zircons to preserve evidence for multiple and complex histories from the lunar crust and surface.

SAMPLE AND METHODS

Zircon 17B-4 originates from sample 73235, a clast-rich aphanitic breccia collected at Station 3, on the rim of a 10 m crater during Apollo 17. Sample 73235 was part of the "light mantle" material visible on the south side of the Taurus-Littrow Valley; this "light mantle" material is interpreted as landslide deposits sourced from the adjacent South Massif (Wolfe et al., 1981; Hurwitz and Kring, 2016). Sample 73235 is comprised of a dark, aphanitic matrix component, and a younger, lighter more "porous" breccia component (Dence et al., 1976; Wolfe et al., 1981). Dating of the dark matrix material by $^{40}Ar/^{39}Ar$ (Turner and Cadogan, 1975) yielded plateau ages of 3946 ± 95 Ma. This age, as well as all other $^{40}Ar/^{39}Ar$ ages referenced in this work, have been recalculated using a preferred total ^{40}K decay constant of $\lambda = 5.463 \times 10^{-10}$ yr^{-1} (Min et al., 2000), and fluence monitor ages referenced to a Fish Canyon Tuff sanidine age of 28.201 Ma (Schmitz, 2012; MMhb-1 = 527.0 ± 0.3, Renne et al., 1998; Hb3gr = 1081.5 ± 2.4

Ma, Jourdan et al., 2006). The $^{40}Ar/^{39}Ar$ age of 73235 overlaps closely with the age of the Serenitatis impact, 3970 ± 27 Ma (Stöffler et al., 2006). This age for Serenitatis is based on the arguments of Dalrymple and Ryder (1996) and Stöffler et al. (2006), and recalculated from the $^{40}Ar/^{39}Ar$ data of Dalrymple and Ryder (1996) (samples 72395, 72535, and 76315; see Dalrymple and Ryder (1996) for further discussion of samples) using preferred decay constants and reference mineral ages (see above).

Zircon 17B-4 is an isolated zircon within the dark matrix of 73235,87 (Fig. 1b). Cathodoluminescence signals are subdued, with a series of diffuse bright bands running perpendicular to the long dimension of the grain. A single, irregular bright feature, with several micro-inclusions distributed along its length is sub-parallel to these bands (Fig. 1a). Oxygen isotope ratios are homogeneous ($\delta^{18}O_{avg}$ = 5.48 ± 0.27‰ 2SD, *n*=9) while Ti concentrations are highly variable (15 – 255 µg/g) (Spicuzza et al., 2011; Valley et al., 2014a). A series of four SIMS U-Pb analyses were made along the length of the grain, followed by an APT lift-out, which is parallel to observable banding and adjacent to the oldest SIMS spot analysis (see below for analytical methods). Following the APT lift-out, Raman analyses were completed spatially correlated to SIMS spots (and the APT lift-out).

U-Pb SIMS Dating

U-Pb isotopes, as well as [U] and [Th], were measured by SIMS, using a Sensitive High-Resolution Ion Microprobe with Reverse Geometry (SHRIMP-RG) at the Stanford-USGS SHRIMP-RG Laboratory. Each analysis consisted of a pre-sputter raster of the beam followed by sputtering from a centralized 18-23 µm spot. The analysis routine included six peak-hopping cycles, moving sequentially between $^{90}Zr_2{}^{16}O^+$ (a normalizing species), $^{180}Hf^{16}O^+$, $^{204}Pb^+$, a

$^{204}Pb^{+}$ background, $^{206}Pb^{+}$, $^{207}Pb^{+}$, $^{208}Pb^{+}$, $^{238}U^{+}$, $^{232}Th^{16}O^{+}$, $^{238}U^{16}O^{+}$ and $^{238}U^{16}O_2^{+}$. Zircon standard reference material 91500 (Wiedenbeck, et al., 2004), mounted in an adjacent mount within the SHRIMP-RG analysis chamber, was analyzed and is used as the primary standard for both age, and U and Th concentrations. Common Pb was monitored through measurement of ^{204}Pb; common Pb in all analyses is extremely low, and corrections to both $^{207}Pb^{*}$ and $^{206}Pb^{*}$ are based on Stacey and Kramers (1975). Reduction of raw data was completed in SQUID with further data analysis and visualization completed using Isoplot (Ludwig, 2008).

Raman Spectroscopy

Raman spectroscopy was completed to provide semi-quantitative estimates for the present-day radiation damage states through measurement of the peak position and full width at half maximum of the $v_3(SiO_4)$ vibrational mode ($FWHM_{v3(SiO4)}$). Spot analyses were completed on a LabRAM HR Evo at the Institut für Mineralogie und Kristallographie at the University of Vienna, Austria. Raman spots are correlated with individual SIMS U-Pb analyses (Fig. 1b). All analyses used a 632.8 nm He-Ne laser, with a 1800-grove/mm grating. Analyses included two accumulations at 60 seconds to allow for spike corrections. Measured $FWHM_{v3(SiO4)}$ were corrected for the apparatus function following Váczi (2014), assuming a convolution of Gaussian (instrumental) and Lorentzian (physical) band shapes. Background correction and peak fitting for spot analyses was completed in PeakFit v4.12.

The total α-dose, D_{total}, for a zircon grain (or zircon domains) can be calculated based on zircon age, U, and Th concentrations:

$$D_{total} = 8 \cdot {}^{238}N(\exp(\lambda_{238}t) - 1) + 7 \cdot {}^{235}N(\exp(\lambda_{235}t) - 1) + 6 \cdot {}^{232}N(\exp(\lambda_{232}t) - 1) \quad [2]$$

Where D_{total} is in units of α-decays/mg, λ_{238}, λ_{235} and λ_{232} are the decay constants for ^{238}U, ^{235}U and ^{232}Th respectively, *t* is the age of the zircon (or zircon domain) and ^{238}N, ^{235}N and ^{232}N are the number of ^{238}U, ^{235}U and ^{232}Th atoms per milligram zircon. This can be compared with the present-day damage states, D_{eff}, representing the effective (i.e., not annealed) α-dose based on the empirical calibration of Nasdala et al. (2001):

$$D_{eff} \approx \frac{FWHM_{\nu3(SiO4)} - 1.2}{1.4} \quad [2]$$

Where in eqn. 2, D_{eff} is in units of 10^{15} α-decays/mg. By comparing the calculated and measured damage states, it is possible to determine whether a specific zircon domain preserves all of its radiation damage and, if not, the percentage that is preserved (fractional dose) and the percentage of annealing (fractional annealing). The fraction of preserved damage can be used to model a "radiation damage age" (Pidgeon, 2014) assuming *complete annealing* at some time in the past, followed by *complete damage retention to the present.* In many cases it can be difficult to demonstrate the assumptions behind a radiation damage age, as well as other simplifications that are appropriate (e.g., Nasdala et al., 2001, 2002; Pidgeon 2014) and thus the significance of radiation damage ages is equivocal. However, these ages can be treated in a semi-quantitative fashion and if annealing has occurred, they constrain the *maximum* age for *most recent* annealing.

Atom Probe Tomography

APT is a combination of a projection-style microscope, and time-of-flight mass spectrometer, in which a needle-shaped specimen, with an end tip radius on the order of 50-100

nm, is placed in a high electric potential, and either voltage pulses (for electrical conductors) or laser pulses are used to induce time-correlated evaporation of constituent components (Gault et al., 2012; Larson et al., 2013). The detection of field-evaporated species on a position-sensitive detector allows for species identification (based on mass-to-charge state ratio) and their three-dimensional spatial reconstruction within the original sample. The current generation of instrumentation have detection limits ~10 parts-per-million atomic (ppma), mass-resolving-power ($M/\Delta M_{FWHM}$) or ~1000, and sub-nanometer spatial resolution. This combination of capabilities enables detection of components with isotope sensitivity, and reconstruction of positions with sub-nanometer spatial resolution.

A series of needle-shaped specimens for APT analysis were prepared from a single FIB (focused ion beam) lift-out taken adjacent to U-Pb analysis 17B.4-1.1 (Fig. 1a and 1b); the long dimension of the wedge-shaped lift-out was deliberately oriented parallel to banding within the zircon (Fig. 1). The wedge-shaped lift-out was sectioned onto a Si-microtip array, and annular-milling-fastened tips for APT analysis. Specimens were run on two different atom probe instruments: a CAMECA LEAP 5000 XS (straight flight path configuration) and a LEAP 5000 XR (reflectron configuration) at the CAMECA Atom Probe Technology Center in Madison, Wisconsin. Reconstructions, ranging and cluster analysis were performed using CAMECA's Integrated Visualization and Analysis Software (IVAS 3.6.12). The reconstruction of data sets was approached individually, utilizing spectral ranges refined during preliminary reconstruction and data analysis. Reconstructions used a voltage-based radius evolution model (Table 3).

RESULTS

Four U-Pb SIMS analyses of 17B-4 yield a range in $^{207}Pb/^{206}Pb$ age from 4338 ± 12 to 4392 ± 12 Ma (2SD) and between 1 and 4% discordance (Fig. 1c; Table 1). U and Th concentrations are relatively consistent across the grain, varying by ~25% (156 – 200 µg/g for U, and 81 – 115 µg/g for Th; Th/U varies from 0.58 to 0.68). The oldest and most concordant analysis on 17B-4 is 1% discordant, with a $^{207}Pb/^{206}Pb$ age of 4392 ± 12 Ma (±2SD), while the remaining three analyses are statistically discordant 3-4%. A regression of these data yields an upper intercept of 4416 ± 50 Ma (2SD), and a lower intercept of 2841 ± 760 Ma. We take the oldest $^{207}Pb/^{206}Pb$ age (4392 ± 12 Ma) to be the best value for the crystallization age of zircon 17B-4, though we note that this age is statistically indistinguishable from the upper discordia intercept. The combination of U and Th concentrations, and an age of 4392 (± 12) Ma yield total α-doses from 4.9×10^{15} to 6.3×10^{15} α-decays/mg. If unannealed, these α-doses represent damage states a factor of 2-3 times the first percolation point (Ewing et al., 2003).

Electron backscatter diffraction (EBSD) band contrast, and Raman spot analyses are both consistent with preservation of significant radiation damage in zircon 17B-4 (see Appendix 2 for summary of EBSD mapping details). The grain exhibits poor EBSD band contrast (Fig. 1d), which manifests as poor indexing of backscatter diffraction patterns (Fig. 1e). Band contrast is a measure of the intensity variations for Kikuchi diffraction bands relative to the overall intensity of the electron diffraction pattern, and is a measure of "pattern quality." The lack of indexing in EBSD mapping complicates quantitative assessment of shock and/or deformation microstructures; however, combined with the lack of definitive textural boundaries in SEM imaging, we do not anticipate grain scale microstructures to have influenced U-Pb systematics in the grain.

Measurement of $FWHM_{v3(SiO4)}$ by Raman (Nasdala et al., 2001) further documents significant radiation damage accumulation; corrected Raman bandwidths range from 30.0 to 34.8 cm^{-1} (Table 3). For values of $FWHM_{v3(SiO4)}$ > 25-30 cm^{-1}, fitting of peaks becomes less reliable due to peak asymmetry and scattering from amorphous domains in zircon (Nasdala et al., 2001); however, the observed range in bandwidths give effective doses of 2.1 to 2.4×10^{15} α-decays/mg, and "radiation damage ages" (*sensu* Pidgeon, 2014; Blum et al., 2018) of 2.45 to 2.70 Ga. Based on modeling of the percolation transition, it is estimated that the grain at present between ~60-70% crystalline by volume (Trachenko et al., 2000).

Atom Probe Tomography

Mass spectra for five APT specimens show relatively consistent behavior in ion speciation and charge state ratios from specimen-to-specimen. Zircon APT data are broadly consistent with zircon composition, consistent with APT-based compositions within the published literature (see La Fontaine et al., 2017 and Saxey et al., 2018 for further discussion regarding compositional analysis by APT). The trace elements, Y, Yb, U, Hf, and Pb are detectable within the bulk data sets. In this work, we focus on the spatial distribution of Pb, and quantification of $^{207}Pb/^{206}Pb$ ratios; these aspects of data analysis leverage *relative* concentrations and can be considered independent of the more general experimental complexities to APT compositional analysis (Valley et al., 2015; La Fontaine et al., 2017; Saxey et al., 2018).

APT data sets for 17B-4 contain several 5-10 nm sub-spherical domains enriched in Pb at the 0.1-1.0 atom % level (Fig. 2). Quantification of $^{208}Pb^{2+}$ and $^{207}Pb^{2+}$ in bulk data is inhibited by the presence of the $Si_2O_3^+$ peak at 104 Da, which exhibits a significant tail on the low-mass-to-charge (low-m/n) side obscuring the trace $^{207}Pb^{2+}$ signals at 103.5 Da, respectively (Fig. 2a).

We do not attempt to deconvolve these peaks to calculate bulk $^{207}Pb/^{206}Pb$ ratios; uncertainties for the $^{207}Pb^{2+}$ and $^{206}Pb^{2+}$ signals in the bulk data are large due to low signal-to-noise, and we have limited *a priori* constraints to account for the additional complications of correcting for the 104 Da peak tail in the 103-104 Da range. Importantly, the overlap between the 103.0, 103.5 and 104.0 peaks is absent within Pb-rich clusters (Fig. 2b), as signal-to-noise is significantly improved and the relative magnitude of both the 104 Da peak, and the low-m/n tail, is diminished. This enables isotopic analysis of the 103.0 and 103.5 Da peaks, following the general considerations of Blum et al. (2018). Pb-rich domains have been isolated from a total of five APT data sets through the use of isoconcentration surfaces. In each case, a voxel size of [1.0, 1.0, 1.0] nm in the [x,y,z] dimensions, and a delocalization of [6.0, 6.0, 3.0] nm effectively describes the boundary between clusters and the surrounding matrix. The compositional threshold for clustering varies between 0.2-0.6 atomic % Pb; this variation is not considered quantitative, as the 104 Da peak tail varies spatially within the data set.

A subset of data sets were collected with longer time-of-flight timing windows (i.e., collection of ions with times-of-flight extending above 250 Da). Within the Pb-rich regions, we observe the presence of peaks at 206 and 207 Da (Fig. 2c); Given the Pb-rich nature of clusters, this is consistent with the field evaporation of $^{206}Pb^{+}$ and $^{207}Pb^{+}$. This is the first identification of singly charged $^{207}Pb^{+}$ and $^{206}Pb^{+}$ in zircon APT data sets; typically, Pb is found in the doubly charged state, at 103.0 and 103.5 Da respectively (e.g., Valley et al., 2014b; 2015). The presence of Pb^{+} at 206 and 207 Da is particularly advantageous for two reasons: (1) these data provide additional Pb counts in a situation where counting statistics constitute the greatest error in isotope measurements, and (2) given the convolved signals in the *bulk* APT data at 103.5 Da (due to 104 Da peak tail), the quantification of $^{206}Pb^{+}$ and $^{207}Pb^{+}$ allows for an independent check

on both the uniqueness of Pb enrichment, and the observed isotope ratios within Pb-rich domains. More generally, the measurement of singly charged Pb would enable the measurement of $^{208}Pb^{+}$, as there is no known interference at 208 Da.

The ranging (i.e., identification and integration of ion counts within mass spectra) and quantification of Pb isotopes follow the general considerations discussed by Blum et al. (2018). Table 2 summarizes the ^{206}Pb and ^{207}Pb counts, for both the 1+ and 2+ charge states on a cluster by cluster basis. The $^{207}Pb/^{206}Pb$ ratios for all clusters and charge states overlap within uncertainty, with particularly good agreement between the $^{207}Pb/^{206}Pb$ ratios for (1) large clusters with larger numbers of counts, (2) the 1+ and 2+ charge states. The aggregate ^{207}Pb and ^{206}Pb signal (all clusters and all charge states) clusters yield a $^{207}Pb/^{206}Pb$ isotope ratio of 1.42 ± 0.07 (2SD) (Table 2). For this reason, we treat the aggregate Pb signals as representative of a single common clustering event in the past.

DISCUSSION

The combination of SIMS, SEM, Raman spectroscopy, and APT provide a means to reconstruct the thermal and structural evolution of zircon 17B-4 in unique detail. In the following sections, we will first detail the combined constraints afforded by these techniques, followed by their implications and finally their geological significance.

Age and thermal history of zircon 17B-4:

APT data for zircon 17B-4 document, for the first time, the presence of Pb-rich nanoclusters in lunar zircon. The combination of low common-Pb demonstrated by SIMS analysis, and high $^{207}Pb/^{206}Pb$ ratios within clusters preclude these features from originating during zircon crystallization, as they require the accumulation of radiogenic Pb after

crystallization and grain-scale closure. While similar nanoscale clusters have been documented on Earth, these data establish that the thermal and structural controls for cluster formation are present on the Moon.

The Pb-rich clusters within APT data sets, indicate at least one period of Pb migration occurred within the history of the zircon grain. We model cluster formation in order to determine the approximate age of Pb migration into clusters (Valley et al., 2014b, 2015; Blum et al., 2018; Fig. 3 and 4). The model assumes: (1) a homogeneous parent (uranium) distribution on the scale of the APT lift-out (~1 μm), (2) radioactive decay is the only time-dependent influence on parent U concentrations after crystallization, and (3) no radiogenic Pb is added to clusters between the time of clustering and today (i.e., measured ratios are approximately equal to the isotope ratio at the time of cluster formation). The resulting history includes homogenous ingrowth of radiogenic ^{207}Pb and ^{206}Pb between crystallization at 4392 Ma and the cluster formation episode, migration of Pb to clusters at some time point, followed by homogeneous ingrowth of radiogenic Pb outside of clusters thereafter (Fig. 3b). Based on this model, a crystallization age of 4392 Ma, and a cluster ^{207}Pb/^{206}Pb ratio of 1.42 ± 0.07, places cluster formation at ~540 Myr after crystallization, at 3850 +150/-170 Ma (2SD; Fig. 3 and 4a).

This cluster formation age is notable for two reasons. First and foremost, this age matches the ^{40}Ar/^{39}Ar age for the host breccia (sample 73235; 3946 ± 95 Ma, Turner and Cadogan, 1975), which, as discussed above, records formation during the Serenitatis impact event. We take this as compelling evidence that Pb clustering at the nanoscale was associated with the broad thermal manifestations of the Serenitatis basin forming impact at ~3970 Ma (Stöffler et al., 2006; Fig. 1). Secondly, the cluster age of 3850 +150/170 Ma is distinct from the lower discordia intercept age of 2840 ± 750 Ma (Fig. 1c). If Pb nanoclusters *and* micron-scale discordance (measured by

SIMS) formed during a single event, these ages should be the same, as either: (1) discordant SIMS analyses should lie on a cord between 4392 and ~3860 Ma, or (2) isotope ratios in clusters should be $^{207}Pb/^{206}Pb = 1.01$, the predicted ratio assuming clustering at 2841 Ma after crystallization at 4392 Ma. The discrepancy between the cluster formation age and lower discordia intercept suggests the combined micron-scale and nanoscale U-Pb systematics preserve crystallization age at 4392 ±12 Ma, as well as *two distinct periods of Pb movement*.

A framework to reconcile the different thermal histories implied by nanoscale and micron-scale U-Pb requires consideration of the nanoscale behavior of Pb, particularly with regards to Pb-rich nano-clusters. The retention of unique $^{207}Pb/^{206}Pb$ ratios though multiple thermal episodes, (this thesis, Chapter 5), and the preservation of $^{207}Pb/^{206}Pb = 1.42$ in clusters within zircon 17B-4 indicate Pb-rich domains can retain Pb, and Pb-isotope ratios (Fig. 4c and 4d). This is particularly relevant, as traditional models of Pb-loss, and interpretation of U-Pb discordia, implicitly assume all Pb (and the different Pb isotopes) behave identically during Pb loss (this thesis, Chapter 5). While the individual isotopes are assumed not to be fractionated by the processes of Pb loss, the differential retention of Pb in domains with different $^{207}Pb/^{206}Pb$ ratio would invalidate the common assumptions of Pb loss and requires that the temporal significance of the discordia be revised. Quantitative modeling of a two-stage process (i.e., clustering followed by Pb-loss, see this thesis, Chapter 5) predicts that false discordia will be constructed from micron-scale analyses that project to a concordia intercept systematically *younger* than the actual age of Pb-loss (Fig. 4d).

Figure 4 shows model calculations for clustering followed by poly-domain Pb loss. An estimate of the timing Pb-loss (after clustering) can be made by finding the time *after the initial cluster event*, for which the matrix region (i.e., outside clusters) has a composition equivalent to

the y-intercept of the discordia in the Tera-Wasserburg concordia diagram (Fig. 4c and 4d). In principle, this is equivalent to identifying the $^{207}Pb/^{206}Pb$ component lost during the Pb-loss event, and reconstructing the time at which this composition existed as the mobile Pb component (this thesis, Chapter 5). For zircon 17B-4, we estimate Pb-loss occurred at ~3.5 Ga, after cluster formation at ~3.9 Ga. In light of this modeling, we can predict that: (1) the lower discordia intercept of 2841 ± 750 Ma is a minimum age for Pb-loss (Fig. 4d). Note that the complexities discussed above do not affect the accuracy of the upper discordia intercept (also discussed in this thesis, Chapter 5). The agreement between this the upper intercept age of 4416 ± 50 for 17B-4, and the concordance of analysis 17B.4-1.1, provides a high degree of confidence that the $^{207}Pb/^{206}Pb$ age of 4392 ± 12 Ma is a robust estimate of the crystallization age for 17B-4.

Based on a crystallization age of 4392 Ma, and measured [U] and [Th], zircon 17B-4 would have accumulated between 1.0 to 1.3×10^{15} α-decays/mg between crystallization and the time of the Serenitatis impact and ~3900 Ma. These doses, along with the lack of identifiable shock microstructures within zircon 17B-4, suggests radiation damage represents a likely structural control on element mobility. The number and timing of annealing episodes after 3.9 Ga are not well constrained, but several lines of evidence suggest sample 73235 experienced repeated thermal cycling, including: (1) hypothesized Pb-loss at ~3.5 Ga (see discussion above), (2) low temperature $^{40}Ar/^{39}Ar$ release steps with apparent ages as young as 2.0-2.5 Ga in Phinney et al. (1975) and Turner and Cadogan (1975), and (3) radiation damage ages of 2.45-2.7 Ga for zircon 17B-4. Low-temperature $^{40}Ar/^{39}Ar$ release steps have been interpreted as a *maximum* age for the *most recent* high-temperature episode (Shuster et al., 2010; Boehnke and Harrison, 2016). Given that clustering in 17B-4 and breccia formation are correlated at 3.9 Ga, and zircon 17B-4 has not been separated from the breccia, these events have been shared between the zircon and

its breccia host. As summarized in Fig. 3, it is suspected that these younger thermal events relate to excavation of the sample from the South Massif, and transient thermal episodes associated with "farming" of the lunar surface.

Geological Implications

The new combination of APT and SIMS analyses in this work detail complex scale-dependence U-Pb isotope systematics in the zircon, but provide details to accurately reconstruct the thermal history for the zircon grain. As illustrated above, the scale dependence of Pb behavior can present a significant complication to traditional interpretation of the timing of Pb-loss. A false discordia results from sequential nanoscale trapping of Pb in clusters, followed by micron-scale loss of Pb from surrounding matrix. Given the prolonged history of impacts on the Moon, and the repeated thermal cycling of lunar materials, these processes may be a widespread aspect of U-Pb zircon behavior on the Moon. While this complicates interpretation of micron-scale discordance trends measured by SIMS or TIMS, U-Pb measurements at the grain and nanoscale enables the reconstruction of multistage heating histories.

The ability to reconstruct the U-Pb systematics of zircon 17B-4 at the nanometer scale provides a high degree of confidence in the 4392 ± 12 Ma crystallization age for zircon 17B-4. Zircon grains with crystallization ages older than 4.39 Ga are rare on the Moon, constituting <2% of the ~500 analyzed grains (Fig. 5; this thesis, Chapter 4). The age of 4392 Ma makes zircon 17B-4 is one of the oldest known lunar zircon grains. As discussed by Nemchin et al. (2009), the crystallization of zircon in Zr-rich lunar melts is associated with the formation of the KREEP reservoir following differentiation of the lunar magma ocean (LMO) and formation of the Moon's flotation crust. Implicit in this thermal and tectonic evolution is the fact that

solidification of the LMO and the formation of the KREEP reservoir, post-date any Moon-forming impact between the proto-Earth and a Mars-sized planetesimal, Theia. The existence of multiple zircons with ages >4390 Ma is important for identifying the formation of a Zr-rich reservoir as a widespread phenomenon. The antiquity of zircon 17B-4, as well as other >4.39 Ga zircon grains, argues against a "young" (4.35 – 4.37 Ga) age for the Moon forming impact (e.g., Borg et al., 2015).

The geochronology from other Apollo 17 samples provides additional context for nanoscale clustering, and the thermal events preserved at the Apollo 17 landing site (Fig. 5). The cluster formation age of 3850 Ma (APT) is shown in Fig. 5, along with a compilation of (1) zircon U-Pb ages by SIMS from Apollo 12, 14, 15 and 17 (this thesis, Chapter 4), (2) phosphate U-Pb ages by SIMS from Apollo 17 (Thiessen et al., 2017), (3) $^{40}Ar/^{39}Ar$ plateau ages for Apollo 17 samples, and (4) the weighted mean U-Pb age for impact melt zircons dated by NanoSIMS (Zhang et al., 2018). These data demonstrate both the distinct zircon-age distributions present for the different Apollo landing sites (this thesis, Chapter 4) and the widespread ~3.9 Ga overprint in the Apollo 17 sample suite. The extent to which this overprint represents Imbrium versus Serenitatis deposits remains a topic of debate (e.g., Hurwitz and Kring, 2016; Bottke and Norman, 2017; Zhang et al., 2018). The cluster ages presented here do not resolve this debate but are consistent with the 3.9 Ga thermal signature imparted on the Apollo 17 site. While we see compelling reasons to correlate cluster formation (and the broader geochronology of the Apollo 17 site) with the Serenitatis impact, the observation of impact-induced Pb migration is independent of the basin source.

The match between cluster model ages and the Ar-Ar data for breccia 73235 is significant in that this represents both the first time Pb migration has been correlated with an impact, and the

first time it has been possible to infer the date of an impact using the Pb-isotope ratios in nanoclusters. These data further refine the structural and thermal behavior controlling impact-induced mobility. Shock microstructures (fracturing, low angle grain boundaries, granular zircon, microtwin and reidite lamellae) all represent defect-rich domains or crystallographic boundaries that can act as either (1) fast pathways for mobility of Pb, or (2) structural traps for Pb and other non-formula-unit elements. If sufficiently large, both diffusive Pb-loss and trapping of locally unsupported radiogenic Pb will result in inaccurate U-Pb age systematics on the micron scale measured by SIMS. It is likely that high temperatures are required to drive significant element migration, and that the *formation* of structural defects and *thermal activation of element migration* can be decoupled in shock environments.

CONCLUDING REMARKS

While zircon remains one of the most reliable geochonometers for studying the early evolution of the Earth-Moon system, the need to understand the nuances and scale dependence of U-Pb isotope behavior is becoming increasingly apparent. The ability to track the isotopic evolution at atomic-scale in zircon 17B-4 demonstrates that these processes record otherwise cryptic aspects of the thermal history of a zircon grain, and can be particularly powerful in understanding the history of *ex situ* grains. The combination of SIMS, SEM, Raman spectroscopy and APT documents the repeated thermal cycling of zircon 17B-4 over the past 4.4 billion years, including Pb migration at nm-scale during basin formation at 3.9 Ga, selective Pb-loss at μm-scale ~3.5 Ga, and annealing <3.0 Ga. There exists significant potential for APT to contribute to lunar and terrestrial chronology, as the technique is highly sensitive to Pb re-distribution at the near atomic scale, and APT is uniquely suited to detect and quantify cryptic Pb

movement early in Earth history, a time period where micron-scale analyses struggle to detect and quantify U-Pb isotope discordance.

ACKNOWLEDGEMENTS

We thank Brian Hess, for his aid and attention in preparing valuable zircon samples. This research was funded by the US National Science Foundation (EAR-1144454, EAR-1524336), and the US Department of Energy, Office of Basic Energy Sciences, Geosciences Division under award number DE-FG02-93ER14389. WiscSIMS is supported by NSF (EAR-1355590, -1658823) and UW-Madison. The authors acknowledge the use of facilities supported by the University of Wisconsin, College of Engineering and the Materials Research and Engineering Center (NSF DMR-121288) and Nanoscale Science and Engineering Center (NSF DMR-0832760).

REFERENCES

Blum, T.B., Reinhard, D.A., Chen, Y., Prosa, T.J., Larson, D.J., Valley, J.W. (2018) Uncertainty and sensitivity analysis for spatial and spectral processing of Pb-Pb geochronology by atom probe tomography, in Microstructural Geochronology: Planetary Records Down to Atom Scale, edited by Desmond E. Moser, Fernando Corfu, Steven M. Reddy, James R. Darling, and Kimberly Tait, John Wiley & Sons, Inc., Hoboken, NJ, 232, 327–349.

Bottke, W.F., Norman, M.D. (2017) The Late Heavy Bombardment. Annual review in Earth and Planetary Sciences, 45, 619-647.

Boehnke, P., Harrison, T.M. (2016) Illusory late Heavy Bombardments. Proceedings of the National Academy of Sciences, 201611535, DOI:10.1073/pnas.1611535113

Borg, L.E., Gaffney, A.M., Shearer, C.K. (2015) A review of lunar chronology revealing a preponderance of 4.34-4.37 Ga ages. Meteoritics and Planetary Science, 50, 715-732.

Crow, C.A., McKeegan, K.D., Moser, D.E. (2017) Coordinated U-Pb geochronology, trace element, Ti-in-zircon thermometry and microstructural analysis of Apollo zircons. Geochimica et Cosmochimica Acta, 202, 264-284.

Dalrymple, G.B., Ryder, G. (1996) Argon-40/Argon-39 age spectra of Apollo 17 highlands breccia samples by laser step heating and the age of the Serenitatis basin. Journal of Geophysical Research, 101, 26,069-26,084.

Dence, M.R., Grieve, R.A.F., Plant, A.G. (1976) Apollo 17 grey breccias and crustal composition in the Serenitatis Basin region. Proc. 7th Lunar Sci Conf., 1821-1832.

Ewing, R.C., Meldrum, A., Wang, L., Weber, W.J., Corrales, L.R. (2003) Radiation effects in zircon. Reviews in Mineralogy and Geochemistry, 53, 387-425.

Gault, B., Moody, M.P., Cairney, J.M., Ringer, S. (2012) Atom Probe Microscopy, Springer. 396 p.

Grange, M.L., Nemchin, A.A., Pidgeon, R.T., Timms, N., Muhling, J.R., Kennedy, A.K. (2009) Thermal history recorded by the Apollo 17 impact melt breccia 73217. Geochimica et Cosmochimica Acta, 73, 3097-3107.

Hurwitz, D., Kring, D.A. (2016) Identifying the geologic context of Apollo 17 impact melt breccias. Earth and Planetary Science Letters, 436, 64-70.

Jourdan, F., Verati, C., Feraud, G. (2006) Intercalibration of the Hb3gr $^{40}Ar/^{39}Ar$ dating standard. Chemical Geology, 231, 177-189.

La Fontaine A., Piazolo, S., Trimby, P., Yang, L., Cairney, J.M. (2017) Laser-Assisted Atom Probe Tomography of Deformed Minerals: A Zircon Case Study. Microscopy and Microanalysis, 23, 404-413.

Larson, D.L., Prosa, T.J., Ulfig, R.M., Geiser, B.P., Kelly, T.F., (2013) Local Electrode Atom Probe: A User's Guide. Springer. 318 p.

Ludwig, K.R. (2008) User's manual for Isoplot 3.70: A Geochronological Toolkit for Microsoft Excel. Berkeley Geochronology Center, Special Publication No. 4.

Meyer, C., Williams, I.S., Compston, W. (1996) Uranium-lead ages for lunar zircons: Evidence for a prolonged period of granophyre formation from 4.32 to 3.88 Ga, Meteoritics and Planetary Science, 31, 370-387.

Min, K., Mundil, R., Renne, P., Ludwig, K. (2000) A test for systematic errors in $^{40}Ar/^{39}Ar$ geochronology through comparison with U/Pb analysis of 1.1-Ga rhyolite. Geochimica et Cosmochimica Acta, (64) 73-98.

Nasdala, L., Wenzel, M., Vavra, G., Irmer, G., Wenzel, T., Kober, B. (2001) Metamictization of natural zircon: accumulation versus thermal annealing of radioactivity-induced damage, Contributions to Mineralogy and Petrology, 141, 125-144.

Nemchin, A.A., Pidgeon, R.T., Whitehouse, M.J., Vaughn, J.P., Meyer, C. (2008) SIMS U-Pb study of zircon from Apollo 14 and 17 breccias: Implications for the evolution off lunar KREEP. Geochimica et Cosmochimica Acta, 72, 668-689.

Nemchin, A., Timms, N., Pidgeon, R., Geisler, T., Reddy, S., Meyer, C. (2009) Timing of crystallization of the lunar magma ocean constrained by the oldest zircon, Nature Geoscience, 2, 133-136.

Peterman, E.M., Reddy, S.M., Saxey, D.W., Snoeyenbos, D.R., Rickard, W.D.A., Fougerouse, E.M., Kylander-Clark A.R.C. (2016) Nanogeochronology of discordant zircon measured by atom probe microscopy of Pb-enriched dislocation loops, Science Advances, 2, e1601318.

Piazolo, S., La Fontaine, A., Trimby, P., Harley, S., Yang, L., Armstrong, R., Cairney, J.M. (2016) Deformation-induced trace element redistribution in zircon revealed using atom probe tomography, Nature Communications, 7, 10490.

Pidgeon R.T. (2014) Zircon radiation damage ages. Chemical Geology, 367, 13-22.

Pidgeon, R.T., Merle, R.E., Grange, M.L., Nemchin, A.A., Whitehouse, M.J. (2016) Annealing of radiation damage in zircons from Apollo 14 impact breccia 14311: Implications for the thermal history of the breccia, Meteoritics and Planetary Science, 51, 155-166.

Phinney, D., Kahl, S.B., Reynolds, J.H. (1975) ^{40}Ar-^{39}Ar dating of Apollo 16 and 17 rocks. Proc. Lunar Sci. Conf. 6th. 1593-1608.

Reddy, S.M., Riessen, A., Saxey, D.W., Johnson, T.E., Rickard, W.D.A., Fougerouse, D., Fisher, S., Prosa, T.J., Rice, K.P., Reinhard, D.A., Chen, Y., Olson, D. (2016) Mechanisms of deformation-induced trace element migration in zircon resolved by atom probe tomography and correlative microscopy. Geochimica et Cosmochimica Acta, 195, 158-170.

Renne, P.R., Swisher, C.C., Deino, A.L., Karner, D.B., Owens, T.L., DePaulo, D.J. (1998) Intercalibration of standards, absolute ages and uncertainties in ^{40}Ar/^{39}Ar dating, Chemical Geology, 145, 117-152.

Saxey, D.W., Reddy, S.M., Fougerouse, D., Rickard, W.D.A. (2018) the Optimization of Zircon Analyses by Laser-Assisted Atom Probe Microscopy: Insights from the 91500 Zircon Standard, *in* Microstructural Geochronology: Planetary Records Down to Atom Scale, edited by Desmond E. Moser, Fernando Corfu, Steven M. Reddy, James R. Darling, and Kimberly Tait, John Wiley & Sons, Inc., Hoboken, NJ, 232, 293-314.

Schmitz, M., (2012) Radiogenic Isotope Geochemistry, *in* Geologic Time Scale 2012, edited by Felix M. Gradstein, James G. Ogg, Mark Schmitz, Gabi Ogg, Elsevier, 115-126.

Shuster, D.L., Balco, G., Cassata, W.S., Fernandes, V.A., Garrick-Bethell, I., Weiss, B.P. (2010) A record of impacts preserved in the lunar regolith. Earth and Planetary Science Letters, 290, 155-165.

Spicuzza, M.J., Valley, J.W., Kitajima, K., Ushikubo, T. (2011) Oxygen isotope ratios and trace element concentrations in zircons from lunar rocks and regolith, 42nd Lunar and Planetary Science Conference, The Woodlands, Texas, #2445.

Stacey, J.S., Kramers, J.D. (1975) Approximation of terrestrial lead isotope evolution by a two-stage model. Earth and Planetary Science Letters, 26, 207-221.

Stöffler, D., Ryder, G., Ivanov, B.A., Artemieva, N.A., Cintala, M.J., Grieve, R.A.F. (2006) Cratering History and Lunar Chronology. Reviews in Mineralogy and Geochemistry, 60, 519-596.

Thiessen, F., Nemchin, A.A., Snape, J.F., Whitehouse, M.J., Bellucci, J.J. (2017) Impact history of the Apollo 17 landing site reveled by U-Pb SIMS ages. Meteoritics and Planetary Science, 52, 584-611.

Thiessen, F., Nemchin, A.A., Snape, J.F., Bellucci, J.J., Whitehouse, M.J. (2018) Apollo breccia 12013: Impact-induced partial Pb loss in zircon and its implications for lunar geochronology. Geochimica et Cosmochimica Acta, 230, 94-111.

Timms, N.E., Reddy, S.M., Healy, D., Nemchin, A.A., Grange, M.L., Pidgeon, R.T., Hart, R. (2012) Resolution of impact-related microstructures in lunar zircon: A shock deformation mechanism map. Meteoritics and Planetary Science, 47, 120-141.

Timms, N.E., Erickson, T.M., Pearce, M.A., Cavosie, A.J., Schmieder, M., Tohver, E., Reddy, S.M., Zanetti, M.R., Nemchin, A.A., Wittmann, A (2017) A pressure-temperature phase diagram for zircon at extreme conditions. Earth-Science Reviews, 165, 185-202.

Trachenko, K., Dove, M.T., Salje, E. (2000) Modelling the percolation-type transition in radiation damage. Journal of Applied Physics, 87, 7702-7707.

Turner, G., Cadogan, P.H. (1975) The history of lunar bombardment inferred from $^{40}Ar/^{39}Ar$ dating of highland rocks. Proc. 6th Lunar Sci. Conference, 1509-1538.

Váczi, T. (2014) A new, simple approximation for the deconvolution of instrumental broadening in spectroscopic band profiles. Applied Spectroscopy, 68, 1274-1278.

Valley, J.W., Spicuzza, M.J., Ushikubo, T. (2014a) Correlated $\delta^{18}O$ and [Ti] in lunar zircons: a terrestrial perspective for magma temperatures and water content on the Moon, Contributions to Mineralogy and Petrology, 167, 956. doi:10.1007/s00410-013-0956-4.

Valley J.W., Cavosie, A.J., Ushikubo, T., Reinhard, D.A., Lawrence, D.F., Larson, D.J., Clifton, P.H., Kelly, T.F., Wilde, S.A., Moser, D.E., Spicuzza, M.J. (2014b) Hadean age for post-magma-ocean zircon confirmed by atom probe tomography, Nature Geoscience, 7, 219-223.

Valley, J.W. Reinhard, D.A., Cavosie, A.J., Ushikubo, T., Lawrence, D.F., Larson, D.J., Kelly, T.F., Snoeyenbos, D.R., Strickland, A. (2015) Nano- and Micro-geochronology in Hadean and Archean zircons by atom-probe tomography and SIMS: New tools for old minerals, American Mineralogist, 100, 1355-1377.

Wiedenbeck, M., Hanchar, J.H., Peck, W.H., Sylvester, P., Valley, J., Whitehouse, M., Kronz, A., Morishita, Y., Nasdala, L., et al. Further characterization of the 91500 zircon crystal. Geostandards and Geoanalytical Research, 28, 9-39.

Wolfe, E.W., Bailey, N.G., Luccchitta, B.K., Muehlberger, W.R., Scott, D.H., Sutton, R.L., Wilshire, H.G. (1981) The Geologic Investigation of the Taurus-Littrow Valley: Apollo 17 Landing Site. U.S. Geological Survey Professional Paper 1080.

Zhang, A.-C., Taylor, L.A., Wang, R.-W., Li, Q.-L., Li, X.-H., Patchen, A.D., Liu, Y. (2012) Thermal history of Apollo 12 granite and KREEP-rich rock: Clues from Pb/Pb ages of zircon in lunar breccia 12013. Geochimica et Cosmochimica Acta, 95, 1-14.

Zhang, B., Lin, Y., Moser, D.E., Shieh, S.R., Bouvier, A. (2018) Imbrium zircon age for Apollo 73155 Serenitatis impact melt breccia: implications for the lunar bombardment history. LPI Contribution 2107.

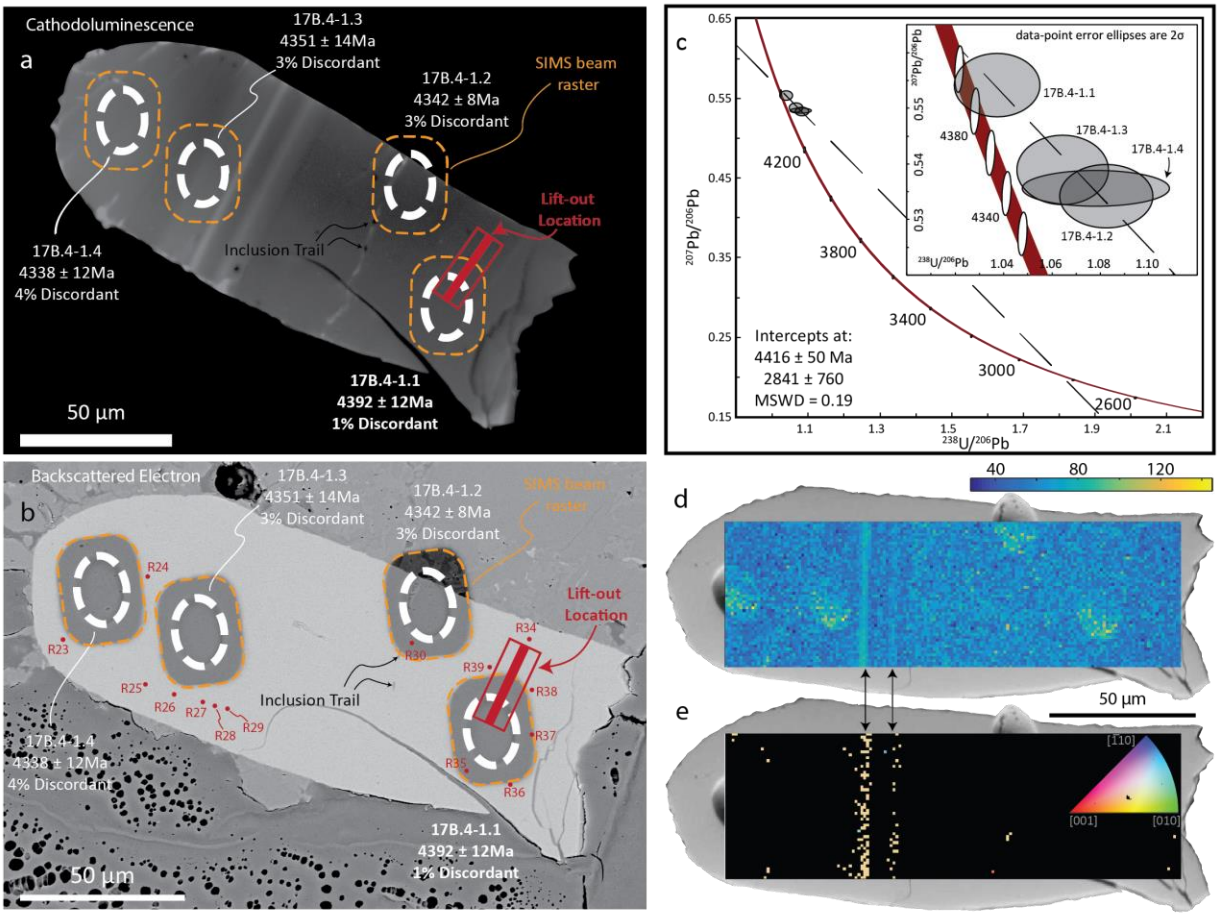

Figure 1: Summary of U-Pb, EBSD and Raman analysis of lunar zircon 17B-4. (**a**) CL image of 17B-4. SIMS pits and the location of the APT lift-out are indicated. Note: zircon 17B-4 appears isolated in the image as adjacent phases in the host breccia possess high (over saturated) relative CL intensities and have been removed for clarity. (**b**) Backscattered electron image of 17B-4 showing SIMS pits, APT lift-out, and adjacent breccia matrix (to the top right of grain). Black spots in bottom right corner are voids in epoxy. Raman spot analyses are shown as red dots. Labeled analyses correlate with data in Table 1 (**c**) Tera-Wasserburg concordia for U-Pb analyses on 17B-4. Labeled analyses correlate with ages in (**b**) and data in Table 1. Significance of the discordia regression is discussed in text. (**d**) band contrast and (**e**) crystal orientation from EBSD mapping. Dark pixels in Fig. 4e represent locations where no solution could be found for the observed electron backscatter diffraction pattern.

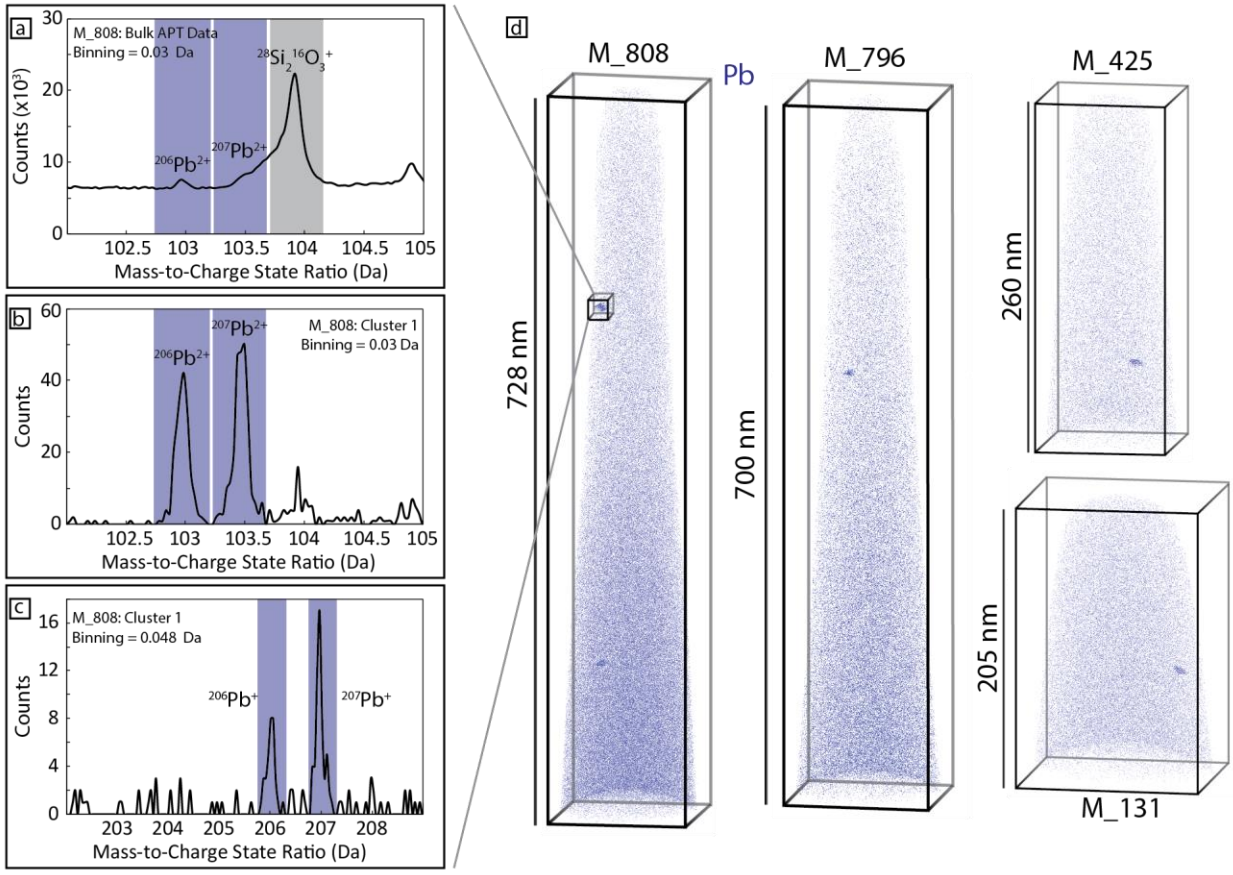

Figure 2: Summary of Pb data from APT data sets from Lunar zircon 17B-4, including representative spectra relevant to Pb characterization, (on the left) and Pb distributions shown on the right. (**a**) A representative example of the Pb peak-tailing interference at 104 Da with the position of doubly charged ^{206}Pb and ^{207}Pb at 103.0 and 103.5 Da respectively. (**b**) The same region of the mass spectra shown in (a) but for a single cluster in data set M_808. Doubly charged Pb isotopes are well resolved with minimal interference from the adjacent peak at 104 Da. (**c**) Peaks at 206 and 207 Da, consistent with the presence of singly charged Pb. (d) Pb atom maps for four APT specimens from the FIB lift-out (Fig. 1a and 1b), showing Pb rich clusters.

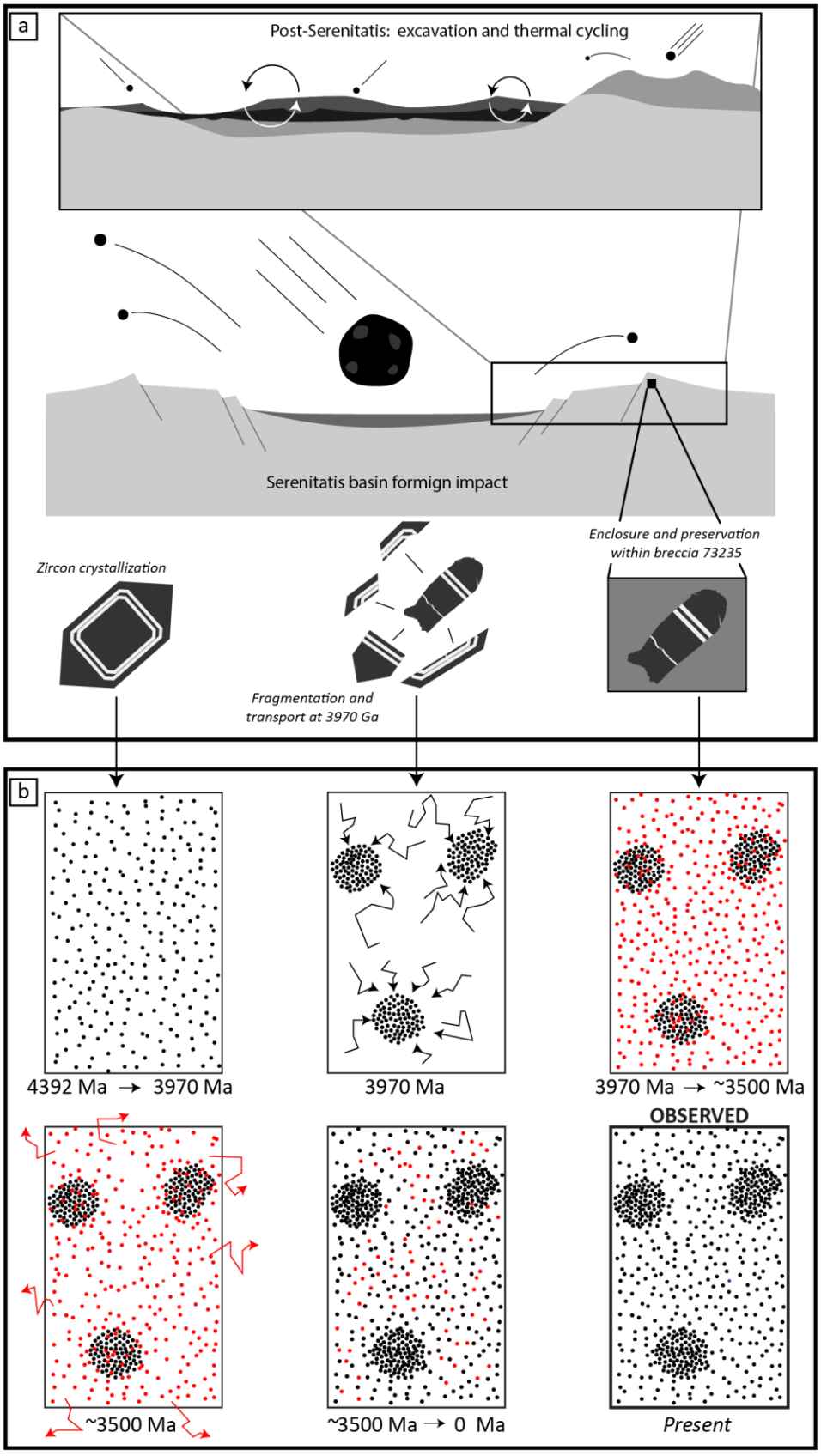
a
Post-Serenitatis: excavation and thermal cycling
Serenitatis basin formign impact
Zircon crystallization
Fragmentation and transport at 3970 Ga
Enclosure and preservation within breccia 73235
b
4392 Ma → 3970 Ma
3970 Ma
3970 Ma → ~3500 Ma
OBSERVED
~3500 Ma
~3500 Ma → 0 Ma
Present

Figure 3: Summary of the thermal/mechanical evolution of lunar zircon 17B-4. (**a**) The inferred geologic history for zircon 17B-4, collected in lunar breccia sample 73235 at the Apollo 17 landing site. After crystallization at 4392 Ma, the zircon was fragmented, transported and heated during the Serenitatis basin-forming impact (3970 Ma), followed by excavation and heating. (**b**) Schematic representation of the nanoscale Pb evolution of 73235, including: crystallization at 4392 Ma; Pb ingrowth, between 4392 Ma and the Serenitatis impact at 3970 Ma; cluster formation, clustering Pb at 3970 Ma; ingrowth of Pb from 3970 to ~3500 Ma; partial Pb-loss on the micron-scale at 3500 Ma (no Pb loss from clusters); and Pb ingrowth between 3500 Ma and the present.

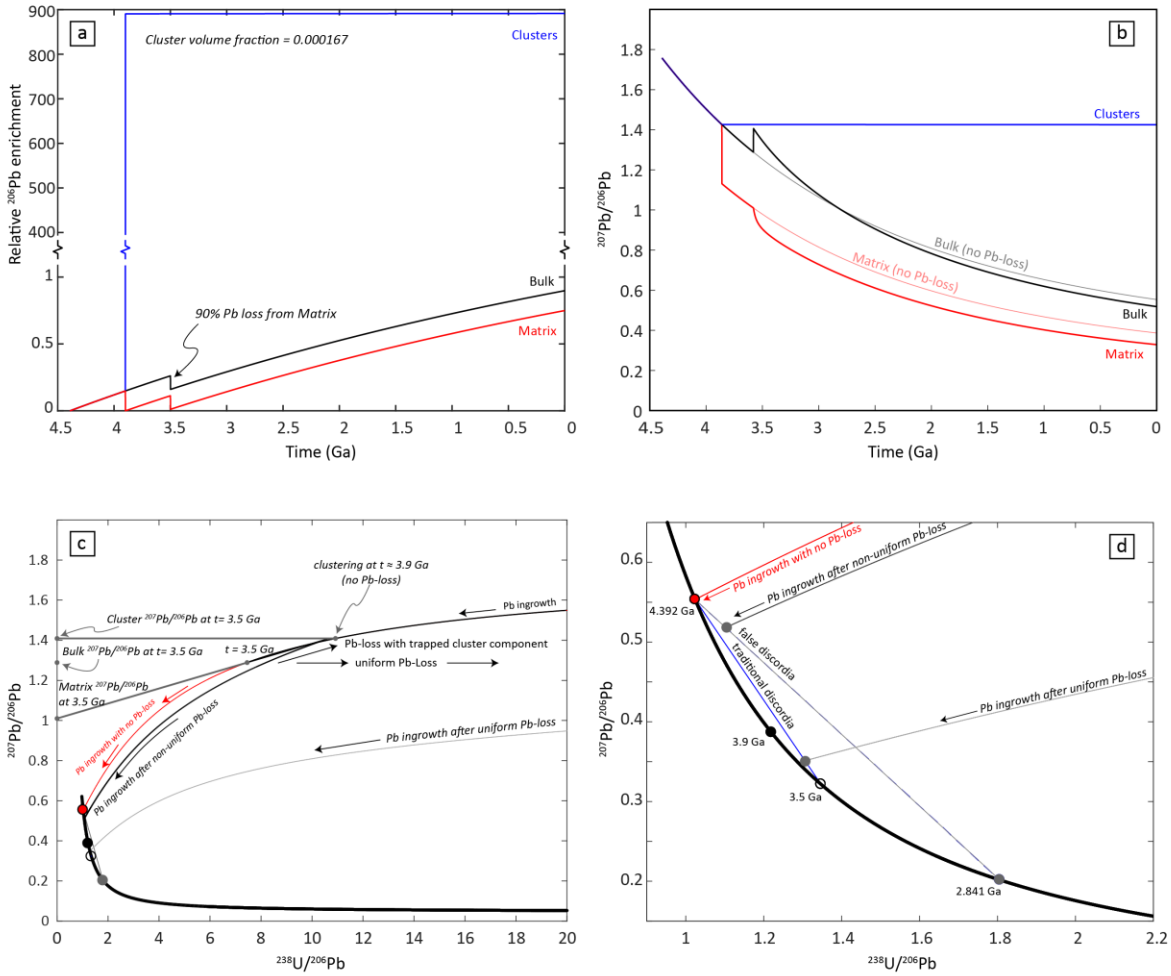

Figure 4: Summary of modeling for combine nanoscale clustering and subsequent Pb loss, following the model derived in this thesis, Chapter 5. Modeling uses a crystallization age of 4392 Ma, and a cluster formation age of 3900 Ma, and Pb-loss at 3500 Ma. (**a**) modeling of ^{206}Pb concentrations and ^{207}Pb/^{206}Pb vs. age (time before present). Concentrations are relative, and are normalized to the bulk Pb concentration accumulated from crystallization to the present. (**b**) Modeling of ^{207}Pb/^{206}Pb ratios in different domains (clusters, bulk zircon, and matrix zircon outside of clusters) in cases with and without Pb loss at 3500 Ma. x-axis is time before present. **(c)** Wide view of Tera-Wasserburg concordia showing Pb ingrowth curves. Pb ingrowth curves show cluster isotope ratios, traditional Pb loss (no clustering) and Pb loss (with clustering, see text for details). The red curve shows ingrowth with no Pb loss; the grey ingrowth curve tracks bulk (micron-scale isotope ratios traditional Pb loss (no clustering), and the black ingrowth curve tracks the bulk (micron scale) isotope ratios for Pb-loss with clustering. **(d)** close-up view of the Tera-Wasserburg concordia diagram from (**c**), showing the end-points for the data in figure 4c. Note that traditional Pb loss (no clustering) results in microns scale data that fall on the 3500 Ma discordia, while Pb loss in the presence of nanoclusters generates a false concordia, requiring additional information in order to interpret. See text for further details.

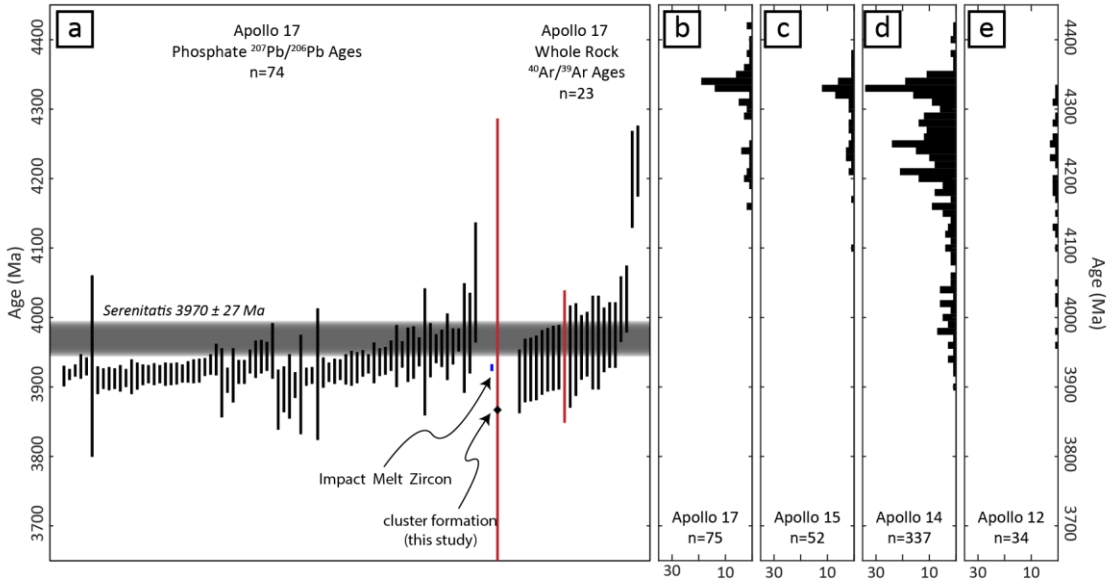

Figure 5: **(a)** Summary of geochronology from Apollo 17, including $^{40}Ar/^{39}Ar$ (Dalrymple and Ryder, 1996; Turner and Cadogan, 1975), impact-melt zircon (Zhang et al., 2018) and U-Pb phosphates (Thiessen et al., 2017) and Pb-nanoclusters in zircon (this study). All Ar-Ar ages have been corrected for updated decay constants and fluence monitor ages (see text for discussion). Age of Serenitatis (3970 ± 26 Ma) based on Stöffler et al., 2006. **(b-e)** Summary of zircon crystallization ages for Apollo 12, 14, 15 and 17 (this thesis, Chapter 4; see Chapter 4 for references).

Table 1: Summary of SHRIMP-RG U-Pb age analyses for lunar zircon 17B-4.

Zircon - Spot	Th (µg/g)	U (µg/g)	Th/U	$^{204}Pb/^{206}Pb$	1σ	$^{207}Pb^*/^{206}Pb^*$	1σ	$^{207}Pb^*/^{235}U$	1σ	$^{206}Pb^*/^{238}U$	1σ	ρ	$^{206}Pb^*/^{238}U$ Age (Ma)	1σ (Ma)	$^{207}Pb^*/^{206}Pb^*$ Age (Ma)	1σ (Ma)	Disc.
17B.4-1.1	109	187	0.58	-3.4E-6	100	0.554	0.42	73.7	0.8	0.964	0.7	0.86	4351	22	4392	6	+1
17B.4-1.2	115	200	0.57	1.6E-5	50	0.536	0.25	68.5	1.2	0.928	1.2	0.98	4230	36	4342	4	+3
17B.4-1.3	81	158	0.51	-1.2E-5	58	0.539	0.47	69.8	0.9	0.939	0.7	0.84	4270	23	4351	7	+3
17B.4-1.4	105	156	0.68	2.0E-5	45	0.534	0.43	68.1	0.8	0.924	0.7	0.86	4218	23	4338	6	+4

*indicates ^{204}Pb corrected radiogenic Pb.
errors are 1σ (%) unless otherwise specified.

Table 2: Summary of Pb isotope data for clustered regions of 17B-4 APT data sets.

	^{206}T	^{206}B	^{206}S	^{207}T	^{207}B	^{207}S	$^{207}Pb/^{206}Pb$	±2σ	^{206}T	^{206}B	^{206}S	^{207}T	^{207}B	^{207}S	$^{207}Pb/^{206}Pb$	±2σ	$^{207}Pb/^{206}Pb$	±2σ	$t_{cluster}$	±2σ
	Pb^{2+} at 103.0 and 103.5 Da								Pb^+ at 206 and 207 Da								Total Pb (Pb^{2+} and Pb^+)		(Ga)	(Ga)
M_425																				
Cluster 1	156	8.2	147.8	214	8.8	205.2	1.39	0.31	22	11.1	10.9	26	8.6	17.4	1.60	1.67	1.40	0.17	3.81	-0.36/ +0.30
M_808																				
Cluster 1	192	3.7	188.3	254	4.7	249.3	1.32	0.26	33	5.8	27.2	56	5.2	50.8	1.87	0.96	1.39	0.14	3.79	-0.30/ +0.25
Cluster 2	64	6.0	58.0	101	7.5	93.5	1.61	0.56	5	1.5	3.5	10	1.3	8.7	2.46	3.61	1.66	0.27	4.25	-0.47/ +0.14
M_796																				
Cluster 1	124	6.8	117.2	172	7.2	164.9	1.41	0.35	44	4.6	39.4	41	6.0	35.0	0.89	0.44	1.28	0.17	3.56	-0.42/ +0.34
M_131																				
Cluster 1	192	19.9	172.1	261	16.7	244.3	1.42	0.30	-	-	-	-	-	-	-	-	1.42	0.30	3.85	-0.68/ +0.48
M_168‡																				
Cluster 1	-	-	-	-	-	-	-	-	38	7.5	30.6	64	7.5	56.9	1.85	0.92	1.85	0.92	4.39	-1.84/ +0
TOTAL	**728**	**44.5**	**683.5**	**1002**	**44.8**	**957.2**	**1.40**	0.14	**142**	**30.4**	**111.6**	**197**	**28.6**	**168.7**	**1.51**	0.41	**1.42**	0.07	**3.85**	- 0.17/0. 15

n = number of clusters; T = total counts; B = background counts; S = signal = T-B
‡Data set M_168 is from a straight flight path instrument, and the 103.0 and 103.5 Da ranges are insufficiently resolved to produce confident measurement of $^{206}Pb^{2+}$ and $^{207}Pb^{2+}$ signals. We note that this is considered independently from overlaps with 104 Da peak tails (see text for further discussion).

Table 3: Atom probe tomography data acquisition settings and run summary for zircon 17B-4.

Specimen/Data Set	**R5091_168796**	**R5091_168808**	**R5091_169425**
Instrument Model	**LEAP 5000 XR**	**LEAP 5000 XR**	**LEAP 5000 XR**
Instrument Settings			
Laser Wavelength (nm)	355	355	355
Laser Pulse Energy (pJ)	400	400	200
Pulse Frequency (kHz)	(variable)	(variable)	125
Evaporation Control	Detection Rate	Detection Rate	Detection Rate
Target Detection Rate (ions/pulse)	0.005	0.005-0.01	0.005
Nominal Flight Path (mm)	382	382	382
Set Point Temperature (K)	50	50	50
Sample Temperature (K)	50.0	49.81	50.02
Chamber Pressure (Torr)	$3.2x10^{-11}$	$6.4x10^{-11}$	$1.2x10^{-10}$
Data Summary			
LAS Root Version	15.41.342j	15.41.342j	15.41.342j
CAMECAROOT Version	15.43.393e	15.43.393e	15.43.393e
Analysis Software			
Total Ions:	212,086,142	194,982,288	50,000,142
Single	168,779,827	148,609,349	37,137,873
Multiple	41,672,301	44,902,389	1,277,763
Partial	1,634,014	1,470,550	484,506
Volt./Bowl Corr. Peak (Da)	16 Da	16 Da	16 Da
Mass Calib. (peaks/interp.)	9/lin.	9/lin.	9/lin.
†(M/ΔM) for $^{16}O_2^+$	1309	1308	1298
††($M/\Delta M_{10}$)	605	604	594
time independent background (ppm/ns)	38.1	33.2	43.9
Reconstruction			
Pre-/Post-analysis Imaging	SEM/none	SEM/none	SEM/none
Radius Evolution Model	Voltage	Voltage	Voltage
Field Factor (k)	3.3	3.3	3.3
Image Compression Factor	1.65	1.65	1.65
Evap. Field (V/nm)	28.0	28.0	28.0
Detector Efficiency	0.52	0.52	0.52
Avg. Atomic Volume (nm^3)	0.0108	0.0108	0.0108

†ΔM is full width at half maximum.
††ΔM_{10} is full width at tenth maximum.

Table 3 (cont.): Atom probe tomography data acquisition settings and run summary for zircon 17B-4.

Specimen/Data Set	**R5079_171168**	**R5091_171131**
Instrument Model	**LEAP 5000 XS**	**LEAP 5000 XR**
Instrument Settings		
Laser Wavelength (nm)	355	355
Laser Pulse Energy (pJ)	300	300
Pulse Frequency (kHz)	variable	(variable)
Evaporation Control	Detection Rate	Detection Rate
Target Detection Rate (ions/pulse)	0.005	0.005
Nominal Flight Path (mm)	100	382
Set Point Temperature (K)	50	50
Sample Temperature (K)	41.4	60.02
Chamber Pressure (Torr)	2.3×10^{-10}	6.0×10^{-11}
Data Summary		
LAS Root Version	15.43.393k	15.41.342j
CAMECAROOT Version	15.43.393e	15.43.393e
Analysis Software		
Total Ions:	202,552,578	75,091,406
Single	154,980,331	58,536,267
Multiple	43,761,379	15,751,178
Partial	3,810,868	803,961
Volt./Bowl Corr. Peak (Da)	16	16 Da
Mass Calib. (peaks/interp.)	9/lin.	9/lin.
$^{\dagger}(M/\Delta M)$ for $^{16}O_2^+$	724	1309
$^{\dagger\dagger}(M/\Delta M_{10})$	316	581
time independent background (ppm/ns)	180.9	68.5
Reconstruction		
Pre-/Post-analysis Imaging	SEM/none	SEM/none
Radius Evolution Model	Voltage	Voltage
Field Factor (k)	3.3	3.3
Image Compression Factor	1.65	1.65
Evap. Field (V/nm)	28.0	28.0
Detector Efficiency	0.80	0.52
Avg. Atomic Volume (nm^3)	0.0108	0.0108

$^{\dagger}\Delta M$ is full width at half maximum.

$^{\dagger\dagger}\Delta M_{10}$ is full width at tenth maximum.

APPENDICES

Appendix 1: Summary of sample splits, and lithologic associations for lunar zircon grains studies in Chapters 4 and 5.

Zircon	Mission	Sample	Lithology/Textural Relation
12R-1	Apollo 12	12023,1	unconsolidated regolith (< 1 mm fraction)
12R-2	Apollo 12	12023,1	unconsolidated regolith (< 1 mm fraction)
12R-3	Apollo 12	12023,1	unconsolidated regolith (< 1 mm fraction)
12R-7	Apollo 12	12023,1	unconsolidated regolith (< 1 mm fraction)
12R-8	Apollo 12	12023,1	unconsolidated regolith (< 1 mm fraction)
14R-1	Apollo 14	14240,1	unconsolidated regolith (< 1 mm fraction)
14R-2	Apollo 14	14240,1	unconsolidated regolith (< 1 mm fraction)
14R-3	Apollo 14	14240,1	unconsolidated regolith (< 1 mm fraction)
14R-4	Apollo 14	14240,80	unconsolidated regolith (< 1 mm fraction)
15Q-3	Apollo 15	15405, 217	fractured zircon, separated from quartz monzodiorite clast
15Q-4	Apollo 15	15405, 217	fractured zircon, separated from quartz monzodiorite clast
15B-1-1	Apollo 15	15455,55	isolated grain within impact melt breccia
15B-1-2	Apollo 15	15455,55	isolated grain within impact melt breccia
17B-4	Apollo 17	73235,87	isolated grain within impact melt breccia

Appendix 2: Summary of analytical conditions for electron backscatter diffraction mapping. See Chapters 4 and 5 for further analytical details and summary of results.

SEM Model	**Hitachi S3400-N**	**Hitachi S3400-N**	**Hitachi S3400-N**	**Hitachi S3400-N**	**Hitachi S3400-N**	**Hitachi S3400-N**
Zircon/Map	**12R-2**	**12R-7_1**	**12R-7_2**	**15Q-3**	**15Q-4**	**17B-4**
Instrument Settings						
EBSD Software	HKL Channel 5	HKL Channel 5	HKL Channel 5	HKL Channel 5	HKL Channel 5	HKL Channel 5
Conductive Coat	None	None	None	None	None	None
Acc. Voltage (kV)	20	20	20	20	20	20
Working Distance (mm)	23.5	23.5	23.5	23.5	23.5	23.5
Spot Size	-	-	-	-	-	-
Tilt	70°	70°	70°	70°	70°	70°
Software and Acquisition Settings						
EBSP collection time per frame (ms)	45	45	45	43	45	45
EBSP noise reduction (frames)	400	400	400	400	400	400
Binning	2x2	2x2	2x2	2x2	2x2	2x2
Gain	(high)	(high)	(high)	(high)	(high)	(high)
Hough Resolution	70	70	70	70	70	70
Band Detect.(min/max)	6/7	6/7	6/7	6/7	6/7	6/7
Mean band contrast	115.8	130.3	129.5	132.9	112.5	69.4
X steps	142	209	74	414	222	156
Y steps	186	94	135	256	135	50
Step Distance (μm)	0.5	1.0	0.5	0.25	0.5	1.0
*Average MAD**	0.3849	0.4434	0.449	0.472	0.3963	0.7222
Noise Reduction	none	none	none		none	none
n neighbor zero solution extrapolation	-	-	-	-	-	-
Kuwahara Filter	-	-	-	-	-	-
Data Analysis Software	MTEX (v4.3.1)	MTEX (v4.3.1)	MTEX (v4.3.1)	MTEX (v4.3.1)	MTEX (v4.3.1)	MTEX (v4.3.1)

*Mean Angular Deviation

Appendix 3: Summary of $v_3(SiO_4)$ Raman measurements for lunar zircon grains. See Chapters 4 and 5 for analytical details and discussion of results. SHRIMP-RG in column 2 correlate with data in Table 1 of Chapter 4.

Raman Spot Analysis	SHRIMP-RG Analysis	Wavenumber Shift	$FWHM_{v3(SiO4)}$ (Meas.)	$FWHM_{v3(SiO4)}$ (Corr.)	Th	U	$^{207}Pb/^{206}Pb$ Age	D_{total}	D_{eff}	Frac. Dose	Radiation Damage Age
		(cm^{-1})	(cm^{-1})	(cm^{-1})	(µg/g)	(µg/g)	(Ma)	(10^{15} α/mg)	(10^{15} α/mg)	(10^{15} α/mg)	(Ma)
12R-1_4	12R.1-1.3	1004.21	7.93	7.84	29	42	**4054**	**1.12**	**0.47**	**0.42**	2329
12R-1_5	12R.1-1.3	1004.39	7.90	7.81	29	42	**4054**	**1.12**	**0.47**	**0.42**	2329
12R-1_6	12R.1-1.3	1004.33	8.14	8.05	29	42	**4054**	**1.12**	**0.49**	**0.44**	2403
Mean		1004.31	7.99	7.90							
S.D.		0.09	0.13	0.13							
Max		1004.39	8.14	8.05							
Min		1004.21	7.90	7.81							
12R-1_10	12R.1-1.1	1004.37	8.08	7.99	25	37	**4054**	**0.99**	**0.49**	**0.49**	2642
12R-1_11	12R.1-1.1	1004.45	8.21	8.12	25	37	**4054**	**0.99**	**0.49**	**0.50**	2642
12R-1_12	12R.1-1.1	1004.67	8.11	8.02	25	37	**4054**	**0.99**	**0.49**	**0.49**	2642
Mean		1004.50	8.13	8.05							
S.D.		0.16	0.07	0.07							
Max		1004.67	8.21	8.12							
Min		1004.37	8.08	7.99							
12R-1_14	12R.1-1.2	1004.48	8.16	8.07	25	37	**4054**	**0.99**	**0.49**	**0.50**	2642
12R-1_15	12R.1-1.2	1004.81	8.23	8.14	25	37	**4054**	**0.99**	**0.50**	**0.50**	2681
12R-1_16	12R.1-1.2	1004.79	7.93	7.84	25	37	**4054**	**0.99**	**0.47**	**0.48**	2564
Mean		1004.69	8.11	8.02							
S.D.		0.19	0.16	0.16							
Max		1004.81	8.23	8.14							
Min		1004.48	7.93	7.84							

Raman Spot Analysis	SHRIMP-RG Analysis	Wavenumber Shift	$FWHM_{v3(SiO4)}$ (Meas.)	$FWHM_{v3(SiO4)}$ (Corr.)	Th	U	$^{207}Pb/^{206}Pb$ Age	D_{total}	D_{eff}	Frac. Dose	Radiation Damage Age
12R-2_2	12R.2-1.1	1005.25	6.00	5.88	11	32	**4103**	**0.84**	0.33	**0.40**	2292
12R-2_3	12R.2-1.1	1005.42	6.12	6.01	11	32	**4103**	**0.84**	0.34	**0.41**	2344
12R-2_4	12R.2-1.1	1005.47	6.12	6.01	11	32	**4103**	**0.84**	0.34	**0.41**	2344
Mean		1005.38	6.08	5.96							
S.D.		0.12	0.07	0.07							
Max		1005.47	6.12	6.01							
Min		1005.25	6.00	5.88							
12R-2_6	12R.2-1.2	1004.59	7.28	7.18	14	45	**4103**	**1.17**	0.43	**0.36**	2172
12R-2_7	12R.2-1.2	1005.3	6.29	6.18	14	45	**4103**	**1.17**	0.36	**0.30**	1888
12R-2_8	12R.2-1.2	1004.86	7.08	6.98	14	45	**4103**	**1.17**	0.41	**0.35**	2093
Mean		1004.92	6.88	6.78							
S.D.		0.36	0.52	0.53							
Max		1005.30	7.28	7.18							
Min		1004.59	6.29	6.18							
12R-2_10	12R.2-1.3	1005	6.28	6.17	17	47	**4103**	**1.23**	0.35	**0.29**	1766
12R-2_11	12R.2-1.3	1005.02	6.86	6.76	17	47	**4103**	**1.23**	0.40	**0.32**	1969
12R-2_12	12R.2-1.3	1004.56	7.05	6.95	17	47	**4103**	**1.23**	0.41	**0.33**	2008
Mean		1004.86	6.73	6.63							
S.D.		0.26	0.40	0.41							
Max		1005.02	7.05	6.95							
Min		1004.56	6.28	6.17							

Raman Spot Analysis	SHRIMP-RG Analysis	Wavenumber Shift	$FWHM_{v3(SiO4)}$ (Meas.)	$FWHM_{v3(SiO4)}$ (Corr.)	Th	U	$^{207}Pb/^{206}Pb$ Age	D_{total}	D_{eff}	Frac. Dose	Radiation Damage Age
12R-3_2	12R.3-1.1	1005.41	5.11	4.97	9	17	**3960**	**0.43**	**0.27**	**0.63**	3042
12R-3_3	12R.3-1.1	1005.23	5.31	5.18	9	17	**3960**	**0.43**	**0.28**	**0.67**	3115
12R-3_4	12R.3-1.1	1005.23	5.27	5.14	9	17	**3960**	**0.43**	**0.28**	**0.66**	3115
Mean		1005.29	5.23	5.10							
S.D.		0.10	0.11	0.11							
Max		1005.41	5.31	5.18							
Min		1005.23	5.11	4.97							
12R-3_5	12R.3-1.2	1005.26	5.72	5.60	9	17	**3960**	**0.43**	**0.31**	**0.74**	3320
12R-3_7	12R.3-1.2	1004.77	5.63	5.51	9	17	**3960**	**0.43**	**0.31**	**0.72**	3320
12R-3_8	12R.3-1.2	1005.47	5.45	5.32	9	17	**3960**	**0.43**	**0.29**	**0.69**	3185
Mean		1005.17	5.60	5.47							
S.D.		0.36	0.14	0.14							
Max		1005.47	5.72	5.60							
Min		1004.77	5.45	5.32							
12R-7_2	12R.7-1.5	1003.81	7.71	7.62	23	38	**4202**	**1.08**	**0.46**	**0.42**	2497
12R-7_3	12R.7-1.5	1004.16	7.59	7.50	23	38	**4202**	**1.08**	**0.45**	**0.42**	2456
12R-7_4	12R.7-1.5	1004.17	7.64	7.55	23	38	**4202**	**1.08**	**0.45**	**0.42**	2456
Mean		1004.05	7.65	7.55							
S.D.		0.21	0.06	0.06							
Max		1004.17	7.71	7.62							
Min		1003.81	7.59	7.50							

Raman Spot Analysis	SHRIMP-RG Analysis	Wavenumber Shift	$FWHM_{v3(SiO4)}$ (Meas.)	$FWHM_{v3(SiO4)}$ (Corr.)	Th	U	$^{207}Pb/^{206}Pb$ Age	D_{total}	D_{eff}	Frac. Dose	Radiation Damage Age
12R-7_5	12R.7-1.4	1003.42	7.86	7.77	24	39	**4202**	**1.11**	**0.47**	**0.42**	2485
12R-7_6	12R.7-1.4	1003.66	8.00	7.91	24	39	**4202**	**1.11**	**0.48**	**0.43**	2524
12R-7_9	12R.7-1.4	1002.93	8.35	8.27	24	39	**4202**	**1.11**	**0.50**	**0.45**	2600
Mean		1003.34	8.07	7.98							
S.D.		0.37	0.25	0.26							
Max		1003.66	8.35	8.27							
Min		1002.93	7.86	7.77							
12R-7_10d	12R.7-1.3	1002.91	8.59	8.51	26	40	**4202**	**1.15**	**0.52**	**0.46**	2615
12R-7_11	12R.7-1.3	1003.57	8.00	7.91	26	40	**4202**	**1.15**	**0.48**	**0.42**	2467
12R-7_12	12R.7-1.3	1003.58	8.11	8.02	26	40	**4202**	**1.15**	**0.49**	**0.42**	2505
Mean		1003.35	8.23	8.15							
S.D.		0.38	0.31	0.32							
Max		1003.58	8.59	8.51							
Min		1002.91	8.00	7.91							
12R-7_13	12R.7-1.2	1002.34	10.43	10.36	24	39	**4202**	**1.11**	**0.65**	**0.59**	3112
12R-7_14	12R.7-1.2	1003.57	7.85	7.76	24	39	**4202**	**1.11**	**0.47**	**0.42**	2485
12R-7_15	12R.7-1.2	1003.39	9.01	8.93	24	39	**4202**	**1.11**	**0.55**	**0.50**	2782
Mean		1003.10	9.10	9.02							
S.D.		0.66	1.29	1.30							
Max		1003.57	10.43	10.36							
Min		1002.34	7.85	7.76							

Raman Spot Analysis	SHRIMP-RG Analysis	Wavenumber Shift	$FWHM_{v3(SiO4)}$ (Meas.)	$FWHM_{v3(SiO4)}$ (Corr.)	Th	U	$^{207}Pb/^{206}Pb$ Age	D_{total}	D_{eff}	Frac. Dose	Radiation Damage Age
12R-7_16	12R.7-1.1	1003.53	7.72	7.63	20	33	**4202**	**0.94**	**0.46**	**0.49**	2762
12R-7_17	12R.7-1.1	1003.96	7.50	7.41	20	33	**4202**	**0.94**	**0.44**	**0.47**	2677
12R-7_18	12R.7-1.1	1003.55	7.70	7.61	20	33	**4202**	**0.94**	**0.46**	**0.49**	2762
Mean		1003.68	7.64	7.55							
S.D.		0.24	0.12	0.12							
Max		1003.96	7.72	7.63							
Min		1003.53	7.50	7.41							
12R-8_2	12R.8-1.3	1002.98	10.53	10.46	30	77	**4253**	**2.19**	**0.66**	**0.30**	1972
12R-8_3	12R.8-1.3	1001.88	10.23	10.16	30	77	**4253**	**2.19**	**0.64**	**0.29**	1923
12R-8_4	12R.8-1.3	1003.51	9.85	9.78	30	77	**4253**	**2.19**	**0.61**	**0.28**	1850
Mean		1002.79	10.20	10.13							
S.D.		0.83	0.34	0.34							
Max		1003.51	10.53	10.46							
Min		1001.88	9.85	9.78							
12R-8_5	12R.8-1.2	1003.42	9.87	9.80	29	75	**4253**	**2.13**	**0.61**	**0.29**	1891
12R-8_7	12R.8-1.2	1003.89	8.83	8.75	29	75	**4253**	**2.13**	**0.54**	**0.25**	1711
12R-8_8	12R.8-1.2	1003.3	9.39	9.31	29	75	**4253**	**2.13**	**0.58**	**0.27**	1815
Mean		1003.54	9.36	9.29							
S.D.		0.31	0.52	0.52							
Max		1003.89	9.87	9.80							
Min		1003.30	8.83	8.75							

Raman Spot Analysis	SHRIMP-RG Analysis	Wavenumber Shift	$FWHM_{v3(SiO4)}$ (Meas.)	$FWHM_{v3(SiO4)}$ (Corr.)	Th	U	$^{207}Pb/^{206}Pb$ Age	D_{total}	D_{eff}	Frac. Dose	Radiation Damage Age
12R-8_10	12R.8-1.1	1003.86	8.59	8.51	20	58	**4253**	**1.64**	**0.52**	**0.32**	2057
12R-8_11	12R.8-1.1	1003.86	8.75	8.67	20	58	**4253**	**1.64**	**0.53**	**0.32**	2088
12R-8_12	12R.8-1.1	1003.78	7.69	7.60	20	58	**4253**	**1.64**	**0.46**	**0.28**	1865
Mean		1003.83	8.34	8.26							
S.D.		0.05	0.57	0.58							
Max		1003.86	8.75	8.67							
Min		1003.78	7.69	7.60							
14R-1_2	14R.1-1.1	1006.51	4.50	4.35	5	11	**4273**	**0.32**	**0.22**	**0.70**	3530
14R-1_3	14R.1-1.1	1006.68	4.19	4.02	5	11	**4273**	**0.32**	**0.20**	**0.63**	3337
14R-1_4	14R.1-1.1	1006.66	4.33	4.17	5	11	**4273**	**0.32**	**0.21**	**0.66**	3436
14R-1_5	14R.1-1.1	1006.69	4.21	4.04	5	11	**4273**	**0.32**	**0.20**	**0.64**	3337
Mean		1006.64	4.31	4.15							
S.D.		0.08	0.14	0.15							
Max		1006.69	4.50	4.35							
Min		1006.51	4.19	4.02							
14R-1_6	14R.1-1.2	1006.67	4.21	4.04	4	10	**4273**	**0.29**	**0.20**	**0.71**	3547
14R-1_7	14R.1-1.2	1006.78	4.35	4.19	4	10	**4273**	**0.29**	**0.21**	**0.74**	3645
14R-1_8	14R.1-1.2	1006.7	4.17	4.00	4	10	**4273**	**0.29**	**0.20**	**0.70**	3547
Mean		1006.72	4.24	4.08							
S.D.		0.06	0.09	0.10							
Max		1006.78	4.35	4.19							
Min		1006.67	4.17	4.00							

Raman Spot Analysis	SHRIMP-RG Analysis	Wavenumber Shift	$FWHM_{v3(SiO4)}$ (Meas.)	$FWHM_{v3(SiO4)}$ (Corr.)	Th	U	$^{207}Pb/^{206}Pb$ Age	D_{total}	D_{eff}	Frac. Dose	Radiation Damage Age
14R-2_2	14R.2-1.3	1004.91	5.74	5.62	11	23	4347	0.70	0.32	**0.45**	2799
14R-2_3	14R.2-1.3	1005.51	5.20	5.07	11	23	4347	0.70	0.28	**0.40**	2547
Mean		1005.21	5.47	5.34							2673
S.D.		0.42	0.38	0.39							
Max		1005.51	5.74	5.62							
Min		1004.91	5.20	5.07							
14R-2_4	14R.2-1.1	1005.87	4.76	4.61	15	26	4347	0.80	0.24	**0.31**	2035
14R-2_5	14R.2-1.1	1005.99	4.73	4.58	15	26	4347	0.80	0.24	**0.30**	2035
Mean		1005.93	4.75	4.60							2035
S.D.		0.08	0.02	0.02							
Max		1005.99	4.76	4.61							
Min		1005.87	4.73	4.58							
14R-2_6	14R.2-1.2	1005.68	5.10	4.96	9	28	4347	0.83	0.27	**0.32**	2184
14R-2_7	14R.2-1.2	1005.69	4.60	4.45	9	28	4347	0.83	0.23	**0.28**	1925
14R-2_9	14R.2-1.2	1007.00	3.93	3.75	9	28	4347	0.83	0.18	**0.22**	1573
Mean		1006.12	4.54	4.39							1749
S.D.		0.76	0.59	0.61							
Max		1007.00	5.10	4.96							
Min		1005.68	3.93	3.75							

Raman Spot Analysis	SHRIMP-RG Analysis	Wavenumber Shift	$FWHM_{v3(SiO4)}$ (Meas.)	$FWHM_{v3(SiO4)}$ (Corr.)	Th	U	$^{207}Pb/^{206}Pb$ Age	D_{total}	D_{eff}	Frac. Dose	Radiation Damage Age
14R-4_2	14R.4-1.1	1006.28	4.88	4.74	6	16	**4252**	**0.45**	0.25	**0.56**	3059
14R-4_3	14R.4-1.1	1006.24	4.89	4.75	6	16	**4252**	**0.45**	0.25	**0.56**	3059
14R-4_4	14R.4-1.1	1006.39	4.86	4.72	6	16	**4252**	**0.45**	0.25	**0.55**	3059
14R-4_5	14R.4-1.1	1006.01	4.97	4.83	6	16	**4252**	**0.45**	0.26	0.57	3137
Mean		1006.23	4.90	4.76							
S.D.		0.16	0.05	0.05							
Max		1006.39	4.97	4.83							
Min		1006.01	4.86	4.72							
15Q-3_2	15Q.3-1.1	1000.97	12.84	12.78	28	82	**4344**	**2.43**	**0.83**	**0.34**	2260
15Q-3_3	15Q.3-1.1	1001.04	13.02	12.97	28	82	**4344**	**2.43**	**0.84**	**0.35**	2281
15Q-3_4	15Q.3-1.1	1000.95	12.92	12.87	28	82	**4344**	**2.43**	**0.83**	**0.34**	2260
Mean		1000.99	12.93	12.87							
S.D.		0.05	0.09	0.09							
Max		1001.04	13.02	12.97							
Min		1000.95	12.84	12.78							
15Q-3_5	15Q.3-1.2	1002.03	9.93	9.86	20	53	**4344**	**1.58**	**0.62**	**0.39**	2506
15Q-3_7	15Q.3-1.2	1003.51	7.40	7.31	20	53	**4344**	**1.58**	**0.44**	**0.28**	1925
15Q-3_8	15Q.3-1.2	1002.01	10.40	10.33	20	53	**4344**	**1.58**	**0.65**	**0.41**	2593
Mean		1002.52	9.24	9.17							
S.D.		0.86	1.61	1.63							
Max		1003.51	10.40	10.33							
Min		1002.01	7.40	7.31							

Raman Spot Analysis	SHRIMP-RG Analysis	Wavenumber Shift	$FWHM_{v3(SiO4)}$ (Meas.)	$FWHM_{v3(SiO4)}$ (Corr.)	Th	U	$^{207}Pb/^{206}Pb$ Age	D_{total}	D_{eff}	Frac. Dose	Radiation Damage Age
15Q-3_9	15Q.3-1.3	1000.98	12.21	12.15	26	70	**4344**	**2.08**	**0.78**	**0.38**	2420
15Q-3_10	15Q.3-1.3	1003.22	7.74	7.65	26	70	**4344**	**2.08**	**0.46**	**0.22**	1589
15Q-3_11	15Q.3-1.3	1002.09	9.73	9.66	26	70	**4344**	**2.08**	**0.60**	**0.29**	1977
Mean		1002.10	9.89	9.82							
S.D.		1.12	2.24	2.26							
Max		1003.22	12.21	12.15							
Min		1000.98	7.74	7.65							
15Q-4_1	15Q.4-1.1	1004.26	6.28	6.17	11	32	**4335**	**0.95**	**0.35**	**0.38**	2395
15Q-4_6	15Q.4-1.1	1003.68	6.02	5.90	11	32	**4335**	**0.95**	**0.34**	**0.36**	2344
Mean		1003.97	6.15	6.04							
S.D.		0.41	0.18	0.19							
Max		1004.26	6.28	6.17							
Min		1003.68	6.02	5.90							
15Q-4_11	15Q.4-1.2	1004.65	5.62	5.50	11	29	**4335**	**0.86**	**0.31**	**0.36**	2344
15Q-4_12	15Q.4-1.2	1004.18	5.82	5.70	11	29	**4335**	**0.86**	**0.32**	**0.37**	2400
15Q-4_13	15Q.4-1.2	1004.37	6.03	5.91	11	29	**4335**	**0.86**	**0.34**	**0.39**	2509
15Q-4_15	15Q.4-1.2	1004.39	5.83	5.71	11	29	**4335**	**0.86**	**0.32**	**0.37**	2400
15Q-4_16	15Q.4-1.2	1002.69	5.81	5.69	11	29	**4335**	**0.86**	**0.32**	**0.37**	2400
15Q-4_18	15Q.4-1.2	1004.52	5.52	5.39	11	29	**4335**	**0.86**	**0.30**	**0.35**	2286
Mean		1004.13	5.77	5.65							
S.D.		0.72	0.18	0.18							
Max		1004.65	6.03	5.91							
Min		1002.69	5.52	5.39							

Raman Spot Analysis	SHRIMP-RG Analysis	Wavenumber Shift	$FWHM_{v3(SiO4)}$ (Meas.)	$FWHM_{v3(SiO4)}$ (Corr.)	Th	U	$^{207}Pb/^{206}Pb$ Age	D_{total}	D_{eff}	Frac. Dose	Radiation Damage Age
15B-1-1-1_2	15B.1.1-1.1	1006.06	4.39	4.23	8	16	**4307**	**0.47**	0.22	**0.46**	2770
15B-1-1-1_3	15B.1.1-1.1	1006.45	4.11	3.94	8	16	**4307**	**0.47**	0.20	**0.41**	2589
15B-1-1-1_4	15B.1.1-1.1	1006.44	4.51	4.36	8	16	**4307**	**0.47**	0.23	**0.47**	2856
Mean		1006.32	4.34	4.18							
S.D.		0.22	0.21	0.21							
Max		1006.45	4.51	4.36							
Min		1006.06	4.11	3.94							
17B-4_23	17B.4-1.4	998.93	30.30	30.28	105	156	4392	4.90	2.08	0.42	2656
17B-4_24	17B.4-1.4	998.57	31.04	31.02	105	156	4392	4.90	2.13	0.43	2701
Mean		998.75	30.67	30.65							
S.D.		0.25	0.52	0.52							
Max		998.93	31.04	31.02							
Min		998.57	30.30	30.28							
17B-4_25	17B.4-1.3	999.16	30.84	30.82	81	158	4392	4.91	2.12	0.43	2719
17B-4_26	17B.4-1.3	997.46	30.04	30.02	81	158	4392	4.91	2.06	0.42	2664
17B-4_27	17B.4-1.3	998.32	30.70	30.68	81	158	4392	4.91	2.11	0.43	2710
17B-4_28	17B.4-1.3	998.27	30.60	30.58	81	158	4392	4.91	2.10	0.43	2701
17B-4_29	17B.4-1.3	997.82	30.49	30.47	81	158	4392	4.91	2.09	0.43	2692
Mean		998.21	30.53	30.51							
S.D.		0.64	0.30	0.30							
Max		999.16	30.84	30.82							
Min		997.46	30.04	30.02							

Raman Spot Analysis	SHRIMP-RG Analysis	Wavenumber Shift	$FWHM_{v3(SiO4)}$ (Meas.)	$FWHM_{v3(SiO4)}$ (Corr.)	Th	U	$^{207}Pb/^{206}Pb$ Age	D_{total}	D_{eff}	Frac. Dose	Radiation Damage Age
17B-4_30	17B.4-1.2	999.55	34.12	34.10	115	200	4392	6.26	2.35	0.38	2452
Mean		999.55	34.12	34.10							
S.D.		-	-	-							
Max		999.55	34.12	34.10							
Min		999.55	34.12	34.10							
17B-4_34	17B.4-1.1	1000.72	31.03	31.23	109	187	4392	5.86	2.14	0.37	2401
17B-4_35	17B.4-1.1	999.50	34.16	34.14	109	187	4392	5.86	2.35	0.40	2573
17B-4_36	17B.4-1.1	998.50	31.93	31.91	109	187	4392	5.86	2.19	0.37	2443
17B-4_37	17B.4-1.1	998.72	32.99	32.97	109	187	4392	5.86	2.27	0.39	2509
17B-4_38	17B.4-1.1	999.40	34.79	34.77	109	187	4392	5.86	2.40	0.41	2612
Mean		999.37	32.98	33.00							
S.D.		0.87	1.55	1.48							
Max		1000.72	34.79	34.77							
Min		998.50	31.03	31.23							

Appendix 4: Imaging and SIMS analyses for Lunar zircon grains (from Valley et al., 2014). Note that zircon grains 12R-5, 12R-6, 15Q-1, 15Q-2, and 15B-1-2 were not analyzed in the course of this thesis.

REFERENCES

Valley, J.W., Spicuzza, M.J., Ushikubo, T. (2014) Correlated $\delta^{18}O$ and [Ti] in lunar zircons: a terrestrial perspective for magma temperatures and water content on the Moon, Contributions to Mineralogy and Petrology, 167:956.

Figure A4.1 (below, pg. 199): BSE imaging of lunar zircon grains from Valley et al. (2014). Black circles denote 10 μm SIMS analyses for $\delta^{18}O$, and white circles are trace element analyses (including Ti). White numbers which include a single decimal denote oxygen isotope values (‰, VSMOW), while non-decimal values denote Ti concentrations (μg/g). See Valley et al. (2014) for further details.

Figure A4.2 (below, pg. 200): Cathodoluminescence images of lunar zircon grains from Valley et al. (2014). See Fig. A4.1 (above) for placement of oxygen and trace element SIMS analyses.

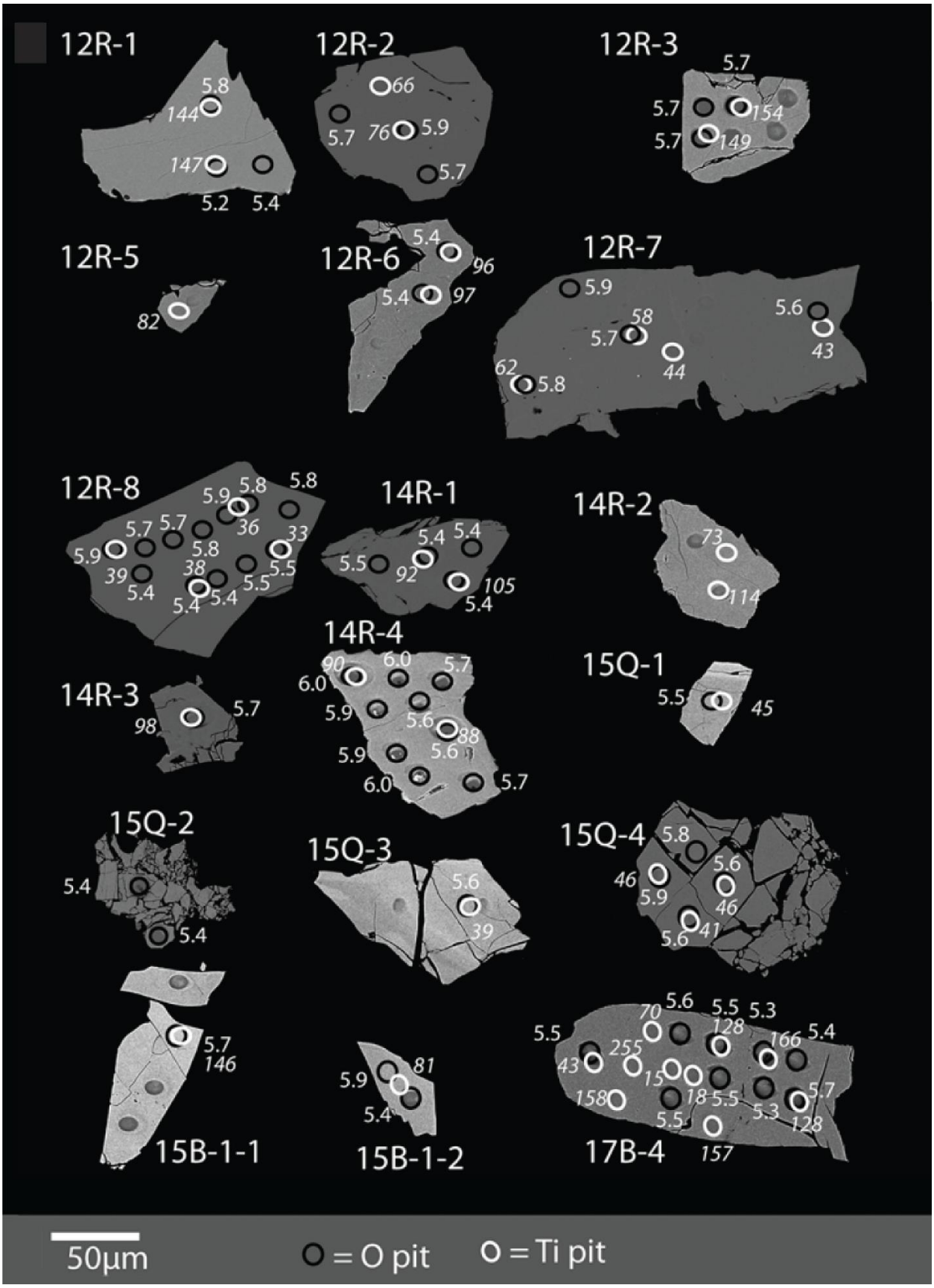
12R-1
5.8
144
147
5.2
5.4
12R-2
66
5.7
76
5.9
5.7
12R-3
5.7
5.7
154
5.7
149
12R-5
82
12R-6
5.4
96
5.4
97
12R-7
5.9
58
5.7
5.6
43
44
62
5.8
12R-8
5.9
5.8
5.8
5.7
5.7
36
33
5.9
5.8
39
38
5.5
5.5
5.4
5.4
5.4
14R-1
5.4
5.4
5.5
92
105
5.4
14R-2
73
114
14R-4
90
6.0
5.7
6.0
5.9
5.6
88
5.9
5.6
6.0
5.7
14R-3
98
5.7
15Q-1
5.5
45
15Q-2
5.4
5.4
15Q-3
5.6
39
15Q-4
5.8
46
5.6
5.9
46
5.6
41
5.7
146
15B-1-1
5.9
81
5.4
15B-1-2
5.5
70
5.6
5.5
5.3
128
166
5.4
43
255
15
158
18
5.5
5.3
5.7
128
5.5
157
17B-4
50µm
O = O pit
O = Ti pit

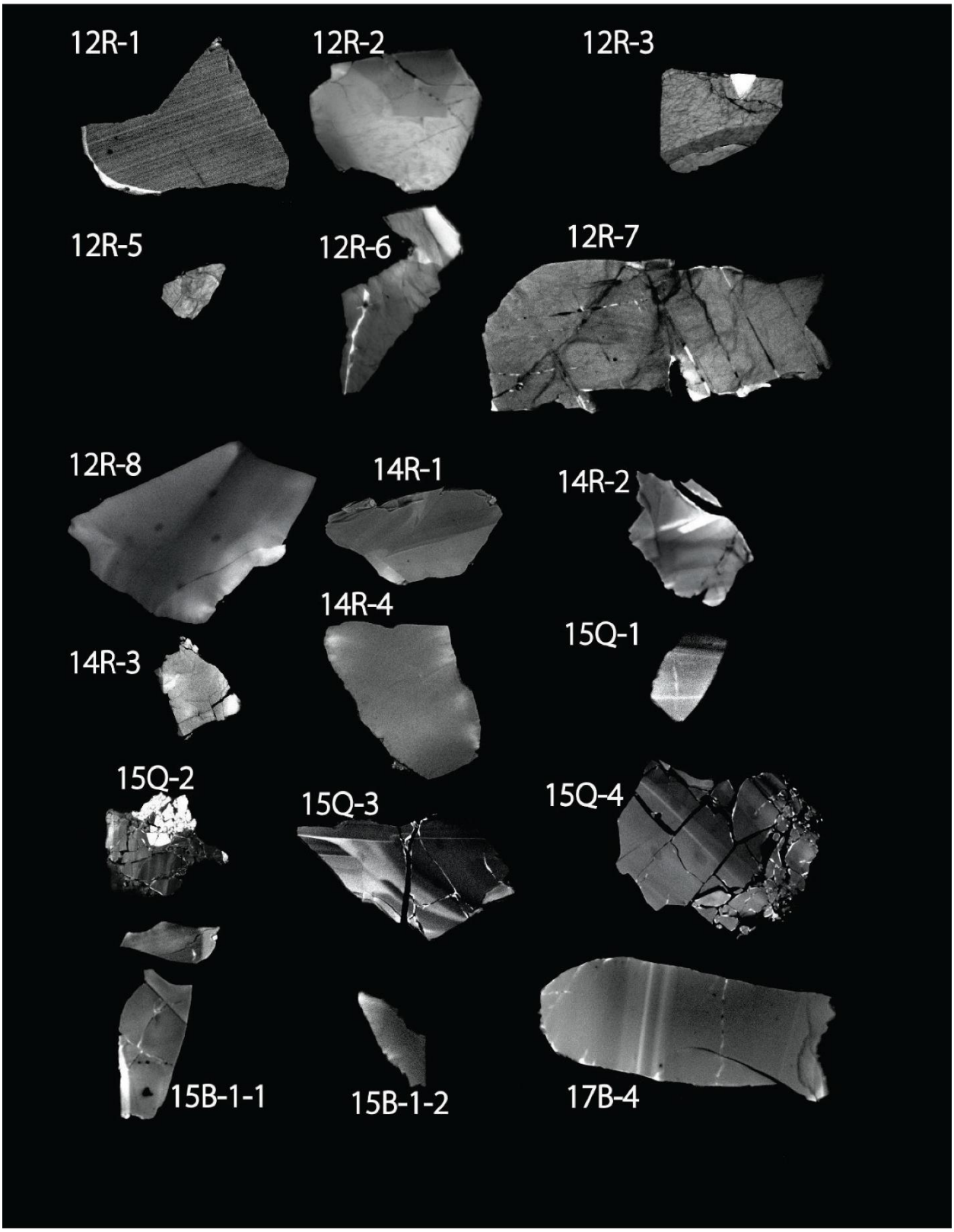
12R-1
12R-2
12R-3
12R-5
12R-6
12R-7
12R-8
14R-1
14R-2
14R-4
14R-3
15Q-1
15Q-2
15Q-3
15Q-4
15B-1-1
15B-1-2
17B-4

Appendix 5: Summary of new and existing data for zircons 01JH-13b 5M 4-2, 01JH-13b 5M 10-2, and 01JH-13b 5M 7-1. New data, including EBSD, Raman, and APT (for 01JH-13b 5M 4-2 and 01JH-13b 5M 10-2) were completed as part of this thesis. Existing data, including trace elements, δ^7Li, δ^{18}O and OH/O data are summarized below.

Zircon Grains:

Zircons 01JH-13b 5M 4-2, 01JH-13b 5M 10-2, and 01JH-54b 2.5NM2 7-1 are >3900 Ma detrital zircon grains from the Jack Hills Australia, collected and described as part of the Ph.D. thesis of Aaron J. Cavosie (Cavosie, 2005). Zircons 01JH-13b 5M 4-2 and 01JH-13b 5M 10-2 originate from sample 01JH-13, collected from Lat./Long. 26º 10' 00.3" S/116º 59' 28.9" E. Zircon 01JH-54b 2.5NM-2 7-1 was separated from sample 01JH-54, collected from Lat./Long. 26º 10' 01.0" S/116º 59' 27.9" E.

Existing Data

Zircons 01JH-13b 5M 4-2, 01JH-13b 5M 10-2, and 01JH-54b 2.5NM2 7-1 have been the subject of several geochemical studies, including U-Pb (Cavosie, 2005), δ^{18}O (Cavosie et al., unpublished), combined δ^{18}O and OH/O (Cameron et al., unpublished data), δ^7Li (Ushikubo et al., 2008), and trace elements (Li, P, Ca, Ti, V, Fe, Y, REE, Th and U; Bouvier et al. 2011). Many of these data were compiled by Ushikubo et al. (2008). Spot locations and data are summarized in Fig. A5.1-A5.3, and Tables A5.1-A5.3. U-Pb spot locations and data are detailed below (Figs. A5.4-A5.6, Table A5.6).

REFERENCES

Bouvier, A.-S., Ushikubo, T., Kita, N.T., Cavosie, A.J., Kozdon, R., Valley, J.W. (2011) Li isotopes and trace elements as a petrogenetic tracer in zircon: insights from Archean TTGs and sanukitoids. Contributions to Mineralogy and Petrology, 163, 745-768.

Cavosie, A.J. (2005) Geochemistry of greater than 3900 Ma detrital zircons from Jack Hills, Western Australia. University of Wisconsin-Madison, Doctoral Thesis.

Cavosie, A.J., Wilde, S.A., Liu, D., Weiblen, P.W., Valley, J.W. (2004) Internal zoning and U-Th-Pb chemistry of Jack Hills detrital zircons: a mineral record of early Archean to Mesoproterozoic (4348-1576 Ma) magmatism. Precambrian Research, 135, 251-279.

Geisler, T., Pidgeon, R.T., Bronswijk, W.V., Pleysier, R. (2001) Kinetics of thermal recovery and recrystallization of partially metamict zircon: a Raman spectroscopic study, European Journal of Mineralogy, 13, 1163-1176.

Váczi, T. (2014) A new, simple approximation for the deconvolution of instrumental broadening in spectroscopic band profiles. Applied Spectroscopy, 68, 1274-1278.

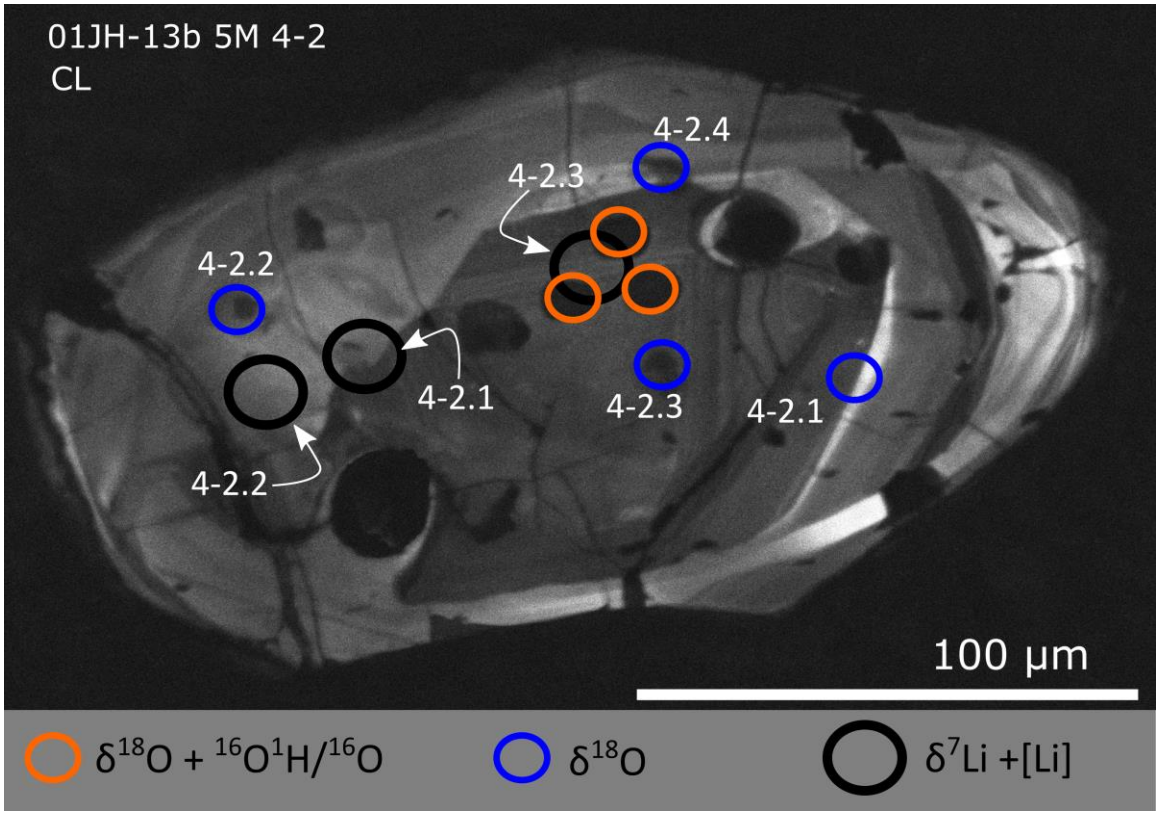

Figure A5.1: Pit locations for SIMS analyses on zircon 01JH-13b 5M 4-2. Pit designations correlate with data in Tables A5.1-A5.3. U-Pb pit locations can be found in Fig. A5.4.

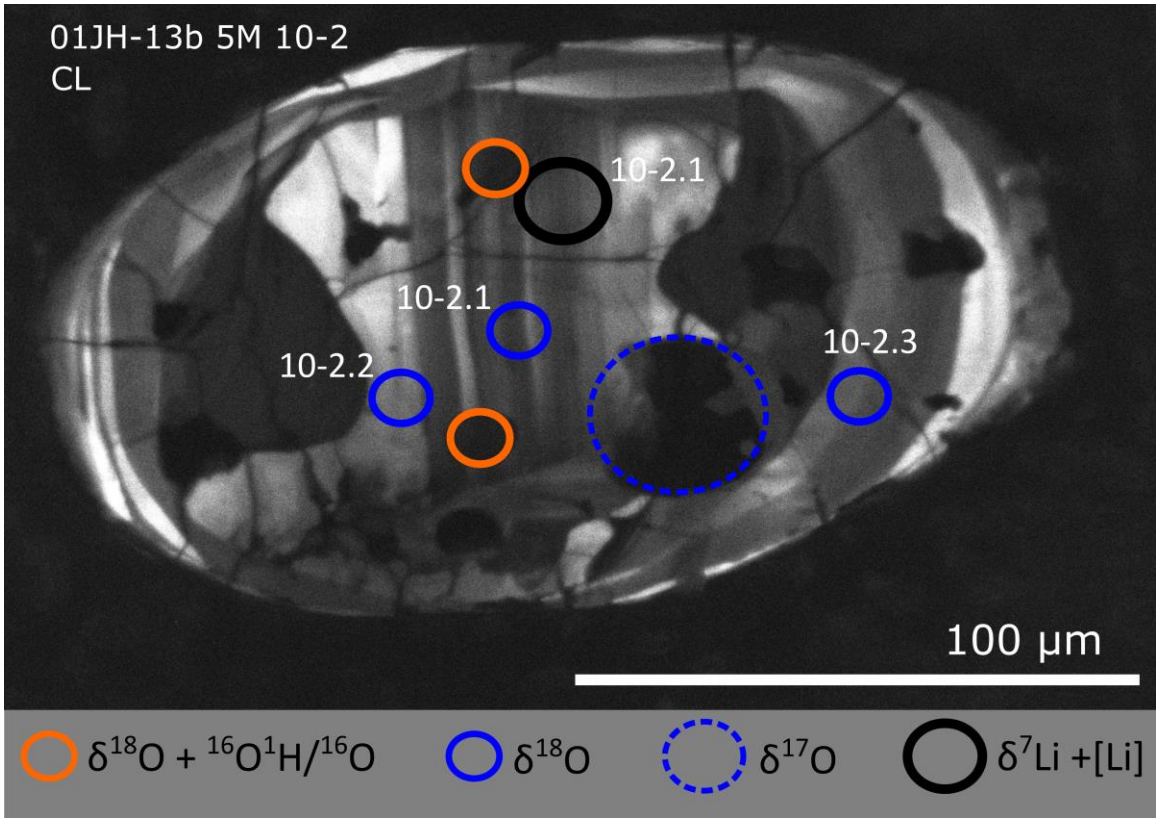

Figure A5.2: Pit locations for SIMS analyses on zircon 01JH-13b 5M 10-2. Pit designations correlate with data in Tables A5.1-A5.3. U-Pb data are summarized in Fig. A5.5.

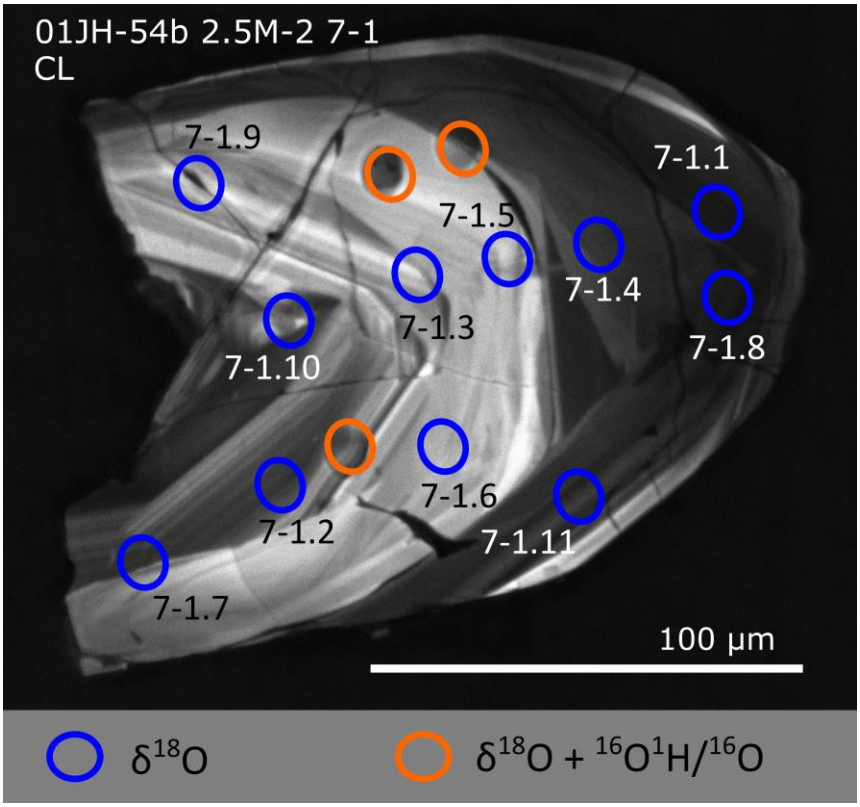

Figure A5.3: Pit locations for SIMS analyses on zircon 01JH-54b 2.5M2 7-1. Pit designations correlate with data in Tables A5.1-A5.3. U-Pb data are summarized in Fig. A5.6.

Table A5.1: Li concentrations and δ^7Li. See Fig. A5.1-A5.3 for pit locations. Data from Ushikubo et al. (2008).

	Domain	Li (ppm)	d^7Li (‰)	±2σ
01JH-13b 5M 4-2				
4-2.1	core/rim	41.9	-16.7	2.2
4-2.2	rim	37.8	-6.6	2.8
4-2.3	core	25.3	-12.1	2.8
01JH-13b 5M 10-2				
10-2.1	core	13.5	-8.5	2.5
01JH-54b 2.5NM2 7-1				
(no data)	-	-	-	-

Table A5.2: Summary of δ^{18}O analyses (Cavosie et al., unpublished data). See Fig. A5.1-A5.3 for pit locations.

	Domain	δ^{18}O (‰, VSMOW)	±2σ
01JH-13b 5M 4-2			
5M 4-2.1	core	4.38	0.32
5M 4-2.2	rim	3.81	0.32
5M 4-2.3	core	4.46	0.32
5M 4-2.4	rim	3.76	0.32
01JH-13b 5M 10-2			
5M 10-2.1	core	6.15	0.32
5M 10-2.2	core	5.32	0.32
5M 10-2.3	rim(?)	5.49	0.32
01JH-54b 2.5NM2 7-1			
2.5NM2 7-1.1	rim	5.97	0.30
2.5NM2 7-1.2	core	6.74	0.30
2.5NM2 7-1.3	core	6.71	0.30
2.5NM2 7-1.4	rim	6.15	0.30
2.5NM2 7-1.5	core	6.79	0.30
2.5NM2 7-1.6	core	6.69	0.30
2.5NM2 7-1.7	core	6.57	0.30
2.5NM2 7-1.8	rim	6.03	0.30
2.5NM2 7-1.9	core	6.09	0.30
2.5NM2 7-1.10	core	6.73	0.30
2.5NM2 7-1.11	rim	6.28	0.30

Table A5.3: Trace element data (Bouvier et al., 2011).

	01JH-13b 5M 4-2.3	01JH-13b-10-2.1	01JH-54b 2.5M2 7-1
Notes:	Good Analysis	On Crack	No Data
Li	34.8	28.5	-
P	548	1112	-
Ca	11.2	114	-
Ti	14.1	38.1	-
V	0.68	2.0	-
Fe	231.1	546	-
Y	3,141	1770	-
La	0.11	1.1	-
Ce	21.6	32.8	-
Pr	0.7	3.27	-
Nd	6.7	14.0	-
Sm	13.1	12.0	-
Eu	1.6	2.08	-
Gd	31.8	21.1	-
Tb	34	21.7	-
Dy	302	182	-
Ho	103	58.4	-
Er	455	250	-
Tm	90.1	50.7	-
Yb	716	426	-
Lu	125	76.9	-
Th	260	686	-
U	273	295	-
Th/U	0.95	2.33	-
(Y+REE)/(P+Li)	2.26	0.75	-
(Y+REE)/P	2.98	0.84	-
Σ REE (ppm)	1900	1075	-
Ca+Fe (ppm)	242.3	660	-
Ce/Ce*	18.8	4.1	-
Eu/Eu*	0.24	0.17	-
$(Sm/La)_N$	206	0.059	-

SEM Imaging and EBSD Characterization:

SEM imaging was completed to characterize the internal zircon textures; this included secondary electron, backscattered electron, and cathodoluminescence imaging modes (Fig. A5.4-A5.6) using a Hitachi S3400-N SEM at UW-Madison in the Dept. of Geoscience, Ray and Mary Wilcox SEM Lab. EBSD data collection and initial data analysis was completed in HKL Aztec, software with additional analysis and visualization done using the MTEX toolbox (v.4.5.0) in MATLAB (Fig. A5.7-A5.8).

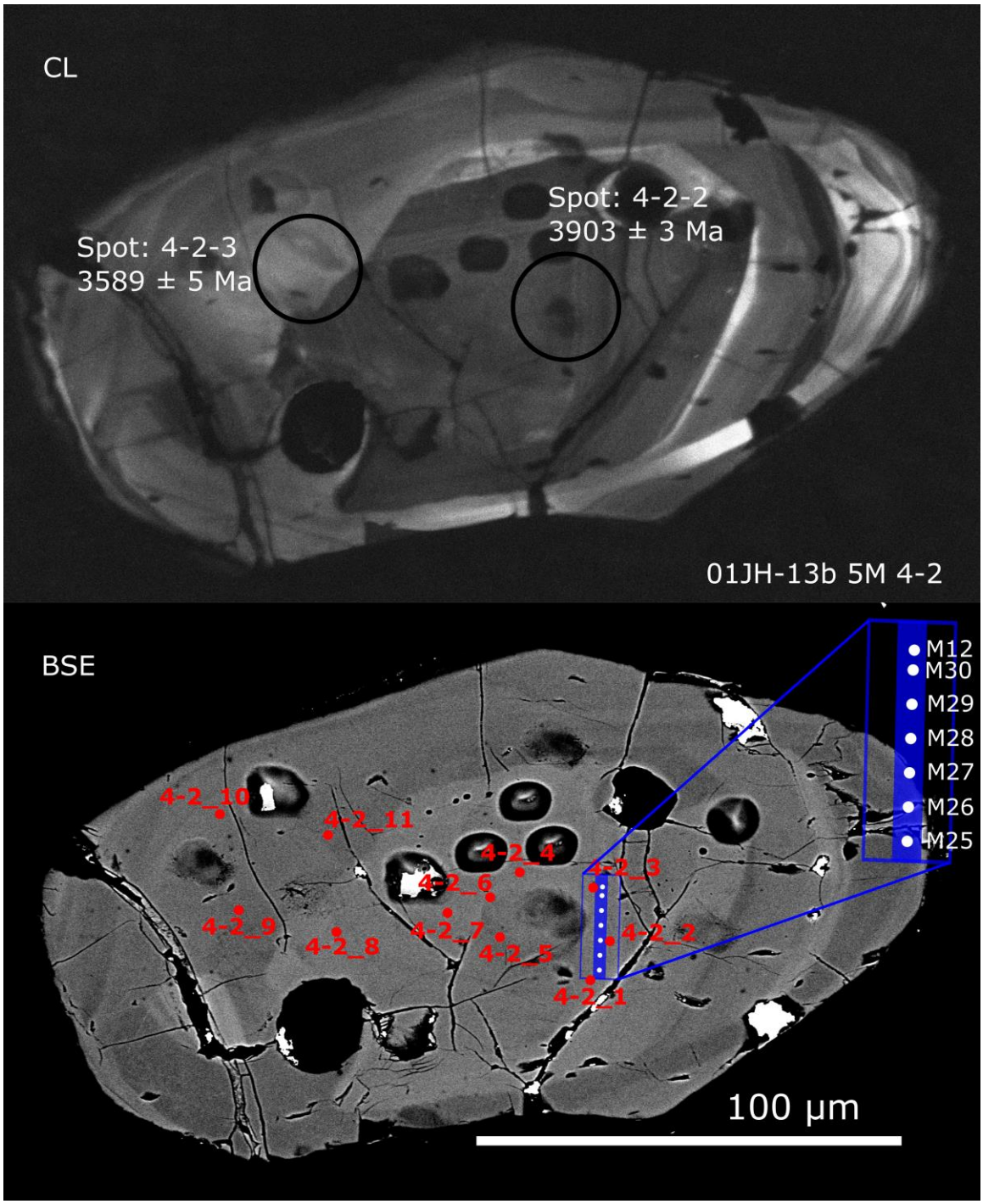

Figure A5.4: CL and BSE imaging of Jack Hills zircon 01JH-13b 5M 4-2. SIMS U-Pb analyses shown as red circles (from Cavosie, 2005, Table A5.6). Raman spot analyses shown as filled red spots. APT lift-out and approximate location of specific tips are shown in blue and white respectively.

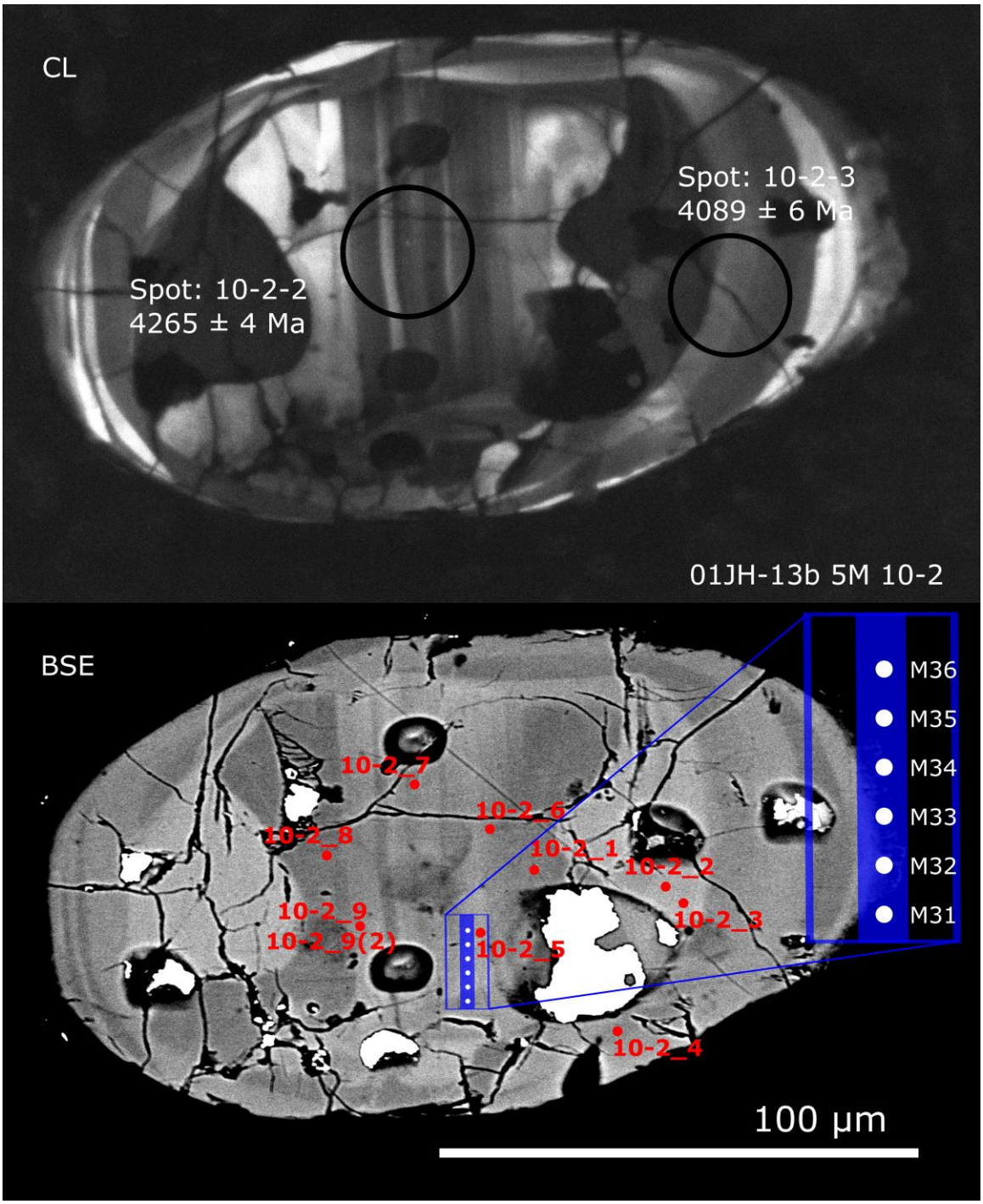

Figure A5.5: CL and BSE imaging of Jack Hills zircon 01JH-13b 5M 10-2. SIMS U-Pb analyses shown as red circles (from Cavosie, 2005, Table A5.6). Raman spot analyses shown as filled red spots. APT lift-out and approximate location of specific tips are shown in blue and white respectively.

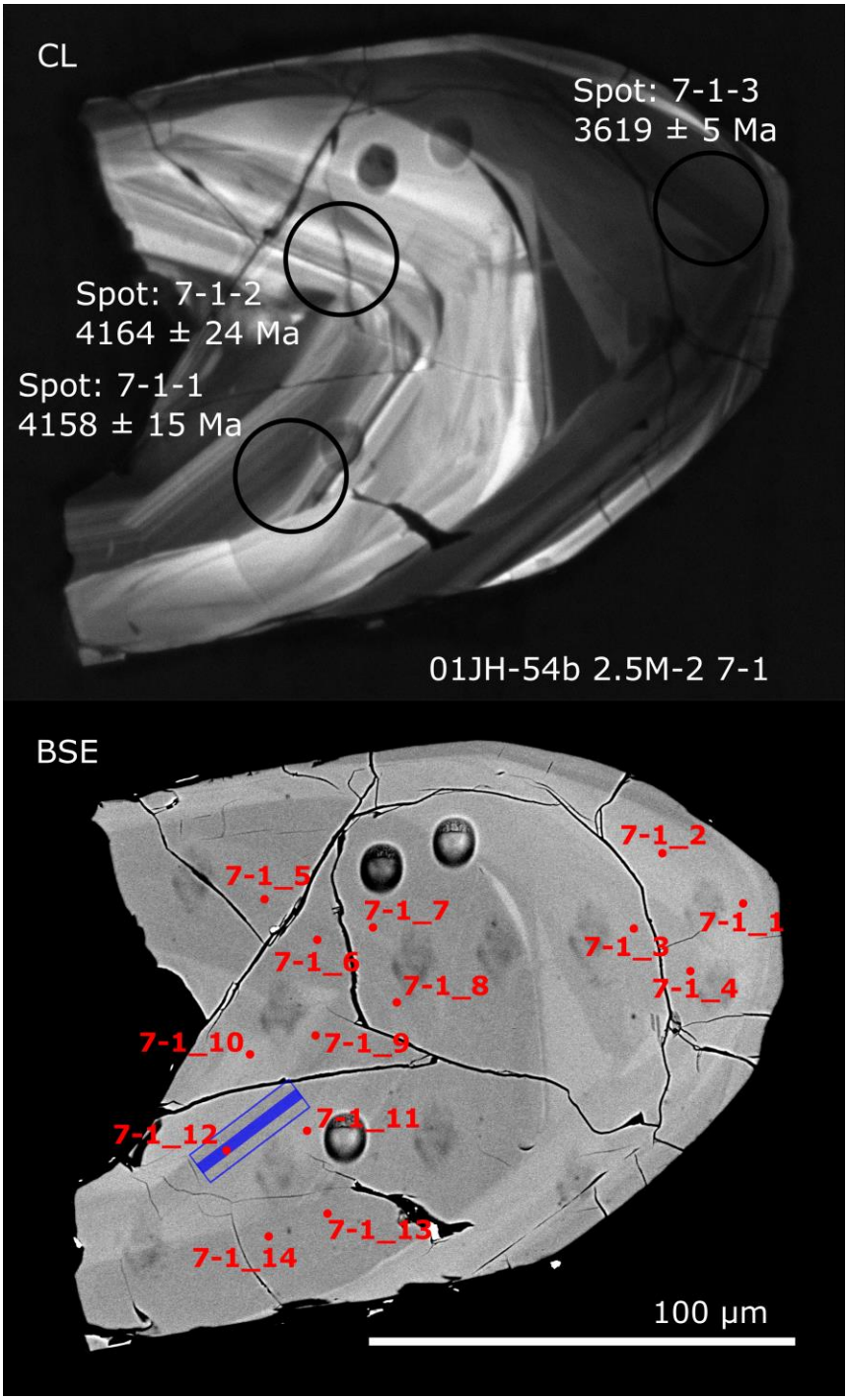

Figure A5.6: CL and BSE imaging of Jack Hills zircon 01JH-54b 2.5NM2 7-1. SIMS U-Pb analyses shown as red circles (from Cavosie, 2005, Table A5.6). Raman spot analyses shown as filled red spots. APT lift-out is shown in blue. Note: Several tips were fastened from the APT lift-out, however, all these tips failed during analysis before gathering significant data.

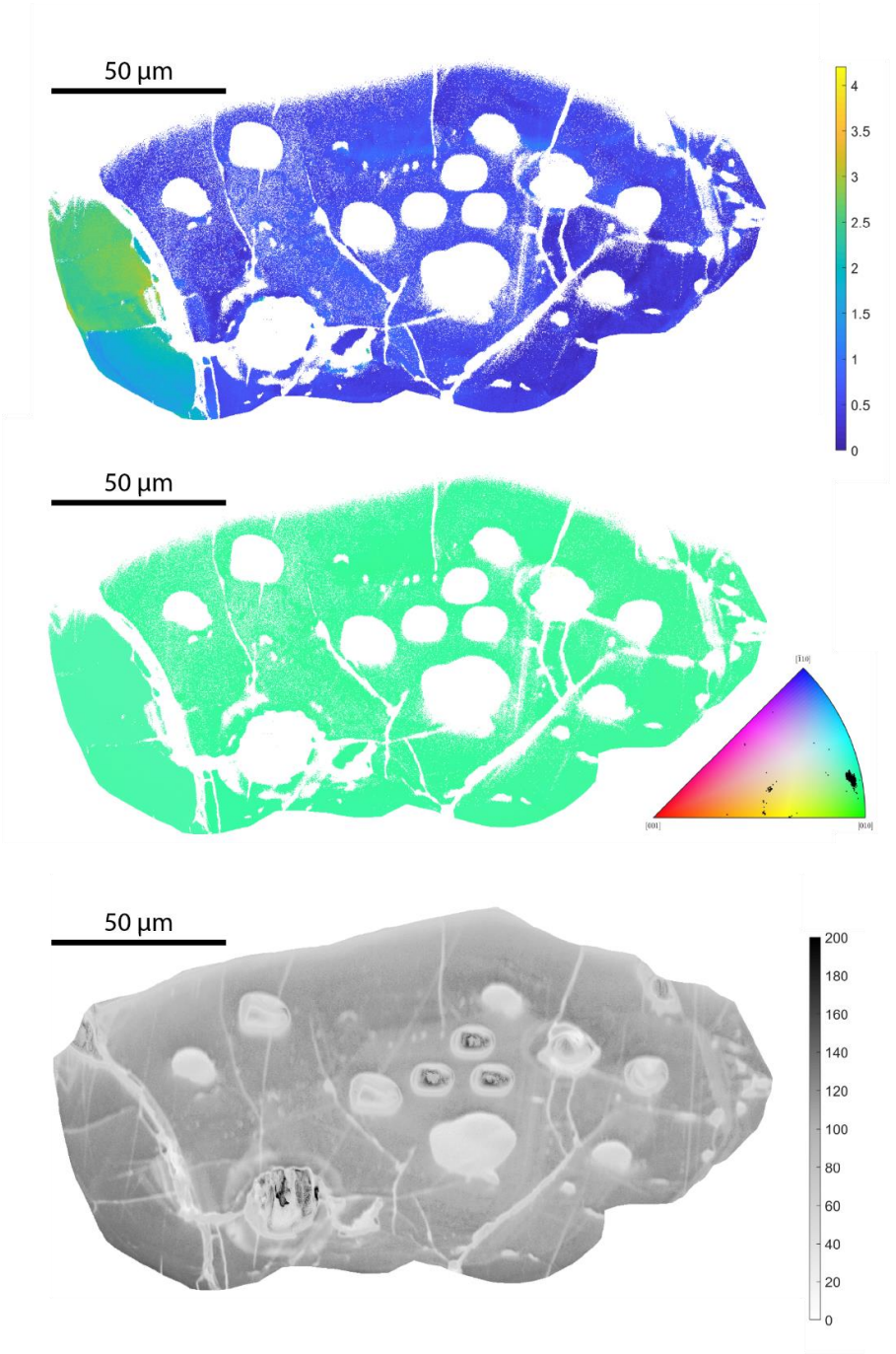

Figure A5.7: Summary of EBSD mapping for Jack Hills zircon 01JH-13b 5M 4-2. Blank regions are associated with poor indexing in SIMS pits, voids, and/or cracks. Top: misorientation relative to the mean. Color scale is in degrees. Middle: crystallographic orientation, showing surface normal crystallographic direction, colored according to inverse pole figure (inset). Lower: band contrast map (relative units).

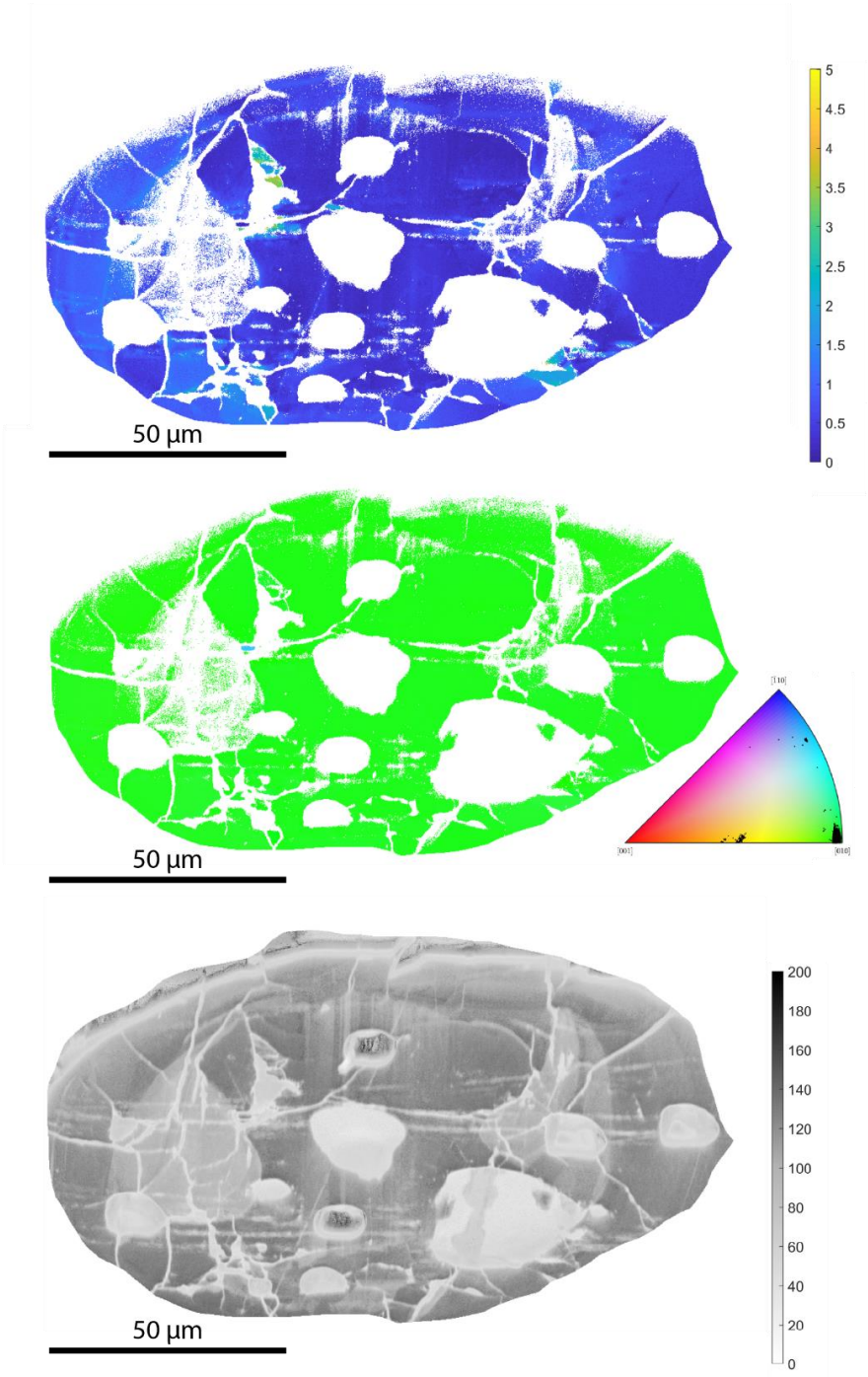

Figure A5.8: Summary of EBSD mapping for Jack Hills zircon 01JH-13b 5M 10-2. Blank regions are associated with poor indexing in SIMS pits, voids, and/or cracks. Top: misorientation relative to the mean. Color scale is in degrees. Middle: crystallographic orientation, showing surface normal crystallographic direction, colored according to inverse pole figure (inset). Lower: band contrast map (relative units).

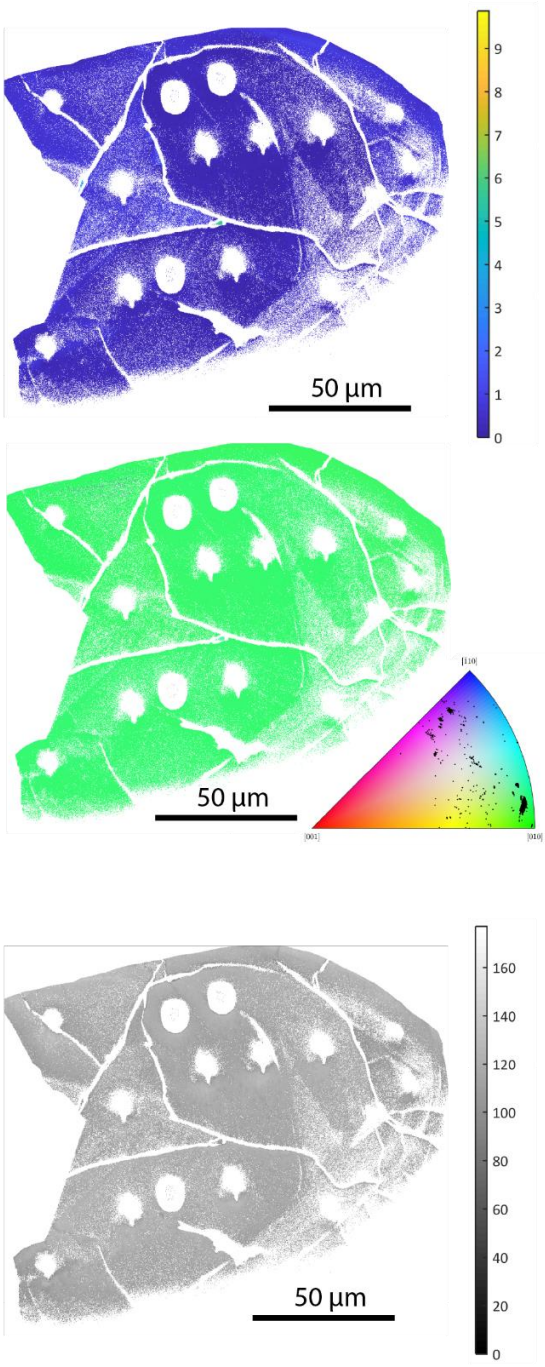

Figure A5.9: Summary of EBSD mapping for Jack Hills zircon 01JH-54b 2.5NM2 7-1. Blank regions are associated with poor indexing in SIMS pits, voids, and/or cracks. Top: misorientation relative to the mean. Color scale is in degrees. Middle: crystallographic orientation, showing surface normal crystallographic direction, colored according to inverse pole figure (inset). Lower: band contrast map.

Raman Spectroscopy:

Raman spot analyses were completed on a LabRAM HR at the Institut für Mineralogie und Kristallographie at the University of Vienna, Austria. Raman spots are correlated with individual SIMS U-Pb analyses. All analyses used a 632.8 nm He-Ne laser, with a 1800 groove/mm grating, and make a spike correction through completion of two analysis cycles. Counting times varied between 5 sec. (x2) and 10 sec. (x2). Measured $\nu_3(SiO_4)$ FWHM were corrected for the apparatus function following Váczi (2014), assuming a convolution of Gaussian (instrumental) and Lorentzian (physical) band shapes. Background correction and peak fitting for spot analyses was completed in PeakFit v4.12. Compositional variations are expected to contribute one of the most significant uncertainties in correlating between SIMS U-Pb data, and Raman spot analyses; SIMS analyses average U and Th concentrations over ~300 μm^3, while Raman analyses integrate signals from $\geq$5 μm^3. Between 2-5 spot analyses were positioned around each SIMS analysis pit to characterize the natural variability in structural state associated with a given SIMS analysis.

Raman mapping (Fig. A5.10-A5.12) was completed on a LabRAM HR Evo at the Institut für Mineralogie und Kristallographie at the University of Vienna, Austria. Mapping setup is summarized in Table A5.4. The mapping of grain 01JH-13b 5M 10-2 suffered from shift in focus at some point during mapping and thus the mapped data reflects Raman behavior several microns below the surface imaged by SEM and EBSD. Spot data are robust and are a reliable measure of zircon structure (and structural variation) at the surface, near SIMS analyses and APT lift-outs.

Individual Raman spectra were processed using LabSpec6 software, fit spectra shown in Fig. A5.10-A5.12. Low signal-to-noise spectra so not produce reliable fits and can be culled from the data based on the ratio of max peak counts within the $\nu_3(SiO_4)$ peak, and the height of the fit background (at the equivalent wavenumber position). The culled spectra, as well as the mapped wavenumber shift and band broadening measured in the culled spectra, are shown. Also shown are the wavenumber and $FWHM_{\nu3(SiO4)}$ data for each mapped pixel, along with the contoured data, and the radiation damage accumulation trend (Geisler et al., 2001).

Table A5.4: Summary of Raman mapping setup for zircons 01JH-13b 5M 4-2, 01JH-13b 5M 10-2, and 01JH-54b 2.5NM2 7-1. Fig. A5.10-A5.12

Instrument Model	**LabRAM HR Evo**	**LabRAM HR Evo**	**LabRAM HR Evo**
Zircon	**01JH-13b 5M 4-2**	**01JH-13b 5M 10-2**	**01JH-54b 2.5NM2 7-1**
Instrument and Acquisition Settings			
Laser Wavelength (nm)	633	633	633
Grating (g/mm)	1800	1800	1800
Slit (μm)	100	100	100
Aperture (μm)	300	300	200
Objective	100x	100x	100x
Acquisition software	LabSpec6	LabSpec6	LabSpec6
Acquisition time (sec/spot)	2.0	2.0	2.0
Spike filter	mult. accum.	mult. accum.	mult. accum.
Accumulations	2	2	2
Binning	1	1	1
Step size (x,y) (μm)	(0.9, 0.9)	(0.9, 0.9)	(0.9, 0.9)
Software and Acquisition Settings			
Data Analysis Software	LabSpec6	LabSpec6	LabSpec6
Bkgnd/baseline corr.	polynom. (1)	polynom. (1)	polynom. (1)
Peak shape model	Gauss + Lor	Gauss + Lor	Gauss + Lor

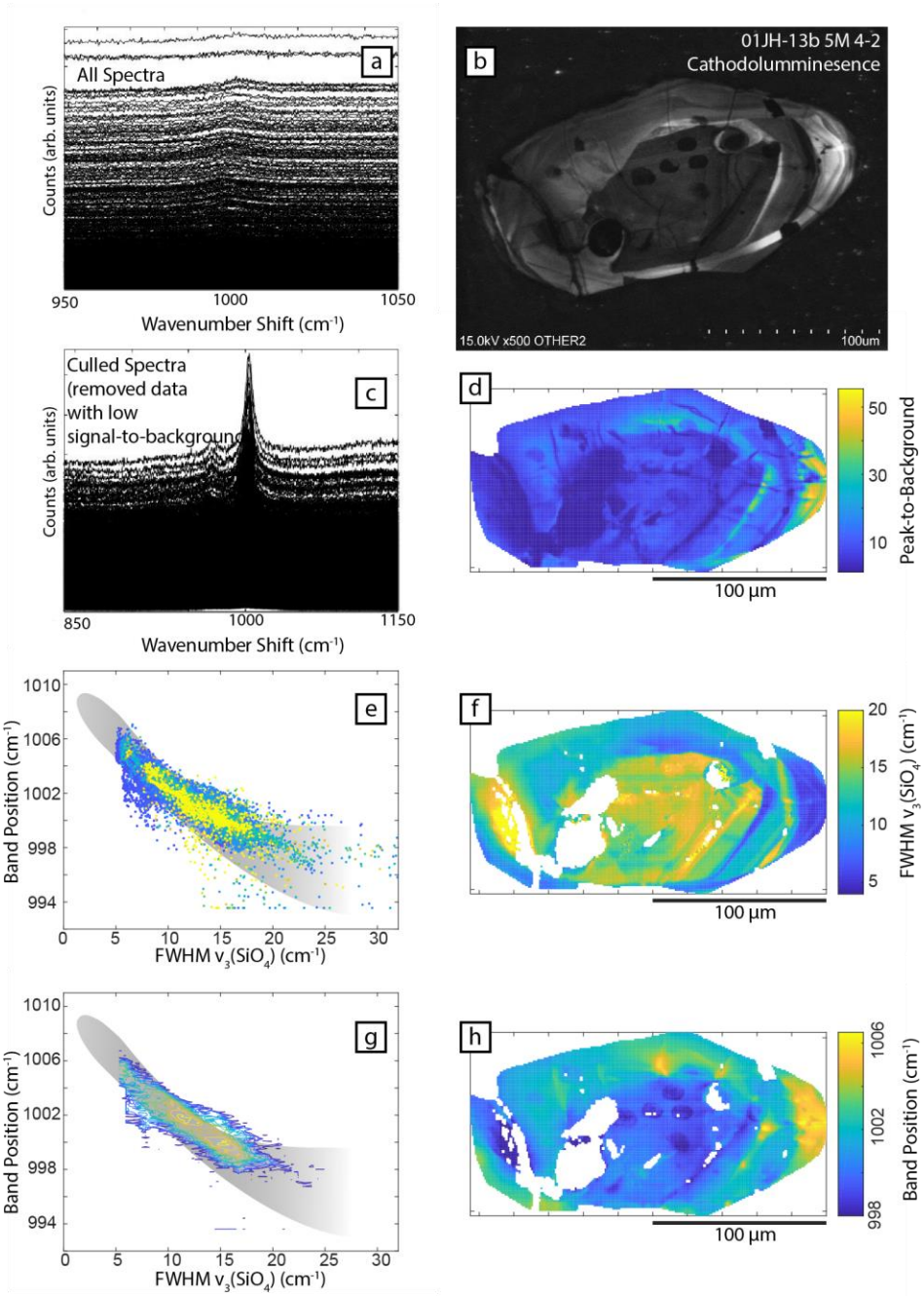

Figure A5.10: Summary of Raman mapping for Jack Hills zircon 01JH-13b 5M 4-2. (a) All Raman spectra. (b) CL image of zircon. (c) Culled Raman spectra – see text above for details. (d) spatial variability in T/B_{fit} (see text above, for details). (e) plot of $\nu_3(SiO_4)$ peak position versus band broadening for individual pixels (all data). Grey band is the empirical "radiation damage accumulation" trend of Geisler et al. 2001. (f) $\nu_3(SiO_4)$ FWHM (g) contour plot of data in (e). (h) Map of (culled) $\nu_3(SiO_4)$ peak position.

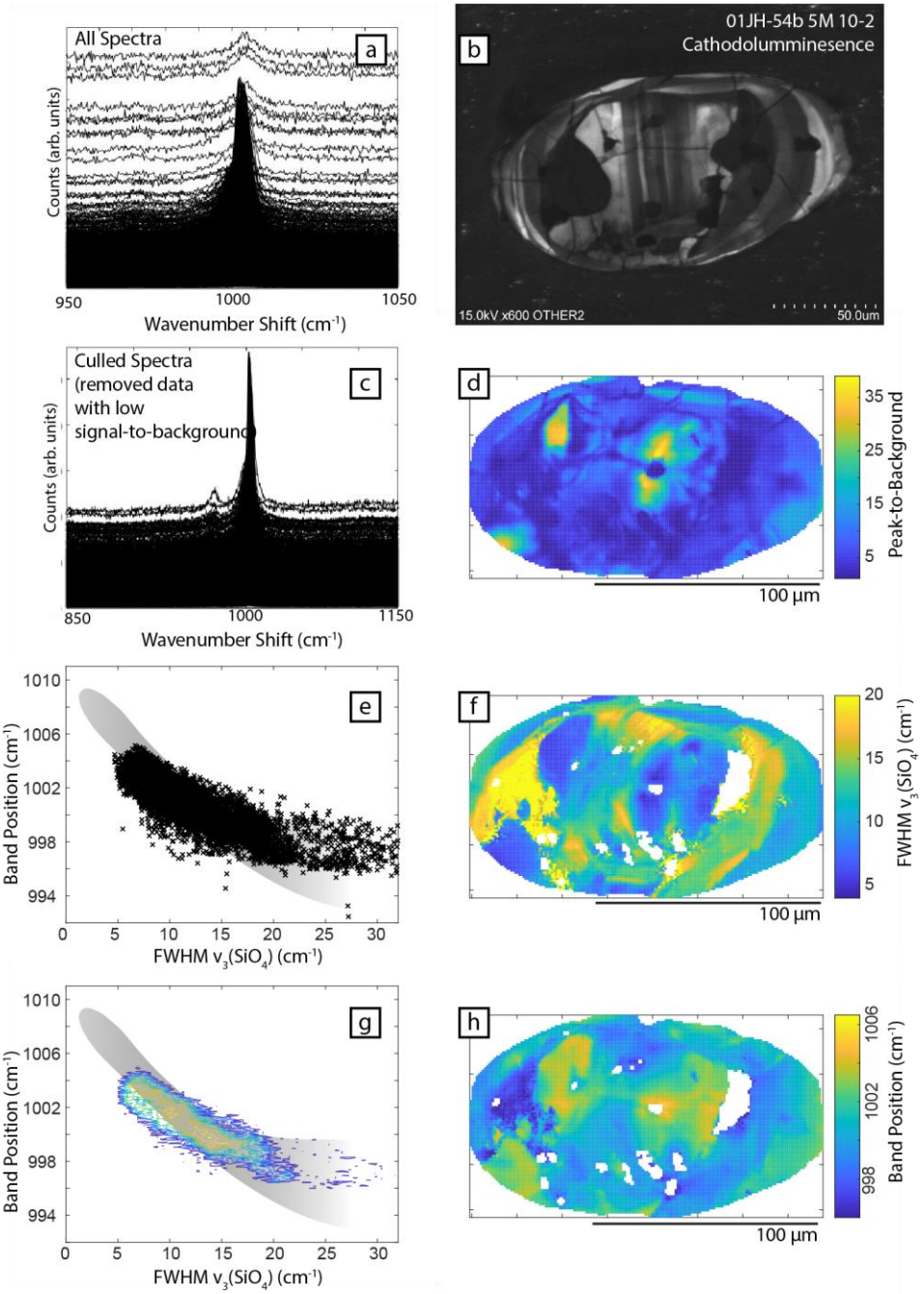

Figure A5.11: Summary of Raman mapping for Jack Hills zircon 01JH-13b 5M 10-2. (a) All Raman spectra. (b) CL image of zircon. (c) Culled Raman spectra – see text above for details. (d) spatial variability in T/B_{fit} (see text for details). (e) plot of $\nu_3(SiO_4)$ peak position versus band broadening for individual pixels (all data). Grey band is the empirical "radiation damage accumulation" trend of Geisler et al. 2001. (f) $\nu_3(SiO_4)$ FWHM (g) contour plot of data in (e). (h) Map of (culled) $\nu_3(SiO_4)$ peak position.

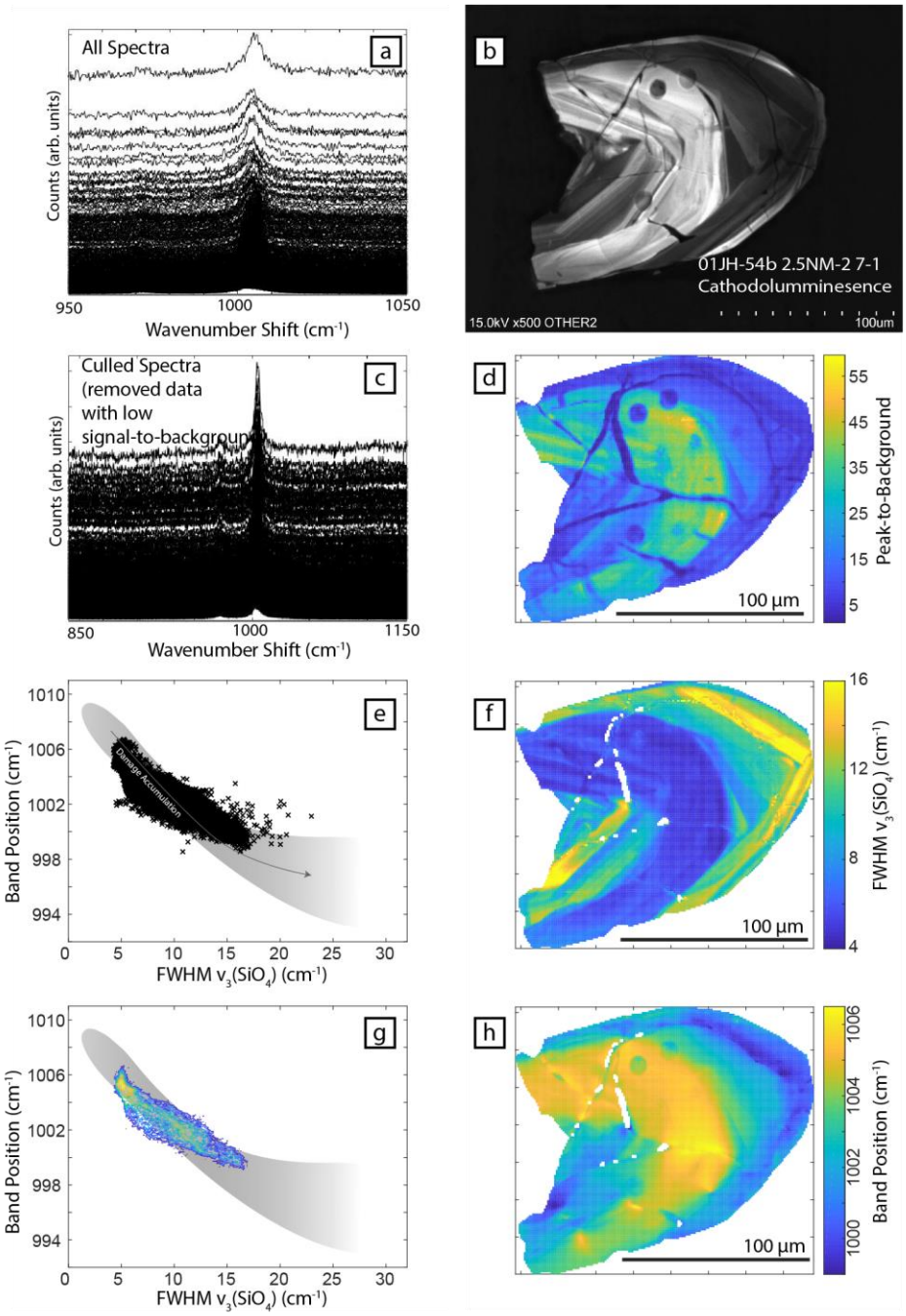

Figure A5.12: Summary of Raman mapping for Jack Hills zircon 01JH-54B 2.5NM2 7-1. (a) All Raman spectra. (b) CL image of zircon. (c) Culled Raman spectra – see text above for details. (d) spatial variability in T/B_{fit} (see text for details). (e) plot of $\nu_3(SiO_4)$ peak position versus band broadening for individual pixels (all data). Grey band is the empirical "radiation damage accumulation" trend of Geisler et al. 2001. (f) $\nu_3(SiO_4)$ FWHM (g) contour plot of data in (e). (h) Map of (culled) $\nu_3(SiO_4)$ peak position.

Atom Probe Tomography

Atom probe data was collected at the Max-Plank-Institut fur Eisenforschung, on both a LEAP 5000 XS, and LEAP 5000 XR (See table A5.5 for a summary of experimental setup and run conditions). FIB lift-outs were prepared in zircon core domains, along CL banding, and correlated with SIMS analyses (Fig. A5.4-A5.6). Data was gathered for zircons 01JH-13b 5M 4-2 and 01JH-13b 5M 10-2; however, the specimens made for 01JH-54b 2.5NM2 7-1 failed to produce data (tips failed in the instrument before generating significant data). Data reconstruction and analysis was completed using IVAS 3.6.12.

Table A5.5: Atom Probe Tomography data acquisition settings and run summary: four tips from 01JH-13b 5M 4-2 and two tips from 01JH-13b 5M 10-2.

Specimen/Data Set	**R76_29139**	**R76_29156**	**R96_29312**
Sample	**01JH-13b 5M 4-2**	**01JH-13b 5M 4-2**	**01JH-13b 5M 4-2**
Coupon Post	**M25**	**M26**	**M29**
Instrument Model	**LEAP 5000 XS**	**LEAP 5000 XS**	**LEAP 5000 XR**
Instrument Settings			
Laser Wavelength (nm)	355	355	355
Laser Pulse Energy (pJ)	400	400	400
Pulse Frequency (kHz)	250	250	200
Evaporation Control	Detection Rate	Detection Rate	Detection Rate
Target Detection Rate (ions/pulse)	0.015	0.015	0.01
Nominal Flight Path (mm)	100	100	382
Set Point Temperature (K)	50	50	50
Sample Temperature (K)	50.0	50.0	49.78
Chamber Pressure (Torr)	$3.3x10^{-11}$	$4.0x10^{-11}$	$4.5x10^{-11}$
Data Summary			
LAS Root Version	15.43.393l	15.43.393l	15.43.393l
CAMECAROOT Version	15.43.393k	15.43.393k	15.43.393e
Analysis Software	IVAS 3.6.14	IVAS 3.6.14	IVAS 3.6.14
Total Ions:	105,074,016	201,939,978	73,366,466
Single	72,540,991	140,012,280	48,382,315
Multiple	31,410,266	59,858,857	24,512,275
Partial	1,122,759	2,068,841	471,876
Volt./Bowl Corr. Peak (Da)	16 Da	16 Da	16 Da
Mass Calib. (peaks/interp.)	9/lin.	9/lin.	9/lin.
$^{\dagger}(M/\Delta M)$ for $^{16}O_2^+$	763	811	1291
$^{\dagger\dagger}(M/\Delta M_{10})$	316	349	603
time independent background (ppm/ns)	27.8	56.6	46.6
Reconstruction			
Final specimen state	Intact	Intact	Intact
Pre-/Post-analysis Imaging	SEM/SEM	SEM/SEM	SEM/none
Radius Evolution Model	Voltage	Voltage	Voltage
Field Factor (k)	3.30	3.30	3.30
Image Compression Factor	1.65	1.65	1.65
Evap. Field (V/nm)	28	28	28
Detector Efficiency	0.80	0.80	0.52
Avg. Atomic Volume (nm^3)	0.0108	0.0108	0.0108

$^{\dagger}\Delta M$ is full width at half maximum.

$^{\dagger\dagger}\Delta M_{10}$ is full width at tenth maximum.

Table A5.5 (cont.): Atom Probe Tomography data acquisition settings and run summary.

Specimen/Data Set	**R76_29165**	**R76_29169**	**R96_29434**
Sample	**01JH-13b 5M 10-2**	**01JH-13b 5M 10-2**	**01JH-13b 5M 10-2**
Coupon Post	**M32**	**M33**	**M35**
Instrument Model	**LEAP 5000 XS**	**LEAP 5000 XS**	**LEAP 5000 XR**
Instrument Settings			
Laser Wavelength (nm)	355	355	355
Laser Pulse Energy (pJ)	200	200	400
Pulse Frequency (kHz)	250	250	125
Evaporation Control	Detection Rate	Detection Rate	Detection Rate
Target Detection Rate (ions/pulse)	0.015	0.015	0.005
Nominal Flight Path (mm)	100	100	382
Set Point Temperature (K)	50	50	50
Sample Temperature (K)	50.0	50.0	50.03
Chamber Pressure (Torr)	3.2×10^{-11}	4.4×10^{-11}	4.0×10^{-11}
Data Summary			
LAS Root Version	15.43.393l	15.43.393l	15.43.393l
CAMECAROOT Version	15.43.393k	15.43.393e	15.43.393e
Analysis Software	IVAS 3.6.14	IVAS 3.6.14	IVAS 3.6.14
Total Ions:	20,405,854	105,446,810	59,412,925
Single	12,072,537	63,451,097	42,406,268
Multiple	8,143,242	41,068,027	16,648,217
Partial	190,075	927,686	358,440
Volt./Bowl Corr. Peak (Da)	16 Da	16 Da	16 Da
Mass Calib. (peaks/interp.)	9/lin.	9/lin.	9/lin.
†(M/ΔM) for $^{16}O_2^+$	764	770	1352
††(M/ΔM_{10})	334	348	634
time independent background (ppm/ns)	18.0	16.1	15.5
Reconstruction			
Final specimen state	Fractured	Fractured	Fractured
Pre-/Post-analysis Imaging	SEM/none	SEM/none	SEM/none
Radius Evolution Model	Voltage	Voltage	Voltage
Field Factor (k)	3.30	3.30	3.30
Image Compression Factor	1.65	1.65	1.65
Evap. Field (V/nm)	28	28	28
Detector Efficiency	0.80	0.80	0.52
Avg. Atomic Volume (nm^3)	0.0108	0.0108	0.0108

†ΔM is full width at half maximum.
††ΔM_{10} is full width at tenth maximum.

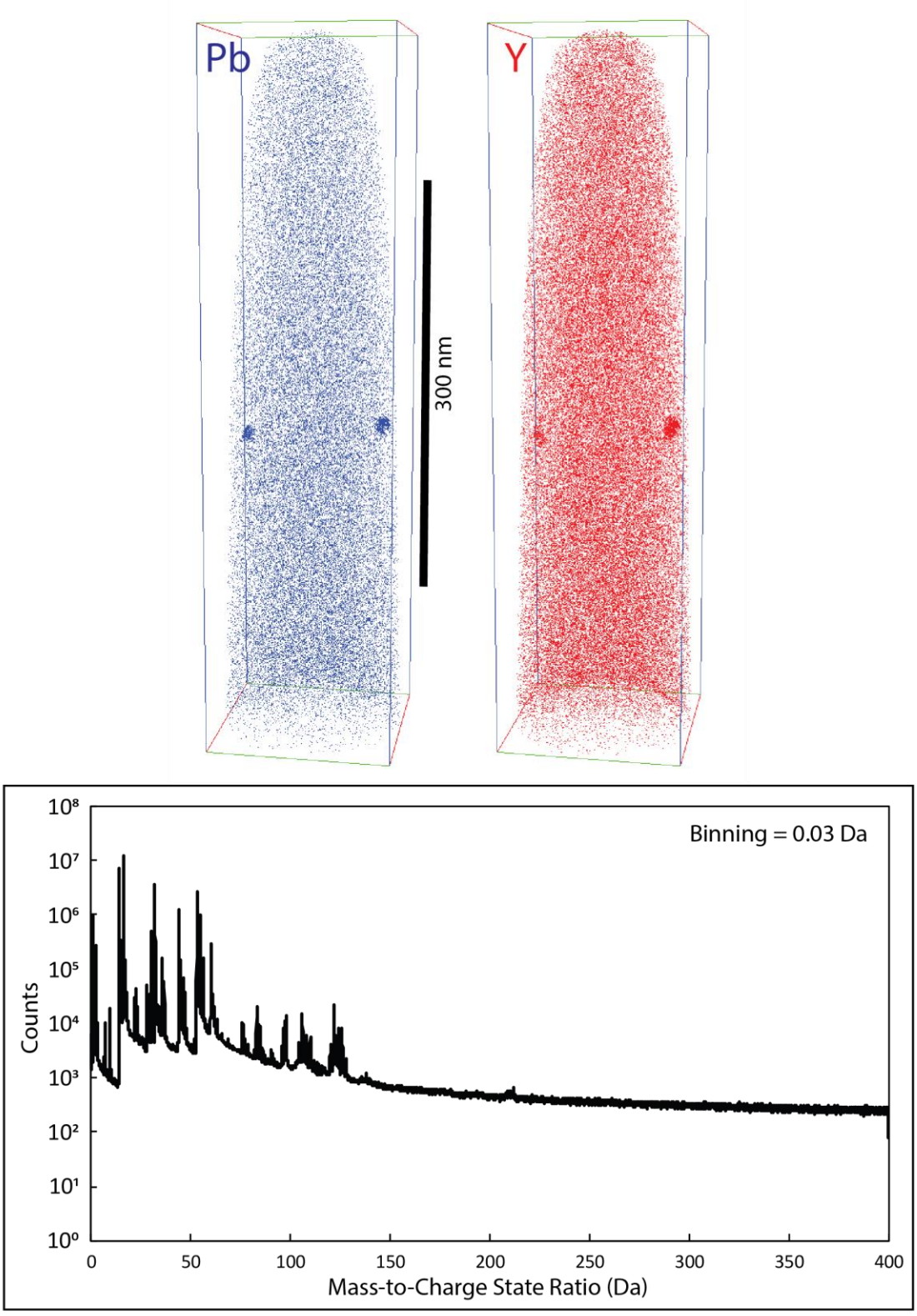

Figure A5.13: Summary of Y (red) and Pb (blue) maps for data set R76_29139 (zircon 01JH-13b 5M 4-2), as well as the mass spectra for the bulk data set.

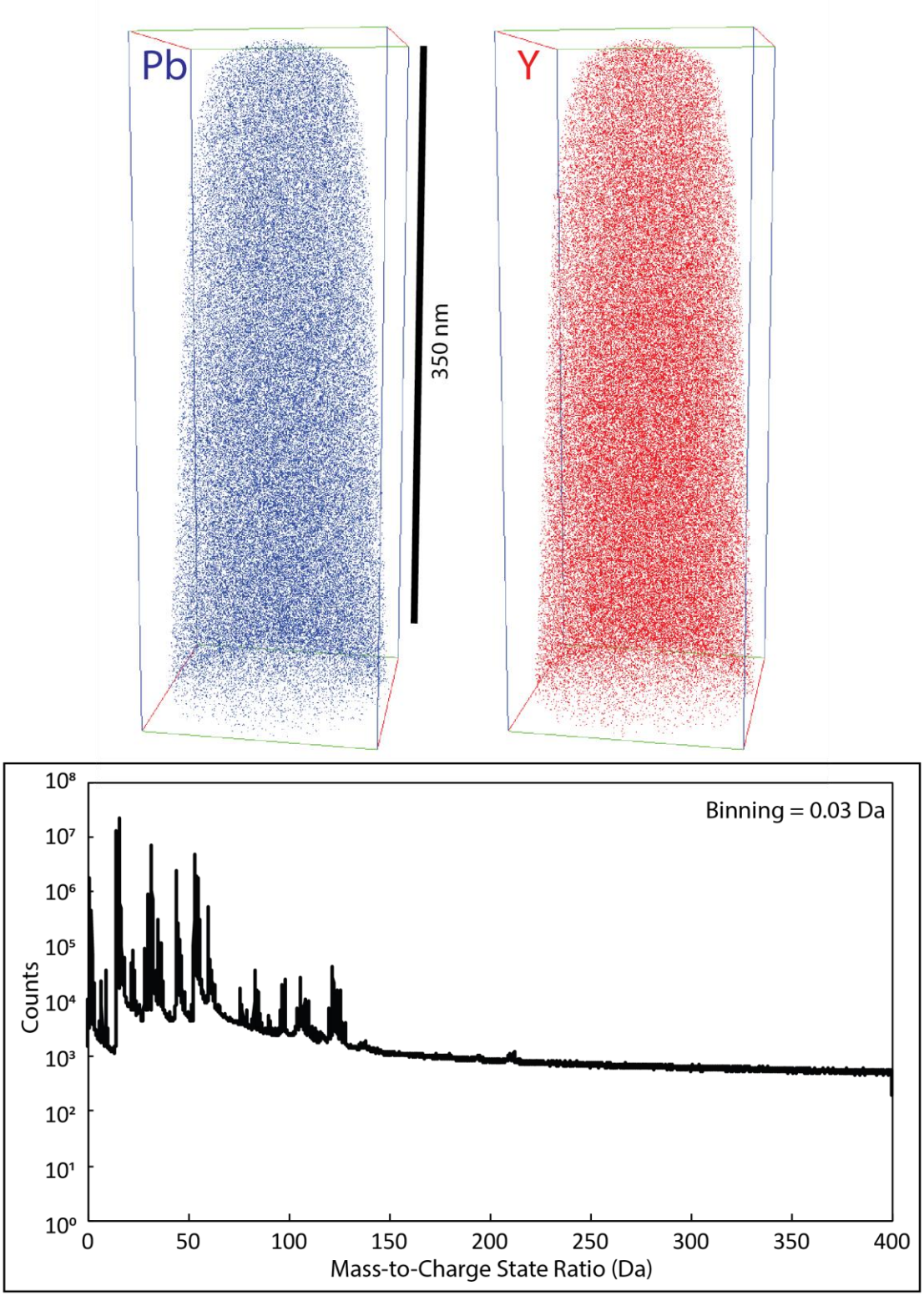

Figure A5.14: Summary of Y (red) and Pb (blue) maps for data set R76_29156 (zircon 01JH-13b 5M 4-2), as well as the mass spectra for the bulk data set.

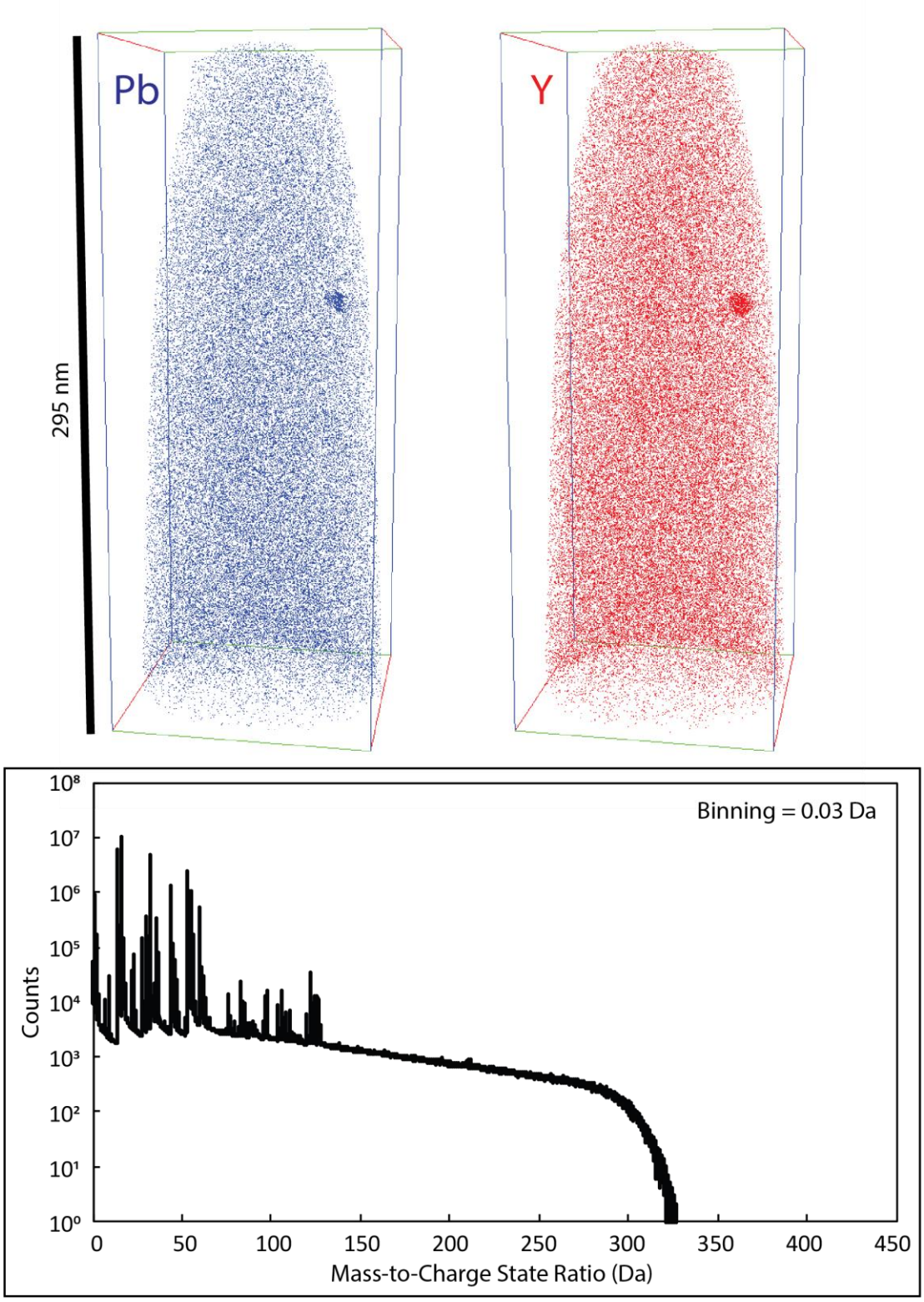

Figure A5.15: Summary of Y (red) and Pb (blue) maps for data set R96_29312 (zircon 01JH-13b 5M 4-2), as well as the mass spectra for the bulk data set.

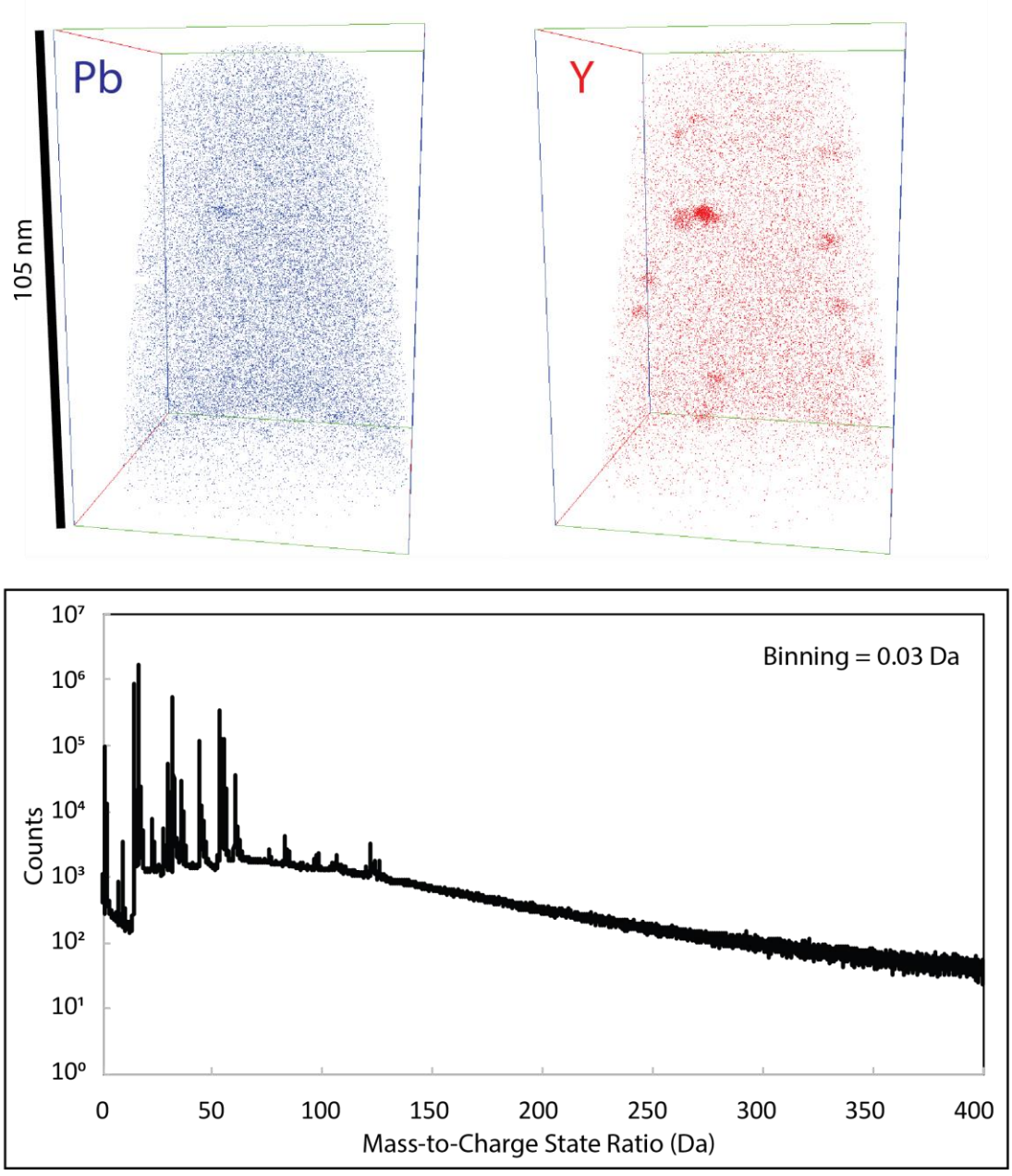

Figure A5.16: Summary of Y (red) and Pb (blue) maps for data set R76_29165 (zircon 01JH-13b 5M 10-2), as well as the mass spectra for the bulk data set.

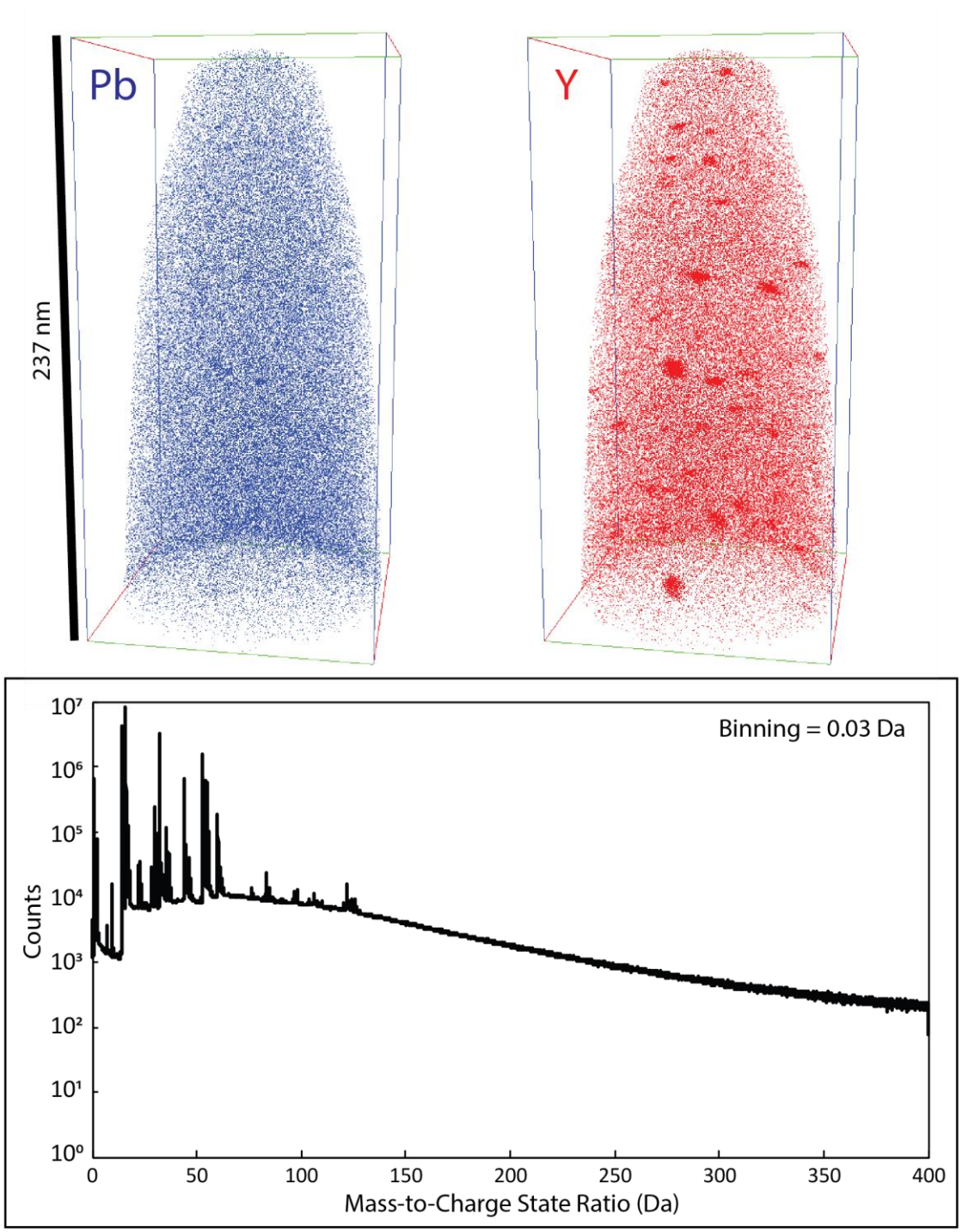

Figure A5.17: Summary of Y (red) and Pb (blue) maps for data set R76_29169 (zircon 01JH-13b 5M 10-2), as well as the mass spectra for the bulk data set.

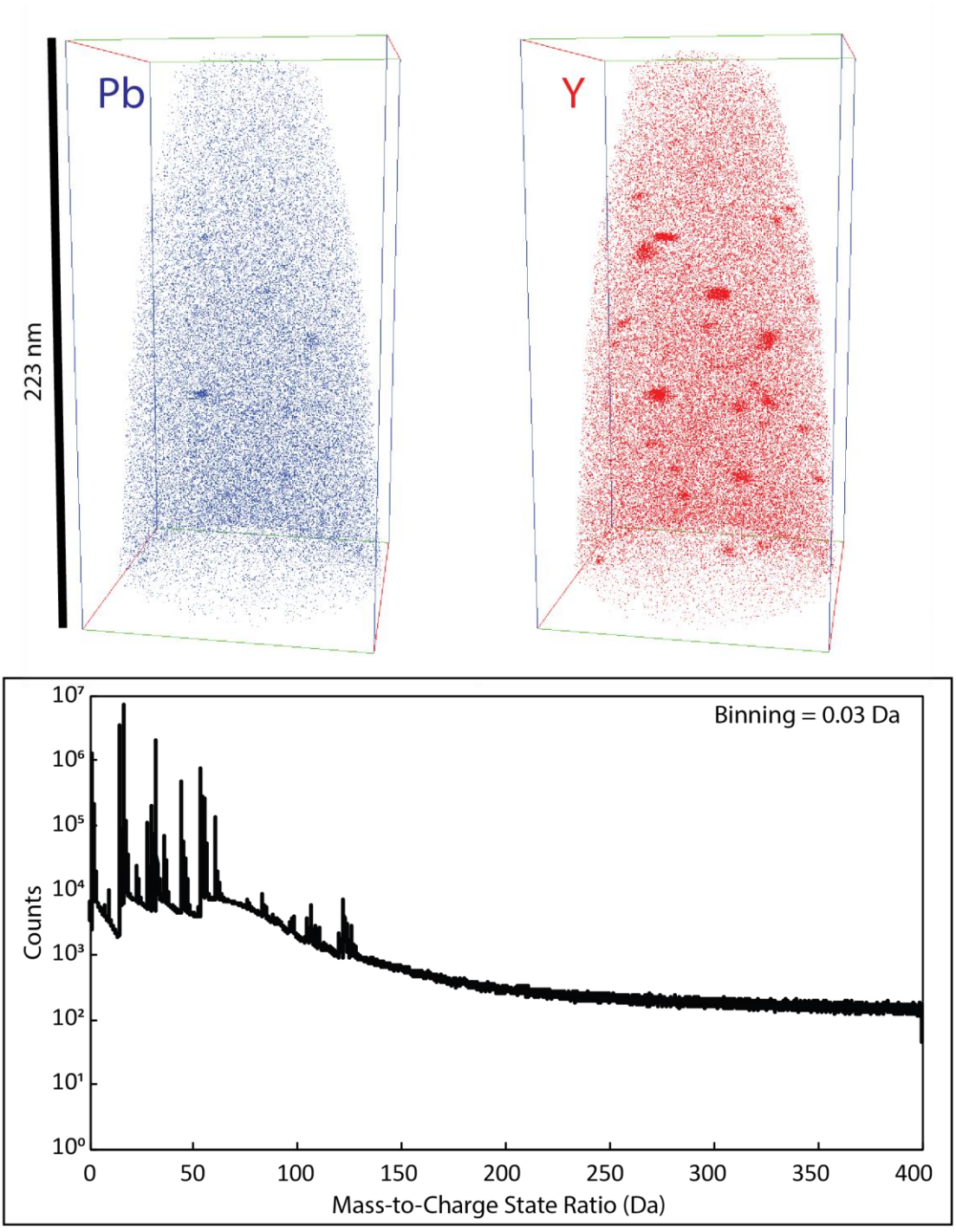

Figure A5.18: Summary of Y (red) and Pb (blue) maps for data set R96_29434(zircon 01JH-13b 5M 10-2), as well as the mass spectra for the bulk data set.

Table A5.6: Summary of SIMS U-Pb geochronology for Jack Hills zircons 01JH-13b 5M 4-2, 01JH-13b 5M 10-2, and 01JH-54b 2.5NM2 7-1 (Cavosie, 2005).

Sample	Domain	U (µg/g)	Th (µg/g)	Th/U	$^{204}Pb/^{206}Pb$	$^{207}Pb^*/^{206}Pb^*$	1σ	$^{207}Pb^*/^{235}U$	1σ	$^{206}Pb^*/^{238}U$	1σ	$^{206}Pb^*/^{238}U$ Age (Ma)	1σ	$^{207}Pb^*/^{206}Pb^*$ Age (Ma)	1σ	% Conc.
01JH-13b 5M 4-2																
4-2-2	C	256	227	0.89	0.00013	0.39861	0.00078	41.91	0.44	0.7626	0.008	3654	29	3904	3	94
4-2-3	R	123	23	0.19	0.00005	0.32403	0.00101	33.06	0.38	0.7399	0.0083	3571	31	3589	5	99
01JH-13b 5M 10-2																
10-2-2	C	170	184	1.08	0.00003	0.50811	0.00147	66.31	0.74	0.9465	0.0102	4294	34	4265	4	101
10-2-3	R	275	144	0.52	0.00013	0.45103	0.00194	48.96	0.55	0.7873	0.0082	3744	29	4089	6	92
01JH-54b 2.5NM2 7-1																
7-1-1	C	70	29	0.42	0.00009	0.47254	0.00472	57.58	0.85	0.8837	0.0095	4083	33	4158	15	98
7-1-2	C	63	23	0.37	0.00001	0.47462	0.00775	58.06	1.17	0.8872	0.0105	4095	36	4164	24	98
7-1-3	R	314	193	0.61	0.00007	0.33049	0.001	30.74	0.32	0.6746	0.0067	3324	26	3619	5	92

Table A5.7: Raman Spot analyses for Jack Hills zircons 01JH-13b 5M 4-2, 01JH-13b 5M 10-2, and 01JH-54b 2.5NM2 7-1. See Fig., A5.4-A5.6 for locations of Raman analyses.

Spot Analysis	SHRIMP Analysis	Wavenumber Shift (cm^{-1})	$FWHM_{v3(SiO4)}$ (cm^{-1}) (Meas.)	$FWHM_{v3(SiO4)}$ (cm-1) (Corr.)	D_{eff} (10^{15} α/mg)	Th (µg/g)	U (µg/g)	$^{207}Pb/^{206}Pb$ Age (Ma)	D_{total} ($x10^{15}$ α/mg)	Frac. Anneal.	Rad Damage Age (Ma)
10-2_1	10-2-3	1004.8	6.40	6.3	0.36	144	275	4089	7.329	0.95	348
10-2_2	10-2-3	1000.5	13.41	13.4	0.87	144	275	4089	7.329	0.88	806
10-2_3	10-2-3	999.6	15.72	15.7	1.03	144	275	4089	7.329	0.86	942
10-2_4	10-2-3	1000.8	12.14	12.1	0.78	144	275	4089	7.329	0.89	728
Mean		1001.4	11.92	11.9	0.761	144	275	4089	7.329	0.90	712
S.D.		2.3	3.97	4.0	0.285						
Max		1004.8	15.72	15.7	1.034						
Min		999.6	6.40	6.3	0.364						

Spot Analysis	SHRIMP Analysis	Wavenumber Shift (cm^{-1})	$FWHM_{v3(SiO4)}$ (cm^{-1}) (Meas.)	$FWHM_{v3(SiO4)}$ (cm-1) (Corr.)	D_{eff} (10^{15} α/mg)	Th (μg/g)	U (μg/g)	$^{207}Pb/^{206}Pb$ Age (Ma)	D_{total} ($x10^{15}$ α/mg)	Frac. Anneal.	Rad Damage Age (Ma)
10-2_5*	10-2-2	999.1	17.79	17.8	1.18	184	170	4265	5.301	0.78	1490
10-2_6	10-2-2	1002.9	8.59	8.5	0.52	184	170	4265	5.301	0.90	707
10-2_7	10-2-2	1002.3	9.53	9.5	0.59	184	170	4265	5.301	0.89	796
10-2_8	10-2-2	1004.3	6.62	6.5	0.38	184	170	4265	5.301	0.93	525
10-2_9	10-2-2	1000.9	12.57	12.5	0.81	184	170	4265	5.301	0.85	1066
10-2_9(2)	10-2-2	1000.9	12.51	12.5	0.80	184	170	4265	5.301	0.85	1054
Mean		1001.7	11.27	11.2	0.714	184	170	4265	5.301	0.87	950
S.D.		1.8	3.94	4.0	0.283						
Max		1004.3	17.79	17.8	1.182						
Min		999.1	6.62	6.5	0.379						
4-2_1*	4-2-2	999.6	14.56	14.5	0.95	227	256	3903	6.525	0.85	876
4-2_2*	4-2-2	999.3	16.20	16.2	1.07	227	256	3903	6.525	0.84	977
4-2_3*	4-2-2	999.5	15.87	15.8	1.04	227	256	3903	6.525	0.84	952
4-2_4	4-2-2	999.7	16.14	16.1	1.06	227	256	3903	6.525	0.84	969
4-2_5	4-2-2	1000.6	12.80	12.7	0.82	227	256	3903	6.525	0.87	764
4-2_6	4-2-2	999.5	13.71	13.7	0.89	227	256	3903	6.525	0.86	825
4-2_7	4-2-2	1000.2	14.17	14.1	0.92	227	256	3903	6.525	0.86	850
Mean		999.8	14.78	14.7	0.966	227	256	3903	6.525	0.85	890
S.D.		0.5	1.33	1.3	0.095						
Max		1000.6	16.20	16.2	1.068						
Min		999.3	12.80	12.7	0.824						

Spot Analysis	SHRIMP Analysis	Wavenumber Shift (cm^{-1})	$FWHM_{v3(SiO4)}$ (cm^{-1}) (Meas.)	$FWHM_{v3(SiO4)}$ (cm-1) (Corr.)	D_{eff} (10^{15} α/mg)	Th (μg/g)	U (μg/g)	$^{207}Pb/^{206}Pb$ Age (Ma)	D_{total} ($x10^{15}$ α/mg)	Frac. Anneal.	Rad Damage Age (Ma)
4-2_9	4-2-3	1002.7	10.24	10.2	0.64	23	123	3589	2.433	0.74	1343
4-2_10	4-2-3	1002.4	11.26	11.2	0.71	23	123	3589	2.433	0.71	1468
4-2_11	4-2-3	1002.3	11.02	11.0	0.70	23	123	3589	2.433	0.71	1450
Mean		1002.5	10.84	10.8	0.684	23	123	3589	2.433	0.72	1422
S.D.		0.2	0.53	0.5	0.038						
Max		1002.7	11.26	11.2	0.714						
Min		1002.3	10.24	10.2	0.641						
7-1_1	7-1-3	1001.2	11.88	11.8	0.76	193	314	3619	6.715	0.89	617
7-1_2	7-1-3	1000.9	11.71	11.7	0.75	193	314	3619	6.715	0.89	609
7-1_3	7-1-3	1002.6	9.78	9.7	0.61	193	314	3619	6.715	0.91	500
7-1_4	7-1-3	1002.2	10.11	10.0	0.63	193	314	3619	6.715	0.91	516
Mean		1001.7	10.87	10.8	0.686	193	314	3619	6.715	0.90	560
S.D.		0.8	1.08	1.1	0.078						
Max		1002.6	11.88	11.8	0.759						
Min		1000.9	9.78	9.7	0.608						
7-1_5	7-1-2	1005.4	4.82	4.7	0.25	23	63	4164	1.708	0.85	1022
7-1_6	7-1-2	1005.0	6.03	5.9	0.34	23	63	4164	1.708	0.80	1343
7-1_7	7-1-2	1005.1	5.23	5.1	0.28	23	63	4164	1.708	0.84	1132
7-1_8	7-1-2	1005.1	5.50	5.4	0.30	23	63	4164	1.708	0.83	1203
7-1_9	7-1-2	1003.0	9.72	9.6	0.60	23	63	4164	1.708	0.65	2150
7-1_10	7-1-2	1002.9	7.01	6.9	0.41	23	63	4164	1.708	0.76	1578
Mean		1004.4	6.38	6.3	0.362	23	63	4164	1.708	0.79	1418
S.D.		1.1	1.80	1.8	0.130						
Max		1005.4	9.72	9.6	0.603						
Min		1002.9	4.82	4.7	0.249						

Spot Analysis	SHRIMP Analysis	Wavenumber Shift (cm^{-1})	$FWHM_{v3(SiO4)}$ (cm^{-1}) (Meas.)	$FWHM_{v3(SiO4)}$ (cm-1) (Corr.)	D_{eff} (10^{15} α/mg)	Th (μg/g)	U (μg/g)	$^{207}Pb/^{206}Pb$ Age (Ma)	D_{total} ($x10^{15}$ α/mg)	Frac. Anneal.	Rad Damage Age (Ma)
7-1_11	7-1-1	1002.5	9.81	9.7	0.61	29	70	4158	1.904	0.68	1990
7-1_12*	7-1-1	1002.4	9.01	8.9	0.55	29	70	4158	1.904	0.71	1831
7-1_13	7-1-1	1004.8	5.23	5.1	0.28	29	70	4158	1.904	0.85	1020
7-1_14	7-1-1	1004.0	5.58	5.5	0.30	29	70	4158	1.904	0.84	1086
Mean		1003.4	7.41	7.3	0.436	29	70	4158	1.904	0.77	1508
S.D.		1.2	2.34	2.4	0.169						
Max		1004.8	9.81	9.7	0.610						
Min		1002.4	5.23	5.1	0.279						

*Denotes Raman analyses proximal to APT lift-out.

Appendix 6: Mount images for lunar zircon mounts LZ1 and LZ2 (data in Chapter 4) and additional mounts QMD1, QMD2, QMD3, and QMD4.

Lunar zircon mounts LZ1 and LZ2 were made in preparation for U-Pb analyses at the Stanford-USGS SHRIMP Lab. Lunar zircon grains were originally mounted individually in separate mounts with standard reference materials. It was determined that U-Pb dating of the grains required they be concentrated in a smaller number of epoxy mounts. To facilitate this, original mounts were trimmed to form small blocks, with the lunar zircons and their associated reference grains, then remounted along with a block of standards provided by M. Coble at Stanford. Below are images of the completed mounts. Note: zircons 12R-5 and 12R-6 were lost prior to remounting, but the blocks were remounted for completeness.

QMD mounts 1-4 contain small fragments of granitic material from lunar sample 15405,217. No data for these grains are within this thesis, but images of the surfaces, and zircons exposed within them, are provided below.

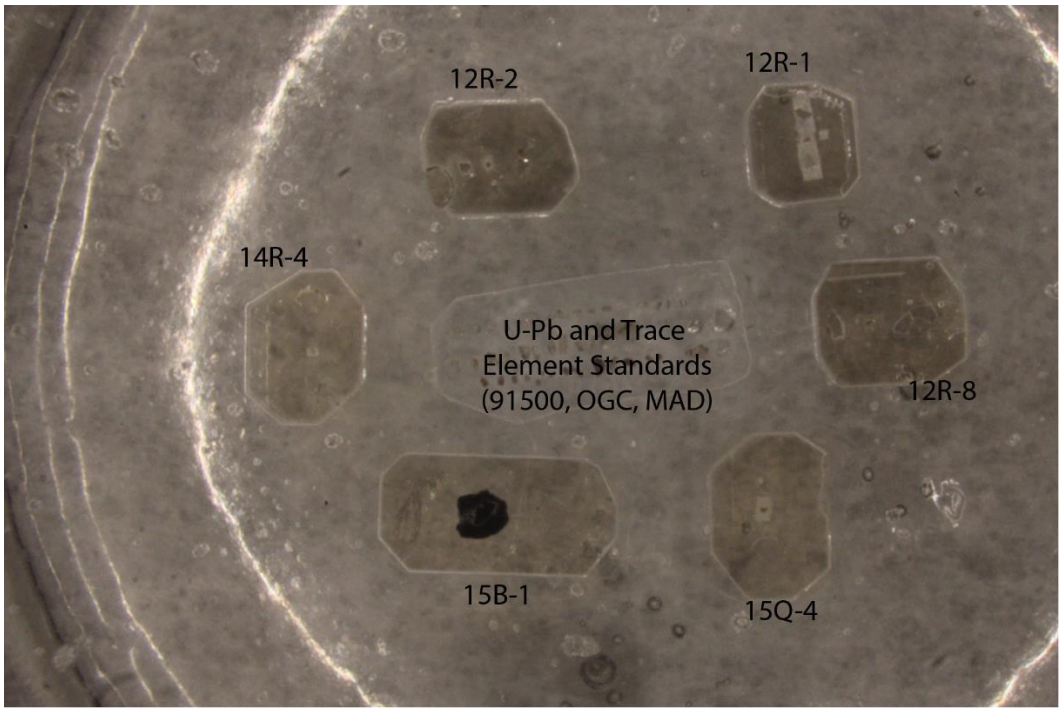

Mount LZ 1

Mount LZ 2

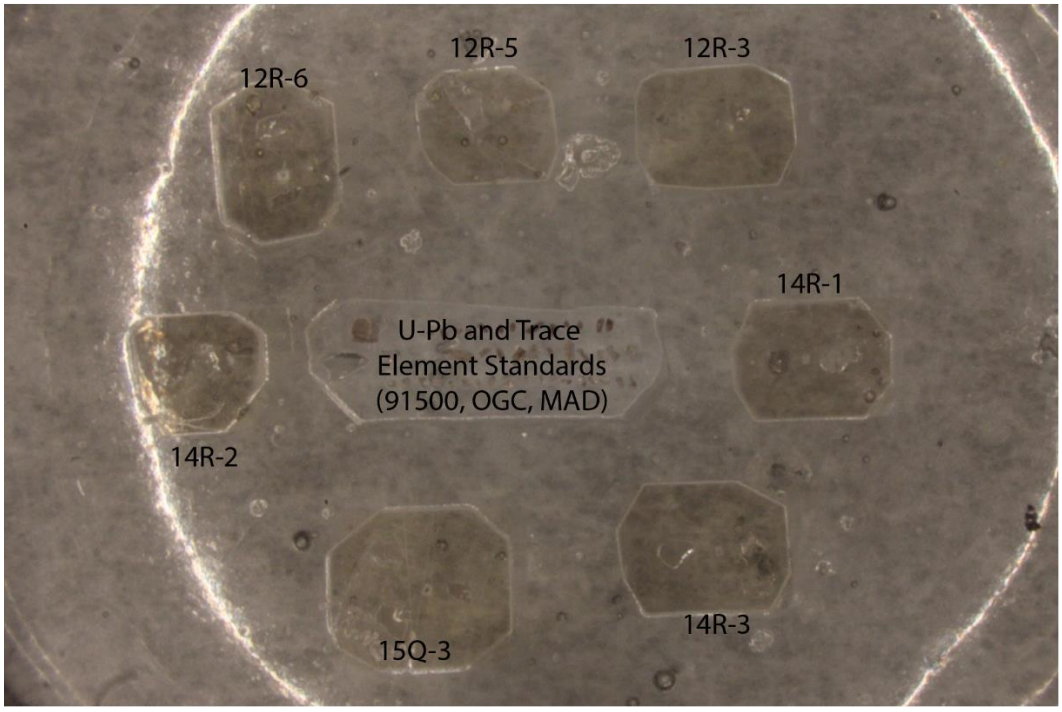

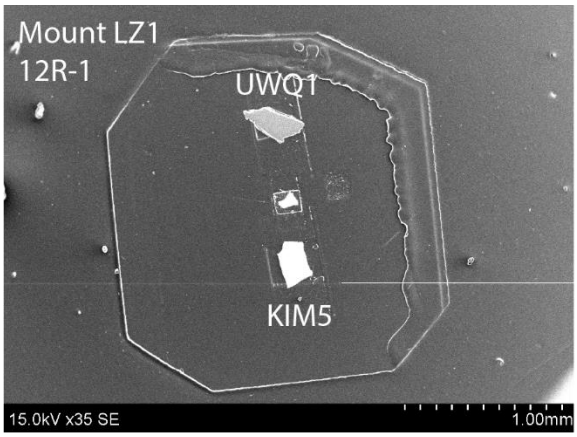
Mount LZ1
12R-1
UWQ1
KIM5
15.0kV x35 SE
1.00mm

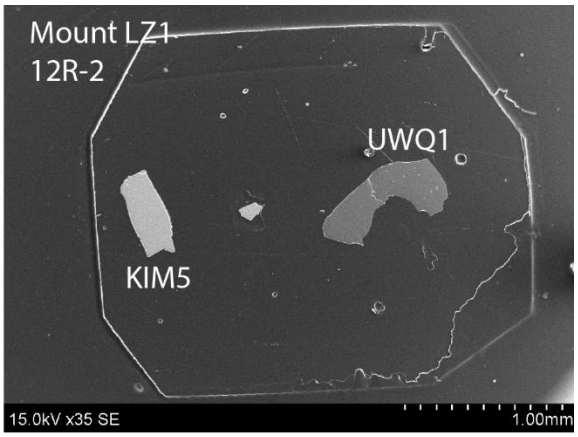
Mount LZ1
12R-2
UWQ1
KIM5
15.0kV x35 SE
1.00mm

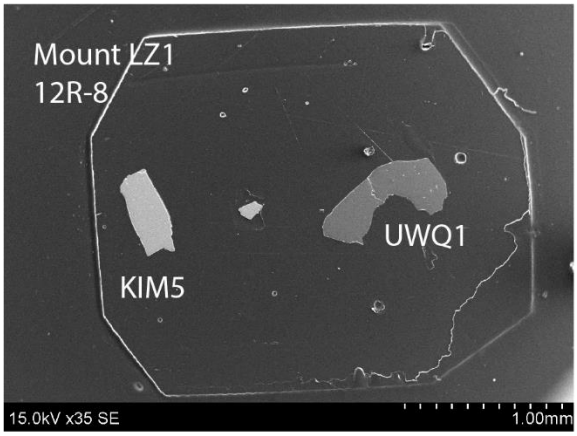
Mount LZ1
12R-8
UWQ1
KIM5
15.0kV x35 SE
1.00mm

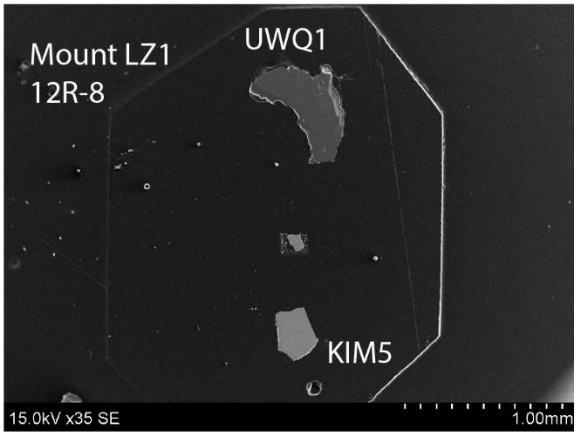
Mount LZ1
12R-8
UWQ1
KIM5
15.0kV x35 SE
1.00mm

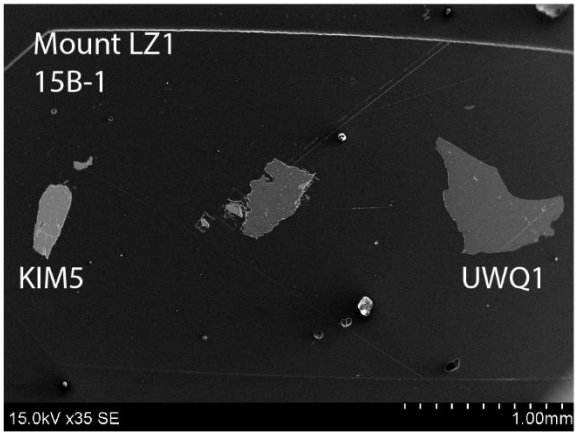
Mount LZ1
15B-1
KIM5
UWQ1
15.0kV x35 SE
1.00mm

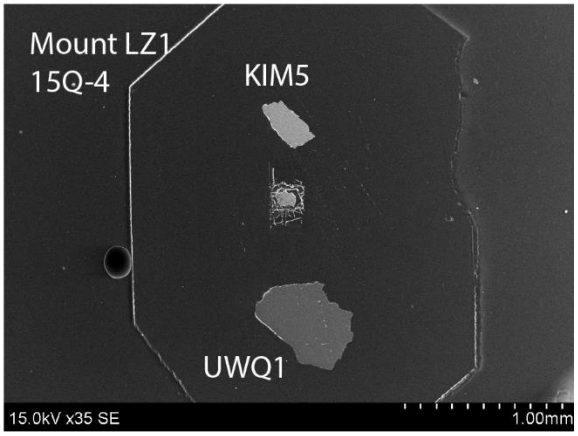
Mount LZ1
15Q-4
KIM5
UWQ1
15.0kV x35 SE
1.00mm

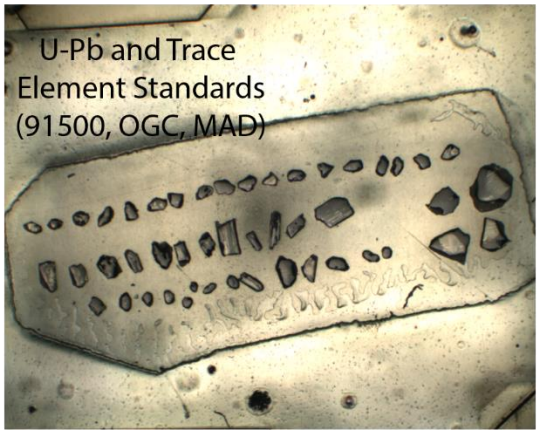
U-Pb and Trace
Element Standards
(91500, OGC, MAD)

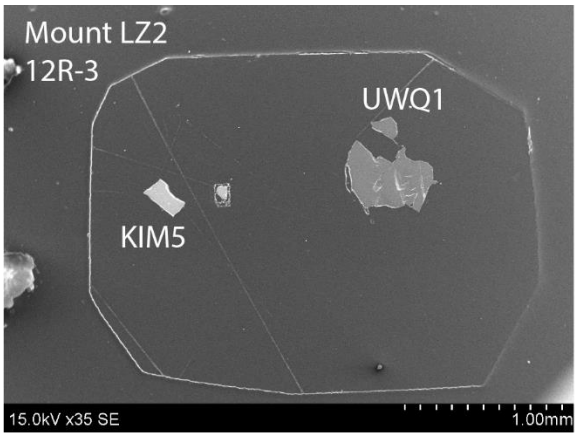
Mount LZ2
12R-3
UWQ1
KIM5
15.0kV x35 SE
1.00mm

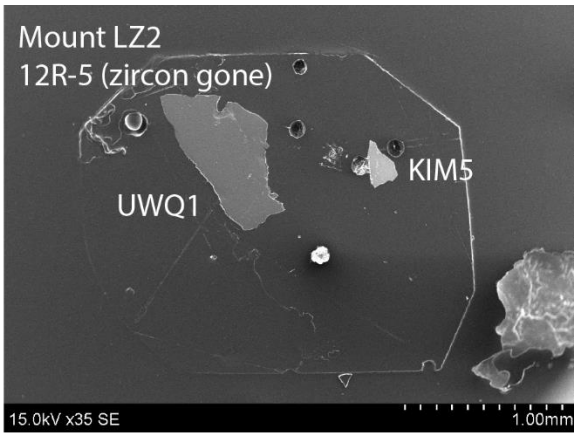
Mount LZ2
12R-5 (zircon gone)
KIM5
UWQ1
15.0kV x35 SE
1.00mm

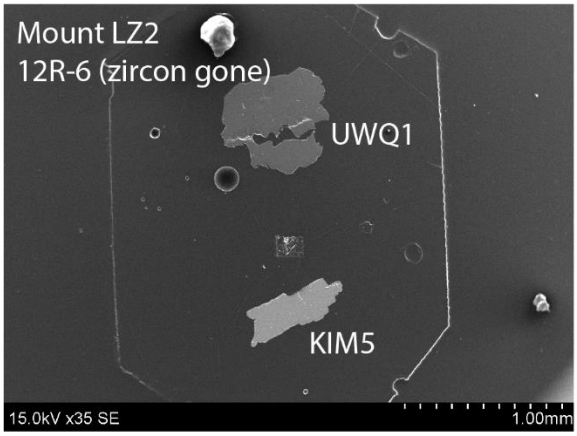
Mount LZ2
12R-6 (zircon gone)
UWQ1
KIM5
15.0kV x35 SE
1.00mm

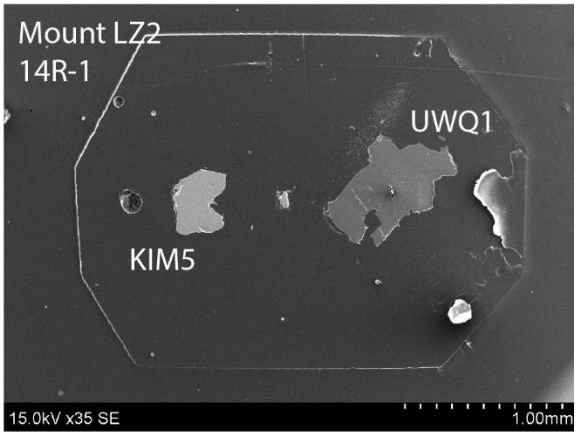
Mount LZ2
14R-1
UWQ1
KIM5
15.0kV x35 SE
1.00mm

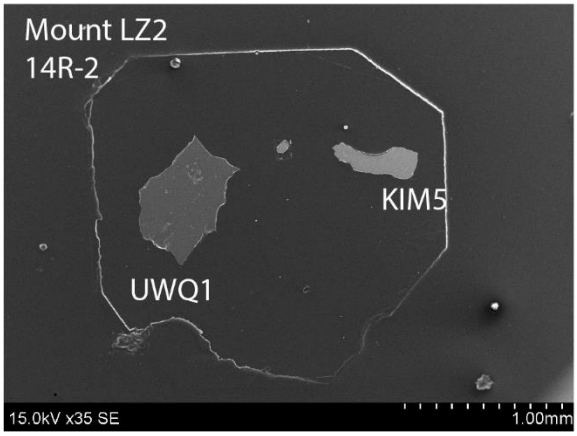
Mount LZ2
14R-2
KIM5
UWQ1
15.0kV x35 SE
1.00mm

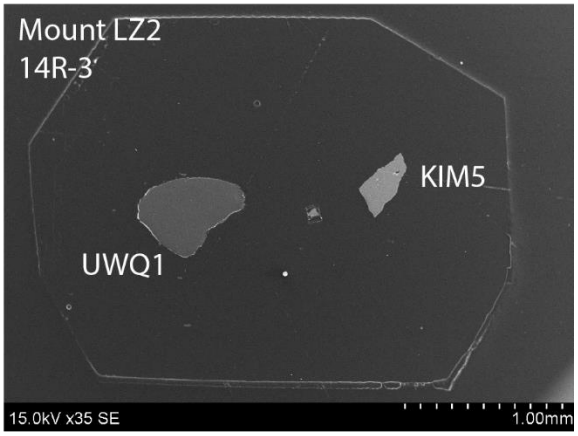
Mount LZ2
14R-3
KIM5
UWQ1
15.0kV x35 SE
1.00mm

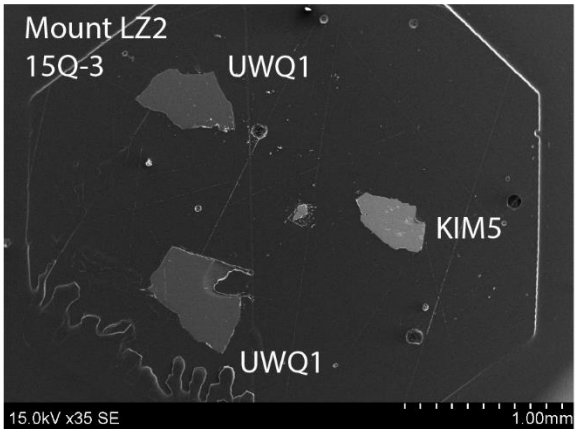
Mount LZ2
15Q-3
UWQ1
KIM5
UWQ1
15.0kV x35 SE
1.00mm

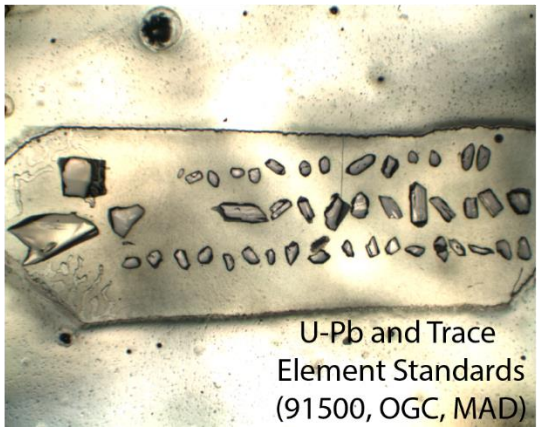
U-Pb and Trace
Element Standards
(91500, OGC, MAD)

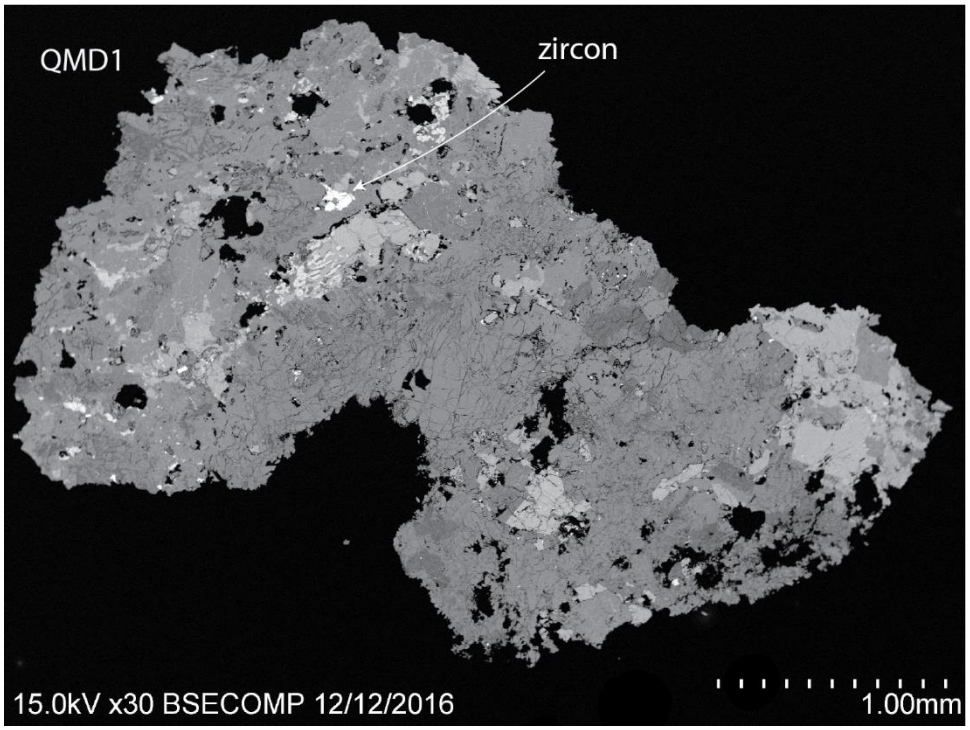
QMD1
zircon
15.0kV x30 BSECOMP 12/12/2016
1.00mm

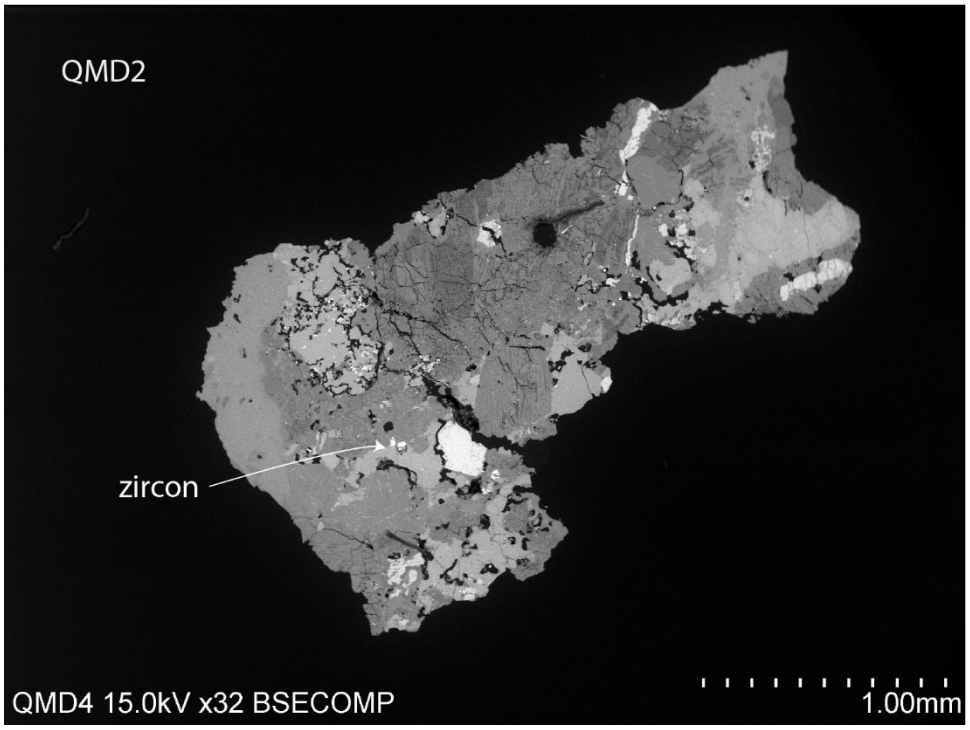
QMD2
zircon
QMD4 15.0kV x32 BSECOMP
1.00mm

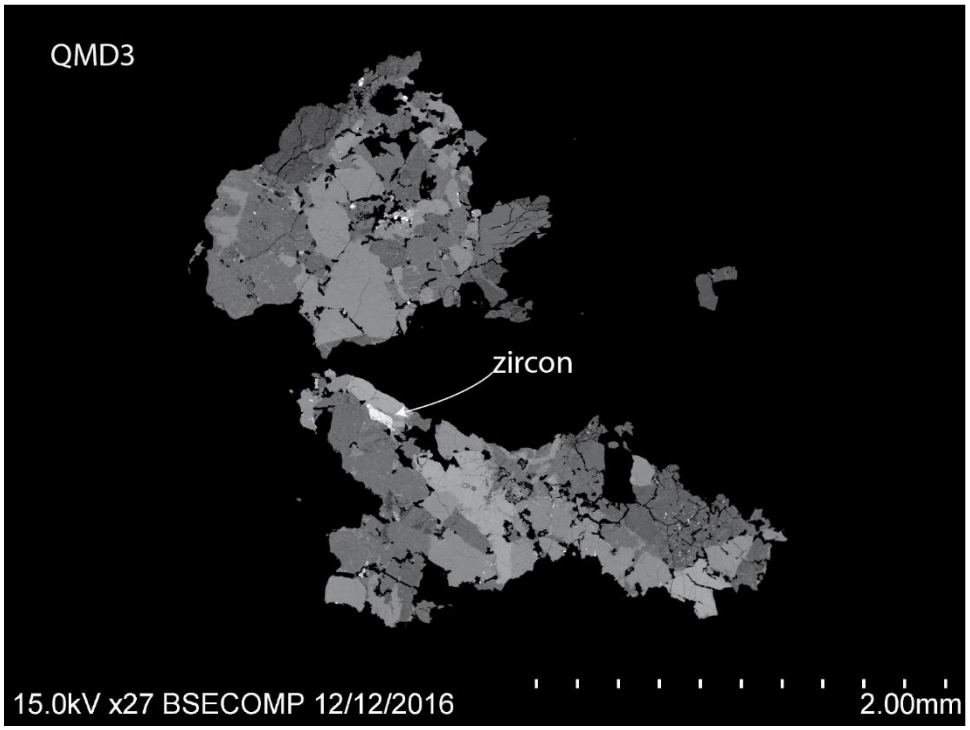
QMD3
zircon
15.0kV x27 BSECOMP 12/12/2016
2.00mm

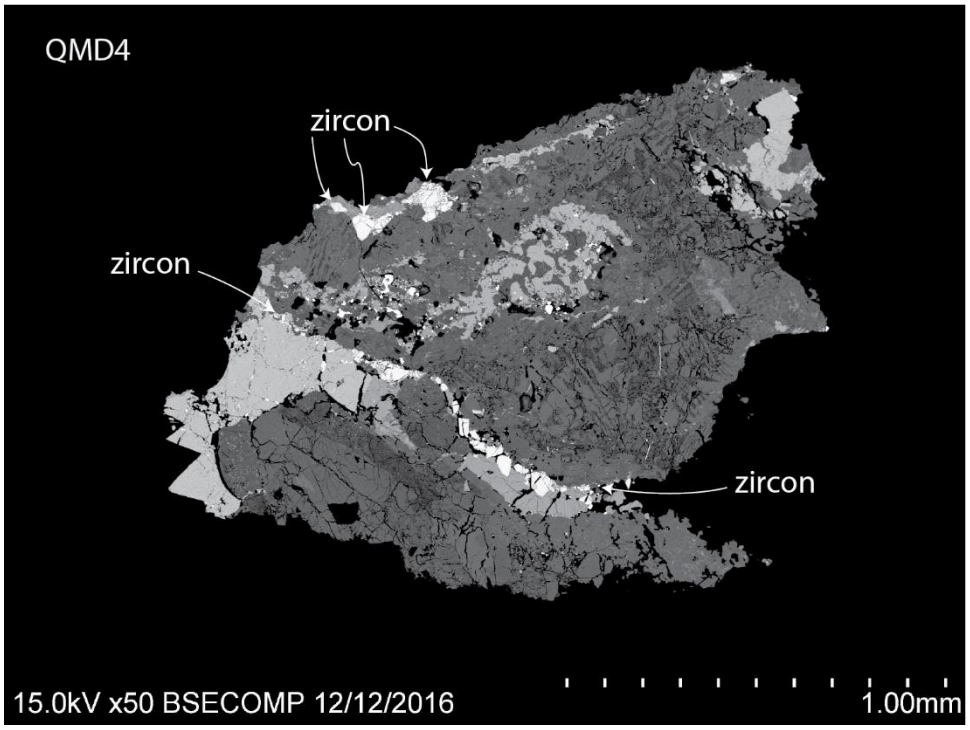
QMD4
zircon
zircon
zircon
15.0kV x50 BSECOMP 12/12/2016
1.00mm